# A comprehensive study of the young star cluster HD 97950 in NGC 3603

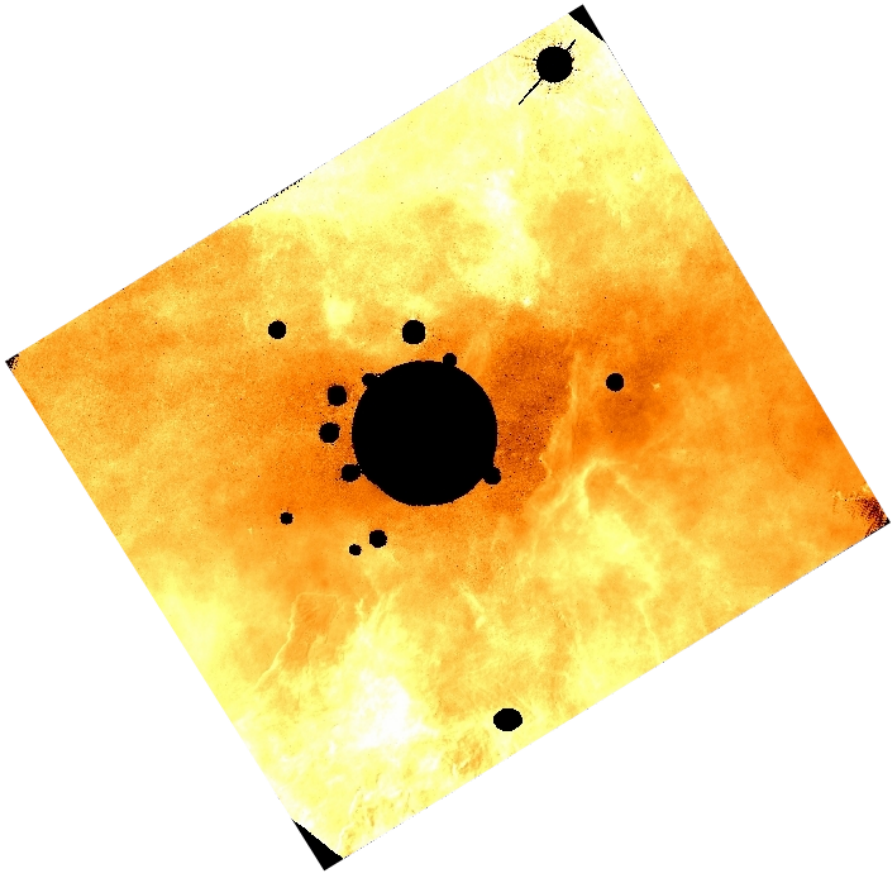

**Xiaoying Pang**

Dissertation

submitted to the

Combined Faculties for the Natural Sciences and for Mathematics

of the Ruperto–Carola University of Heidelberg, Germany

for the degree of

Doctor of Natural Sciences

presented by

Xiaoying Pang

Born in Zhanjiang, China

Oral examination: $21^{st}$ May 2012

# A comprehensive study of the young star cluster HD 97950 in NGC 3603

Xiaoying Pang

Referees: Prof. Dr. Eva K. Grebel
Dr. Henrik Beuther

To my parents
whose suppport and love have been invaluable

# *How great Thou art*

*O Lord my God,*
*When I in awesome wonder*
*Consider all the world Thy Hand hath made,*
*I see the stars*
*I hear the rolling thunder*
*Thy power throughout the universe displayed;*
*My Saviour God, to Thee,*
*How great Thou art!*
*Then sings my soul,*
*My Saviour God, to Thee,*
*How great Thou art!*
*When through the woods*
*And forest glades I wander*
*I hear the birds*
*Sing sweetly in the trees;*
*When I look down*
*From lofty mountain grandeur*
*And hear the brook*
*And feel the gentle breeze;*
*And when I think,*
*That God, His Son not sparing;*
*Sent Him to die,*
*I scarce can take it in;*
*That on the Cross,*
*My burden gladly bearing,*
*He bled and died*
*To take away my sin.*
*When Christ shall come,*
*With shouts of acclamation,*
*And take me home,*
*What joy shall fill my heart!*
*Then I shall bow*
*In humble adoration*
*And there proclaim,*
*”My God, how great Thou art!”*

# Abstract

I study the young massive star cluster HD 97950 located in the Galactic giant H II region NGC 3603. My goals are (1) to estimate the survival probability of the cluster, (2) to investigate the origin of its mass segregation, and (3) to investigate the interplay between the cluster and the surrounding interstellar medium (ISM). All the studies are done with data of the Hubble Space Telescope. I determine the cluster velocity dispersion from the stars' relative proper motions, and calculate the virial mass of the cluster. The cluster star formation efficiency is estimated to be about 50%, which suggests that the HD 97950 cluster will most likely survive as a bound cluster to gas expulsion. I apply the $\Lambda$ minimum spanning tree technique to measure the mass segregation down to $30\,\mathrm{M}_{\odot}$. The high-mass stars are more segregated than low-mass stars, implying that the mass segregation in HD 97950 is mostly of dynamical origin. To improve the age determination for the cluster stars that are severely reddened by the surrounding dusty ISM, I compute a pixel-to-pixel distribution of the gas reddening, $E(B-V)_{\mathrm{g}}$, associated with the cluster. The radial profiles of $E(B-V)_{\mathrm{g}}$ show significant spatial variations around HD 97950. Using $UBVRI$ photometry, I estimate the stellar reddening of cluster stars. After correcting for foreground reddening, the total to selective extinction ratio in the cluster is $R_V = 3.49 \pm 0.79$. The extinction curve in the $UBVRI$ filters in the cluster is greyer than the average Galactic extinction laws, but close to the extinction law for starburst galaxies. This indicates that stellar feedback from massive stars changes the dust properties in the HD 97950 cluster in a similar way as in starburst galaxies.



# Zusammenfassung

Ich studiere den jungen massereichen Sternhaufen HD 97950 in der Riesen-H II-Region NGC -3603 im Carina-Spiralarm. Ich schätze seine Überlebenswahrscheinlichkeit ab, untersuche die Ursachen seiner Massensegregation und studiere das Wechselspiel zwischen dem Sternhaufen und dem umgebenden interstellaren Medium (ISM). Alle Untersuchungen verwenden Daten des Hubble-Teleskops(HST). Ich bestimme die Geschwindigkeitsdispersion des Sternhaufens aus der relativen Eigenbewegung seiner Sterne und berechne seine Virialmasse. Die Sternenstehungseffizienz des Sternhaufens (SFE) schätze ich auf etwa 50%, was nahelegt, dass HD 97950 den Ausstoß seines Gases als gebundener Sternhaufen üeberleben wird. Ich verwende die $\Lambda$ minimum spanning tree Technik zur Messung der Segregation oberhalb $30\,\mathrm{M}_{\odot}$. Massive Sterne unterliegen stärkerer Segregation, was nahelegt, dass die Massensegregation primär dynamischer Natur ist. Um die Altersbestimmung für Sterne zu verbessern, die durch das ISM starke Verfärbung erfahren, berechne ich die Verteilung des Farbexzesses $E(B-V)_{\mathrm{g}}$ des mit dem Sternhaufen assoziierten Gases Pixel für Pixel. Die Radialprofile von $E(B-V)_{\mathrm{g}}$ zeigen signifikante räumliche Variationen um HD 97950. Anhand von $UBVRI$-Photometrie erforsche ich die stellare Verfärbung in der Region. Die Extinktionskurven in den $UBVRI$ Filtern sind grauer als die Gesetze der mittleren galaktischen Extinktion,ähneln aber dem Extinktionsgesetz für Starburstgalaxien. Dies deutet darauf hin, dass massive Sterne die Staubeigenschaften in HD 97950 durch Rückkopplung verñdern, ähnlich wie in Starburstgalaxien.

# Contents

# List of Figures

# List of Tables

# 1 Introduction

Show respect to the stars in the heaven:
*And beware lest you raise your eyes to heaven, and when you see the sun and the moon and the stars, all the host of heaven, you be drawn away and bow down to them and serve them, things that the Lord your God has allotted to all the peoples under the whole heaven. (Matthew 2:1-23)*

## 1.1 The cradles of star formation – giant molecular clouds

Molecular clouds are the coolest ($T \sim 10\,\mathrm{K}$) objects in the Universe, which exist in the interstellar medium (ISM) where they are sufficiently shielded by dust with a visual extinction of $A_V \sim 0.5$ (Pringle et al. 2001). Therefore, only infrared or even longer-wavelength imaging can probe them deeply. In our Milky Way, they contain about half of the mass of the ISM within the solar circle (Dame et al. 1993). Most of the mass of the molecular ISM is in the form of giant molecular clouds (GMCs) with masses of $10^{5-6}\,\mathrm{M}_\odot$, diameters of about 50 pc, and average densities of $n_{\mathrm{H}_2} \sim 10^2\,\mathrm{cm}^{-3}$ (Williams et al. 2000). They often are highly irregular, clumpy and filamentary (see Figure 1.1). When the molecular gas in GMCs is compressed (e.g., by spiral shocks: Shu et al. 1972), a sufficient fraction of it may become self-gravitating and dense enough to initiate star formation.

The dense cores in GMCs, which reach an average density of $n_{\mathrm{H}_2} \sim 10^5\,\mathrm{cm}^{-3}$, are the places to form individual stars or multiple stellar systems. These active star-forming sites in GMCs contain clear signatures of both low-mass and high-mass star formation. Figure 1.1 shows the dense cores of the Rosette molecular cloud taken with Herschel Space Telescope. The bright smudges are dusty cores containing high-mass protostars. The small spots near the center of the image are lower mass protostars.

The star-forming cores usually belong to bound star-forming clumps where stellar clusters

form. Figure 1.2 shows an image taken with the Wide Field Camera 3 on board the Hubble Space Telescope of the GMC 30 Doradus, which is a turbulent star-forming region in the Large Magellanic Cloud. The star formation in 30 Doradus created the massive cluster R 136, in which many blue massive stars radiate high-energy photons and expel stellar winds to disperse the surrounding gas. This feedback and radiation created an H II region and triggers continuing star formation in the ambient molecular clouds (Walborn et al. 1999).

Figure 1.1: Infrared image of the Rosette molecular cloud. The Herschel Space Telescope observes the infrared light emitted by dust. This image is a three-color composite consisting of wavelengths at 70 microns (blue), 160 microns (green) and 250 microns (red). It was made with observations from Herschel's Photoconductor Array Camera and Spectrometer (PACS) and the Spectral and Photometric Imaging Receiver (SPIRE). Credits: ESA/PACS & SPIRE Consortium/HOBYS Key Programme Consortia.

GMCs appear to be the sites of essentially all the star formation that is occurring in the Galaxy. However, only about 10 percent of the mass of a typical GMC is sufficiently shielded from photoionization by a column density of dust corresponding to $A_V \geq 3 - 4$ (Bertoldi & Mckee 1996) to form stars. The majority of the molecular gas in GMCs will be quickly disassociated back into atomic form by the general UV background photon flux from the new-born massive stars, which can eventually disperse GMCs within several dynamical timescales ($3 \times 10^7$ yr).

## 1.2 Star formation in clustered environment

The gravitational collapse of the most massive cores in GMCs and subsequent star formation produces a combination of single stellar objects and multiple stellar systems. These objects and

Figure 1.2: An image of 30 Doradus taken in ultraviolet, visible, and red light by Hubble's Wide Field Camera 3. The blue color is light from the hottest, most massive stars; the green from the glow of oxygen; and the red from $H_\alpha$ emission.

systems will fall together into the gravitational potential well to form a star cluster (Bate et al. 2003). In the Milky Way, about 70% of the O-type stars reside in young clusters or associations (Gies 1987). Therefore, stars are typically formed in clustered environments (Lada & Lada 2003). This statement is supported by observations that 96% of the stars in the nearby Orion B star-forming region are clustered (Clarke et al. 2000). De Wit et al. (2005) statistically show that ∼50% of the remaining Galactic field population are contributed by runaway stars from star clusters. Hence, clusters are the primary mode of star formation in the Galaxy.

Stars in the clusters can be roughly divided into two groups based on their mass, low-mass ($< 8\,\mathrm{M}_\odot$) and high-mass ($> 8\,\mathrm{M}_\odot$). Low-mass star forms in a time shorter than the Kelvin-Helmholz time, which is the time needed to radiate away a significant fraction of the thermal energy of a contracting star,

$$t_{\mathrm{KH}} = Gm^2/RL, \tag{1.1}$$

where $G$ is the gravitational constant, and $m$, $R$, $L$ are the mass, radius, and luminosity of a star, respectively.

### 1.2.1 Low-mass star formation

Low-mass stars form from gravitationally bound isothermal dense cores (Larson 2003), which undergo gravitational collapse and become very centrally concentrated. The density profile of

dense cores approximates Bonnor-Ebert spheres, which is the density profile under substantial external pressure, as suggested from observations (Alves et al. 2001; Kirk et al. 2005),

$$\rho = \frac{\rho_c R_c^2}{R_c^2 + r^2}, \tag{1.2}$$

where $\rho_c$ is the central density of sphere, $R_c$ is the radius of sphere, and $r$ is the distance from the center of sphere. Additionally, turbulence can act positively on low-mass star formation by stabilizing GMCs and allowing smaller scales to collapse gravitationally (Bonazzola et al. 1992). Afterwards, low-mass stars undergo extensive pre-main-sequence evolution in the Hertzsprung-Russell diagram, from the point on the birthline, where they cease accreting and begin the main sequence phase (Larson 1972).

The low-mass extreme of star formation is the formation of brown dwarfs. They are objects with mass as of less than $0.08\,\mathrm{M}_\odot$ that fail to ignite hydrogen burning in the core, which is characteristic of stars on the main sequence. Large-scale hydrodynamical calculations have been performed to investigate their formation from the collapse and fragmentation of turbulent molecular clouds (e.g., Burkert et al. 1997; Bonnell 1997; Bate at al. 2003). Most simulations suggest that the low-mass objects in the clump stop accreting before they reach stellar masses ($0.08\,\mathrm{M}_\odot$). They were ejected from the regions of dense gas soon after their formation by dynamically unstable multiple systems, and end up as brown dwarfs. The ejection process is believed to be very efficient, producing roughly equal number of low-mass stars and brown dwarfs (Bate at al. 2002).

### 1.2.2 High-mass star formation

Different from low-mass star formation, the high-mass protostars have an accretion time longer than the Kelvin-Helmholtz time, so that they can ignite nuclear burning while still accreting gas. During this accretion, massive protostars must overcome two powerful feedback effects – radiation pressure and photoionization (Larson & Starrfield 1971), which does not apply to low-mass star formation. There are four main models that try to solve the problem of high-mass star formation.

1) Infall model

Stahler et al. (1980) suggested a high accretion rate of massive protostars in order to overcome the effects of radiation pressure,

$$\dot{m}_* = c_{\mathrm{eff}}^3/G, \tag{1.3}$$

where $c_{\mathrm{eff}}$ is the effective sound speed including effects of thermal gas pressure, magnetic pressure, and turbulence. In the high-mass star-forming region, the gas is heated up due to the radiation of massive protostars. Thus $c_{\mathrm{eff}}$ increases dramatically, leading to an accretion rate of the order of $10^{-3}\,\mathrm{M}_\odot\,\mathrm{year}^{-1}$ (Wolfire & Cassinelli 1987). Nakano et al. (2000) inferred an accretion rate of $10^{-2}\,\mathrm{M}_\odot\,\mathrm{year}^{-1}$ from the infrared source IRc2 in the Orion Nebula, based on the assumption of equation (1.3). With such an accretion rate, high-mass stars can be formed within a few thousand years.

2) Turbulent core model

McKee & Tan (2002) proposed that stars form in self-similar turbulent, gravitationally bound

cores. The protostellar accretion rate is determined by the surface density of the protostellar core. For a typical surface density of $1\,\mathrm{g\,cm^{-2}}$ in star-forming cores, the resulting accretion rate is of the order of $10^{-3}\,\mathrm{M_\odot\,year^{-1}}$. The time to form a star of $60\,\mathrm{M_\odot}$ is at the order of $10^5$ years (McKee & Tan 2003).

3) Competitive accretion model

During the gravitational collapse, stars are formed primarily by the capture and subsequent accretion of matter that is initially unbound to the star (Bonnell et al. 1997). During this subsequent accretion period, protostars compete for gas from a common reservoir. This process is called "competitive accretion". Bonnell et al. (1997, 2001) show that a few protostars gain most of the mass, which are the ones that reside primarily in the central region of a clump. These "lucky" protostars in the center continue accreting via Bondi-Hoyle (BH) accretion: $\dot{m}_* \propto m_*^2$, which is spherical accretion onto an object. The accretion rate $\dot{m}_*$ is proportional to the mass of the protostar $m_*$. These protostars will become massive stars later on. However, the BH accretion rate is much smaller than that expected in the turbulent core model (McKee & Tan 2003). Edgar & Clarke (2004) have shown that the radiation halts BH accretion when the star is moving supersonically relative to the gas for stars above $10\,\mathrm{M_\odot}$.

4) Stellar collision model

Another suggestion for the high-mass star formation is via stellar collisions in regions of stellar densities of $\sim 10^8\,\mathrm{stars\,pc^{-3}}$ (Bonnell et al. 1998). However, such a high stellar density is two orders of magnitude higher than the observed value of $4 \times 10^5\,\mathrm{stars\,pc^{-3}}$ from prestellar cores in the GMC W3.

## 1.3 Initial mass function

The initial mass function (IMF) specifies the distribution in mass of a freshly formed stellar population. The standard IMF is generally presented by a power-law,

$$dN \propto m^{-\alpha} dm, \tag{1.4}$$

or a log-normal type mass distribution,

$$dN \propto m^{\Gamma} d(\log m), \tag{1.5}$$

where $\Gamma = -(\alpha - 1)$. The slope of the IMF was originally derived by Salpeter (1955), who found $\alpha = 2.35$ or $\Gamma = -1.35$. The recent IMF of Kroupa (2001) is a three-part segmented power-law with breaks at $0.08\,\mathrm{M_\odot}$ and $0.5\,\mathrm{M_\odot}$ (Figure 1.3), and with a similar slope to the Salpeter (1995) law at the high-mass part.

$$\begin{aligned} dN &\propto m^{-1.3} d(\log m) \;\; (m \geq 0.5\,\mathrm{M_\odot}) \\ dN &\propto m^{-0.3} d(\log m) \;\; (0.08 \leq m \leq 0.5\,\mathrm{M_\odot}) \\ dN &\propto m^{0.7} d(\log m) \;\; (m \leq 0.08\,\mathrm{M_\odot}) \end{aligned} \tag{1.6}$$

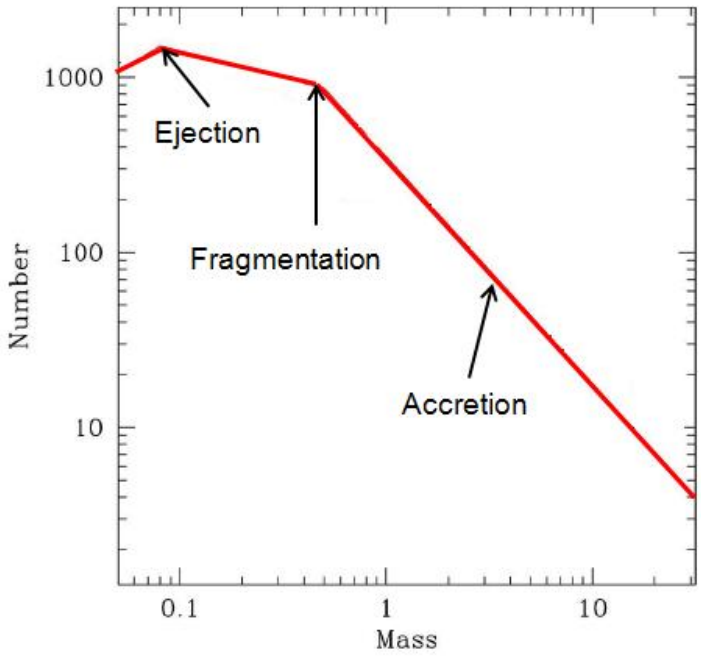


Figure 1.3: The Kroupa (2001) segmented power-law IMF. Individual physical processes that determine the shape of the IMF are indicated at the appropriate parts of the IMF.

One of the goals of considerable theoretical studies of star formation is to understand the origin of the IMF and the physics that determine the distribution of stellar masses (Scalo 1986; Kroupa 2001, 2002; Chabrier 2003). The Salpeter slope shows no significant change for stars above the characteristic mass, which is the turnover of upper-mass IMF [0.5 $\mathrm{M}_{\odot}$ for Kroupa (2001) IMF], over a wide range of star-forming environments from observations (Kroupa 2001; Luhman et al. 2000; Corbelli et al. 2005) and hydrodynamical calculations (Bate et al. 2003; Bate 2009). This might imply that the IMF is independent of the mean density, turbulence level, magnetic field strength, and to large extent also metallicity (McKee & Ostriker 2007). However, in their most recent work, Kroupa et al. (2011) argue that the IMF depends on the star-formation rate density and on the metallicity of the stars. The IMF becomes top-heavy for a star-formation rate density above $0.1\mathrm{M}_{\odot}/(\mathrm{yr\,pc}^3)$ on a pc scale, and becomes increasingly bottom-heavy with increasing metallicity.

There are a number of physical processes which are likely to take place during the star formation process and thus affect the resulting distribution of stellar mass. First of all, gravity is the force that plays a positive role in star formation. It generates clumpy structure from the smooth ISM through gravitational fragmentation. The primary requirement for gravitational fragmentation is an initial overdensity which generates the focus of gravity. Several possibilities can initiate an overdensity, such as a small density perturbations triggered by turbulence (Silk 1982), or de-

formations in the form of sheets (Burkert & Hartmann 2004), or filaments (Bastien et al. 1991).

The minimum mass for which gravitational fragmentation can occur is the Jeans mass, which is the mass necessary for an object to be bound gravitationally against its thermal pressure,

$$M_{\rm Jeans} \approx 1.1(T_{10}^{3/2})(\rho_{19}^{-1/2})\,{\rm M}_{\odot}, \tag{1.7}$$

where $\rho_{19}$ is the gas density in units of $10^{-19}\,{\rm g\,cm^{-3}}$ and $T_{10}$ is the temperature in units of 10 K. At the typical temperature of a molecular cloud of 10 K, and the typical density of a star-forming clump of $10^{-18}$ to $10^{-19}\,{\rm g\,cm^{-3}}$, the typical Jeans mass is around 0.3–1 ${\rm M}_{\odot}$ (Klessen et al. 1998; Bate et al. 2003), which agrees with the characteristic stellar mass of the IMF (Kroupa 2001). Stellar masses significantly lower than the characteristic stellar mass can also be explained by gravitational fragmentation at higher gas density.

However, the Jeans mass is too small to account for the high-mass star formation. Instead gas accretion plays the major role in building up the mass of stars (Section 1.2.2). There is a roughly linear correlation between an object's final mass and its accretion time (Bate & Bonnell 2005). Therefore, protostars must continue accretion for a long time until they reach high masses. This accretion can be mass-dependent (Bonnell et al. 2001) or gas density dependent (Bonell et al. 1997). The more massive the pre-stellar cores, the more competitive they are in gas accretion (Bonnell et al. 2001). On the contrary, the low-mass stars or brown dwarfs stop accreting due to being ejected from their natal environment through stellar interactions. We show the individual processes determining different portions of the IMF in Figure 1.3 (Bonnell et al. 2007).

## 1.4 Dynamical evolution of star cluster

As soon as the star formation in a clustered environment takes off, dynamical evolution begins (Pringle et al. 2001). Testi et al. (2000) find that the Serpens pre-stellar cores are subclustering, which suggests that the fragmentation process in the clump is hierarchical and that young star clusters are assembled by the merger of substructures (Bonell et al. 2003). After the formation of stars in the cluster, dynamical evolution is driven by two-body relaxation. The relaxation time (equation 1.8) is the timescale on which stars tend to establish a Maxwellian velocity distribution,

$$t_{\rm rh} \sim 2\times10^{8}\,{\rm year}\left(\frac{M}{10^{6}\,{\rm M}_{\odot}}\right)^{1/2}\left(\frac{r_{\rm vir}}{1\,{\rm pc}}\right)^{3/2}\left(\frac{\langle m\rangle}{{\rm M}_{\odot}}\right)^{-1}, \tag{1.8}$$

where $M$ is the mass of a cluster, $r_{\rm vir}$ is the cluster virial radius (see its expression in equation 1.9), and $\langle m\rangle$ is the global mean stellar mass in a cluster.

$$r_{\rm vir} = \frac{GM^2}{2|U|}, \tag{1.9}$$

where $U$ is the total potential energy of a cluster.

The two-body relaxation drives the cluster toward energy equipartition. Thus the kinematic energy of stars of different masses will be: $mv^2 \sim$constant ($v$ is the individual space velocity

of a star and $m$ is stellar mass). Therefore, high-mass stars are expected to slow down and sink to the center of the cluster, and low-mass stars move further away from the cluster center with high velocities. A small fraction of the latter may even have velocities larger than the escape velocity and can consequently escape (Binney & Tremaine 1987). This results in dynamical mass segregation.

### 1.4.1 Mass segregation

#### To observe mass segregation

To quantify the effect of mass segregation, the differences in the spatial distribution of high- and low-mass stars, the commonly used methods are to measure (1) the change in the slope of the radial mass function, in which case mass segregation manifests as a flatter slope in the inner annuli (Sung & Bessell 2004; Harayama et al. 2008; Pang et al. 2010); (2) the radial differences in the ratio of high- to low-mass stars (Hillenbrand 1997); (3) the cumulative radial density distribution of samples of different masses (Hillenbrand & Hartmann 1998); and (4) the mean radius of the high- and low-mass star distributions (de Grijs et al. 2002). However, these methods of determining the presence of mass segregation depend on 1) the determination of the cluster center, which is usually difficult to define; 2) the number of mass bins; 3) the size of the bins for mass which can affect the variation of the shape and the slope of the mass function (Ascenso et al. 2009; Gouliermis et al. 2004).

Therefore, Allison et al. (2009a) propose the use of the minimum spanning tree (MST) method to quantify the amount of mass segregation in a cluster. The MST of a sample of stars is the path connecting positions of all stars with the shortest pathlength without closed loops. By comparing the mean MST length of $n$ random stars ($\langle l_{\mathrm{n_{rand}}} \rangle$) with that of the observed $n_{\mathrm{th}}$-most massive stars ($l_{\mathrm{n_{th\ massive}}}$) in the clusters, we can quantify to which mass the cluster is segregated by a ratio,

$$\Lambda = \frac{\langle l_{\mathrm{n_{rand}}} \rangle}{l_{\mathrm{n_{th\ massive}}}}. \tag{1.10}$$

When $\Lambda$ is significantly larger than 1, it indicates mass segregation. Instead of taking the average $\Lambda$ from a set of simulations, Yu et al. (2011) suggest to measure the $\Lambda' = \log(\langle l_{\mathrm{n_{rand}}} \rangle / l_{\mathrm{n_{th\ massive}}})$ which has a smaller dispersion than $\Lambda$. Olczak et al. (2011) discuss the different methods commonly used to evaluate mass segregation in star clusters, and argue that the MST method is superior to the other methods, since it does not make assumptions about symmetry or the location of the center of the distribution nor is it affected by uncertainties introduced by binning (Küpper et al. 2011).

The Orion Nebula Cluster (ONC, $\sim$ 1 Myr) is found to be mass-segregated down to $5\,\mathrm{M}_{\odot}$ using the MST method (Allison et al. 2009b). The occurrence of mass segregation in young star clusters (e.g., NGC3603, Pang et al. 2010; the ONC, Hillenbrand & Hartmann 1998; Arches, Stolte et al. 2002) suggests that either the higher-mass stars formed in the center of the clusters, called primordial segregation, or that they moved there since their formation, called dynamical segregation.

### Primordial segregation

The age of very young star clusters is generally less than a relaxation time such that dynamical mass segregation cannot have fully occurred yet. N-body simulations of Bonnell & Davies (1998) investigated the evolution of virialized and subvirial smooth Plummer spheres. They showed that dynamical segregation cannot occur rapidly enough to explain the observed mass segregation in the ONC. Instead, the mass segregation is at least partially primordial. There are two major scenarios explaining the occurrence of primordial segregation in a young star cluster.

(1) According to the competitive accretion theory (Bonnell 2001), fragmentation occurs at a characteristic mass set by the Jeans instability. The protostellar seeds' accretion rate differs in different positions in the gas potential well. Protostars moving slowly through the cluster center would accrete more material than those in the outskirts. Therefore high-mass stars form preferentially at the bottom of the cluster potential well. This would naturally lead to primordial mass segregation.

(2) The core collapse model (McKee & Tan 2003) argues that the mass accreted by high-mass stars depends on the properties of the pre-existing gas in the GMC. This gas produces the seeds of stars in the first place. The high-mass cores are located well inside the half-mass radius of the parent clump. If stars acquire their mass from a core and do not move far during formation, then a degree of continuous mass segregation follows naturally.

Both high-mass star formation theories can be interpreted to imply that the mass of a star depends on its location in such a way that the structure of a cluster is highly segregated when gravitational dynamics become dominant. In this case, mass segregation is not the eventual result of a cluster trying to achieve equipartition, but perhaps the starting point.

### Dynamical segregation

However, Moeckel & Bate (2010) suggest that primordial mass segregation is transient and disappears after 1 Myr because of binary interactions. Dynamical mass segregation will manifest itself later depending on the cluster relaxation timescale. The time of dynamical segregation is mass dependent,

$$t_{\rm seg} \sim \frac{\langle m \rangle}{m} t_{\rm rh}, \tag{1.11}$$

where $m$ is the stellar mass and $\langle m \rangle$ is the global mean stellar mass in a cluster. Thus high-mass stars can be segregated very rapidly. Allison et al. (2009b) show that dynamical mass segregation can occur within the first 1 Myr in the life of star clusters as massive as the ONC ($10^3\,{\rm M}_\odot$), by adopting initially subvirial velocities and a clumpy stellar distribution. Actually, both the GMCs and embedded star clusters are observed to have significant levels of substructure in their density distribution (Williams et al. 2000; Lada & Lada 2003). Signatures of subvirial dynamics are observed in star-forming regions (Belloche et al. 2001; Kirk et al. 2007; Proszkow et al. 2009). Thus the assumption of initial substructure and subvirial velocities for cluster evolution is more realistic than a virialized Plummer sphere (Bonnell & Davies 1998). Additionally, the more clumpy and cooler the cluster is, the higher the degree of mass segregation (Allison et al. 2010). A subvirial

state leads to higher merger rates in the star forming clumps and hence faster mass segregation (McMillan et al. 2007; Proszkow & Adams 2009; Moekel & Bonnell 2009). Last but not least, Moeckel & Bate (2010) point out that the speed of dynamical segregation also depends on the efficiency of gas removal from the cluster. Slower or no gas removal results in a shorter relaxation timescale, hence faster dynamical mass segregation.

### 1.4.2 Gas dispersal

Only a small percent of the gas in GMCs can be turned into stars (Lada & Lada 2003; see Section 1.2), which indicates that the potentials of the young clusters are dominated by gas. Feedback from the high-mass stars, e.g., supernovae and stellar winds, will remove the gas within a few Myr and change the potential of the cluster significantly. Afterwards, the cluster expands from an initial radius of 1-2 pc over 4-10 Myr, depending on how quickly the gas is removed. Most clusters will lose a significant degree of stellar mass after the gas dispersal, which may lead to the destruction of them, usually referred to as infant mortality (Lada & Lada 2003). Over the past years, many studies worked on the processes and effects of gas dispersal on the evolution of young clusters (Hills 1980; Goodwin & Bastian 2006; Bastian & Goodwin 2006; Baumgardt & Kroupa 2007). Analytical models by Hills (1980) show that a young cluster needs a star formation efficiency (SFE) above 50 percent to survive the rapid dispersal of gas. Recent simulations of Goodwin & Bastian (2006) decrease the SFE requirement for a cluster remaining bound after gas removal to 30 percent. However, more sophisticated semi-analytic and numerical models suggest that when the gas is removed on a timescale significantly longer than the crossing time, the cluster still can survive with a SFE as low as 20 percent (Geyer & Burkert 2001; Baumgardt & Kroupa 2007). The final surviving clusters will have only a small fraction of their initial mass. Some clusters lose most of their stars and only the cluster cores remain (Baumgardt & Kroupa 2007).

All the previous work has concentrated on clusters that are in virial equilibrium and that have a Plummer density distribution. However, observations show that stars do not form in dynamical equilibrium nor in a smooth distribution (Bressert et al. 2010), but in substructures and with subvirial velocities (Section 1.4.1). Therefore, not only the depth of the gas potential, but also the dynamical state at the onset of gas expulsion determines the survival of the cluster (Goodwin 2009). Goodwin (2009) notes that if the gas removal occurs when the cluster is still dynamically subvirial, then the probability that the cluster can survive will be increased greatly.

## 1.5 Dust extinction

The star-forming region is shielded against photoionization by a large amount of dust (Figure 1.1 & 1.2), which consists of small solid particles (e.g., C, O, Mg, Si compounds), mainly less than $\sim 1\,\mu\mathrm{m}$ in size, mixed with the interstellar gas (Draine 2010). This dust obscures the light of stars by absorption and scattering, referred to as "extinction". Trumpler (1930) was the first to study interstellar dust. Using stars with negligible obscuration along the line of sight as "standard candles", he compared the spectrum of the reddened stars to the "standard candles" with similar

spectral types and derived the extinction at a specific wavelength $\lambda$. The extinction $A_\lambda$ measured in magnitudes is defined by

$$A_\lambda(\mathrm{mag}) = 2.5\log_{10}[F_\lambda^0/F_\lambda] \tag{1.12}$$

where $F_\lambda$ is the observed flux from the reddened star, and $F_\lambda^0$ is the flux of the standard candle. $A_\lambda$ can also be defined to be the difference between the observed magnitude $m(\lambda)$ at wavelength $\lambda$ and the unreddened magnitude of $m_0(\lambda)$,

$$A_\lambda(\mathrm{mag}) = (m - m_0)_\lambda \tag{1.13}$$

The extinction is the smallest in the infrared, and increases slightly in the optical, with typically an excess in the UV at 2175 Å, then rises to shorter wavelengths with a power-law-like dependence. The wavelength dependence of the extinction is the so-called extinction curve. The slope of the extinction curve at visible wavelengths is characterized by a dimensionless ratio, which is also called the total to selective extinction ratio,

$$R_V = \frac{A_V}{A_B - A_V} = \frac{A_V}{E(B-V)}, \tag{1.14}$$

where $A_B$ and $A_V$ are the extinctions measured in the $B$ (4405Å) and $V$ (5470Å) photometric bands, and $E(B-V) = A_B - A_V$ is the reddening or color excess at these bands. The Galactic extinction curve shows considerable variation among different lines of sight, indicating different physical processing histories of dust grains in the ISM (Seaton 1979; Savage et al. 1985; Cardelli et al. 1989, 1988; Fitzpatrick et al. 1999; Valencic et al. 2004; Fitzpatrick & Massa 2007, 2009).

### 1.5.1 Dust properties

Thanks to the increasing sensitivity of infrared, far-infrared and sub-mm telescopes, we can probe the properties of interstellar dust in different environments as a diagnostic of the physical conditions in the ISM. The sizes of dust grains are affected significantly by the stellar feedbacks such as from supernovae and stellar winds that generate shocks. Grains with large sizes will be destroyed or reduced to 75% of the initial radius at a shock speed as low as 40 km/s generated by supernovae (Seab & Shull 1983). Furthermore, anisotropic radiation of OB stars pushes away the the grains larger than $0.1\,\mu\mathrm{m}$ by the photodesorption force (Weingartner & Draine 2001). At the same time, the emission of very small grains (VSGs) is usually detected in massive star formation regions where the interstellar radiation field is hard (Churchwell et al. 2006).

On the the other hand, dense interstellar environments are found to favor large dust grains (Chini & Krügel 1983; Mathis 1987; Cardelli et al. 1989; Fitzpatrick & Massa 2009). The dust grain grows in a dark cloud or nebulosity, where its size can grow beyond $0.4\,\mu\mathrm{m}$. Observations of Mathis & Wallenhorst (1981) showed that the number of large silicate particles is enhanced in dense regions. The growth of grain size decreases the extinction ability of dust in the far-ultraviolet (Draine 2009) and increases the radiation emission in infrared, through which we can witness the populations of obscured new-born stars which may form a young star cluster later on.

## 1.6 Young star clusters

When a large number of new-born stars in GMCs become bound to the same gravitational potential well, they form a young star cluster. We define young star clusters (YSCs) to be younger than 100 Myr. Such objects still contain significant amounts of ambient gas and dust (Figure 1.2). They are at the very early stage of stellar evolution and therefore are ideal to test the universality of the IMF. Besides the seemingly universal slope for the upper end of the IMF (above $0.5\,\mathrm{M}_{\odot}$) for many YSCs (Orion, Hillenbrand & Carpenter 2000; $\rho$ Oph, Luhman & Rieke 1998; R136 in Doradus, Massey & Hunter 1998), Smith & Gallagher (2001) suggest that the mass functions of some YSCs may be deficient in low-mass stars and top-heavy. Since few of the most massive stars in a YSC have undergone violent mass-loss with outflows (Brandner et al. 1997a), the majority of them are close to the initial mass, which makes the mass function of YSCs the closest to the original IMF.

However, top-heavy mass functions do exist in the inner part of some YSCs, implying mass segregation (e.g., NGC3603, Pang et al. 2010; the ONC, Hillenbrand & Hartmann 1998; Arches, Stolte et al. 2002; NGC 6611, Bonatto et al. 2006; NGC 2244 and NGC 6530, Chen et al. 2007; M17, Jiang et al. 2002; W3 IRS5, Megeath et al. 2005). The age of most YSCs is still less than the relaxation time, providing not enough time for the equipartition of kinetic energy, so called dynamical segregation. Though simulations have shown that dynamical segregation can occur within a short timescale for clumpy, cold clusters, and for the case of low gas dispersal efficiency (Allison et al. 2009b; Moeckel & Bate 2009; Yu et al. 2011), primordial segregation cannot be excluded (Bonnell & Davies 1998). Investigations of segregated YSCs may lead to the understanding of the origin of mass segregation.

In those segregated YSCs, a large number of high-mass OB stars are located in the cluster core, producing strong stellar feedbacks. The feedbacks such as from supernovae and stellar winds are responsible for producing shocks and destroying dust grains. At the same time, they compress the ambient molecular clouds and may trigger subsequent star formation (see Figure 1.2). Therefore, YSCs are ideal laboratories to understand the interplay between the star formation feedback and the dynamics and energetics of the surrounding ISM.

In order to investigate the IMFs of YSCs, to understand the origin of mass segregation in YSCs, and to study the interactions between YSCs and their environment, we therefore need to know: the age of the cluster (from stellar photometry and spectroscopy), the kinematics of its stars (from spectroscopy and photometry), and the dust emission (from infrared photometry) of its parent molecular cloud. There is one YSC in the Milky Way for which all these data are available from space telescopes, and for which a comprehensive study of YSCs can be done for the first time. This is the cluster HD 97950.

## 1.7 The young star cluster HD 97950

The HD 97950 cluster is located in one of the most massive optically visible giant H II region in the Galaxy, NGC 3603. It contains a large number of massive OB stars ionizing NGC 3603 (Figure 1.4), indicating a young age that is around a few Myr. HD 97950 is also called a starburst cluster,

with a total mass of $\sim 10^4$ $M_\odot$ (Harayama et al. 2008) which makes it one of the most massive young clusters in the Milky Way. This cluster is unique in the following aspects.

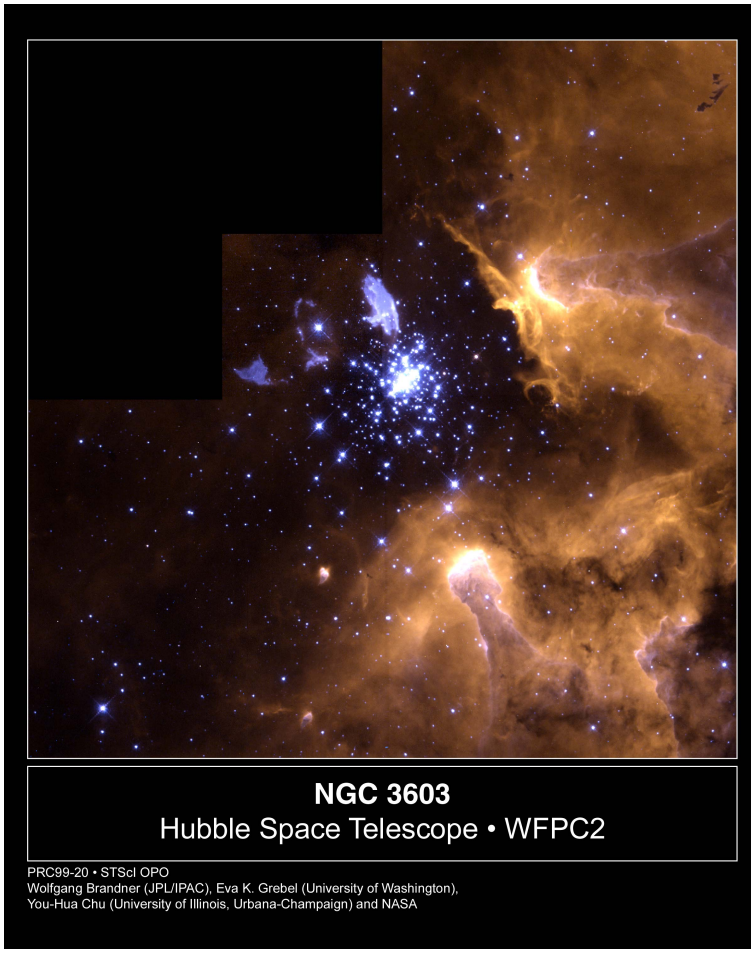


Figure 1.4: The H II region NGC 3603 with its central young star cluster HD 97950, taken by the Wide Field and Planetary Camera 2 on board the Hubble Space Telescope.

(1) Young age with a debatable spread

The HD 97950 cluster host dozens of massive OB stars whose number is ten times higher than in the ONC. Melena et al. (2008) argue that the most massive stars in the HD 97950 cluster are coeval with ages of 1–2 Myr, while less massive stars (20–40 $M_\odot$) show a somewhat larger age spread of up to 4 Myr based on spectral analysis. Recent photometric studies arrived at extended star formation episodes of up to 10 – 20 Myr as indicated by the age spread in pre-main-sequence stars (Beccari et al. 2010). Also the evolved supergiants around the HD 97950 cluster support the idea of a large age spread or alternatively sequential or multiple episodes of star formation (e.g., Moffat et al. 1983; Tapia et al. 2001; Crowther et al. 2008; Melena et al. 2008).

(2) Significant mass segregation

Despite its young age, the HD 97950 cluster shows pronounced mass segregation (e.g., Sung & Bessell 2004; Grebel & Gallagher 2004), with a slope $\Gamma = -0.5 \pm 0.1$ for the mass function in the inner 0.1' annulus (Sung & Bessell 2004). However the origin of the mass segregation is still unclear. Understanding the origin of mass segregation in YSCs would place important constraints on theories of high-mass star formation and cluster evolution.

(3) Differential reddening

The HD 97950 cluster lies in a wind-blown cavity north of a large molecular cloud (e.g., Clayton 1986; Melnick 1989). The gaseous surroundings of the cluster show a complex and variable velocity and density structure (e.g., Clayton 1990; Drissen et al. 1995). Since the nebular density varies spatially, the dust extinction changes with position across the cluster area. The resulting variable reddening is known as differential reddening and was shown to be present in NGC 3603 (e.g., Sagar et al. 2001; Sung & Bessell 2004). As shown by Beccari et al. (2010), pre-main-sequence stars are spatially widely distributed in areas where gas and dust are enhanced and severely affected by differential reddening. Consequently, differential reddening could be one of the causes why the age spread among pre-main-sequence stars in the HD 97950 cluster appears to be as large as up to 10 Myr (Beccari et al. 2010).

Due to its special features, the HD 97950 cluster and its surrounding H II region NGC 3603 were observed by the Hubble Space Telescope (HST) in different filters ranging from the ultraviolet (*F330W*) to the infrared (*F139M*). The photometric data were taken with the Advanced Camera for Surveys (ACS), the Wide Field and Planetary Camera 2 (WFC2), and the Wide Field Camera 3 (WFC3) on board HST. The WFPC2 data were collected in equivalent filters during two different epochs which are ten years apart, providing astrometric data to study stellar kinematics. These comprehensive HST data make the HD 97950 cluster the Rosetta Stone to study 1) the survival probability of YSCs (Chapter 2), 2) the IMF of YSCs (Chapter 3), 3) the origin of mass segregation in YSCs (Chapter 3), and 4) the interplay of the YSCs and their surrounding ISM (Chapter 4 & 5) at the same time. The methods used to study the HD 97950 cluster, which is a template for young massive star clusters in local universe, can be applied to subsequent studies of YSCs in the our own Galaxy and distant galaxies hosting similar starburst clusters.

# 2

# The fate of the young HD 97950 cluster from relative proper motions

Foresee the fate with faith:
*For I know the plans I have for you, declares the Lord, plans for welfare and not for evil, to give you a future and a hope. (Jeremiah 29:11)*

**Abstract** In this chapter, we measure the relative proper motion of stars in the HD 97950 cluster in the HII region NGC 3603, with the data from Hubble Space Telescope Wide Field and Planetary Camera 2 (HST/WFPC2) obtained in 1997 and 2007. Two methods, 1) a relative proper motion cut and 2) a two-Gaussian model fitting over the relative proper motion distribution, are used to determine the membership of over 600 stars in the cluster. The number of determined member stars of these two methods agrees well with each other when we consider stars as members with member probabilities larger than 70 percent. We derived 411 members on the PC chip and 124 on the WFC chips from the second method. The field star contamination on the PC and WFCs is 7 and 25 percent respectively. By subtracting measurement uncertainties from the standard deviation of the relative proper motion, we estimate the velocity dispersion to be $\sigma_c = 10.4 \pm 0.6\,\mathrm{kms}^{-1}$. We adopt this $\sigma_c$ and assume a cluster half-mass radius of 0.7 pc, and compute the virial mass of the cluster HD 97950 to be $1.7 \times 10^5\,\mathrm{M}_\odot$. The total luminosity of the cluster is $L_V \sim 9.4 \times 10^6\,\mathrm{L}_\odot$ when adopting distance of 6.9 kpc and a visual extinction $A_V = 4.5$ mag. The resulting $L_V/M_{dyn}$ ratio is $55\,\mathrm{M}_\odot/\mathrm{L}_\odot$, corresponding to a star formation efficiency of about 50 percent according to the simulations of Good & Bastian. This indicates that the HD 97950 cluster is going to survive the gas expulsion phase and will re-establish equilibrium afterwards.

## 2.1 Introduction

Young massive star clusters (YMCs), younger than 100 Myr and more massive than $10^4\,\mathrm{M}_\odot$ (Portegies Zwart et al. 2010), overlap with old low-mass Galactic globular clusters (GCs) in mass, concentration and size distribution. Sometimes YMCs are referred to as young GCs in the literature. However, the survival of YMCs is an essential issue in building this connection. Many observed young clusters appear to be supervirial with a higher value of dynamical mass compared to the photometric mass (Smith & Gallagher 2001; McCrady et al. 2003; Bastian et al. 2008; Mengel et al. 2008). These clusters are likely expanding and possibly unbound (Goodwin & Bastian 2006).

A violent internal event, such as gas expulsion, could cause the cluster to become unbound. Goodwin & Bastian (2006) show that the expulsion of gas induced by the stellar winds or the first supernova can lower the cluster potential and causes the cluster to expand. Clusters with a star formation efficiency lower than 30% will dissolve in a few dynamical timescales after the phase of gas expulsion. A large fraction of young and embedded clusters are thought to be disrupted as a consequence of gas expulsion, which is often referred to as infant mortality (Lada & Lada 2003). When clusters are formed from dynamically cold (subvirial) collapsing clouds (Allision et al. 2009b), they can survive after the gas expulsion even with a star formation efficiency of only 5% (Portegies Zwart et al. 2010).

Another internal event, evaporation, which is due to the loss of stellar mass of the most massive stars, can cause the cluster to expand. Stars more massive than $50\,\mathrm{M}_\odot$ can lose 90% of their mass within 4 Myr. The expansion will be more severe when the cluster is mass segregated (Vesperini, McMillan & Portegies Zwart 2009). If the mass-loss timescale is much shorter than the dynamical time, the cluster will eventually dissolve (Portegies Zwart et al. 2010).

Moreover, external events such as giant molecular clouds (GMCs) encounters, can also play a destructive role by heating up the young clusters frequently during the early stages of cluster evolution (Spitzer 1958). Only young clusters with density of $10^{3\pm1}\,\mathrm{M}_\odot\,\mathrm{pc}^{-3}$ or higher can resist the destruction by GMCs (Pfalzner 2009).

The survival of YMCs depends on whether they can resist the internal and external destructive events. To estimate the survival probability of YMCs, we need astrometric or spectroscopic data of YMCs that are resolved into single stars, to verify their dynamical state. The Wide Field and Planetary Camera 2 (WFPC2), on board the Hubble Space Telescope (HST), is an excellent tool for astrometric studies. Its superb spatial resolution and image stability enable us to measure motions of the stars in a moderately distant cluster if the cluster is observed at different, sufficiently separated epochs. One uniquely suited YMC HD 97950 ($10^4\,\mathrm{M}_\odot$, Harayama et al. 2008), which is located at a distance of 6.9 kpc (Sung & Bessell 2004) in the giant H II region NGC 3603, was observed by WFPC2 with deep exposures. The cluster images go down to $0.8\,\mathrm{M}_\odot$, which is deeper than available data for the other YMCs (Westerlund 1 & Arches) whose HST observations are limited to stars above $1\,\mathrm{M}_\odot$. There are two epoch (1997 and 2007) WFPC2 data in equivalent filters available for the HD 97950 cluster. These two epoch data provide us with relative proper motions of stars based on which we can investigate the cluster kinematics and therefore its probability of being in the process of disruption.

In this chapter, we analyze the two-epoch WFPC2 observations of the HD 97950 cluster in NGC 3603 to investigate the fate of this young cluster. In Section 2.2 we summarize the photometric observations, completeness and data reduction. In Section 2.3 we infer the relative proper motions of stars in the cluster, including inter-filter and intra-filter centroiding tests for single epoch data. We determine the membership of stars by two methods, a relative proper motion cut and a two-Gaussian model in Section 2.4. In Section 2.5, we infer the velocity dispersion of cluster stars. The fate and dynamical state of the cluster are discussed in Section 2.6. We present our conclusions and summary in Section 2.7.

## 2.2 Observations and data reduction

We analyze deep imaging data of the young HD 97950 cluster in the giant H II region NGC 3603 obtained with the WFPC2 aboard the HST. WFPC2 contains four CCD chips with $800 \times 800$ pixels each. Three of the CCDs – the three wide-field cameras (WFCs) – have an image scale of $0.1''$ per pixel. The fourth CCD – the Planetary Camera (PC) has an image scale of $0.046''$ per pixel (McMaster et al. 2008).

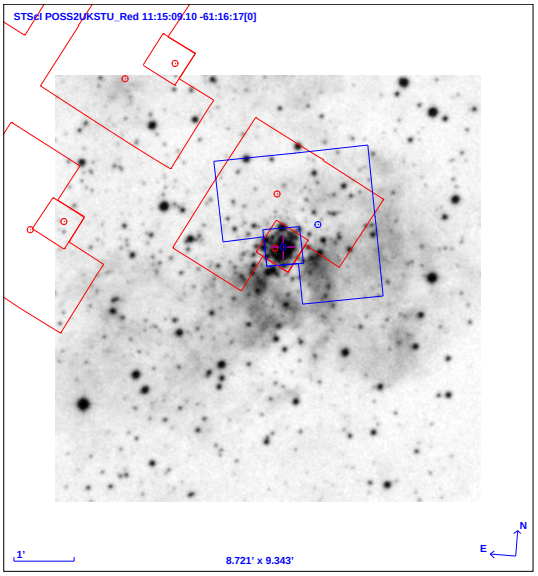


Figure 2.1: Image of a portion of the Galactic H II region NGC 3603 centered on the young ionizing HD 97950 cluster. The image was taken from a photographic plate (POSS2UKSTU-Red) obtained using the UK Schmidt Telescope. The digitized image is available from the Digitized Sky Survey at the Space Telescope Science Institute. The location of the field of view of the HST/WFPC2 observations done in 1997 (blue polygons) and in 2007 (red polygons) is indicated. In both cases the PC chip is centered on the HD 97950 cluster. There is a roll-angle offset of $51^\circ$ between the two epochs.

### 2.2.1 Our two data sets

The data were collected during two different epochs. The first observations were carried out on 1997 July 30 and 31 (program GO 6763, PI: Drissen). In this program the PC chip was centered on the cluster HD 97950 (PC-FIX mode, no drizzling). The footprint of these observations is marked by the blue polygons in Figure 2.1. Exposures were taken in three filters, *F547M* ($\sim V$), *F675W* ($\sim R$), and *F814W* ($\sim I$). *F547M* was chosen instead of the standard *F555W* filter in order to avoid contamination by nebular lines. The red filters *F675W* and F814W were used in order to reach fainter magnitudes in this moderately extincted giant H II region.

The shortest exposures lasted fractions of a second in order to minimize saturating the luminous, massive stars in HD 97950 (only three massive stars ended up being saturated). The longest exposures did not exceed 20 to 30 seconds in order to avoid charge bleeding effects that might have obscured faint stars. Details are given in the exposure time log in Table 2.1.

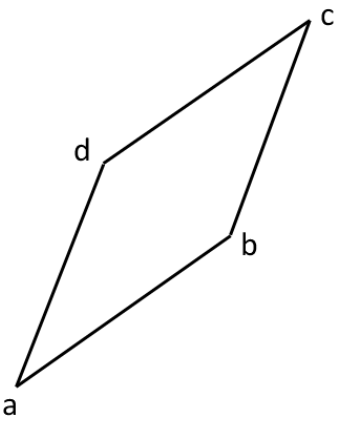


Figure 2.2: The default WFPC2-BOX dither pattern. 2007 images taken at these four positions are named a (0,0), b (11.0, 5.5), c (16.5, 16.5), d (5.5, 11.0) (see Table 2.2).

The second data set was obtained in May 2007 (program GO 11193, PI: Brandner). These data contain exposures in the *F555W* ($\sim V$), *F675W*, and *F814W* filters. These observations surveyed a larger area ($6' \times 6'$) in NGC 3603, covering four different, non-overlapping regions. Each field was observed in a separate visit. Only one of the fields is centered on HD 97950 (red polygons in Figure 2.1). The other three fields point at the north-east part of NGC 3603. In this chapter, we only make use of the first field ("visit 01") because it overlaps with the 1997 observations (Figure 2.1). The 1997 and the 2007 visit 01 observations are rotated by $51^\circ$ with respect to each other. A WFPC2-BOX dither pattern was used for the 2007 observations in order to reduce the crowding effects in the cluster core by an improved point-spread-function (PSF) sampling. The default WFPC2-BOX pattern has the relative pixel coordinates (0, 0), (5.0, 2.5), (7.5, 7.7), (2.5, 5.0) on the WFC chips, and (0, 0), (11.0, 5.5), (16.5, 16.5), (5.5, 11.0) on the PC chip. It describes a parallelogram pattern (Figure 2.2) combining integer-pixel and half-pixel shifts, with a purpose

Table 2.1: Exposure time log of the HST/WFPC2 observations of the HD 97950 cluster

| Filter | Shallow exposures [s] | No. of frame | Median exposures [s] | No. of frame | Deep exposures [s] | No. of frames |
|---|---|---|---|---|---|---|
| | | | 1997 | | | |
| *F547M* | 1 | 3 | 10 | 12 | 30 | 8 |
| *F675W* | 0.4 | 3 | 4 | 12 | 20 | 8 |
| *F814W* | 0.4 | 3 | 5 | 12 | 20 | 8 |
| | | | 2007 visit 01 | | | |
| *F555W* | 0.4 | 4 | 26 | 4 | 100 | 4 |
| *F675W* | – | – | 18 | 4 | 160 | 4 |
| *F814W* | – | – | 18 | 4 | 160 | 4 |

to reject typical detector artifacts.

Throughout this chapter, we will call images with less than 1 second of exposure time "shallow", with 1 to 12 seconds "median", and deeper than 12 seconds "deep". The exposure time log of the 2007 visit 01 observations is also given in Table 2.1.

### 2.2.2 WFPC2 photometry

The photometric reduction was carried out with the photometry package *HSTphot* (Dolphin 2000a), a program developed for crowded-field stellar photometry of WFPC2 data. *HSTphot* is optimized for undersampled PSFs (such as in the case of WFPC2). In short, this program removes cosmic ray hits and carries out PSF photometry using position-dependent, pre-computed *Tiny Tim* (Krist 1993) PSFs (available from [1]) for each of the filters. *HSTphot* also corrects for aperture and charge-transfer-efficiency effects and transforms to the ground-based *UBVRI* filter system following Dolphin (2000b).

Before the photometric reduction, we compute the shifts of the PC chip for the different images. Since the 1997 observations did not use a dither pattern, the offsets between the different images in this epoch is zero. For the 2007 data, we derive the shifts of the PC for their dithered images using the IRAF[2] STSDAS dither package, following the procedure for crowded stellar fields in the HST Dither Handbook (Koekemoer et al. 2002).

We ran *HSTphot* on the shallow, median, and deep images separately for images in single epoch data to obtain three photometric catalogs of stars (shallow, median and deep). The V-band filter images are taken as reference in *HSTphot*. Afterwards, geometric distortions corrections are applied to the positions of stars, achieving an astronomical accuracy of the star positions of 0.03 pixels in both $x$ and $y$ in pixel coordinates of each chip of WFPC2 (Dolphin 2000a). Since

[1] http://purcell.as.arizona.edu/hstphot/

[2] IRAF is distributed by the National Optical Astronomy Observatories, which are operated by the Association of Universities for Research in Astronomy, Inc., under cooperative agreement with the National Science Foundation.

*HSTphot* conveniently converts WFPC2 magnitudes into standard Johnson-Cousins *UBVRI* magnitudes, we will use these magnitudes in the following. Hence both the *F555W* and *F547M* magnitudes were transformed to *V*-band magnitudes, and instead of *F675W* we use *R*, and instead of *F814W I*-band magnitudes. Only images from those filters equivalent to *V* and *I* in both epochs are used in the subsequent analysis. The accuracy of the photometry from *HSTphot* on single stars is 0.01–0.02 mag.

We keep the stars detected by *HSTphot* in the final photometry catalog if they were detected in both the *V* and *I*-band equivalent filters in single epoch images. Furthermore, we require that their signal-to-noise (S/N) ratio is above a threshold of $3.5\sigma$, that their "OBJECT TYPE" value is 1 (which stands for "good" stars as defined in the *HSTphot* manual; Dolphin 2000a). We also consider the value of $\chi^2$, which is the ratio of the observed pixel-to-pixel scatter in the PSF fit residuals to the expected scatter calculated from a predicted model based on the measured detector features. Stars with a $\chi^2$ value smaller than 2.5 are kept in the final catalog. Because the reddening is high in NGC 3603 (Chapter 4 and references therein), the contamination by background galaxies is negligible. Therefore we do not select stars via the *sharpness* parameter, which is usually used to separate stars from extended galaxies.

Figure 2.3 shows the distribution of the photometric errors $\sigma$ determined by *HSTphot* as a function of magnitude. The green circles, red circles, and blue dots represent stars detected in the shallow, median, and deep exposures, respectively. In the left panel (1997 data), bright stars with $V < 13.6$ mag are only detected in the shallow exposures and are saturated in the others. Consequently, these bright stars are included in the final catalog. Between $V \sim 13.6$ and $\sim 15.5$ mag, the shallow and median exposures overlap. We take their common stars, convert their magnitudes into fluxes, and calculate the mean fluxes and colors weighted by photometric uncertainties $\sigma^2$. The mean fluxes were converted back into magnitudes again. The resulting values are then adopted as the new magnitudes and colors of the common stars. Stars fainter than $V = 15.5$ mag in the shallow exposure are rejected because of their large photometric uncertainties. The median and the deep exposures overlap for $V > 15.5$ mag, but we only keep common, magnitude-error-weighted stars in the range of $V = 15.5$ mag to 18.0 mag. Stars fainter than $V = 18$ mag are taken exclusively from the deep exposures.

The same procedure was performed on the 2007 data. Here, however, only one shallow exposure in one filter exists (see Table 2.1). Thus we only obtain median and deep photometry catalogs for the 2007 data. The dashed lines in the right panel of Figure 2.3 indicate the region where we select common stars between the median and the deep 2007 exposures. Stars brighter than $V = 17.5$ mag are taken solely from the median exposure, while stars fainter than 18.5 mag are adopted from the deep exposure only. The color-magnitude diagrams (CMDs) of the final combined star catalog for the 1997 and the 2007 data are presented in Figure 2.4, illustrating the difference in depth of the two data sets.

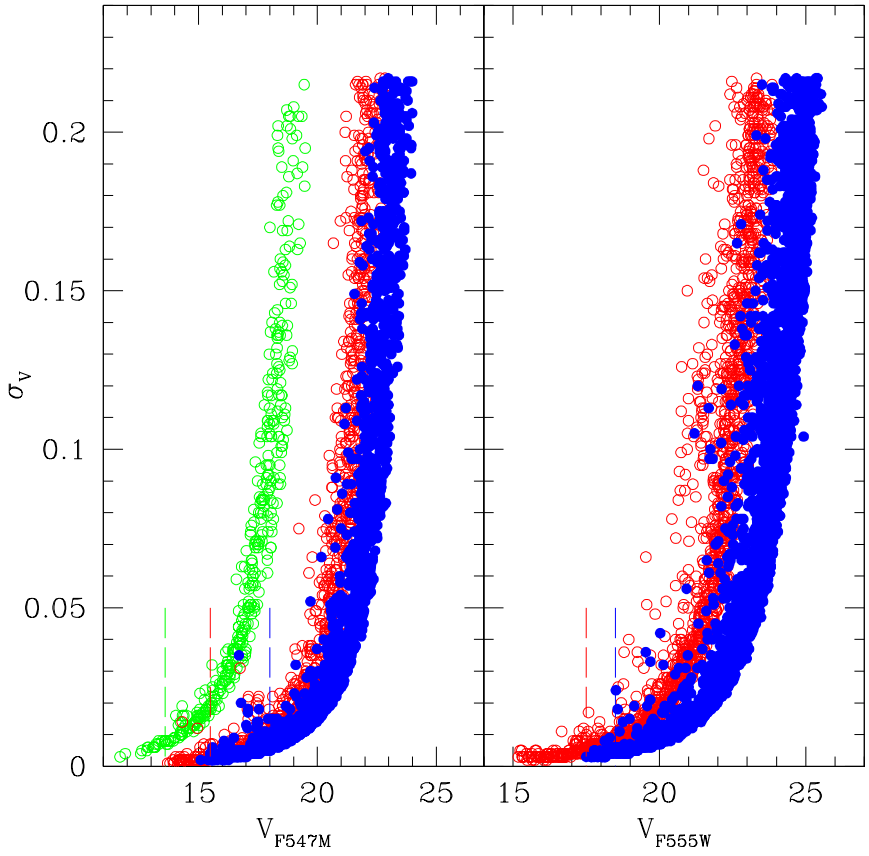


Figure 2.3: Dependence of the photometric uncertainties $\sigma_{\rm V}$ on the $V$-band magnitude for the 1997 (left) and the 2007 data (right). Left: The green circles stand for stars from the shallow exposure, the red circles for stars from the median exposure, and the blue dots for stars from the deep exposure. The mean $V$ magnitude and $(V-I)$ color weighted by their respective photometric errors $\sigma^2$ are calculated for the common stars in the region of $V = 13.6$ to 15.5 mag (shallow and median data), and of $V = 15.5$ to 18.0 mag (median and deep data) as indicated by the vertical dashed lines. Right: The symbols and color coding are the same as in the left panel. Here the mean magnitude and color weighted by $\sigma^2$ are calculated for the common stars in the region of $V = 17.5$ to 18.5 mag combining the median and deep data. Again these boundaries are indicated by vertical dashed lines.

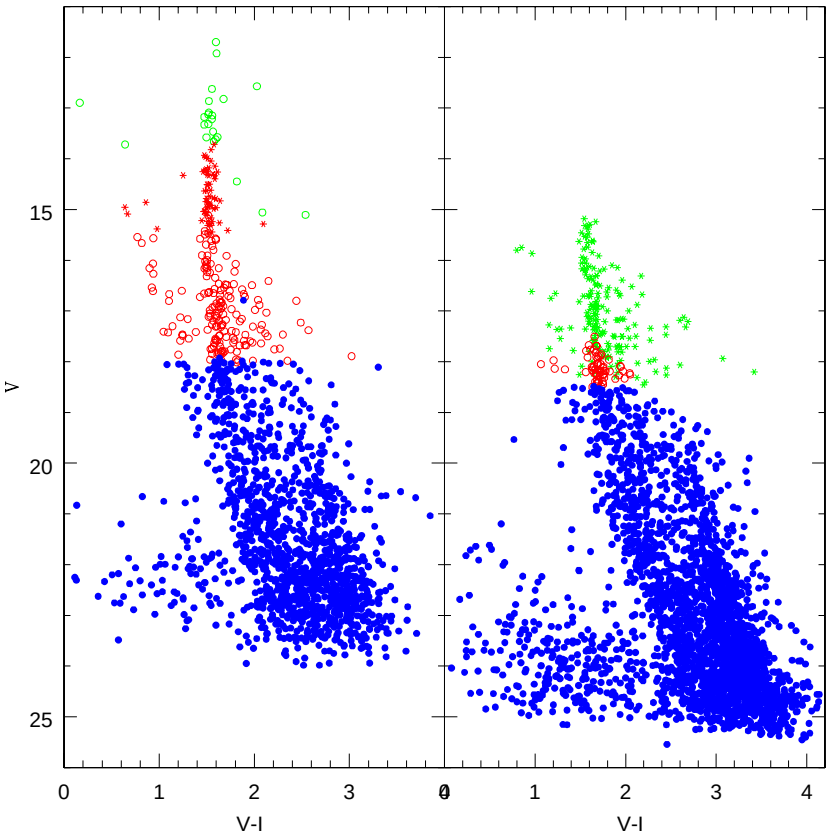


Figure 2.4: CMD of the combined catalog of the 1997 (left panel) and the 2007 (right panel) data. Left panel: The green circles stand for stars from the shallow exposure. The red asterisks and circles denote common stars between the shallow and median exposures, and between the median and deep exposures respectively. The blue dots indicate stars from the deep exposure. Right panel: The green asterisks denote stars from the median exposure only. The red circles indicate stars in common between the median and the deep exposure, while the blue dots are stars from the deep exposure.

### 2.2.3 Photometric completeness

The massive OB stars of the HD 97950 cluster, which outnumber their counterparts in the Orion Nebula Cluster by a factor 10, are found primarily in its central region. In fact, as has been shown by a number of studies, the HD 97950 cluster shows pronounced mass segregation (e.g., Sung & Bessell 2004; Grebel & Gallagher 2004; Harayama et al. 2008; Pang et al. 2010; Pang et al. 2012a). On the median and long exposures, the massive, luminous stars show extended light profiles, luminous diffraction patterns, and in part also charge bleeding. Apart from general blending effects owing to the high stellar density in the cluster center, also the concentration of massive stars in this region makes it more difficult to detect faint stars there. The final combined catalog is incomplete due to these crowding effects and saturation. This affects in particular the PC chip since it was pointed at the dense central region of the HD 97950 cluster. The WFC chips are mostly free of crowding and saturation problems because there the stellar density is much lower and the stars are largely intrinsically faint.

The combined catalog of the 1997 data spans a brighter magnitude range ($\sim 11$ – $\sim 24$ mag) than the 2007 data ($\sim 15$ – $\sim 25$ mag). For the purpose of deriving proper motions we are only interested in the common stars of these two catalogs. Since the completeness of the total catalog of all stars common to both data sets will be limited by the 1997 data set at its faint end, we carry out artificial star experiments only for the PC chip of the 1997 data to estimate the completeness fraction of the detected stars in the HD 97950 cluster.

We perform the artificial star tests using *HSTphot*. We distribute artificial stars, which are 10 times the number of observed stars, evenly in the 1997 PC images and cover the magnitude and color range of the stars following the detections in the shallow ($11 < V < 21$ mag and $0.0 < (V - I) < 3.4$ mag), median ($13 < V < 23$ mag and $0.0 < (V - I) < 4.0$ mag), and deep images ($15 < V < 26$ mag and $-0.5 < (V - I) < 4.0$ mag). In total we create 1.6 million artificial stars, out of which $1.4 \times 10^5$ stars are inserted in the shallow images, $7.6 \times 10^5$ stars in the median images, and $8.4 \times 10^5$ stars in the deep images.

The completeness fraction ($f_{comp}$) is defined as the ratio of the number of recovered artificial stars divided by the total number of inserted stars. We present the resulting completeness fraction diagrams in Figure 2.5. It illustrates that $f_{comp}$ depends on the magnitude and on the position in the cluster. The dotted, dashed, dot-dashed, and solid lines represent the completeness fractions measured in concentric annuli from the inner to the outer cluster regions on the PC chip increasing in $5''$ intervals. The completeness is the lowest in the inner $5''$ circle, where the crowding and saturation effects are the strongest, and increases toward the outer parts.

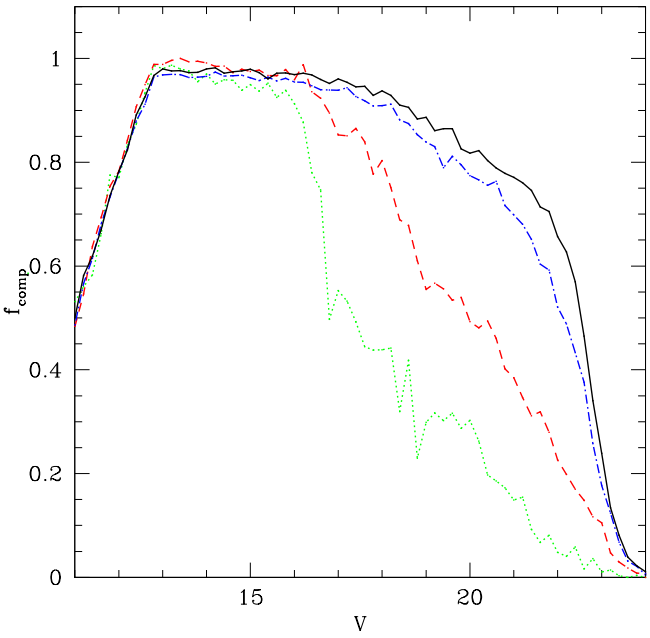


Figure 2.5: Completeness fraction $f_{comp}$ as a function of the observed $V$ magnitude calculated for four concentric annuli on the PC chip. The green dotted line denotes the $f_{comp}$ distribution for a circle with a radius of $r < 5''$ around the center of the HD 97950 cluster. The dashed line shows the completeness fraction for the next larger annulus between $5''$ to $10''$, the dot-dashed line indicates $f_{comp}$ for the annulus between $10''$ to $15''$, and the solid line is for the region outside $r > 15''$.

## 2.3 Relative proper motions

In order to derive relative proper motions for the stars detected in both epochs, we need to transform the stars' positions of the two epochs to a common coordinate system. We proceed as follows: (1) Since both the 1997 and 2007 observations have exposures in *F814W* (*I*), we select 10 common stars in the images of the same chips (PC, WFC2, WFC3, WFC4) of similar exposure times of this filter in the two epochs to do the transformation. (2) We use the stellar coordinates in the 18 s image [dithering position (0,0)] in the *F814W* filter of the 2007 data as measured by *HSTphot* as reference image. As mentioned in Section 2.2.2, the *HSTphot* coordinate accuracy is 0.03 pixels in *x* and *y* on each chip. The corresponding *HSTphot* coordinates of the stars on the 1997 *F814W* image (exposure time 20 s), are transformed to the reference image using the IRAF task *geomap*, which computes the spatial geometric transformation via a polynomial function. The PC and WFC images are processed separately to derive their own transformations. (3) We then use the task *geoxytran* to transform stars of the 2007 combined photometry catalog to the 2007 coordinate system with the transformation derived via *geomap*. (4) Once the stars of the two combined

catalogs from the two epochs are in the same coordinate system, i.e., in the coordinate system of the $I$-band 1997 data, we match the two catalogs to find common stars. Stars with a magnitude difference in $V$ and $I$ of less than 0.3 mag and a coordinate difference less than 1 pixel are selected as common stars.

We use the common stars from step 4) to repeat steps 2) to 4) until the number of common stars from step 4) does not increase anymore. We consider the resulting position difference of the common stars (transformed to the 2007 $I$-band coordinate system) as the relative proper motion. Finally we derive relative proper motions of 627 common stars of two epochs, which include 465

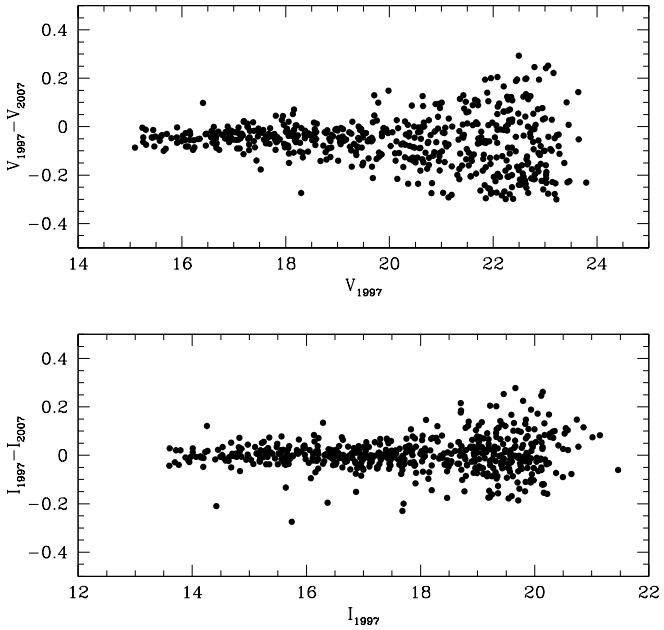


Figure 2.6: The $V$ and the $I$ magnitude difference between the 1997 and 2007 observations of the common stars.

stars from the PC chip, 95 stars from the WFC2 chip, and 67 stars from the WFC4 chip. On the WFC3 chips, we could not find enough bright common stars to do the coordinate transformation. Thus no relative proper motions of stars are derived for the WFC3.

The magnitude differences between the 1997 and 2007 observations of the common stars are shown in Figure 2.6. The mean magnitude difference is 0.05–0.1 mag. The difference increases toward fainter stars due to larger photometric uncertainty at the faint end. Some stars are even with magnitude differences up to 0.2 mag. Moreover, the magnitude difference shows no dependence on the star position, meaning that the crowding is not the culprit. We select stars with large magnitude difference ($|\Delta V| > 0.15$ mag) and plot them in the CMD (Figure 2.7). In Figure 2.7, more than half of the stars with large magnitude difference (majority from the PC chip) are located

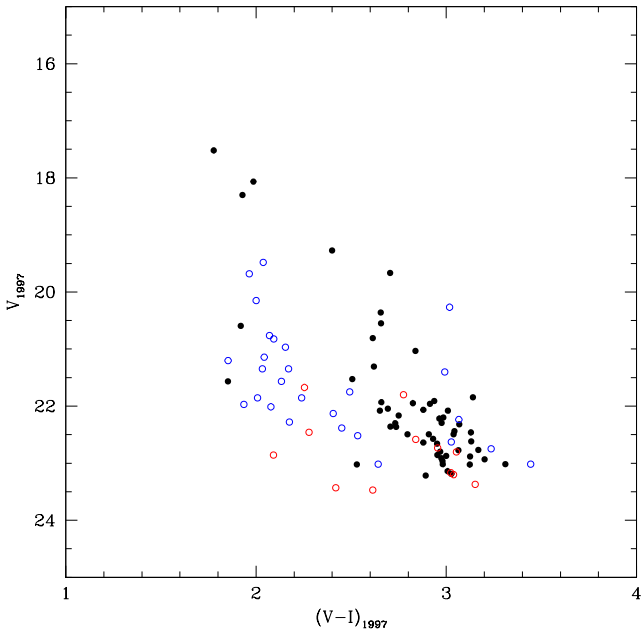


Figure 2.7: CMD of stars with $V$ magnitude difference larger than $|\Delta V| > 0.15$ mag between the two-epoch data. The magnitude for the common stars are taken from the 1997 WFPC2 data. The black dots, red and blue circles are stars on the PC, WFC2 and WFC4 chips, respectively.

along the pre-main-sequence (black dots), and are similar to those pre-main-sequence variables, T Tauri stars (Lata et al. 2011) which have magnitude variability at the order of $\Delta V \sim 0.5$ mag[3]. The large magnitude variation among some stars (especially located on the PC chip) between two epochs might be due to pre-main-sequence variables (e.g., T Tauri), which need to be verified later.

### 2.3.1 Intra-filter centroid offsets in single epoch data

The accuracy of the derived relative proper motions depends on the accuracy of the centroid positions of the stars taken in each filter. The centroid positions are affected by the PSF, the pixel response function, the guiding quality, background subtraction, image distortion, etc. (e.g., Golimowski et al. 1998; Zhai et al. 2011). The centroiding in *HSTphot* is an iterative process. *HSTphot* first scans for peaks in the residual image after sky subtraction. It initially determines the centroid of the star as the pixel-value-weighted averages of the positions of the peak and adjacent pixels. These centroids are then run iteratively. After the convergence of the solution, the star will be kept if its S/N equals or exceeds the user-defined detection threshold.

[3]using the light curve generator function on the the American Association of Variable Star Observers (AAVSO) website: http://www.aavso.org/lcg

Table 2.2: Composition of the subsamples for the test of intra-filter centroid offsets

| Filter | Subsample | Images | Exposure time |
|---|---|---|---|
| | 1997 | | |
| *F547M* | subsample 1 | a, c, e, g, h | 30 s |
| *F547M* | subsample 2 | a, b, d, f, h | 30 s |
| *F814W* | subsample 1 | a, c, e, g, h | 20 s |
| *F814W* | subsample 2 | a, b, d, f, h | 20 s |
| | 2007 | | |
| *F555W* | subsample 1 | a, b, c | 26 s |
| *F555W* | subsample 2 | a, d, c | 26 s |
| *F814W* | subsample 1 | a, b, c | 18 s |
| *F814W* | subsample 2 | a, d, c | 18 s |

The "a" image of each subsample is the reference. The images a, b, c, d in the 2007 data follow a WFPC2-BOX dither pattern (see Figure 2.2).

We evaluate the quality of the centroids of the detected stars by comparing their positions in images obtained in the same filter and with the same exposure time for both $V$ and $I$ in the same epoch to test for intra-filter offsets. For the 1997 data, we choose images in the *F547W* and *F814W* filters with exposure times of 30 s and 20 s, respectively. Similarly, images in the *F555W* and *F814W* filters with exposure times of 26 s and 18 s, respectively, were chosen for the 2007 data. In each of these filters several images with the same exposure time were taken. We separate these images in the same filter and epoch to create two subsamples as input for *HSTphot*. Each subsample contains the same number of images (see Table 2.2). The selection of subsample images is random for the 1997 images. Since the 2007 images were obtained with the WFPC2-BOX dither pattern (Figure 2.2), we separate these images into two subsamples, whose positions are symmetric in the dither pattern. We use the common image as the reference for both subsamples of each filter. Since the spatial resolution of the PC chip is twice higher than the WFC chips, we only use the relative proper motions of stars on the PC chip to estimate the dynamical state and the fate of the cluster. Therefore, the centroid tests are only done on the PC chip.

*HSTphot* is then run on each subsample. We compare the resulting centroid positions of the common stars on the PC chip between two subsamples of a given filter and epoch. The centroid offsets of the common stars along the $x$ and $y$ directions (where $x$ and $y$ always refer to chip coordinates) are shown in Figure 2.8 for the 1997 data and in Figure 2.9 for the 2007 data. The distributions of the centroid offset of the stars in the *F547M* and *F814W* images of 1997 are centered at zero, with a dispersion of $\sigma_{\delta_x} = 0.012$ to $\sigma_{\delta_y} = 0.014$ pixels derived from fitting a Gaussian to their distribution. This indicates a good quality of the centroid of the stars in the 1997 data.

The distributions of the centroid offset of the stars in the 2007 data have a slightly larger dispersion of $\sigma_{\delta_x} = 0.016$ pixels to $\sigma_{\delta_y} = 0.017$ pixels for F814W and an even larger value of

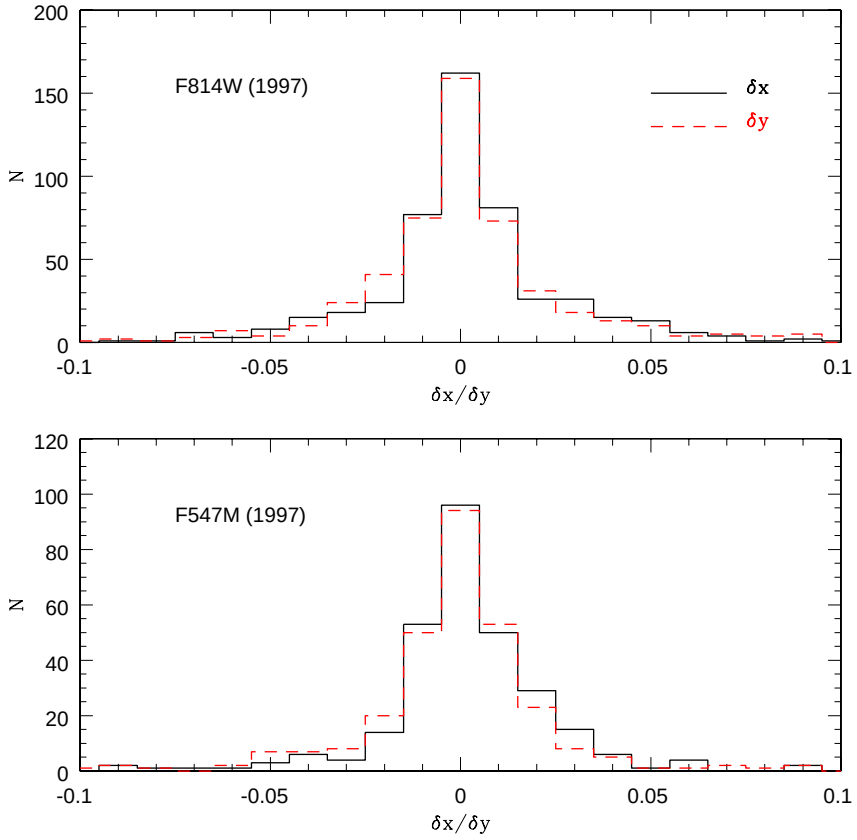


Figure 2.8: Histogram of the intra-filter centroid offsets in $x$ (solid lines) and $y$ (dashed lines) pixel coordinates of stars in images obtained in the *F814W* (upper panel) and *F547M* (lower panel) filters in 1997.

$\sigma_{\delta_x} = 0.019$ pixels to $\sigma_{\delta_y} = 0.023$ pixels for *F555W*. The distribution of the $x$ axis values of the centroid offset in the *F555W* data has its peak at $+0.01$ and is visibly off-centered from zero. A non-negligible fraction of stars even have centroid offsets in the $x$ direction of as much as 0.04 pixels and more in the *F555W* image. We display the spatial distribution of these deviating stars in Figure 2.10, where they are marked by red dots. But they do not show any spatial preference in their location on the PC chip, implying that this is not an effect of geometric distortion. The magnitude of most deviating stars is between 18–20 mag, except for one star with $V = 15.65$ mag that is possibly a binary or variable star. The images of the 2007 data set are dithered, which makes the resulting PSF more complex because the PSF also depends on the particular dither pattern adopted by the observer (e.g., Ibata & Lewis 1998). Furthermore, the subsample of 1997 data contains five images, while the 2007 subsample only consists of three images. Thus the accuracy of the posi-

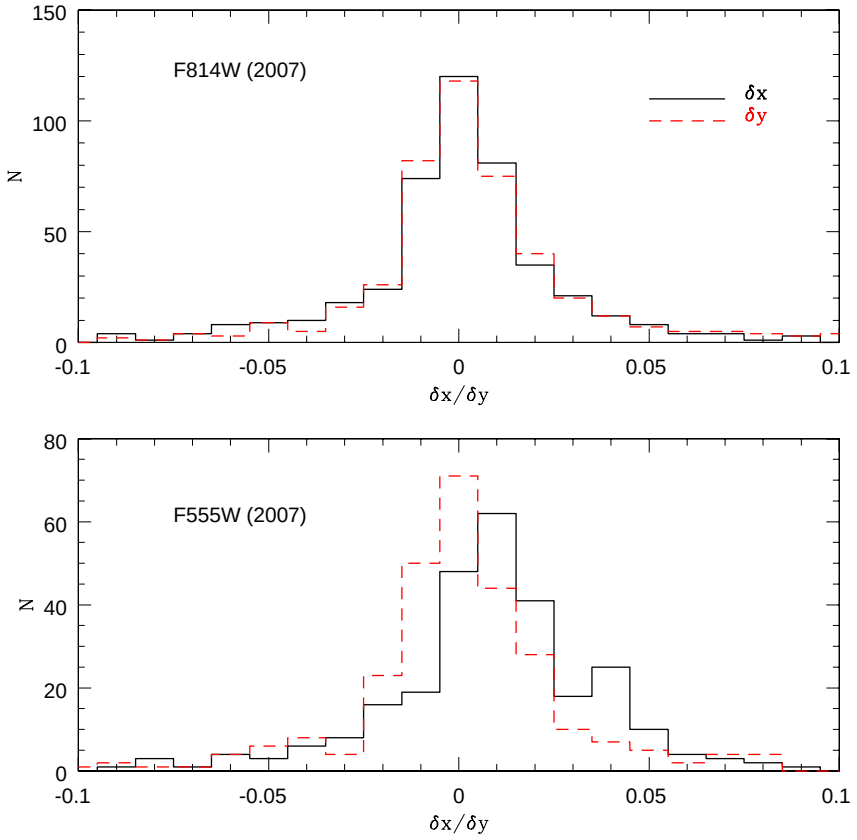


Figure 2.9: Histogram of the intra-filter centroid offsets in $x$ (solid lines) and $y$ (dashed lines) pixel coordinates of stars in images obtained in the *F814W* (upper panel) and *F555W* (lower panel) filters in 2007.

tion of stars from 1997 subsample is higher than in the 2007 data. Nevertheless, the accuracy for relative astrometry of the WFPC2 within one chip (after geometric corrections and the so-called 34th row correction) is 0.03 pixels on the PC (Dolphin 2000). Thus the intra-filter centroid offset of the stars observed in the *F555W* filter is of the order of the astrometric uncertainty.

### 2.3.2 Inter-filter centroid offsets in single epoch data

Stars located in the central regions of the HD 97950 cluster are suffering severe crowding (Section 2.2.3). The HSTphot centroid algorithm combines any two stars separated by less than 1.5 pixels (Dolphin 2000a). Therefore, a close "pair" of stars close to the cluster center may be combined into one single star in the output catalog. If the constituents of the close pair have different brightnesses in a given filter in the same epoch, e.g., one star is brighter in $V$ while the other one is brighter in

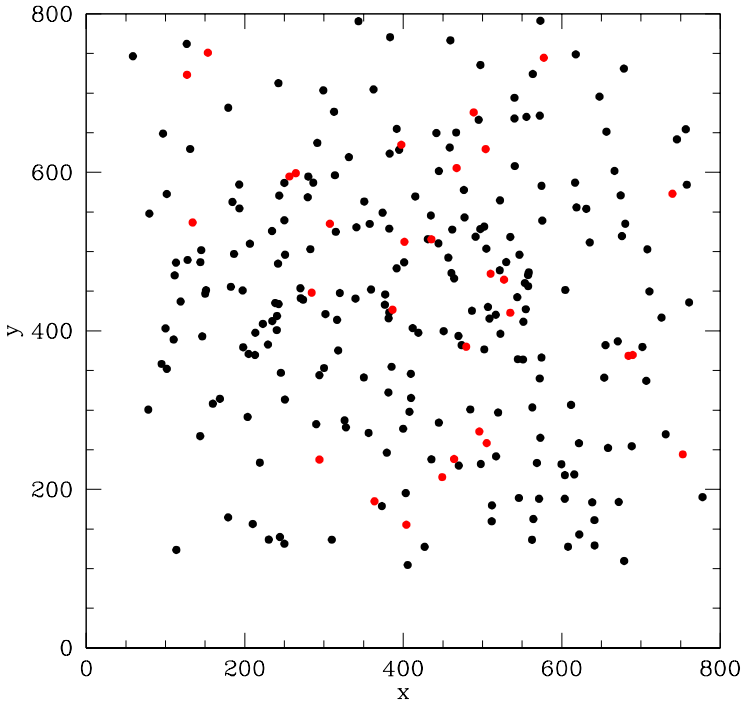


Figure 2.10: Spatial distribution of common stars on the PC chip between two subsamples of data obtained in the *F555W* filter in 2007. The black dots denote stars with intra-filter centroid offsets $\delta_x < 0.03$ pixels, and the red dots indicate stars with $0.03 < \delta_x < 0.05$ pixels (see Figure 2.9).

$I$, the centroid of the star combined from these two filters may have a large offset between the $V$ and $I$ filters, because the centroid of the star in *HSTphot* is the photometric uncertainty-weighted average of the centroids in single filter images (Dolphin 2000a). Furthermore, the variable stars such as T Tauri (mentioned in Section 2.3) showing large magnitude variation, would also have similar effect like the combined stars. If these combined stars or variables are included in the task *geomap* to derive transformation relations between two-epoch images, this will introduce a large uncertainty in the relative proper motion. Therefore, we are running another centroid experiment on the PC chip to find out whether there are stars with a large inter-filter centroid offset in the single epoch data, and remove them from the relative proper motion derivation.

Using the same exposures as the intra-filter centroid offset test, this time we do photometry on the full sample of images in the same filter (combing two subsamples in Table 2.2). We compare the centroids of common stars observed in the $V$ and $I$ filter equivalents of the same epoch. The centroid offsets of the stars along the $x$ and $y$ pixel directions are shown in Figure 2.11. The red dots denote stars having large inter-filter centroid offsets of $\sqrt{\Delta x_{V-I}^2 + \Delta y_{V-I}^2} > 0.3$ pixels, which might be due to brightness differences in $V$ and $I$ of the combined stars or possibly variables

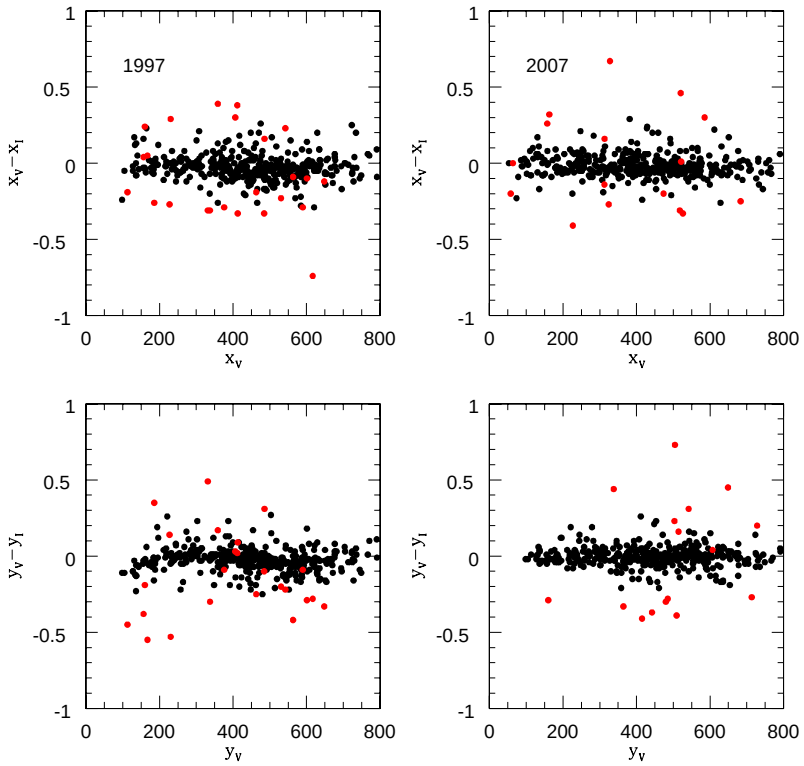


Figure 2.11: Inter-filter centroid offsets for data taken in $V$ and in $I$ in the $x$ and $y$ directions as a function of $V$-band $x$ (upper panels) and $y$ (lower panels) pixel coordinates. The left panels show the 1997 data; the right panels the 2007 data. The red dots are the stars with inter-filter centroid offsets $\sqrt{\Delta x_{V-I}^2 + \Delta y_{V-I}^2} > 0.3$ pixels.

(the mean magnitude difference between $V$ and $I$ is 3 mag for these stars). Figure 2.12 shows the centroid offsets in dependence of magnitude. The inter-filter centroid offset stays fairly constant for a large magnitude range, but increases for faint stars (especially pronounced for $V > 22$ mag). The stars with large inter-filter centroid offsets (red dots) are mostly faint stars, whose magnitude range is similar to the stars with large magnitude variation between two epoch observations (see Figure 2.7).

We reject the stars whose inter-filter centroid offsets are large, ($\sqrt{\Delta x_{V-I}^2 + \Delta y_{V-I}^2} > 0.3$ pixels) during the coordinate transformation between the data sets from the two epochs when *geomap* is applied. The *HSTphot* parameters roundness and sharpness of the rejected stars are shown in Figure 2.13. Sharpness is the ratio of the central pixel value to nearby pixel values. It is usually serves as a diagnostic to separate stars from non-stars. Accepted values for the sharpness of a

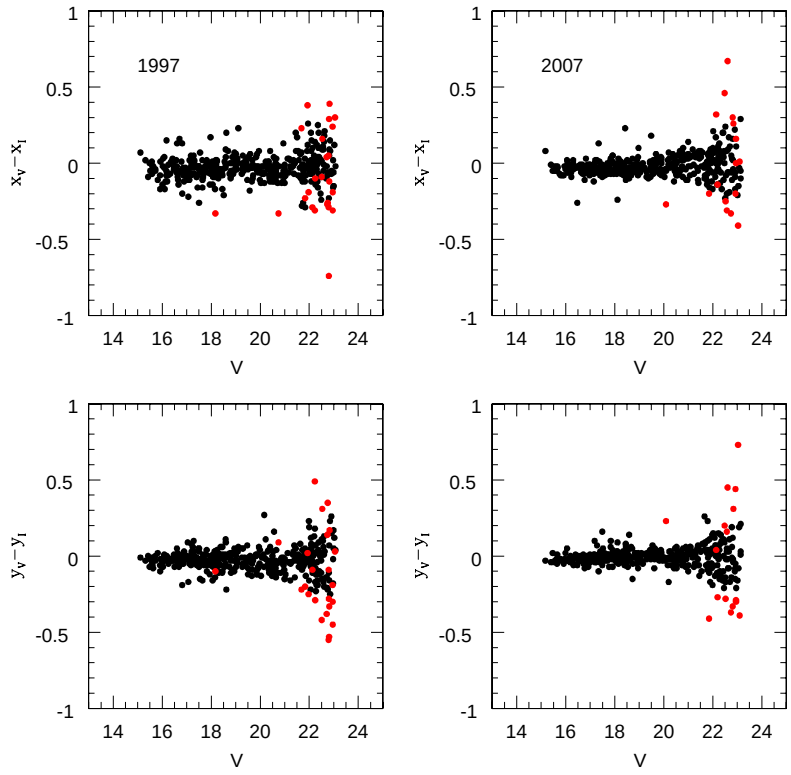


Figure 2.12: The dependence of the inter-filter centroid offset on the $V$ magnitude for the 1997 data (left panels) and the 2007 data (right panels). The red dots are the stars with inter-filter centroid offsets $\sqrt{\Delta x_{V-I}^2 + \Delta y_{V-I}^2} > 0.3$ pixels.

single star are between -0.3 and 0.3. Roundness is the size of the star in $x$-direction minus its size in $y$-direction in pixel coordinates. It is used to separate stars from noise and extended objects. For a good star, the roundness is zero. Compared to the majority of stars whose inter-filter centroid offsets are small (open dots), most of the rejected stars (filled dots) are extended ojects, which are possibly binaries or blends, or T Tauri stars (with accretion disks).

In a word, the intra-filter centroid offsets of the *V* and *I* filters are acceptable considering the order of the astrometric uncertainty. By removing the stars with large inter-filter centroid offsets, we are going to determine membership with acceptable accuracy.

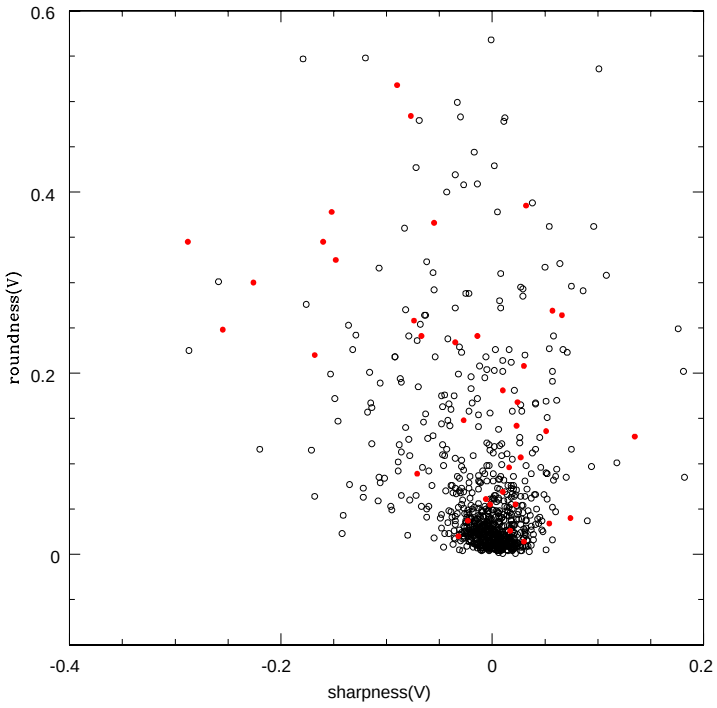


Figure 2.13: The sharpness versus the roundness of stars from single-filter photometry in $V$. The filled dots are the rejected stars with inter-filter centroid offsets of $\sqrt{\Delta x_{V-I}^2 + \Delta y_{V-I}^2} > 0.3$ pixels.

## 2.4 Membership determination

Relative and absolute proper motions are useful tools for the determination of membership probabilities in Galactic star clusters (e.g., Sanders 1971; Ianna et al. 1987; Jones & Walker 1988; Anderson & King 2003). While field stars may show a large range of proper motions, cluster members will show similar values. This is distinguishable in the so-called proper-motion vector point diagram (VPD) which depicts the proper motion by projecting it onto two directions (e.g., the $x$ and $y$ directions of pixel coordinates). Due to the high reddening ($E(B-V) = 1.25$ to 2.1 mag) in the giant H II region NGC 3603 around the HD 97950 cluster (Sung & Bessell 2004), background star contamination is negligible. However, this also prevents us from finding bright distant point sources as reference points for the determination of absolute proper motions. Instead, we use the relative proper motion to separate field stars from cluster stars, which works as efficiently for membership estimates as absolute proper motions.

Hence our work will permit us to mainly remove foreground stars whose relative proper motions are larger than those of the cluster members. We assume the cluster member stars to be all at

the same distance from us, adopting a distance of $d = 6.9$ kpc from Sung & Bessel (2004) for the HD 97950 cluster. At this distance we may ignore the depth extent of the cluster, which is very small as compared to the distance. In the subsections below, two methods are introduced to carry out membership determinations via relative stellar proper motions.

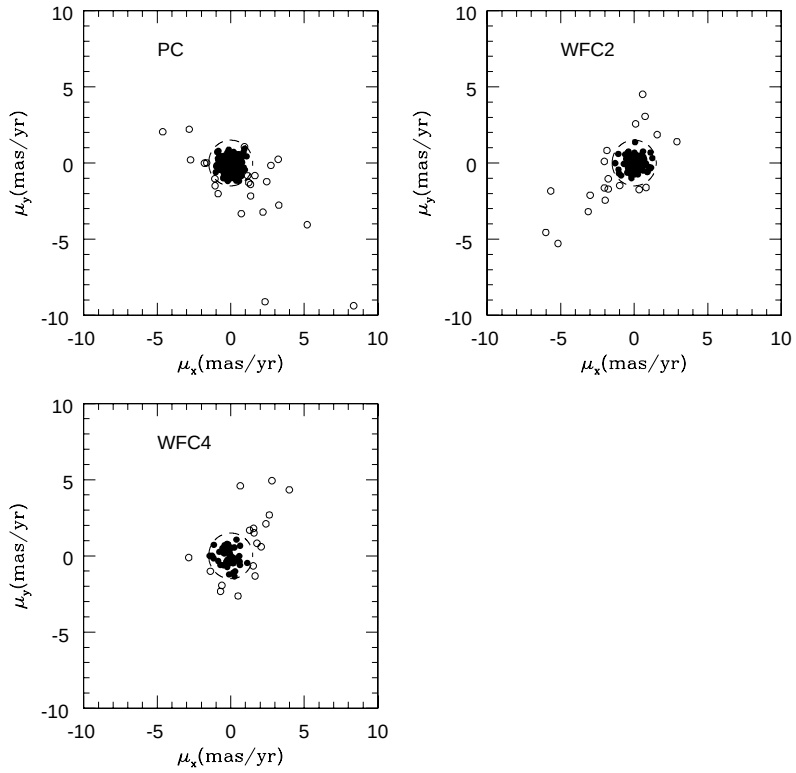


Figure 2.14: Relative proper motion vector point diagram (VPD) for the PC, WFC2, and WFC4 chips. The dashed circle corresponds to a relative proper motion equal to 1.5 mas yr$^{-1}$. The filled dots are member stars with a proper motion of less than 1.5 mas yr$^{-1}$, and the circles are field stars with proper motions larger than that.

### 2.4.1 First method: relative proper motion cut

In the relative proper motion VPD, the member locus is around zero motion. In contrast, the foreground stars scatter around the members exhibiting much larger motions. We select a generous circle around the cluster-motion locus with a radius of 0.3 pixels for the PC and 0.15 pixels for the WFCs, which corresponds to 1.5 mas yr$^{-1}$, to separate members and non-members in the relative proper motion VPD (Figure 2.14). All stars that lie within this circle are considered as member

stars (filled dots), and stars outside of it (open dots) are rejected as foreground field stars.

Assuming the member relative proper motions follow a Gaussian distribution, 1.5 mas yr$^{-1}$ correspond to a $2\sigma$ cut. This method results in 419 likely member stars on the PC chip, 76 member stars on the WFC2 chip, and 50 member stars on the WFC4 chip. The CMD of the probable member stars is displayed in Figure 2.15. The foreground field stars (red dots), which are mostly less affected by extinction than the member stars (circles) form a blue diagonal sequence of stars in the CMD. This "blue sequence" of foreground stars stands out even more clearly in the wider-field ground-based CMD in Figure 4a of Sung & Bessell (2004).

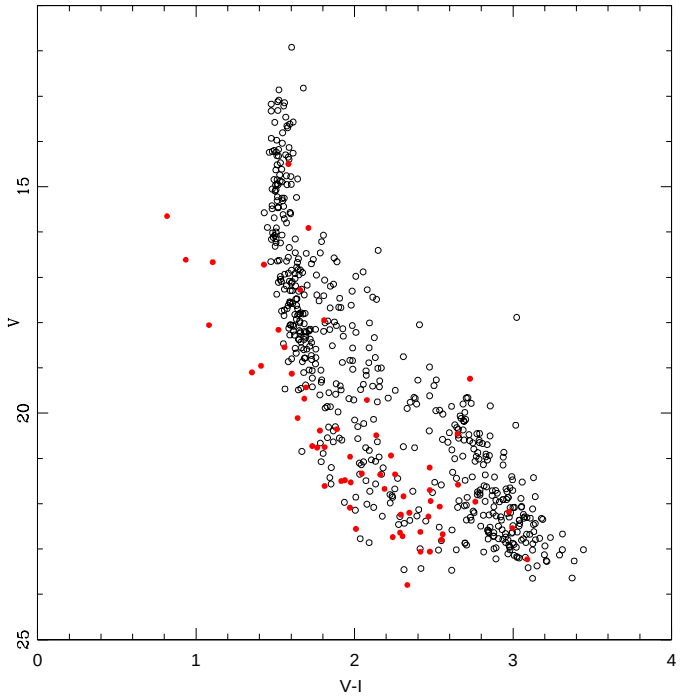


Figure 2.15: CMD of cluster member stars (open circles) and foreground field stars (filled dots) on the PC and the WFC chips of the two-epoch data. The open circles stand for member stars with relative proper motions less than 1.5 mas yr$^{-1}$.

### 2.4.2 Second method: two-Gaussian model

Even though the first method, the proper motion cut, works well in separating out the foreground field stars, we try a more rigorous method to statistically compute the membership probability. Jones & Walker (1988) assumed a Gaussian distribution for the proper motion distributions of the field and the cluster stars. They defined the membership probability of a star with a measured

proper motion as the ratio of the density of cluster stars to the density of cluster-plus-field stars in the proper motion VPD.

1) We adopt the King (1962) model (Equation 2.1) to represent the surface density profile of the observed stars in the cluster:

$$n(r) = k \cdot \left( \frac{1}{[1 + (\frac{r}{r_c})^2]^{1/2}} - \frac{1}{[1 + (\frac{r_t}{r_c})^2]^{1/2}} \right)^2 + n_f \tag{2.1}$$

Here $r$ is the cluster centric distance of the star, $k$ is a coefficient. $r_c$ is the cluster's core radius and $r_t$ is the tidal radius. $n_f$ is the field star density, which is a constant. We used the 443 common stars on the PC chip to construct the stellar surface-density profile of the HD 97950 cluster in Figure 2.16 Since no adjacent field was observed to estimate $n_f$, we fitted the King profile to the observed surface density distribution and derived the parameters $k$, $r_c$, $r_t$, and $n_f$. The black dots in Figure 2.16 represent the surface density of stars per unit area as a function of cluster-centric radius. The black line is the King profile with the best-fit parameters, $k = 3.017$, $r_c = 7.238''$, $r_t = 79.256''$, $n_f = 1.e-3$, weighted with an error of $n/\sqrt{N}$ (where $n$ is the surface density of each annulus and $N$ is the number of stars in each annulus).

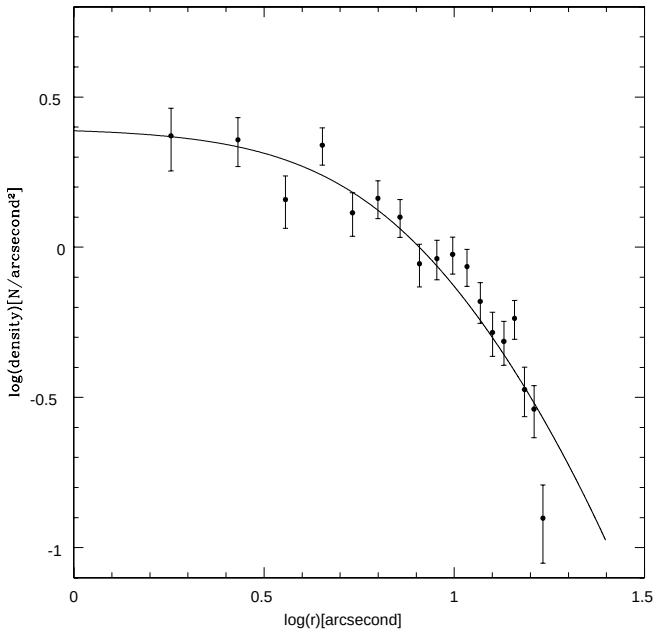


Figure 2.16: Surface density profile of stars in the HD 97950 cluster based on PC chip data. The black line indicates a King model fit with the parameters $k = 3.017$, $r_c = 7.238''$, $r_t = 79.256''$, $\phi = 1.e-3$. The fitting is weighted by the error $n/\sqrt{N}$, where $n$ is the surface density of each annulus and $N$ is the number of stars in each annulus.

2) We assume that the distributions of relative proper motions of the cluster and field are independent of magnitude and cluster-centric distance. We project the relative proper motion into the $x$ and $y$ directions of pixel coordinates. The one-dimensional normalized distribution of the relative proper motion in the $x$ direction, $\phi_x$, is:

$$\begin{aligned}\phi_x &= \phi_{c,x} + \phi_{f,x} \\ &= \frac{a_1}{\sqrt{2\pi\sigma_{x,c}^2}} \exp\left(-0.5\left(\frac{\mu_x - \mu_{x,c}}{\sigma_{x,c}}\right)^2\right) \\ &\quad + \frac{a_0 - a_1}{\sqrt{2\pi\Sigma_{x,f}^2}} \exp\left(-0.5\left(\frac{\mu_x - \mu_{x,f}}{\Sigma_{x,f}}\right)^2\right)\end{aligned} \tag{2.2}$$

$\phi_{c,x}$ is the normalized distribution function of cluster stars in the $x$ direction, while $\phi_{f,x}$ is the normalized distribution function for field stars. Similarly, the normalized distribution of the relative proper motion in the $y$ direction, $\phi_y$, is:

$$\begin{aligned}\phi_y &= \phi_{c,y} + \phi_{f,y} \\ &= \frac{b_1}{\sqrt{2\pi\sigma_{y,c}^2}} \exp\left(-0.5\left(\frac{\mu_y - \mu_{y,c}}{\sigma_{y,c}}\right)^2\right) \\ &\quad + \frac{b_0 - b_1}{\sqrt{2\pi\Sigma_{y,f}^2}} \exp\left(-0.5\left(\frac{\mu_y - \mu_{y,f}}{\Sigma_{y,f}}\right)^2\right)\end{aligned} \tag{2.3}$$

Here $\phi_{c,y}$ is the normalized distribution function of cluster stars in the $y$ direction, while $\phi_{f,y}$ is the one for field stars. $a_0$ and $b_0$ are the normalization factor, $a_0 = b_0 = 0.25$. The parameters of cluster stars are:
$a_1$ = the fraction of cluster stars in $x$;
$b_1$ = the fraction of cluster stars in $y$;
$\sigma_{x,c}$ = the relative proper motion dispersion of cluster stars in $x$;
$\sigma_{y,c}$ = the relative proper motion dispersion of cluster stars in $y$;
$\mu_{x,c}$ = the mean cluster relative proper motion in $x$;
$\mu_{y,c}$ = the mean cluster relative proper motion in $y$.
The parameters of field stars are:
$\Sigma_{x,f}$ = the relative proper motion dispersion of field stars in $x$;
$\Sigma_{y,f}$ = the relative proper motion dispersion of field stars in $y$;
$\mu_{x,f}$ = the mean field relative proper motion in $x$;
$\mu_{y,f}$ = the mean field relative proper motion in $y$.

These ten parameters are derived by fitting the normalized distribution functions to the observed relative proper motion distributions in the $x$ and $y$ directions. Initial guess values for all parameters are given by Sanders (1971). The fitting program iterates, varying the associated parameters, until the distribution function is found that fits best the observed distribution function.

Table 2.3: Fitted parameters for the distribution functions $\phi_x$ and $\phi_y$ of relative proper motions

| Parameters | fit value (mas/yr) |
|---|---|
| $a_1$ | 0.186±0.017 |
| $\sigma_{x,c}$ | 0.268±0.021 |
| $\mu_{x,c}$ | 0.221±0.017 |
| $\Sigma_{x,f}$ | 0.726±0.102 |
| $\mu_{x,f}$ | 0.154±0.079 |
| $b_1$ | 0.151±0.027 |
| $\sigma_{y,c}$ | 0.264±0.029 |
| $\mu_{y,c}$ | 0.293±0.027 |
| $\Sigma_{y,f}$ | 0.541±0.050 |
| $\mu_{y,f}$ | -0.010±0.085 |

The resulting parameters are listed in Table 2.3. Figure 2.17 displays the normalized distribution functions in the $x$ and $y$ directions fitting to the observed relative proper motion distribution of stars on the PC chip. The solid line is the one-dimensional normalized distribution function ($\phi_x$ or $\phi_y$). The dotted line represents the cluster distribution function ($\phi_{c,x}$ or $\phi_{c,y}$) and the dashed line the field stars ($\phi_{f,x}$ or $\phi_{f,y}$). We assume the same surface density profile for stars on the WFC chips as those on the PC chip, and apply the same procedure to the stars on the WFC chips (see Figure 2.18). We combine stars on the WFC2 and WFC4 chips in order to increase the S/N ratio.

The membership probability of each star is calculated according to Equation 12 in Jones & Walker (1988), which is our Equation 2.4:

$$P_{mem} = \frac{(n(r)/n_f)\phi_c}{(n(r)/n_f)\phi_c + \phi_f} \tag{2.4}$$

$\phi_c$ and $\phi_f$ are the two-dimensional normalized distribution functions of proper motions for cluster stars and field stars, $\phi_c = \phi_{c,x} \cdot \phi_{c,y}$ and $\phi_f = \phi_{f,x} \cdot \phi_{f,y}$. Figure 2.19 shows the histogram of the membership probability of stars on the PC and WFC chips. There are two distinct groups, one with high membership probability ($P_{mem} > 0.7$) and the other with a low membership probability ($P_{mem} < 0.2$). We consider stars with $P_{mem} > 0.7$ to be members. This results in 411 members on the PC chip and 124 members on the WFC chips, in good agreement with the result of the first method where we found 419 and 126 members on the PC and WFC chips, respectively. Since membership probabilities of individual stars can be calculated by this method, we consider the two-Gaussian model fitting as a more robust way to determine membership. The photometry and relative proper motions of the member stars from this selection is available in the Appendix Table A.1-A.15.

If we decrease the acceptable membership probability ($P_{mem}$), the overlap ratio between these two methods increases. In Table 2.4, we list the number of member stars of the two methods and the overlap ratio between them in dependence of the chosen membership probability ($P_{mem}$). Generally, the number of stars in our sample is not large enough to see a distinct difference whether

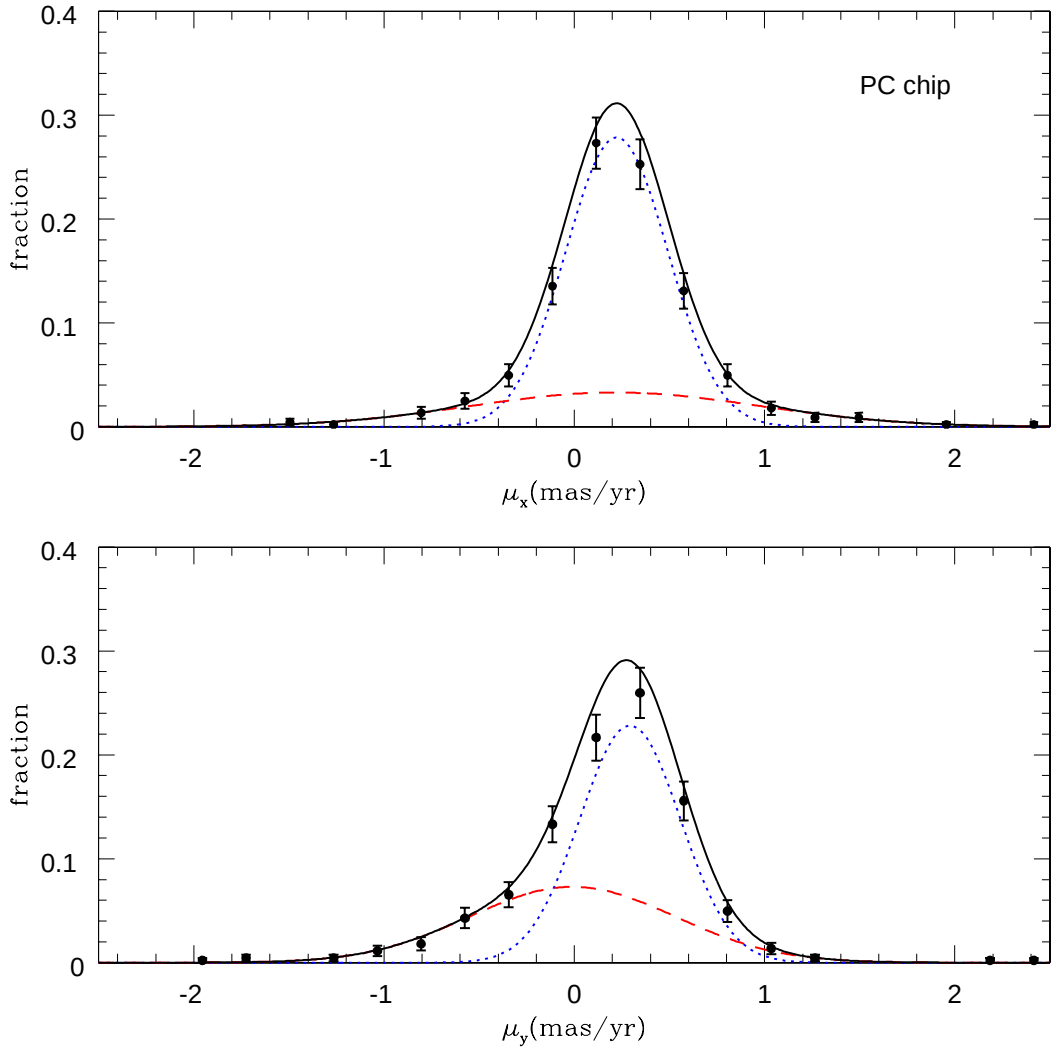


Figure 2.17: Relative proper motion distribution of stars on the PC chip along the $x$ and $y$ directions of pixel coordinates, fitted by a two-component Gaussian distribution (solid line). The dotted lines represent the cluster components ($\phi_{c,x}$ or $\phi_{c,y}$), and the dashed lines the field contamination ($\phi_{f,x}$ or $\phi_{f,y}$). The error bars show the Poisson errors.

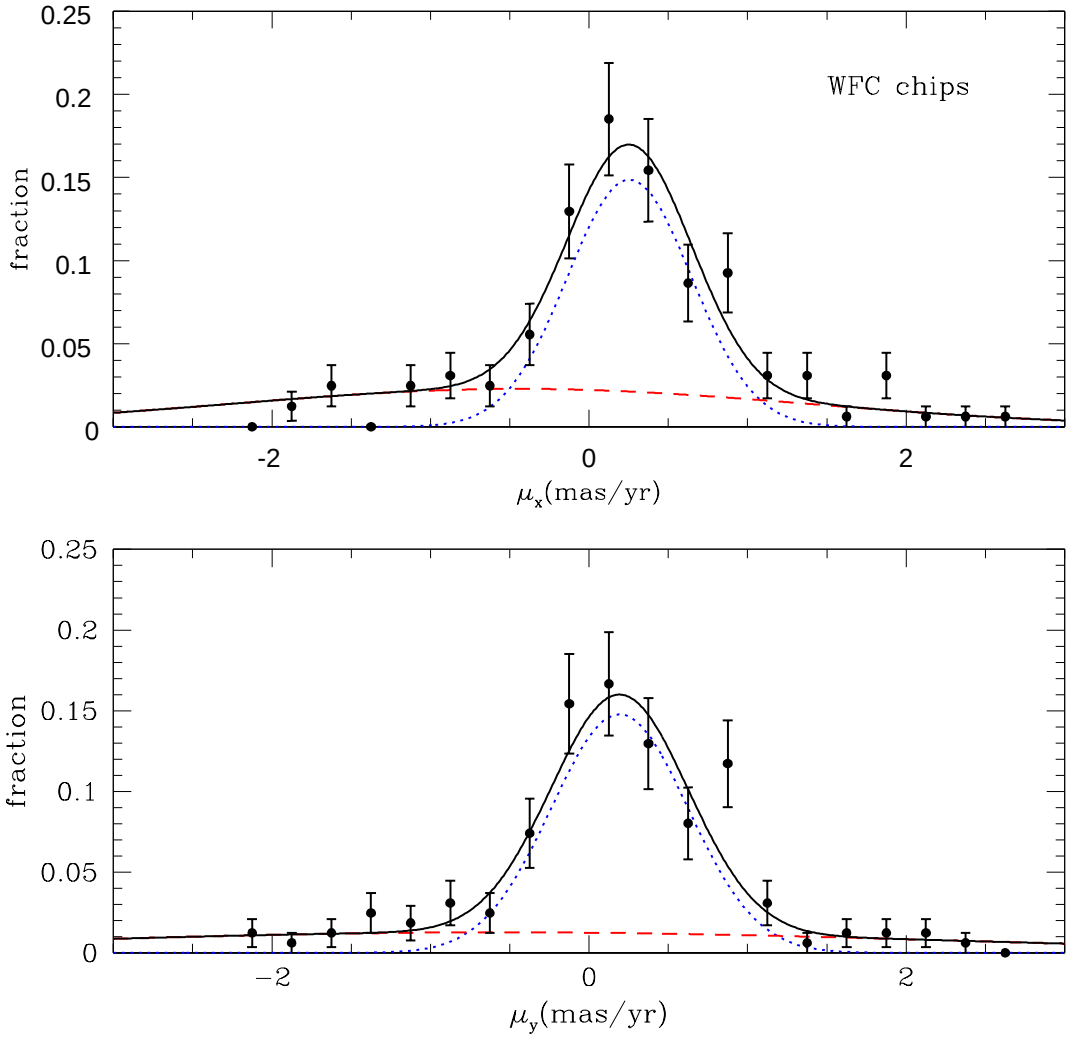


Figure 2.18: Relative proper motion distribution of stars on the WFC (WFC2 & WFC4) chips along the $x$ and $y$ directions of pixel coordinates, fitted by a two-component Gaussian distribution (solid lines). The dotted lines represent the cluster components ($\phi_{c,x}$ or $\phi_{c,y}$), and the dashed lines the field stars ($\phi_{f,x}$ or $\phi_{f,y}$). The error bars show the Poisson errors.

we choose members with $P_{mem} > 0.9$ or $P_{mem} > 0.8$. Figure 2.20 shows the relative proper motion distribution of the 535 members (PC & WFCs), which are the common members between two methods when we consider members with $P_{mem} > 0.7$.

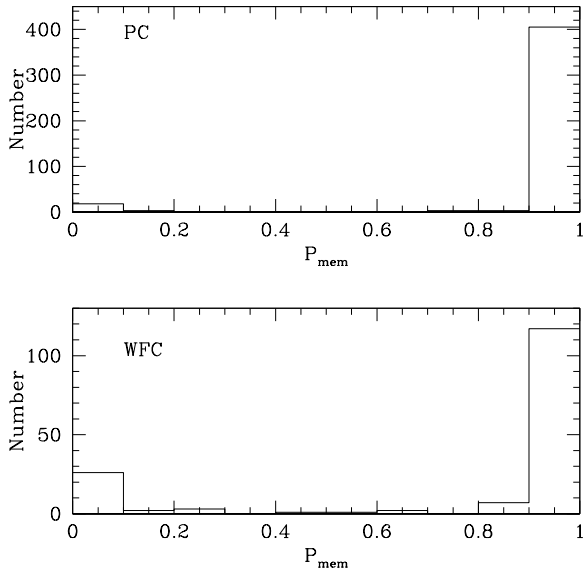


Figure 2.19: Histograms of the membership probability for stars on the PC chip (upper panel) and the WFC chips (lower panel).

### 2.4.3 Relative proper motions of field stars

The contamination by foreground field stars ($P_{mem} < 0.7$) is 7% on the PC chip, and 25.3% the WFC chips. These numbers are derived from the second method of membership determination (Section 2.4.2). The PC chip is centered on the HD 97950 cluster ($r < 20''$), while the WFC chips

Table 2.4: Number of members determined from a relative proper motion cut (first method) and a two-Gaussian fitting (second method)

| First Method | | | Second Method | | Overlap Ratio | |
|---|---|---|---|---|---|---|
| WFC | PC | $P_{mem}$ | WFC | PC | WFCs | PC |
| 126 | 419 | 0.5 | 127 | 413 | 96.8% | 98.6% |
| 126 | 419 | 0.6 | 126 | 412 | 96.8% | 98.3% |
| 126 | 419 | 0.7 | 124 | 411 | 96.0% | 98.1% |
| 126 | 419 | 0.8 | 124 | 408 | 96.0% | 97.4% |
| 126 | 419 | 0.9 | 117 | 405 | 92.9% | 96.7% |

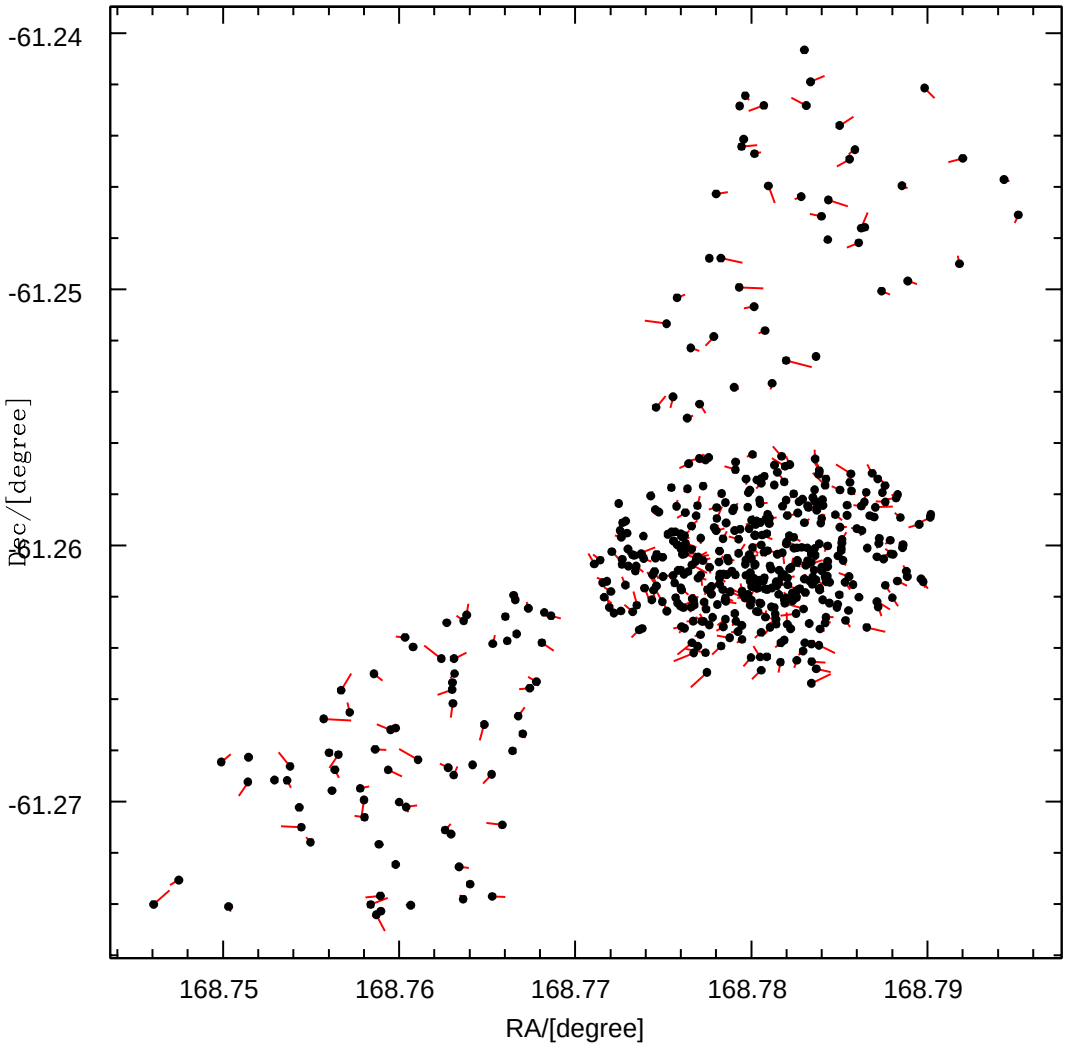


Figure 2.20: Relative proper motion distributions of 535 member stars on the PC and WFC chips in the HD 97950 cluster. Each dot represents one star, the short red lines show the magnitude of relative proper motion of the stars in scale with the direction indicated.

point at the cluster outskirts ($20'' < r < 100''$) with a four times larger field of view than that of the PC chip. Therefore, the field star contamination of each of the WFC chips is about four times of that of the PC chip, assuming a constant distribution of field stars.

The total areas of the WFC2 and WFC4 chips, where the two-epoch data overlap and relative proper motions of stars are derived, amount to about 70 percent of the field of view of one single WFC chip. This explains why the field star fraction of the WFC chips is smaller than four times of that of the PC chip. We display the relative proper motion distribution of field stars on the PC and WFC (WFC2 and WFC4) chips in Figure 2.21. The field stars show no correlation of relative proper motion across the three fields, indicating that they are true non-members.

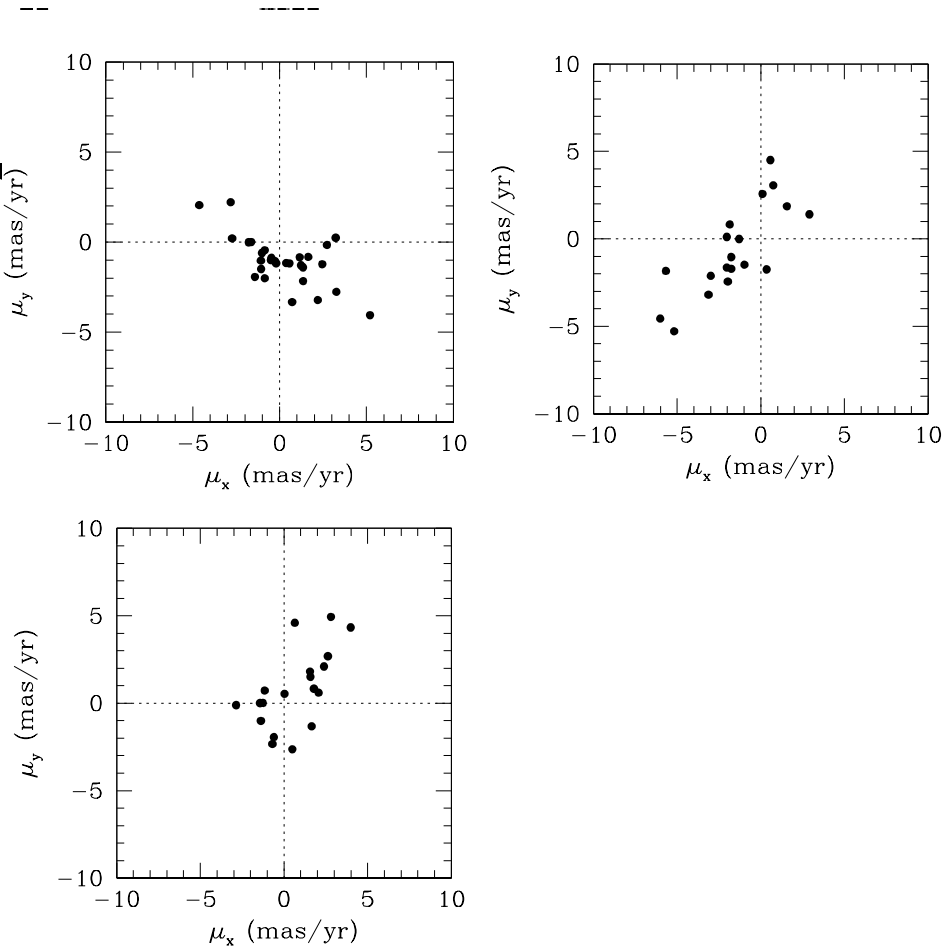


Figure 2.21: Relative proper motion vector point diagrams (VPD) for non-members ($P_{mem} < 0.7$) on the PC, WFC2, and WFC4 chips.

## 2.5 Kinematics

### 2.5.1 Velocity dispersion

Precise velocity dispersion measurements are an essential tool for dynamical mass estimates of star clusters as well as for investigations of their dynamical state. However, *radial* velocity dispersion measurements based on individual stars in compact clusters can be difficult to achieve when the angular diameter of the target cluster is very small and crowding becomes a major issue – a problem that is certainly present in the HD 97950 cluster. Additional exacerbating factors are unrecognized binarity and contributions from field star interlopers (see, e.g., Odenkirchen et al. 2002; Adén et al. 2009). Such contaminants may inflate the resulting radial velocity dispersion.

Lacking a well-defined radial velocity sample of stars in the HD97950 cluster, we instead derive *tangential* velocities from our proper motion estimates. This also permits us to exclude probable non-members based on their deviant proper motion (see Section 2.4).

In Section 2.4.2, we derived the dispersion of the relative proper motions of member stars on the PC chip by fitting $x$- and $y$-coordinate Gaussian distribution functions to the observed relative proper motion distributions: $\sigma_{x,c} = 0.268 \pm 0.021$ mas yr$^{-1}$ ($8.8 \pm 0.7$ km s$^{-1}$; adopt $d = 6.9$ kpc from Sung & Bessell (2004)) and $\sigma_{y,c} = 0.264 \pm 0.027$ mas yr$^{-1}$ ($8.6 \pm 1.0$ km s$^{-1}$). The corresponding velocity dispersion is $\sigma_c = 12.3 \pm 1.0$ km s$^{-1}$.

This velocity dispersion is larger than the value computed by Rochau et al. (2010), who derived $\sigma_{1D} = 0.184\,\mathrm{mas/yr}$ from the averaged one-dimensional proper motions ($\mu_{1D} = (\mu_l + \mu_b)/2$). Assuming an isotropic distribution of velocities ($\mu_{1D} = (\mu_l + \mu_b)/2 = (\mu_x + \mu_y)/2$ and $\sigma_l$=$\sigma_l$=$\sigma_x$=$\sigma_y$), the relation between the dispersion of $\mu_{1D}$, $\mu_x$ and $\mu_y$ is

$$\begin{aligned} \sigma_{1D} &= \sigma(\frac{\mu_x + \mu_y}{2}) \\ &= 1/2\sigma(\mu_x + \mu_y) \\ &= 1/\sqrt{2}\sigma_x = 1/\sqrt{2}\sigma_y \end{aligned} \tag{2.5}$$

Therefore, we should obtain a one-dimensional velocity dispersion of

$$\sigma_x = \sigma_y = \sigma_{1D} \times \sqrt{2} = 0.260 \text{ mas yr}^{-1}.$$

This is very close to the value we derived from the two-Gaussian fitting. Nevertheless, the averaged one-dimensional velocity dispersion is smaller than the non-averaged one-dimensional velocity by almost a factor of two, and therefore makes a difference in estimating the dynamical state of the cluster. Since this method did not consider any errors from observation, the resulting velocity dispersion will be an upper limit to the true value.

#### A second method to estimate the velocity dispersion

Using stars on the PC chip, which points at the cluster center, provides a more reliable velocity dispersion than using stars on the WFC chips because of the higher resolution of the PC. We

compute the observed dispersion (OD) of relative proper motions from stars on the PC chip, which are members based on both methods of membership determination (Section 2.4.1 and 2.4.2). The luminosity function of these members are shown in Figure 2.22. All identified member stars are brighter than $V = 23$ mag. But since the completeness fraction is below 50% for stars fainter than $V = 22$ mag (see Figure 2.5), we only use members brighter than $V = 22$ mag to derive the real dispersion (RD). We assume that the errors of the observed dispersion are the random errors (REs) from the 1997 and 2007 observations. We divide the original single epoch data into two

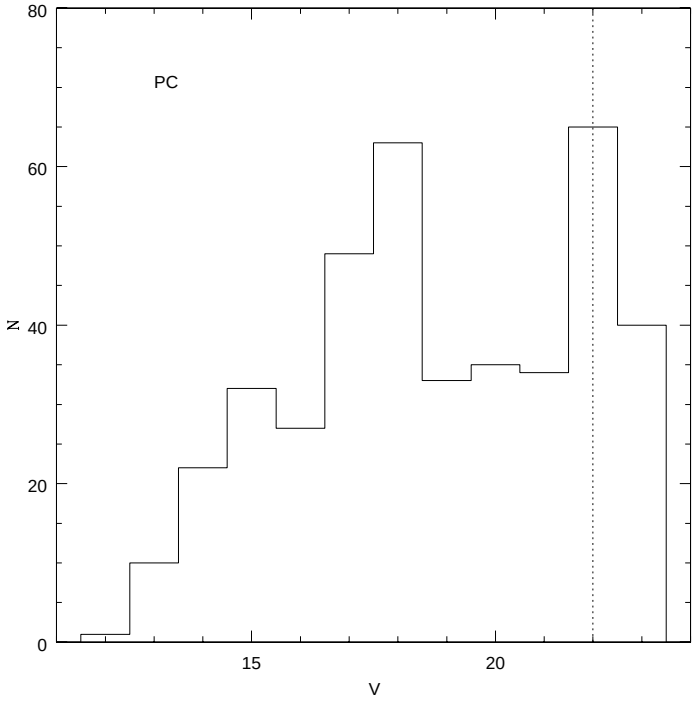


Figure 2.22: Luminosity function of member stars on the PC chip. The dashed line indicates the 50% completeness limit.

subsamples: set$1_{97}$, set$2_{97}$; set$1_{07}$, set$2_{07}$. Each subsample contains two-filter ($V$ & $I$) images. After doing photometry on each subsample, we find common stars with $V < 22$ mag between two subsets of the same epoch. Stars with positional differences less than 0.1 pixels and magnitude differences in $V$ and $I$ of less than 0.1 mag are considered to be common stars. Due to true centroid offsets, CCD defects, and astrometry uncertainties in the measurement of star position from *HSTphot*, the detected positions of the same star in the two subsamples may be slightly offset from one another. The standard deviation of this positional offset is the RE. The following equations illustrate the relations among the REs, the OD and the RD.

Table 2.5: Parameters to Determine Velocity Dispersion

| | | Milli-arcsecond |
|---|---|---|
| OD in x | $\sigma'_x$ | 0.316 |
| OD in y | $\sigma'_y$ | 0.324 |
| RE in x of 1997 data | $\sigma_{x_{97}}$ | 0.172 |
| RE in y of 1997 data | $\sigma_{y_{97}}$ | 0.134 |
| RE in x of 2007 data | $\sigma_{x_{07}}$ | 0.167 |
| RE in y of 2007 data | $\sigma_{y_{07}}$ | 0.167 |
| RD in x | $\sigma_{x,c}$ | 0.206 |
| RD in y | $\sigma_{y,c}$ | 0.243 |

The OD, $\sigma_{\rm OD}$, is a combination of the $x$ ($\sigma'_x$) and $y$ ($\sigma'_y$) components.

$$\sigma^2_{\rm OD} = \sigma'^2_x + \sigma'^2_y \tag{2.6}$$

Each component consists of the RD ($\sigma_{x,c}$, $\sigma_{y,c}$) and the RE ($\sigma_{x,\rm RE}$, $\sigma_{y,\rm RE}$).

$$\sigma'^2_x = \sigma^2_{x,c} + \sigma^2_{x,\rm RE} \tag{2.7}$$

$$\sigma'^2_y = \sigma^2_{y,c} + \sigma^2_{y,\rm RE} \tag{2.8}$$

The RE components originate from the 1997 and 2007 data, respectively.

$$\sigma^2_{x,\rm RE} = \sigma^2_{x_{97}} + \sigma^2_{x_{07}} \tag{2.9}$$

$$\sigma^2_{y,\rm RE} = \sigma^2_{y_{97}} + \sigma^2_{y_{07}} \tag{2.10}$$

$\sigma^2_{x_{97}}$, $\sigma^2_{y_{97}}$ and $\sigma^2_{x_{07}}$, $\sigma^2_{y_{07}}$ are the standard deviations of the star positional offsets between two subsamples in each epoch (see Table 2.5 for their values). We subtract the REs from the OD and obtain the RD components $\sigma_{x,c} = 0.206 \pm 0.56$ mas yr$^{-1}$ and $\sigma_{y,c} = 0.243 \pm 0.49$ mas yr$^{-1}$. By adopting $d = 6.9$ kpc from Sung & Bessell (2004), the one-dimensional velocity dispersion in $x$ and $y$ is $\sigma_{x,c} = 6.74 \pm 0.56$ km s$^{-1}$ and $\sigma_{y,c} = 7.95 \pm 0.49$ km s$^{-1}$. The uncertainty is computed according to Equation 12 in Pryor & Meylan (1993). The corresponding two-dimensional velocity dispersion is $\sigma_c = 10.42 \pm 0.62$ km s$^{-1}$. The observational errors are considered and subtracted from the observed velocity dispersion in this method, making the resulting $\sigma_c$ more reliable than the value derived from a two-Gaussian model fitting. Therefore, we are going to use this value of $\sigma_c$ to estimate the dynamical state of the HD 97950 cluster.

### 2.5.2 Kinematic signatures

#### Relative proper motion dispersion profile

We investigate the profile of the relative proper motion dispersion to look for kinematic signatures of the dynamical evolution of the HD 97950 cluster. Figure 2.23 presents the profile of the relative

proper motion dispersion (red dots) as a function of the $V$-band magnitude of the member stars (circles) on the PC and WFC chips. There is a weak trend of increasing dispersion in relative proper motions from the bright to the faint stars, which, if real, may indicate there is no significant equipartition in the cluster yet.

Figure 2.24 displays the profile of the relative proper motion dispersion as a function of distance from the cluster center (the pointing of the PC chip). The relative proper motion dispersion slightly decreases toward the cluster center where the majority of bright massive stars is located. However, the dispersion does not show a pronounced dependence on the brightness and the location of the stars.

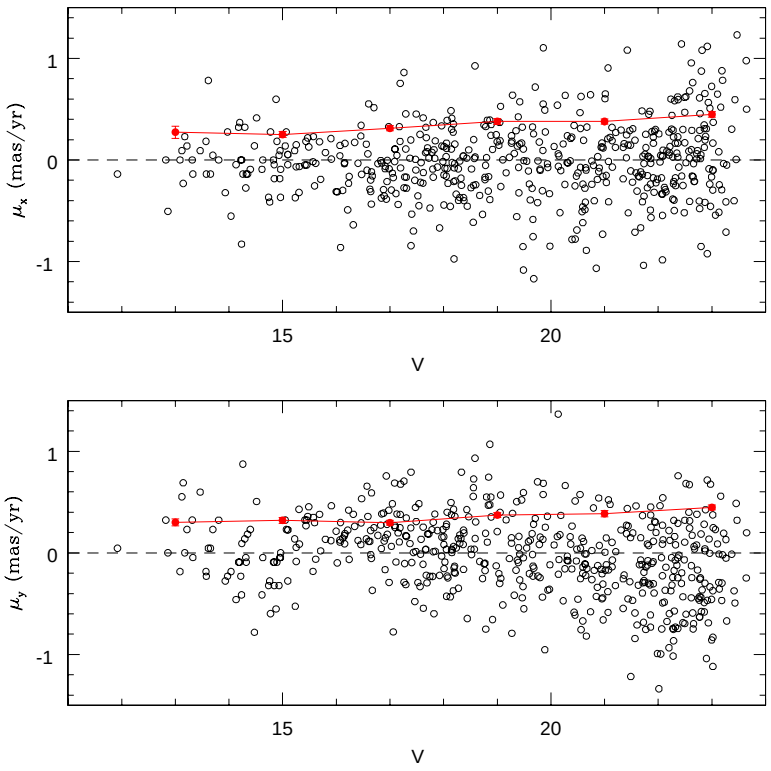


Figure 2.23: Dependence of the relative proper motions (components in the $x$ and $y$ directions of pixel coordinates) of cluster member stars (open circles) on the $V$ magnitude. The filled dots indicate the dispersions of the relative proper motions inside each magnitude bin (binsize = 2 mag).

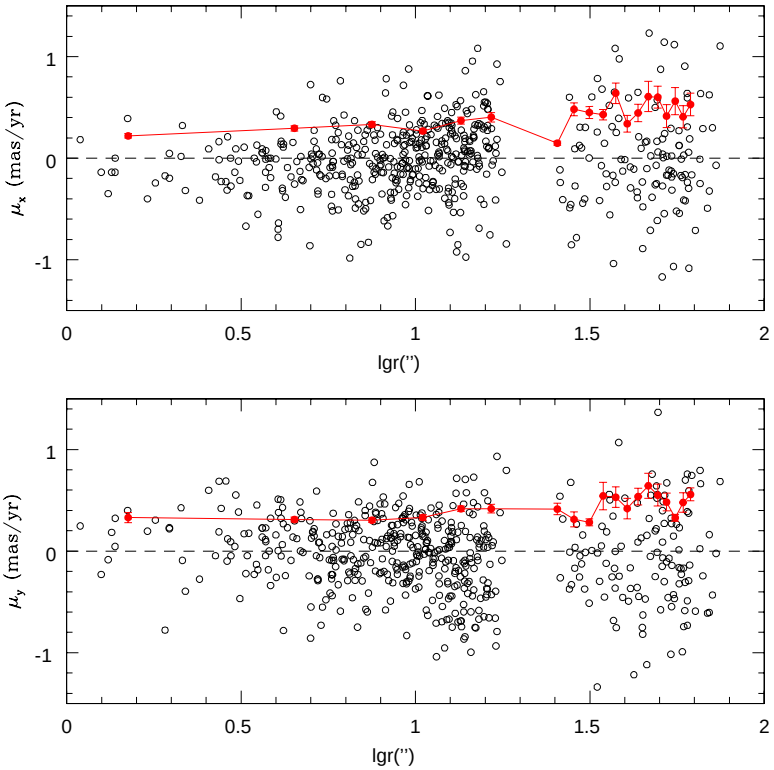


Figure 2.24: Dependence of the relative proper motions (components in the $x$ and $y$ directions of pixel coordinates) of cluster member stars (open circles) on the cluster-centric distance. The filled dots are the dispersions of the relative proper motions inside each annulus (annulus width $= 3''$).

### Tangential velocity profile

We convert the relative proper motion into tangential velocities of member stars on the PC and WFC chips by the following equation:

$$v_t = d \times \mu \tag{2.11}$$

where $v_t$ is the tangential velocity, and $\mu$ is the relative proper motion. We adopt the distance of the cluster $d$ to be 6.9 kpc from Sung & Bessell (2004). With $3 \times 10^7$ s in a year, equation (2.12) can be written as:

$$v_t(\mathrm{km/s}) = 5 \times d(\mathrm{kpc}) \times \mu(\mathrm{mas/yr}) \tag{2.12}$$

The distributions of the tangential velocities of member stars on the PC and WFC chips are shown in Figure 2.25. The upper panel of Figure 2.25 shows the profile of mean tangential velocity (filled dots) of each magnitude bin, and the lower panel displays the mean tangential velocity within each

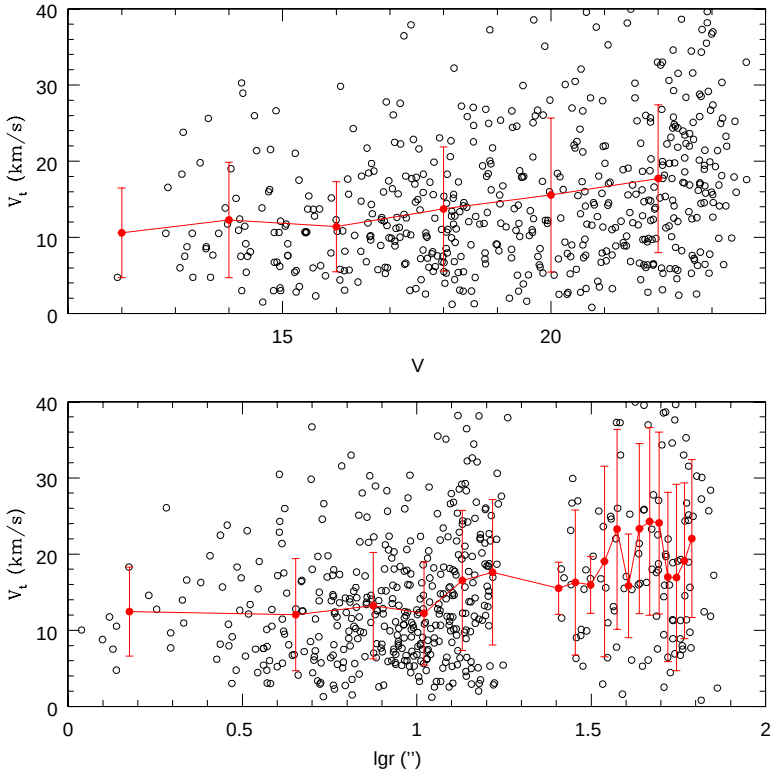


Figure 2.25: Dependence of the tangential velocity on the $V$ magnitude and the cluster-centric distance. The filled dots show the mean velocity in each magnitude bin (binsize = 2 mag; upper panel) and in each annulus (annulus width $= 3''$; lower panel). The error bar shows the corresponding velocity dispersion.

annulus. The tangential velocity increases from bright to faint stars and with increasing cluster radius. However, considering the age of the cluster of (1 Myr – 3 Myr), the dynamical evolution or energy equipartition is mass-dependent, and may not affect all the stars of the volume $r = 20''$ yet (see Chapter 3). Therefore, we separate the stars into smaller volumes (five annuli) and display their tangential velocity profiles in Figure 2.26. The profile shows no dependence on the brightness of stars brighter than $V = 20$ mag and within $12''$. There is a steady increase of tangential velocity for the stars ($15 < V < 23$ mag) in the annulus $12 < r < 20''$. The velocity profile is quite flat for the three outermost annuli, staying around 20 km s$^{-1}$. Recent studies (e.g., Allison et al. 2009a, 2009b; Yu et al. 2011) have suggested that dynamical segregation may happen to young clusters with 1000 $M_\odot$ within 1 Myr if they formed in initially clumpy and subvirial conditions. We do not find significant kinematic evidence to support a dynamical segregation in the HD 97950 cluster, which has a mass of about 10,000 $M_\odot$ (Harayama et al. 2008). However, relative proper

motions of 10 years apart might not be sufficient to probe the kinematic signatures resulted from dynamical segregation in the cluster located 6.9 kpc away. Therefore, third epoch data are needed to increase the accuracy of relative proper motions of the stars in order to unambiguously identify the signature of dynamical segregation in the HD 97950 cluster.

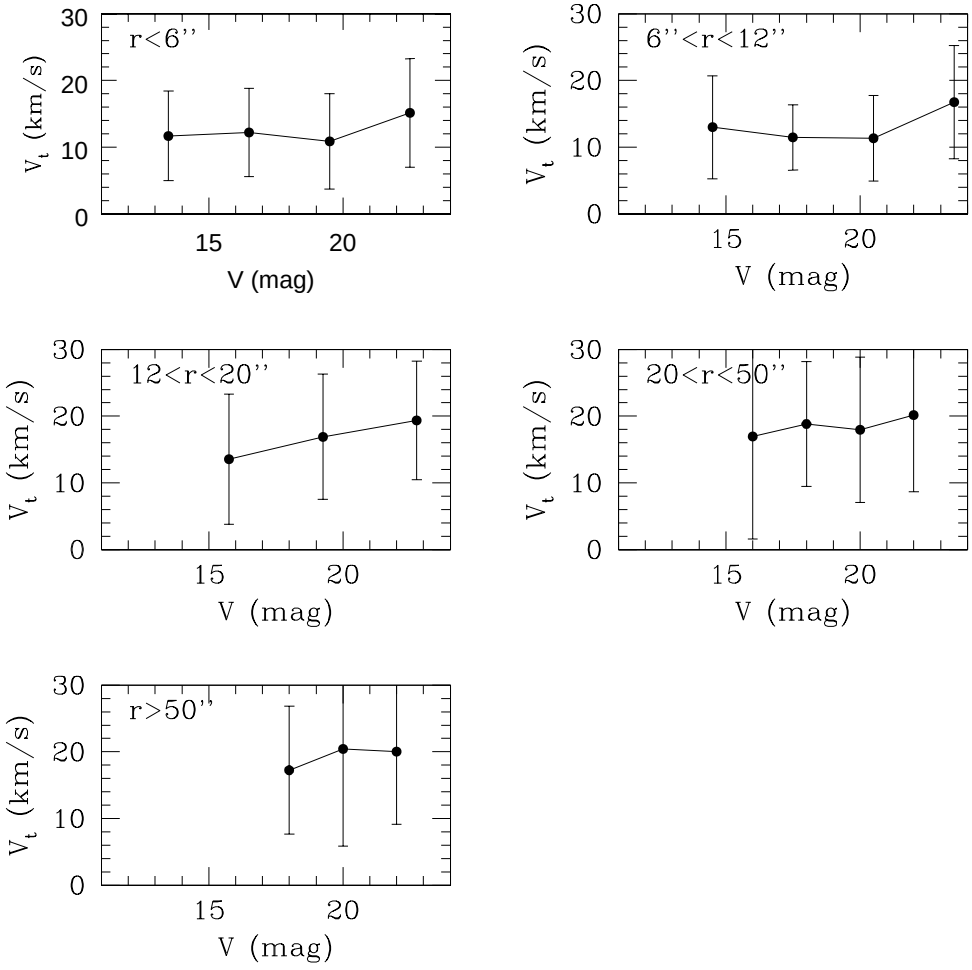


Figure 2.26: Dependence of the mean tangential velocity on the $V$ magnitude in five annuli around the cluster center. The error bar denotes the corresponding velocity dispersion.

## 2.6 The fate of the HD 97950 cluster

We adopt the velocity dispersion $\sigma_c = 10.42$ km s$^{-1}$ in which random errors from observations has been considered, and assume an isotropic velocity distribution, with a half-mass radius of $R_{hm} \sim 0.7$ pc (Harayama et al. 2008), the dynamical mass $M_{dyn}$ of HD 97950 can be calculated from Spitzer's (1987) formula

$$M_{dyn} \sim \eta \frac{R_{hm}\sigma_{vt}^2}{G}$$

resulting in a dynamical mass of $M_{dyn} \sim 1.7 \times 10^5$ M$_\odot$ ($\eta = 9.75$). This mass is more than ten times higher than photometric mass $M_{phot} = 1.6 \times 10^4\,\mathrm{M}_\odot$ derived from observations of the stellar content (Harayama et al. 2008), which was computed by integrating the mass function ($\Gamma = -0.74$) over the mass range 0.1-100 M$_\odot$. This significant difference between $M_{dyn}$ and $M_{phot}$ may indicate the cluster HD 97950 being out of virial equilibrium (Goodwin & Bastian 2006).

In order to better estimate the dynamical state of the cluster, we estimate the cluster luminosity with the 535 member stars on the PC and WFC chips, among which the majority is located within 1 pc from the center. To correct the extinction for the luminosity of the members, we assumed $R_V = 3.55$ and adopted the reddening value E(B-V)=1.25 from (Sung & Bessel 2004). Luminosities of members on the PC chip are corrected for incompleteness (Figure 2.5). The resulting total luminosity is $4.75 \times 10^5\,\mathrm{L}_\odot$, for a distance modulus of 14.2 mag ($d = 6.9$ kpc, Sung & Bessel 2004). But the three massive WN stars (A1, B, C) (Crowther et al. 2010; Schnurr et al. 2008) whose total mass exceeds 400 M$_\odot$, are saturated in our sample. We need to consider their contribution to the cluster luminosity since the luminosity increases dramatically with mass. We add to the cluster luminosity the luminosity of these three WN stars with the values from Table 4 in Crowther et al. (2010) ($L_{V(3WN)} = 8.9 \times 10^6\,\mathrm{L}_\odot$), which are similar to Schmutz & Drissen (1999). Therefore, we estimate the total luminosity of the cluster HD 97950 to be $L_V \sim 9.4 \times 10^6\,\mathrm{L}_\odot$, which is dominated by the three WN stars. The contributions of faint stars to the total luminosity are very small.

The ratio of the total luminosity over the dynamical mass is $L_V/M_{dyn} = 9.4 \times 10^6\,\mathrm{L}_\odot/1.7 \times 10^5$ M$_\odot$ = 55 M$_\odot$/L$_\odot$. According to Figure 5 in Goodwin & Bastian (2006), $L_V/M_{dyn} = 55\,\mathrm{M}_\odot/\mathrm{L}_\odot$ corresponds to a star formation efficiency (SFE) of about 50 percent. The simulations of Goodwin & Bastian shows that young massive clusters can eventually survive the gas expulsion and re-establish equilibrium after the gas expulsion phase if they have a SFE above 30% – 40%. This implies that the HD 97950 cluster, instead of being in the process of dissolution, will survive the violent relaxation. In contrast, Smith et al. (2011) point out that the SFE is not a good measure of the survivability of star clusters that are initially out of equilibrium. Instead these authors propose to consider the initial conditions at the onset of gas expulsion, e.g., the local stellar fraction and the virial ratio. However, Smith et al.'s simulations make the simplification of assigning equal masses to all stars.

On the other hand, our dynamical mass of the HD 97950 cluster might be overestimated when we consider the following aspects.

i) The underlying assumption of the dynamical mass is that the cluster is in virial equilibrium. Goodwin & Bastian (2006) point out that the assumption of virial equilibrium is incorrect for young star clusters and generates the discrepancy between dynamical and luminous masses. However, we find that the cluster may be just at the starting point of equipartition, and may undergo dynamical mass segregation (see Section 2.5.2). The estimated dynamical mass should then be considered to be only an upper limit of the true mass of HD 97950.

ii) Another serious concern is the effect of orbital motion in binaries, which affects the velocity dispersion. Simulations of Gieles et al. (2010) show that the fact that the dynamical mass of the cluster exceeds the photometric mass by up to a factor of 10, can be explained by models of virialized star clusters hosting a massive star population, of which 25 percent is in binaries. HD 97950 hosts dozens of massive OB stars. The binary fraction might thus be quite high since the binary fraction increases with stellar masses (Kouwenhoven et al. 2007). So the binary fraction must be corrected for statistically. To make it worse, the binary fraction in HD 97950 is poorly known. Stolte et al. (2004) estimated the binary fraction of HD 97950 to be 30%. So the observed velocity dispersion would again be an upper limit of the real value if binarity is taken into account. However, the model of Gieles et al. (2010) assumes a virialzed cluster; it is therefore not applicable to HD 97950 which is not in equilibrium. Furthermore, the velocity dispersion we derive is from proper motions, which are less affected by binarity than the radial velocity.

iii) The adopted half-mass radius $R_{hm} \sim 0.7$ pc from Harayama et al. (2008) is derived from stars within $0.5 \sim 2.5$ $M_{\odot}$. As mass segregation is significant for HD 97950 (Sung & Bessell 2004; Harayama et al. 2008; Pang et al. 2010, 2012a), the half-mass radius for high mass stars would be smaller than 0.7 pc.

Therefore, the computed dynamical mass of HD 97950 might be generally overestimated. If we assume a half-mass radius of 0.5 pc (Rochau et al. 2010) to 0.7 pc, the resulting dynamical mass is $M_{dyn} = 1.2 - 1.7 \times 10^5$ $M_{\odot}$. This results in an even higher $L_V/M_{\odot}$ ratio and hence a higher SFE, which implies a higher chance of survival of HD 97950. Moreover, the crossing time $t_{cross} = R_{hm}/\sigma_c$ of the cluster is 4.8 – 6.6 $\times$ $10^4$ yr when we consider the half-mass radius to be 0.5 – 0.7 pc. The gas expulsion timescale is roughly estimated to be $\sim$4.6 Myr for HD 97950 (Pandey et al. 2000). According to the semi-analytic and numerical models (Lada 1984; Geyer & Burkert 2001; Baumgardt & Kroupa 2007), when the gas removal timescale is significantly longer than the crossing time, the cluster can survive with a SFE as low as 20%. This may indicate that HD 97950 will very possibly survive the gas expulsion and remain bound. However, HD 97950 is not the only young massive star cluster that may survive. Westerlund 1, which is about 4 Myr old and 5 times more massive than the HD 97950 cluster, is found to be bound with a star formation efficiency around 45 percent (Mengel 2008). The velocity dispersion of Westerlund 1 measured by Cottaar et al. (2012) is lower than the expected value from virial equilibrium, which indicates a subvirial state of the cluster. According to simulations of Goodwin (2009), the probability that the cluster can survive will be increased greatly if the gas removal occurs when the cluster is still dynamically subvirial. Therefore, Westerlund 1 is probably currently bound and survive for billions of years (Cottaar et al. 2012). Consequently, there is still a chance for a young massive cluster to survive, if its SFE is high enough!

## 2.7 Summary

We analyzed HST/WFPC2 imaging of the HD 97950 cluster in the *F555W* (*F547M*), *F675W* and *F814W* filters obtained in 1997 and in 2007. The main results of our subsequent analysis are:

1. The completeness of the WFPC2 photometry decreases toward the cluster center, where severe crowding exists. The completeness within 5" from the center is below 50% for stars fainter than $V = 17$ mag. In the outer annulus ($r > 15''$), stars brighter than $V = 22.5$ mag is above 50% complete.

2. We derive relative proper motions of 627 common stars between the 1997 and 2007 observations, which include 465 stars from the PC chip, 95 stars the WFC2 chip, and 67 stars the WFC4 chip.

3. We test the inter- and intra-filter centroiding in single epoch images: 1) The distributions of the intra-filter centroid offset of the stars in the *F547M* and *F814W* images of 1997 are centered at zero, both with a dispersion of $\sigma_{\delta_x} = 0.012$ to $\sigma_{\delta_y} = 0.014$ pixels derived from fitting a Gaussian to their distribution. 2) The distributions of the centroid offset of the stars in the 2007 data have a slightly larger dispersion of $\sigma_{\delta_x} = 0.016$ to $\sigma_{\delta_y} = 0.017$ pixels for *F814W* and an even larger value of $\sigma_{\delta_x} = 0.019$ to $\sigma_{\delta_y} = 0.023$ pixels for *F555W*. The distribution of $\delta_x$ of the *F555W* data has its peak at $+0.01$ and is visibly off-centered from zero. A non-negligible fraction of stars even have centroid offsets in the $x$ direction of as much as 0.04 pixels and more in the *F555W* image. However, the intra-filter centroid offset of the stars observed in the *F555W* filter is at the order of the astrometric uncertainty 0.03 pixel on the PC from *HSTphot* (Dolphin 2000a). 3) Stars with inter-filter centroid offsets in single epoch data larger than 0.3 pixels are possibly T Tauri variable stars with accretion disks or blends, or binaries, which we remove before member determination.

4. The membership of stars is determined via two methods: 1) We select member stars located within a generous circle with a radius of 0.3 pixels for the PC and 0.15 pixels for the WFC in the vector point diagram, corresponding to 1.5 mas $\mathrm{yr}^{-1}$. This method results in 419 likely member stars on the PC chip, 76 member stars on the WFC2 chip, and 50 member stars on the WFC4 chip. 2) We fit the relative proper motion distributions with a two-Gaussian model under the assumption that the relative proper motion distributions of the field and cluster stars are Gaussian, which is a more robust method of membership determination. We consider stars with member probabilities, $P_{mem}$, larger then 0.7 to be members. This results in 411 members on the PC chip and and 124 members on the WFC chips. The contamination by foreground field stars ($P_{mem} < 0.7$) is 7% on the PC chip, and 25.3% the WFC chips.

6. The velocity dispersion of the relative proper motion of cluster stars on the PC chip is derived by two methods, by adopting $d = 6.9$ kpc from Sung & Bessell (2004): 1) We derived the dispersion of the relative proper motions by fitting $x$- and $y$-coordinate Gaussian distribution functions to the observed relative proper motion distributions. The corresponding two-dimensional velocity dispersion is $\sigma_c = 12.3 \pm 1.0$ km $\mathrm{s}^{-1}$. 1) We derived the velocity dispersion by subtracting the random errors from the observed dispersion of relative proper motions and obtain the a two-dimensional velocity dispersion of $\sigma_c = 10.42 \pm 0.62$ km $\mathrm{s}^{-1}$, which we consider a more reliable value.

7. The dynamical mass of cluster HD 97950, adopting $\sigma_c = 10.42 \pm 0.62$ km $\mathrm{s}^{-1}$, is more than

ten times higher than the photometric mass $M_{phot} = 1.6 \times 10^4\,\mathrm{M}_\odot$ derived from observations of the stellar content (Harayama et al. 2008). The total luminosity of the cluster HD 97950 corrected for incompleteness is $L_V \sim 9.4 \times 10^6\,\mathrm{L}_\odot$, which is dominated by the three WN stars. The ratio of the total luminosity over the dynamical mass is $L_V/M_{dyn} = 9.4 \times 10^6\ \mathrm{L}_\odot/1.7 \times 10^5\ \mathrm{M}_\odot = 55\ \mathrm{M}_\odot/\mathrm{L}_\odot$, corresponding to a SFE of about 50 percent, which may suggest that the HD 97950 cluster can survive after the gas expulsion and re-establish equilibrium (Goodwin & Bastian 2006).

# 3

# On the origin of mass segregation in HD 97950

The segregation is not true:
*There is neither Jew nor Greek, there is neither slave nor free, there is no male and female, for you are all one in Christ Jesus. (Galatians 3:28)*

**Abstract** We present deep Hubble Space Telescope/Wide Field and Planetary Camera 2 photometry of the young HD 97950 star cluster in the giant H II region NGC 3603. The data were obtained in 1997 and 2007 permitting us to derive membership based on the relative proper motions of the stars. From the resulting color-magnitude diagram we derive an age of $\sim 1$ – 3 Myr for main-sequence and pre-main-sequence stars. The global slope of the incompleteness-corrected mass function is $\Gamma = -0.89 \pm 0.18$ for member stars within $100''$ (the PC and WFC chips), and $\Gamma = -0.94 \pm 0.20$ for members on the PC chip. These mass functions are flatter than a Salpeter slope of $-1.35$. The radially varying mass function shows significant mass segregation ranging from slopes of $-0.26 \pm 0.32$ in the inner $5''$ to $-1.49 \pm 0.33$ in the outermost annulus ($15''$ – $20''$). Stars more massive than 50 $M_\odot$ are found only in the cluster center. The $\Lambda$ minimum spanning tree technique confirms mass segregation down to 30 $M_\odot$. The dependence of $\Lambda$ on mass, i.e., that high-mass stars are more segregated than low mass stars likely implies that the mass segregation is dynamical in origin. While primordial segregation cannot be excluded, the properties of the mass segregation indicate that dynamical mass segregation may have been the dominant process for segregation.

## 3.1 Introduction

The compact HD 97950 cluster in the luminous giant H II region NGC 3603 is one of the most massive compact young star clusters in the Milky Way accessible at optical wavelengths. The cluster's total mass is estimated to be $\sim 10^4$ $M_\odot$ (Harayama et al. 2008). Its three Wolf-Rayet stars not only show characteristics of WN6 stars, but also large hydrogen content in their winds, inferred from a comparison between the strengths of the pure He II lines to the hybrid H$\gamma$+He II line (Drissen et al. 1995), suggesting that they are actually core hydrogen-burning rather than evolved stars (de Koter et al. 1997; Crowther & Dessart 1998). Based on stellar spectral types, Melena et al. (2008) argue that the most massive stars in the HD 97950 cluster are coeval with ages of 1–2 Myr, while less massive stars (20–40 $M_\odot$) show a somewhat larger age spread of up to 4 Myr. Recent photometric studies arrived at a range of ages from an essentially single-burst population of 1 Myr (e.g., Stolte et al. 2004) to extended star formation episodes of up to 10 – 20 Myr as indicated by the age spread in pre-main-sequence stars (Beccari et al. 2010). In the vicinity of the cluster evolved supergiants are found (e.g., Brandner et al. 1997a, b) with ages $\geq 4$ Myr (Crowther et al. 2008; Melena et al. 2008).

Despite its young age, the HD 97950 cluster shows pronounced mass segregation (e.g., Sung & Bessell 2004; Grebel & Gallagher 2004). Mass segregation is often observed in young star clusters (e.g., Stolte et al. 2002; Schilbach et al. 2006; Chen et al. 2007), but its origin is still unclear. Bonnell & Davies (1998) argue that star clusters cannot dynamically segregate in only a few Myr and that therefore mass segregation in young clusters must be primordial. In the competitive accretion scenario (Bonnell et al. 2001; Bonnell & Bate 2006) protostars in the dense central regions of a young star cluster can accrete more material than those in the outskirts, naturally resulting in mass segregation.

McMillan et al. (2007) show that young mass-segregated clusters may be the result of mergers between small clumps that are mass-segregated by either primordial or dynamical means. Allison et al. (2009b, 2010) suggest that observations support that clusters form with initial substructures, and show that for clusters with initially cool (subvirial) and clumpy distributions dynamical mass segregation can occur very rapidly in the cluster's core after it has collapsed ($\sim$ 0.5 – 1 Myr). In contrast to smooth, subvirial clusters, clumpy clusters collapse to much higher densities, enabling fast dynamical segregation.

The initial conditions of star clusters and the origin of mass segregation place important constraints on theories of massive star formation and cluster evolution. In the case of a cluster that formed subvirially and substructured, mass segregation is expected to be observable down to some "limiting mass" (typically a few solar masses; Allison et al. 2009a, 2010). This may be the case in, e.g., the Orion Nebula Cluster (ONC, $\sim$ 1 Myr), which was found to be mass-segregated down to 5 $M_\odot$ using the minimum spanning tree (MST) method (Allison et al. 2009b). Discussing the different methods commonly used to evaluate mass segregation in star clusters, Olczak et al. (2011) argue that the MST method is superior to the other methods, since it does not make assumptions about symmetry or the location of the center of the distribution nor is it affected by uncertainties introduced by binning (see also Allison et al. 2009b; Küpper et al. 2011).

Here we analyze Hubble Space Telescope (HST) observations of the massive HD 97950 cluster

in NGC 3603 obtained with the Wide Field and Planetary Camera 2 (WFPC2). In Section 3.2 we summarize the observations and data reduction. In Section 3.3 we infer the present-day mass function and discuss evidence for mass segregation based on the traditional mass function analysis in concentric annuli. In Section 3.4 we refine and quantify the mass segregation using a MST analysis. We present our conclusions and summary in Section 3.5.

## 3.2 Observations and data reduction

For our analysis of the HD 97950 cluster in NGC 3603 we used deep imaging data obtained with HST/WFPC2. The first observations were carried out in 1997 July (program GO 6763, PI: Drissen). The Planetary Camera (PC) chip was centered on the cluster (see Figure 2.1 in Chapter 2). We obtained shallow, intermediate, and long exposures ranging from fractions of a second to 20 – 30 s in the *F547M*, and *F814W* filters, respectively (Table 2.1 in Chapter 2). Earlier results from analyses of these data were presented by Grebel & Gallagher (2004) and by Sung & Bessell (2004).

The second data set (Figure 2.1 in Chapter 2) was obtained in 2007 September (program GO 11193, PI: Brandner). The longest exposures lasted 100 s (*F555W*) and 160 s (*F814W*), considerably longer than in 1997 (Table 2.1 in Chapter 2). The ten-year epoch difference between the first and the second data set permits us to infer cluster membership using relative proper motions (Section 2.4 in Chapter 2). Preliminary results of this analysis were presented by Pang et al. (2010). Rochau et al. (2010) published a proper motion study of the same combined dataset.

Both data sets were reduced using *HSTphot* (Dolphin 2000a, 2005), a program developed for crowded-field stellar photometry of WFPC2 data. The shifts between the dithered images were determined following Koekemoer et al. (2002). Owing to the smaller pixel scale of the PC chip ($\sim 0.05''$ pixel$^{-1}$) as compared to the three other chips of WFPC2, and since the PC chip was centered on the HD 97950 cluster, we only use the PC data in the analysis of mass segregation. The data from the WFC2 and WFC4 chips are only included in deriving the total mass function of the HD 97950 cluster in Section 3.4. Also, we only use images obtained in the filters either common to both datasets (*F814W*) or at comparable wavebands (*F547M* in the 1997 dataset and *F555W* in the 2007 dataset). These filters correspond to the *I* and *V* bands in the Johnson-Cousins system, respectively. We found 627 common stars on the PC and WFC chips observed in both epochs. The magnitudes of the common stars are taken from 1997 photometry. The position- and magnitude-dependent incompleteness in the detection of point sources was assessed through artificial star experiments in Section 2.2.3 of Chapter 2.

Relative proper motions were derived using common stars observed in the same filter during the two epochs in order to select likely cluster members and to weed out field stars, which have been done in Section 2.3 and 2.4 of Chapter 2. Membership of stars is determined by fitting a two-Gaussian model to the observed relative proper motion distribution. We compute the membership probability (Jones & Walker 1988) and select only stars with member probabilities larger than 0.7 to be cluster members, which are retained in the subsequent analysis. Seventy stars on the PC and WFC chips (11% of the total number of common stars) were thus eliminated as foreground

stars. Because of the high extinction in the NGC 3603 giant H II region (see Chapter 4), we may assume that background stars are effectively obscured and do not significantly contribute to our measurements.

## 3.3 Color-magnitude diagrams

Figure 3.1 shows the color-magnitude diagram (CMD) of the HD 97950 cluster including all common stars measured in the two epochs for the PC chip. The CMD shows a steep main sequence (MS) and a broad region of redder pre-main-sequence (PMS) stars. Also the transition region between the MS and the PMS is rather wide. Like Harayama et al. (2008), we do not see clear evidence of a sequence of equal-mass binaries as earlier suggested by Stolte et al. (2004).

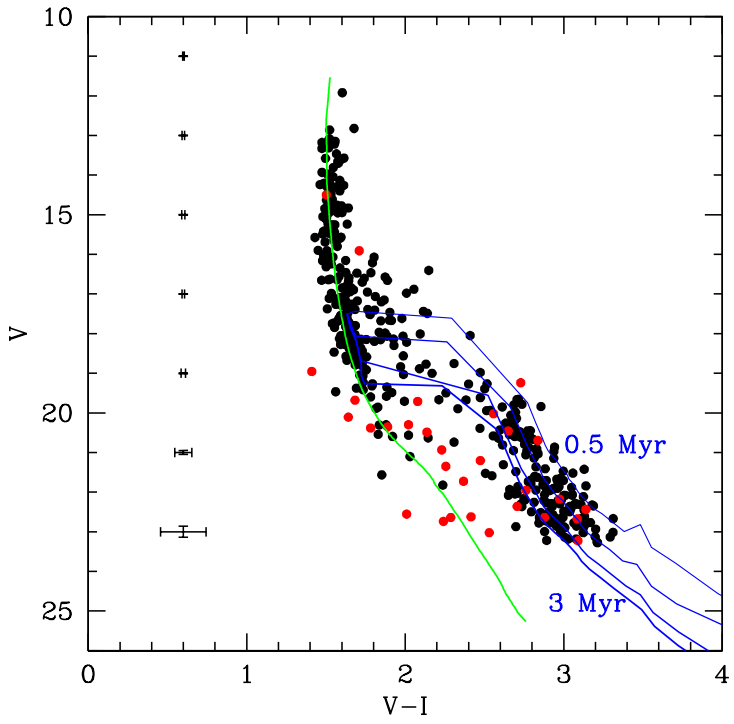


Figure 3.1: CMD of all common stars found in the 1997 and 2007 WFPC2 data (PC chip only). Proper motion members of HD 97950 are shown as black dots, probable non-members are indicated as red dots. We adopted a reddening of $E(B-V) = 1.25$ and a distance modulus of 14.2 mag from Sung & Bessell (2004). The vertical solid green line is a 1 Myr MS isochrone for solar abundance from Lejeune & Schaerer (2001). The blue lines are PMS isochrones from Siess et al. (2000). From right to left (increase of thickness of the lines) isochrones for 0.5, 1, 2, 3 Myr are plotted. Representative mean errors of magnitude and color are indicated on the left.

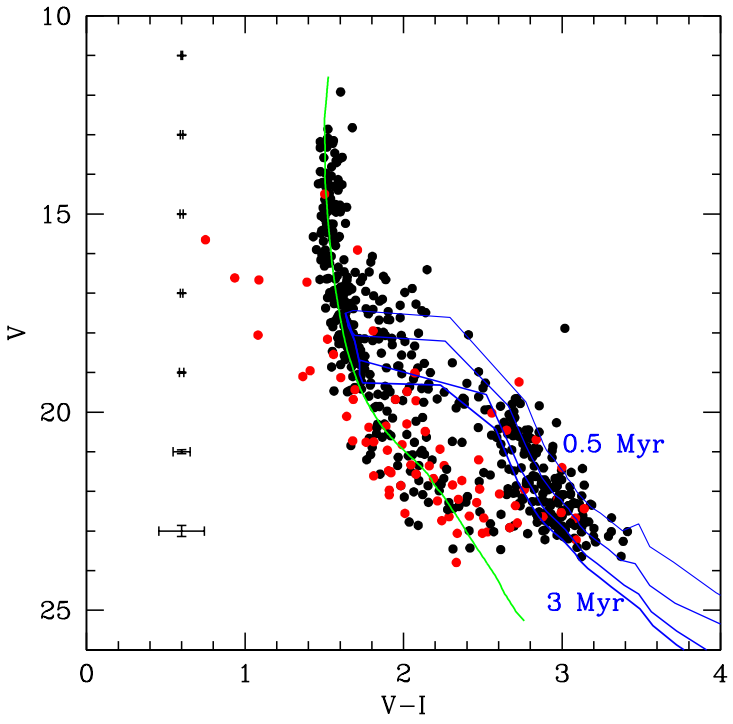


Figure 3.2: CMD of all common stars found in the 1997 and 2007 WFPC2 data (PC + WFCs). Color coding is the same as Figure 3.1. We adopt a reddening of $E(B-V) = 1.25$ and a distance modulus of 14.2 mag from Sung & Bessell (2004) for stars on the PC and WFC chips.

When we include common stars measured on the WFC chips into Figure 3.1, the MS becomes somewhat better populated and broader at the faint end (Figure 3.2). The broadening may be caused by the larger photometric errors or by increased differential reddening across the now larger area. Also, more stars are now found along the PMS. Unlike the core of cluster (PC chip), the WFC chips cover the outer region of the cluster, and are contaminated with more foreground stars (red dots) owing to a four times larger field of view.

We adopt a reddening law of $E(V-I)/E(B-V) = 1.45 \pm 0.05$ and $R_V = 3.55 \pm 0.12$ from Sung & Bessell (2004) for the region $r \leq 100''$ of HD 97950 ($r$ is the cluster centric distance). Their Figure 5 shows that $E(B-V)$ stays unchanged with a value of 1.25 mag for an area of $r \leq 30''$ (see also Moffat 1983), and increases up to 1.4 mag at $r \sim 100''$. Since $E(B-V)$ shows a large scatter at $r > 30''$ (Sung & Bessell 2004), we assume that the uniform extinction of $A_V = 4.44 \pm 0.15$ across the PC ($r \leq 20''$) extends to regions within $100''$ (the WFC chips). The reddening corrected MS on the PC chip aligns with that on the WFC chips (Figure 3.2), indicating our assumption is reasonable. The differential reddening in NGC 3630 will be discussed in detail in Chapter 4 and 5.

Conveniently, *HSTphot* transforms magnitudes in the WFPC2 filter system into the standard Johnson-Cousin system. In order to derive stellar masses along the main sequence, we use the isochrone models of Lejeune & Schaerer (2001). These isochrones extend to masses above 100 $M_\odot$, appropriate for the HD 97950 cluster (see Schnurr et al. 2008). For the PMS stars on WFPC2 images, of which the mass goes down to 0.8 $M_\odot$ (Drissen 1999), we use Siess et al. (2000) isochrones, which cover a larger mass range ($0.1 - 7.0 M_\odot$) than other PMS isochrones. We adopt a distance of $d = 6.9 \pm 0.6$ kpc from Sung & Bessell (2004) and solar metallicity for the HD 97950 cluster (see Hendry et al. 2008) throughout this thesis.

The MS of HD 97950 is well-represented by a Lejeune & Schaerer 1 Myr isochrone (Figure 3.1 & 3.2). Slightly older MS isochrones also provide a good fit, in agreement with spectroscopic age estimates for the massive stars of 1 – 2 Myr (Melena et al. 2008). The Siess isochrones along the PMS locus indicate an age spread of up to 3 Myr, while Beccari et al. (2010) find an even larger spread using much deeper data. The color uncertainties in the area of the bulk of our PMS stars (fainter $V = 19$) increase rapidly, but are still smaller than the width of the color distribution in that area. In the "turn-on" region where PMS stars join the MS we find a broad range of luminosities ($16 < V < 19$), again indicating an age spread. However, non-accreting isochrones, e.g., Siess isochrones, tend to overestimate the stellar ages for stars whose effective temperature is above 3500 K (Hosokawa et al. 2011). Baraffe et al. (2009) suggest that the observed spread of the PMS stars in the Hertzsprung-Russell diagram at ages of a few Myr can be plausibly attributed to a spread in the stellar radius and a different episodic accretion history, instead of an age range as inferred from non-accreting stellar evolutionary models (e.g., Siess 2000). On the other hand, there are a number of possible MS stars (mostly from the WFC chips) visible at $V > 20$ (Figure 3.2), thus below the region where most of the cluster MS stars are located (see also Grebel & Gallagher 2004). Their small proper motions make these faint, candidate MS stars likely cluster members, which seems to corroborate the apparent age spread in the cluster.

## 3.4 The mass function and mass segregation

In order to derive the mass function of the HD 97950 cluster, we count stars in absolute V-magnitude bins spaced such that they cover mass bins with a logarithmic size of 0.2. Using the same procedure as Grebel & Chu (2000), we find the absolute magnitudes corresponding to mass bins along the earlier described isochrones assuming an age of 1 Myr. We applied a color cut of $(V - I) = 2.4$ to separate MS and PMS stars. Since the crowding is severe in the central region of the HD 97950 cluster, we corrected the count rates on the PC chip for incompleteness depending on their positions and magnitudes. We display the completeness dependence on stellar mass in Figure 3.3. In the outer annulus ($r > 15''$), stars above 1.5 $M_\odot$ are larger than 50% complete. As the crowding effects grows stronger inwards, in the region $r < 5''$, only stars more massive than $4 M_\odot$ are with completeness $> 50\%$. Therefore, lots of faint stars in the central part remain undetected. The three luminous Wolf-Rayet stars near the center of HD 97950 (Schnurr et al. 2008; Maíz Apellániz 2008) were added by hand to the highest mass bin, since they are saturated in our WFPC2 photometry. Since stars on the WFC chips ($\sim 100''$) are quite far from the cluster core,

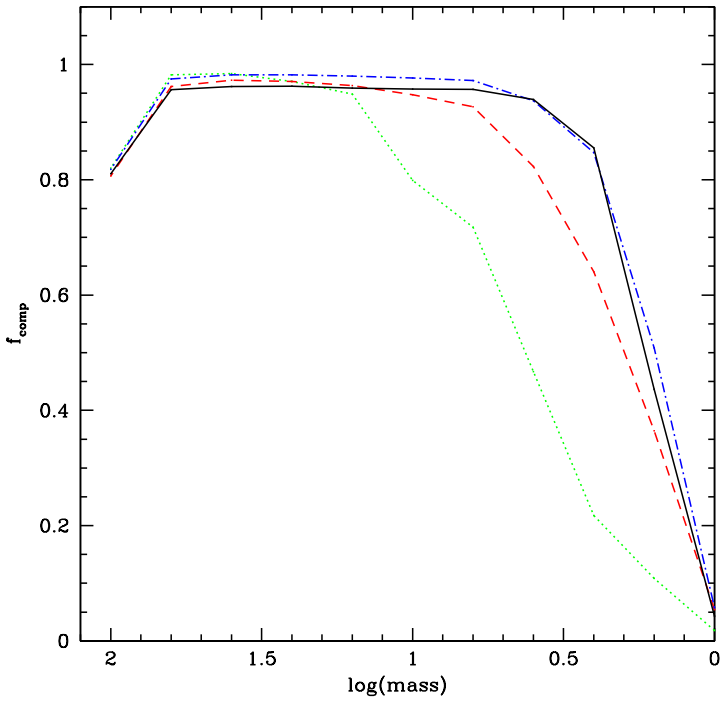


Figure 3.3: Completeness fraction $f_{comp}$ as a function of the stellar mass (in solar masses) of the stars on the PC chip. The uncertainty of the logarithmic stellar mass is $\pm 0.2$. The green dotted line denotes the $f_{comp}$ distribution for a circle with a radius of $r < 5''$ around the center of the HD 97950 cluster. The dashed line shows the completeness fraction for the next larger annulus between $5''$ to $10''$, the dot-dashed line indicates $f_{comp}$ for the annulus between $10''$ to $15''$, and the solid line is for the region outside $r > 15''$.

we assume that the members on the WFC chips are complete.

Fitting the corrected number counts of all relative-proper-motion-selected MS and PMS stars within a mass range of $\sim 1 - 100$ $M_{\odot}$ results in a mass function slope of $\Gamma = -0.89 \pm 0.18$ for all members within $100''$ (on both the PC and WFC chips; solid blue line in Figure 3.4), and $\Gamma = -0.94 \pm 0.20$ for the members on the PC chip ($\sim 20''$) only (short-dashed blue lines in Figure 3.5). Our result is in excellent agreement with the earlier WFPC2 study of Sung & Bessell (2004), who obtained $\Gamma = -0.9 \pm 0.1$ for stars on the PC chip. In Figure 3.5 we also show the mass function of the HD 97950 cluster in different concentric annuli. Two effects stand out: The slope of the mass function increases with radius, and the more massive stars are concentrated in the center and are missing at larger radii.

Our photometric mass function is affected by the uncertainties in the isochrone models used to derive the masses of cluster member stars. One such uncertainty is the unknown amount of

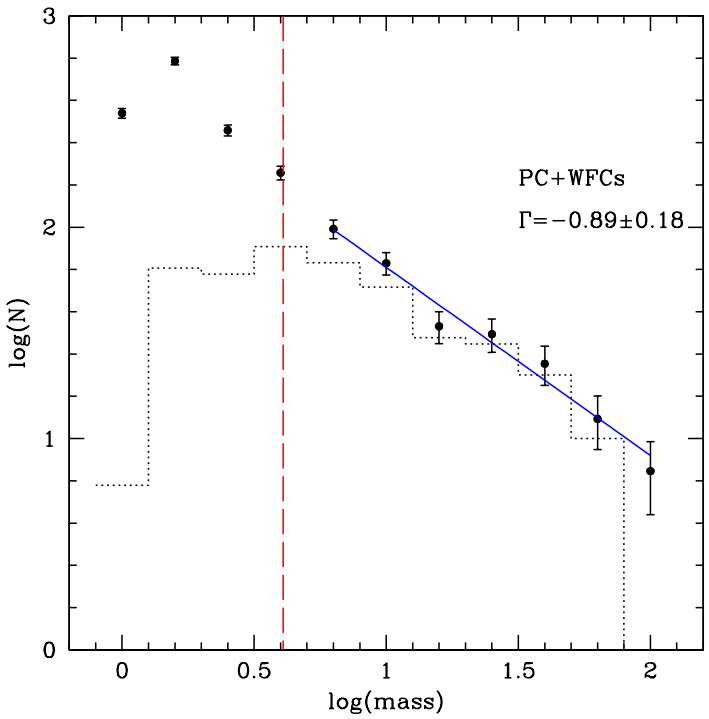


Figure 3.4: Total mass function of all cluster member stars on the PC chip and WFC chips. The dotted histogram is the observed mass function. The filled black dots indicate the mass function corrected for incompleteness. The vertical dashed red line indicates a completeness limit of 50%. The blue solid lines show a weighted linear least-squares fit of the mass function (black filled dots).

stellar rotation that can affect the colors and magnitudes of stars (see, e.g., Grebel et al. 1996). Another uncertainty is unrecognized binarity. Here we implicitly make the simplified assumption that we are dealing with non-rotating, single stars. Also, we neglect the age spread in the cluster, but emphasize that the spectroscopically inferred age spread of 1 – 2 Myr for massive MS stars does not affect the photometrically estimated masses significantly. Moreover, the above analysis of mass segregation in HD 97950 is sensitive to the determination of the position of the cluster center, and the number and size of the radial bins used (e.g., Gouliermis et al. 2004).

Therefore we also apply the Λ-MST-method (Allison et al. 2009a; Parker et al. 2011) to the data. We take a subset of $n$ stars of similar mass (the 1st to $n$th most massive stars, or the $(n+1)$th to $2n$th most massive stars for example) and find the length of the MST that connects those stars. The MST is the shortest path that connects every member of a set of points without closed loops. We then take a large number of random sets of $n$ stars of *any* mass and calculate the median and the 1/6th and 5/6th percentiles to calculate a (possibly unsymmetric) $1\sigma$ error. A subset is mass

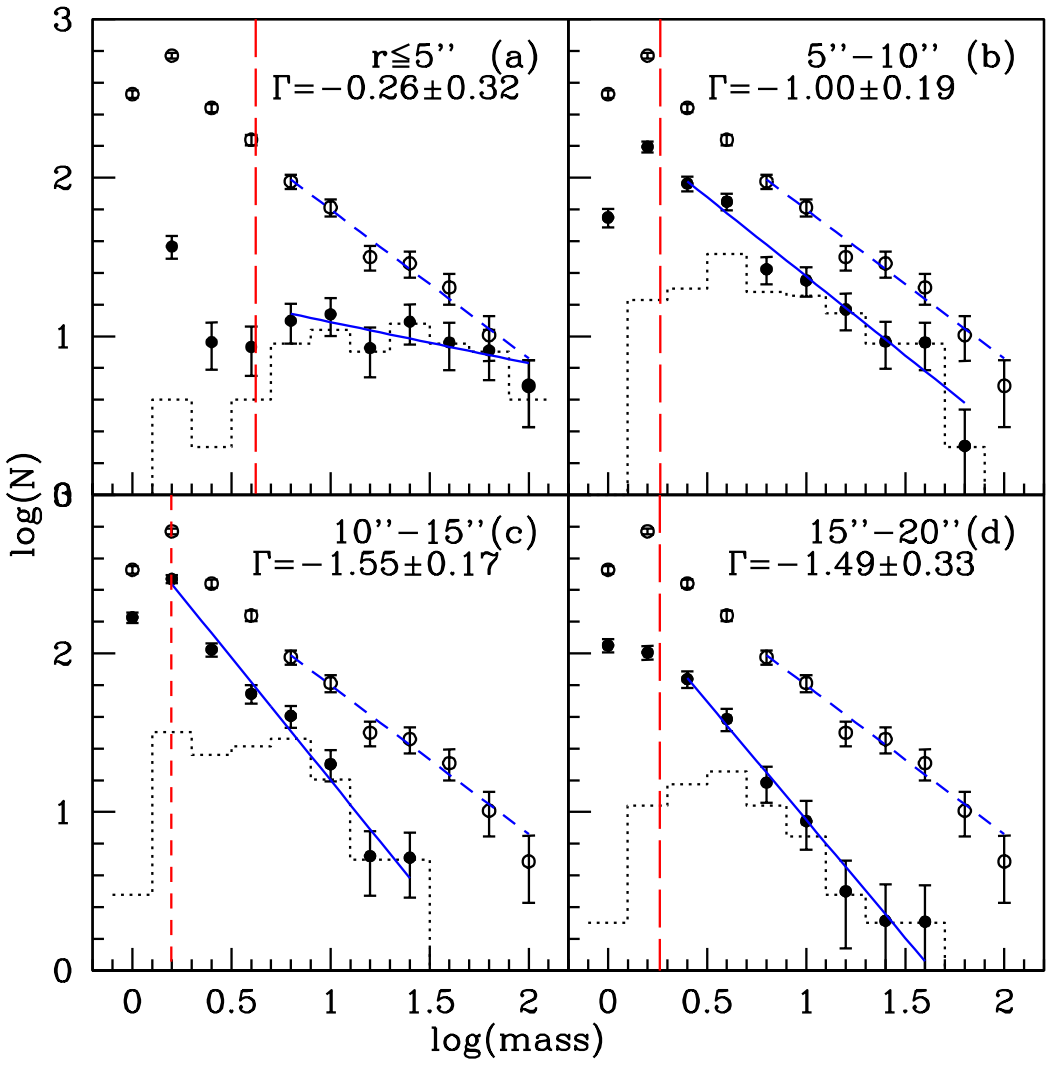


Figure 3.5: Radial mass function of all cluster member stars on the PC chip. Panels (a) to (d) show mass functions in a sequence of increasing annuli. The dotted histogram is the observed mass function. The filled black dots indicate the mass function corrected for incompleteness. The vertical dashed red line indicates a completeness limit of 50%. The blue solid lines show a weighted linear least-squares fit of the mass function of each annulus (black filled dots). The short-dashed blue lines are weighted linear least-squares fits to the total mass function (open circles) on the whole PC chip ($r \leq 20''$) which we plot for comparison in each panel. The resulting slope of the total mass function is $\Gamma = -0.94 \pm 0.20$. The slope of mass function in each annulus is indicated in each panel.

segregated if $\Lambda$ (the ratio of the MST length of random stars over massive stars) is larger than unity, i.e., the stars in that subset are more concentrated in their distribution than a random sample (see Allison et al. 2009a; Maschberger & Clarke 2011; Parker et al. 2011).

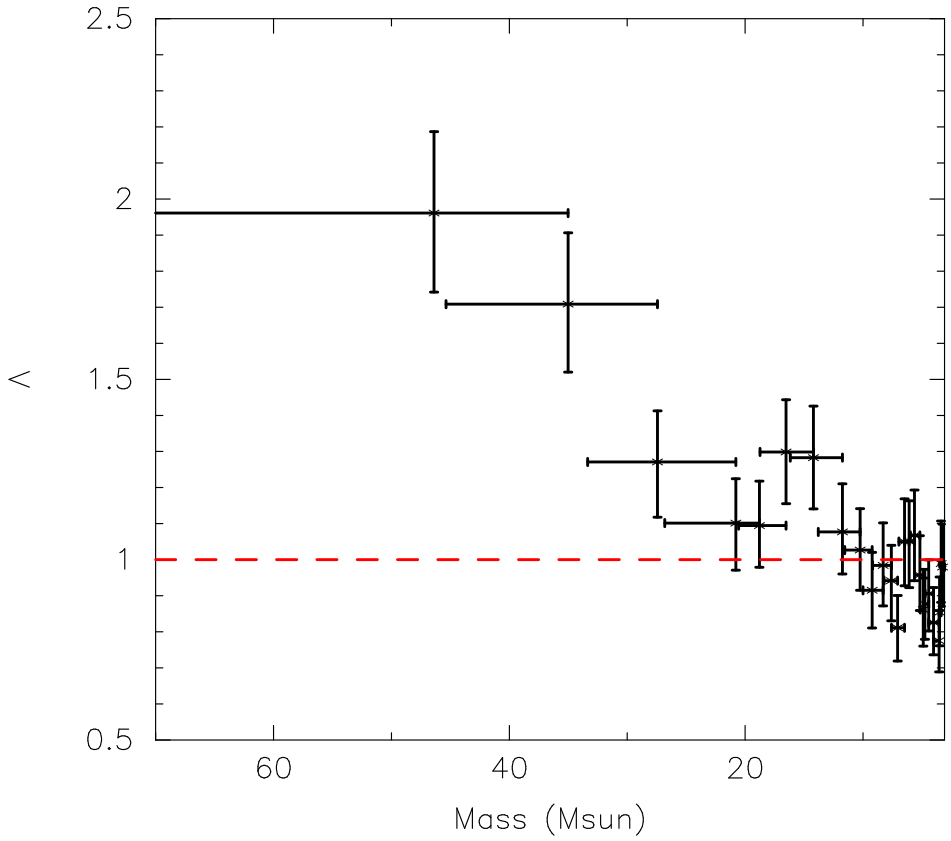


Figure 3.6: The evolution of $\Lambda$ along stellar mass. $\Lambda$ is the ratio of MST length of 20 random stars over 20 massive stars moving in a declining order of mass and in steps of 10 stars. The dashed line indicates a $\Lambda$ of unity, meaning no mass segregation.

Figure 3.6 shows the values of $\Lambda$ for samples of 20 stars moving in steps of 10 stars (therefore every datapoint is uncorrelated with the second datapoint preceding it or following it). The first 20 stars all have masses $> 35$ M$_\odot$, and the second mass bin from the left is in the range $27 - 45$ M$_\odot$. The first two bins have a $\Lambda$ significantly greater than unity – i.e., they are more (centrally) concentrated than random stars. Varying the size of the bins also always shows a significant degree of mass segregation $> 30$ M$_\odot$.

It should be noted that two bins just below $20M_\odot$ also show some evidence of mass segregation. This is due to a close pair of stars of very similar mass ($\sim 18M_\odot$).

## 3.5 Dynamical segregation in the core of the HD 97950 cluster

From Figure 3.6 we can see that the most massive stars $> 30 M_{\odot}$ are mass segregated, and all other mass ranges show no evidence of any mass segregation. It is important to note that (a) HD 97950 is mass segregated above 30 $M_{\odot}$, and (b) all other masses of stars are randomly distributed throughout the cluster. As we shall argue, this strongly suggests a dynamical origin for mass segregation in HD 97950.

Very similar patterns in mass segregation have been observed in the two other clusters analyzed with the $\Lambda$-MST-method: the Orion Nebula Cluster (ONC; Allison et al. 2009a) and Trumpler 14 (Sana et al. 2010). Allison et al. (2009b) proposed a dynamical origin for mass segregation due to two-body relaxation in a dense phase to explain the ONC. They proposed that the ONC underwent a short-lived dense phase in which the two-body relaxation time was very short.

The two-body relaxation time $t_{\rm relax}$ of a system is given by

$$t_{\rm relax} \sim \frac{N}{8{\rm ln}N} t_{\rm cross}$$

where $t_{\rm cross}$ is the crossing time of the system, $N$ is the number of stars. Dynamical mass segregation occurs due to the equipartition of energies in two-body encounters. The rate at which a star will approach equipartition depends on the mass of that star, $M$, relative to the average mass of stars in the system, $\langle m \rangle$. The time to segregate $t_{\rm seg}$ down to a mass $M$ is

$$t_{\rm seg}(M) \sim \frac{\langle m \rangle}{M} t_{\rm relax} = \frac{\langle m \rangle}{M} \frac{N}{8{\rm ln}N} t_{\rm cross}.$$

Allison et al. (2009b) showed that for a dense phase that lasts one crossing time the ONC should mass segregate down to a few $M_{\odot}$, but not below which is what is observed.

Extending the Allison et al. (2009b) argument to HD 97950 suggests that in one crossing time it should mass segregate to a mass of a few tens of $M_{\odot}$ (assuming $N = 10^4$, and $\langle m \rangle = 0.4$ $M_{\odot}$), but not below. This is exactly what is observed in the core of HD 97950. The highest-mass stars are sinking further into the core of the cluster, and are found to be more mass-segregated than lower-mass stars (Figure 3.6). Higher-mass stars are more efficient at this process and thus mass-segregate faster. That the stars in HD 97950 show this dependence on mass, as do purely dynamical and initially non-mass-segregated $N$-body simulations (Allison et al. 2009b, 2010), indicates that dynamical mass segregation was the dominant process for the mass segregation in HD 97950. Furthermore, no formation process (e.g., competitive accretion) is known to produce mass segregation down to one particular mass, but not below.

We also note that binaries may shorten the relaxation time and accelerate segregation. But at the same time, primordial binaries increase the chance of stellar collisions, which lead to the ejection of OB stars (Portegies Zwart et al. 2010), working against the observed mass segregation in the HD 97950 cluster. As no binary sequence can be seen in Figure 3.1 and 3.2, we cannot quantify the presence of binaries in the cluster and their effects on the mass segregation.

## 3.6 Summary

We analyzed broad-band HST/WFPC2 imaging of the star cluster HD 97950 obtained in 1997 and in 2007. We used the epoch difference to establish a relative-proper-motion-selected sample of probable cluster members. The main results of our subsequent analysis are:

1. Melena et al. (2008) derive an age of 1 – 2 Myr for the massive MS stars in HD 97950, consistent with our photometry. For the PMS stars, we find an approximate age spread of up to 3 Myr indicated by non-accreting isochrones (Siess 2000). The spread of the PMS stars in the CMD could also be explained by different stellar radii and accretion histories (Baraffe et al. 2009; Hosokawa et al. 2011). On the other hand, a number of lower-mass MS stars that are relative-proper-motion members (mostly from the WFC chips) and that are located below the broad turn-over region toward the PMS seem to corroborate the apparent age spread in the cluster.

2. As did previous studies, we find a radially varying mass function that is flat and top-heavy near the center of the cluster and that becomes steeper at larger radii. There is pronounced mass segregation, and the stars above $50\ \mathrm{M}_\odot$ are strongly centrally concentrated. The global slope of the incompleteness-corrected mass function is $\Gamma = -0.89 \pm 0.18$ for member stars within $100''$ (the PC and WFC chips), and $\Gamma = -0.94 \pm 0.20$ for members on the PC chip. The slope of radial mass functions varies from $-0.26 \pm 0.32$ within $5''$ from the cluster center to $-1.49 \pm 0.33$ in an annulus of $15''$ – $20''$ around the center.

3. HD 97950 is mass-segregated down to 30 $\mathrm{M}_\odot$ but not below. The most massive stars are the most mass segregated. A simple extension of the Allison et al. (2009b) dynamical model for mass segregation in the ONC suggests that HD 97950 should be mass segregated to a few tens of $\mathrm{M}_\odot$, but not below. This strongly suggests a dynamical origin for mass segregation in HD 97950.

**Parts of this Chapter were submitted to The Astrophysical Journal Letters (Pang, Grebel, Allison, Goodwin, Altmann, Harbeck, Moffat, Drissen, "On the Origin of Mass Segregation in NGC 3603"). This paper is currently under review.**

# 4

# A two-dimensional map of the color excess in NGC 3603

A small cloud, but a big dream:
*The seventh time the servant reported, "A cloud as small as a man's hand is rising from the sea." So Elijah said, "Go and tell Ahab, 'Hitch up your chariot and go down before the rain stops you.' " (1 Kings 18:44)*

**Abstract** Using archival HST/WFC3 images centered on the young HD 97950 star cluster in the giant H II region NGC 3603, we computed the pixel-to-pixel distribution of the color excess, $E(B-V)_{\rm g}$, of the gas associated with this cluster from its H$\alpha$/Pa$\beta$ flux ratio. At the assumed distance of 6.9 kpc, the resulting median color excess within 1 pc from the cluster center is $E(B-V)_{\rm g} = 1.51 \pm 0.04$ mag. Outside the cluster (at $r > 1$ pc), the color excess is seen to increase with cluster-centric distance towards both north and south, reaching a value of about 2.2 mag at $r = 2$ pc from the cluster center. The radial dependence of $E(B-V)_{\rm g}$ westward of the cluster appears rather flat at about 1.55 mag over the distance range 1.2 pc $< r <$ 3 pc. In the eastern direction, $E(B-V)_{\rm g}$ steadily increases from 1.5 mag at $r = 1$ pc to 1.7 mag at $r = 2$ pc, and stays nearly constant at 1.7 mag for 2 pc $< r <$ 3 pc. The different radial profiles and the pixel-to-pixel variations of $E(B-V)_{\rm g}$ clearly indicate the presence of significant differential reddening across the 4.9 pc $\times$4.3 pc area centered on the HD 97950 cluster. We interpret the variations of $E(B-V)_{\rm g}$ as the result of stellar radiation and stellar winds interacting with an inhomogeneous dusty local interstellar medium whose density varies spatially. From the $E(B-V)_{\rm g}$ values measured along the rims of the prominent pillars MM1 and MM2 in the southwest and southeast of the HD 97950 cluster, we estimate an $H_2$ column density of $\log_{10}(N_{\rm H_2}) = 21.7$ and extrapolate it to $\log_{10}(N_{\rm H_2}) = 23$ in the pillars' interior. We find the pillars to be closer to us than the central ionizing cluster and suggest that star formation may be occurring in the pillar heads.

## 4.1 Introduction

The young massive HD 97950 star cluster in the giant H II region NGC 3603 is located in the Sagittarius-Carina arm of the Milky Way. This cluster is one of the most massive young star clusters in the Galaxy ($\sim 10^4$ $M_\odot$, Harayama et al. 2008). It hosts ten times more OB stars than the Orion Nebula Cluster (ONC), including the two most massive binaries currently known in the Galaxy (Schnurr et al. 2008). The HD 97950 cluster displays pronounced mass segregation (e.g., Sung & Bessell 2004; Harayama et al. 2008). Earlier studies trying to age-date the HD 97950 cluster found the massive stars on the upper main sequence (MS) to be very young (e.g., 1 – 2 Myr according to the spectroscopic study by Melena et al. 2008), while the pre-main-sequence stars (PMS) were found to show a larger age spread of 2 – 3 Myr (e.g., Eisenhauer et al. 1998; Grebel 2004, 2005; Harayama et al. 2008; Pang et al. 2010). The PMS stars in the outer cluster regions and in the surroundings of the cluster may, in part, be older, but different authors derive different age ranges (e.g., 4 – 5 Myr; Sung & Bessell 2004; Rochau et al. 2010) or up to 10 Myr (Beccari et al. 2010). Also the evolved supergiants around the HD 97950 cluster support the idea of a large age spread or alternatively sequential or multiple episodes of star formation (e.g., Moffat et al. 1983; Tapia et al. 2001; Crowther et al. 2008; Melena et al. 2008). On the other hand, the size of the wind-blown bubble around the cluster suggests an age much lower than 2.5 Myr when taking the kinetic energy input of the massive stars into account (see discussion in Drissen et al. 1995). At present, the age(s) and the star formation history of the HD 97950 cluster and its surroundings in NGC 3603 are uncertain. One of the uncertainties in stellar age dating is introduced by the high and variable reddening in NGC 3603.

The HD 97950 Cluster lies in a wind-blown cavity north of a large molecular cloud (e.g., Clayton 1986; Melnick 1989). The gaseous surroundings of the cluster show a complex and variable velocity and density structure (e.g., Clayton 1990; Drissen et al. 1995). Since the nebular density varies spatially, one would expect that also the dust extinction changes with position across the cluster area as denser clouds can shield dust from stellar radiation better than less dense clouds. The resulting variable reddening is known as differential reddening and was shown to be present in NGC 3603 (e.g., Sagar et al. 2001). When this effect is not taken properly into account, it may make stars appear redder and hence older in the color-magnitude diagram (CMD) depending on their spatial position with respect to the line of sight. This may introduce a considerable uncertainty in the estimation of stellar ages.

Differential reddening could be one of the causes why the age spread among PMS stars in the HD 97950 cluster appears to be as large as up to 10 Myr. In fact, as shown by Beccari et al. (2010, their Figure 7), PMS stars are spatially more widely distributed than the MS stars and reside in areas with different reddening. Sung & Bessel (2004) find that the color excess of the stars within the HD 97950 cluster (at radii $r < 0.7$ pc with $d = 6.9$ kpc from Sung & Bessell 2004) is $E(B-V)_*$ = 1.25 mag and rapidly increases to 2.1 mag in the outer regions ($r \sim 12$ pc).

We take advantage of the publicly available images of the HD 97950 cluster taken with the Wide Field Camera 3 (WFC3) aboard the Hubble Space Telescope (HST) through narrow-band filters centered on the H$\alpha$ and Pa$\beta$ lines and through broad-band filters sampling the continuum emission, in order to extend the work of Sung & Bessel (2004). We compute a pixel-to-pixel

Table 4.1: WFC3 filter information

| Filter | Central wavelength Å | Filter width Å | PHOTFLAM $\mathrm{ergs/cm^2/Å/e^-}$ | Exposure time s |
|---|---|---|---|---|
| *F555W* | 5308.1 | 1562 | 1.8762E-19 | 1000s |
| *F656N* | 6561.4 | 18 | 1.5380E-17 | 1550s |
| *F814W* | 8029.5 | 1536 | 1.5591E-19 | 990s |
| *F127M* | 12740 | 688 | 9.2164E-20 | 2397.697s |
| *F128N* | 12832 | 159 | 4.1030E-19 | 1197.694s |
| *F139M* | 13838 | 643 | 9.0589E-20 | 2397.697s |

PHOTFLAM is the inverse sensitivity conversion factor.

map of the color excess of gas, $E(B-V)_{\rm g}$, across a $2.43' \times 2.14'$ ($4.9 \times 4.3$ pc) field centered on the HD 97950 cluster. Since the images give the emissions of the gas integrated all along the line of sight, the reddening of the gas that we derive is an upper limit to the true reddening experienced by the stars. Thus the two-dimensional distribution of the color excess associated with the gas is the first step towards correcting individual MS and PMS stars for reddening in the WFC3 field of view. Multi-band stellar photometry will be needed in order to establish the conversion between the reddening of the gas and that of the stars (Chapter 5). This will ultimately allow us to constrain more tightly the age spread of PMS stars and the recent star formation history of the HD 97950 cluster and of its immediate surroundings (Pang et al. 2012b). This chapter focuses on the reddening map of the gas in NGC 3603. The data and their reduction are described in Section 4.2, while the two-dimensional map of the color excess is presented and discussed in Section 4.3. Conclusions and a summary are presented in Section 4.4.

## 4.2 Observations and data reduction

Multi-wavelength imaging of the HD 97950 star cluster was carried out in 2010 with *HST*/WFC3 (proposal ID: 11360, PI: Robert O'Connell). For our analysis we use the optical images taken in the *F555W* ($\sim V$), *F656N* ($H\alpha$), and *F814W* ($\sim I$) filters with the WFC3 UVIS detector (0.04 arcsec pixel$^{-1}$) and near-infrared images in the *F127M* (continuum in *J*), *F128N* ($Pa\beta$), and *F139M* (continuum in *J*) filters obtained with the WFC3 IR detector (0.13 arcsec pixel$^{-1}$). The total exposure time in different filters is summarized in Table 4.1.

All images were reduced with the WFC3 pipeline and the IRAF[1] MULTIDRIZZLE task. We note that no narrow-band filter sampling the continuum emission close to the H$\alpha$ or Pa$\beta$ line was used during the observations. Thus we use the broad-band *V* and *I* filters to estimate continuum in $H\alpha$ and the medium-band *J*-continuum filters (*F127M* and *F139M*) for $Pa\beta$.

[1]IRAF is distributed by the National Optical Astronomy Observatories, which are operated by the Association of Universities for Research in Astronomy, Inc., under cooperative agreement with the National Science Foundation.

Table 4.2: FWHM of each filter image

| Filter | FWHM (arcsecond) |
|---|---|
| *F555W* | 0.037 |
| *F656N* | 0.038 |
| *F814W* | 0.038 |
| *F127M* | 0.225 |
| *F128N* | 0.226 |
| *F139M* | 0.227 |

### 4.2.1 H$\alpha$ and Pa$\beta$ emission

Radiation emitted at shorter wavelengths is absorbed by dust more effectively than photons of longer wavelengths. Given that the H$\alpha$ line (restframe wavelength 6563 Å) is emitted at a shorter wavelength than Pa$\beta$ (restframe wavelength 12802 Å), the interstellar dust along the line of sight decreases the H$\alpha$ flux detected by the observer more than the Pa$\beta$ flux emitted by the same source. Therefore, the observed H$\alpha$/Pa$\beta$ flux ratio is smaller than the theoretical one computed for the same conditions of electron density ($N_e$) and temperature ($T_e$) of the source in the absence of dust.

Equation (4.1) (taken from Calzetti et al. 1996) illustrates the relation between the color excess, $E(B-V)_{\rm g}$ of the interstellar gas, and the observed and theoretical H$\alpha$/Pa$\beta$ flux ratios of this same gas ($R_{\rm obs}$ and $R_{\rm int}$, respectively) under the assumption of a specific extinction law (represented by $\kappa(\lambda)$=$A(\lambda)/E(B-V)$;):

$$E(B-V)_g = \frac{-\log(R_{\rm obs}/R_{\rm int})}{0.4\,[\kappa(\lambda_{\rm H\alpha}) - \kappa(\lambda_{\rm Pa\beta})]}\ \ {\rm mag} \tag{4.1}$$

In order to apply Equation (4.1), we need to derive the H$\alpha$ and Pa$\beta$ emission fluxes per pixel from the available WFC3 images, and for this purpose we make use of IRAF standard routines.

1) We first determine an average point-spread function (PSF) in each filter from the FWHM (full width at half maximum) of 15 – 20 stars in common to all images (IRAF task 'IMEXAME'). See Table 4.2 for the average FWHM of each filter image. Since the PSF is largest in the *F139M* image, we degrade all the other images by convolving them with a Gaussian function whose dispersion, $\sigma^2$, is the difference between the PSF $\sigma^2$ ($\sigma = FWHM/2.35$) of the *F139M* image and that of the image in the filter in question. We also re-scale the optical images by a factor of $-3.25$ to the same pixel scale of the near-infrared using the IRAF task 'MAGNIFY', and align all images to the one taken through the *F139M* filter with the IRAF routines 'GEOMAP' and 'GEOTRAN'. We calibrate all images in flux by multiplying them by their respective filter PHOTFLAM value, which is the inverse sensitivity conversion factor (Table 4.1), as given in the WFC3 manual (Dressel et al. 2010).

2) We derive the flux density of the continuum emission at the H$\alpha$ wavelength by interpolating the flux density $f_{F555W}$ in the *F555W* image and the flux density $f_{F814W}$ in the *F814W* image

pixel by pixel with a simple first-order polynomial ($y = bx + a$), whose slope is:

$$b_1 = \frac{f_{F814W} - f_{F555W}}{\lambda_{F814W} - \lambda_{F555W}} \tag{4.2}$$

$\lambda_{F814W}$ ($\lambda_{F555W}$) is the wavelength of the filter *F814W* (*F555W*). The first-order polynomial is:

$$f = b_1\,\lambda + a_1 \tag{4.3}$$

where $a_1 = f_{F555W} - b_1\,\lambda_{F555W}$. Therefore, the flux density of the continuum at $H\alpha$ is

$$Continuum_{F656N} = b_1\,\lambda_{F656N} + (f_{F555W} - b_1\,\lambda_{F555W})) \tag{4.4}$$

In the same way, the flux density of the continuum at Pa$\beta$ is:

$$Continuum_{F128N} = b_2\,\lambda_{F128N} + a_2\,. \tag{4.5}$$

where $b_2$ and $a_2$ are given by

$$b_2 = \frac{f_{F139M} - f_{F127M}}{\lambda_{F139M} - \lambda_{F127M}} \tag{4.6}$$

$$a_2 = f_{F127M} - b_2\,\lambda_{F127M} \tag{4.7}$$

Such an interpolation allows us to take into account the slope of the continuum emission of the stars and to better remove the stars from the final, pure line-emission images. The flux density of the continuum emission $Continuum_{F656N}$ ($Continuum_{F128N}$) is subtracted from that of *F656N* ($f_{tot_{F656N}}$) (*F128N*; $f_{tot_{F128N}}$) image to get the emission flux density:

$$f_{emission_{F656N}} = f_{tot_{F656N}} - Continuum_{F656N}\,, \tag{4.8}$$

$$f_{emission_{F128N}} = f_{tot_{F128N}} - Continuum_{F128N}\,. \tag{4.9}$$

The flux density is multiplied by the width of the corresponding narrow-band filter ($\Delta\lambda_{F656N}$ and $\Delta\lambda_{F128N}$), so that the pure emission fluxes of *F656N* and *F128N* are

$$F_{emission_{F656N}} = f_{emission_{F656N}}\,\Delta\lambda_{F656N} \tag{4.10}$$

$$F_{emission_{F128N}} = f_{emission_{F128N}}\,\Delta\lambda_{F128N}. \tag{4.11}$$

In this way we are able to construct the images of the pure H$\alpha$ and Pa$\beta$ emission as well as their observed $R_{\rm obs}$ flux ratio.

3) We derive $R_{\rm int} = 17.546$ from Osterbrock (1989) under the assumption that $T_e = 10\,000$ K and $N_e = 100$ cm$^{-3}$. We adopt a normal extinction law with a ratio of total to selective extinction of $R_V = 3.1$, and derive $\kappa(\lambda_{\rm H\alpha}) = 2.355$ and $\kappa(\lambda_{\rm Pa\beta}) = 0.7644$ from Fitzpatrick's (1999) extinction law. Finally, we apply Equation (4.1) to the image of the observed $R_{\rm obs}$ flux ratio to construct the pixel-to-pixel map of $E(B-V)_{\rm g}$ shown in Figure 4.1. In panel (a) of Figure 4.2 we show the histogram of the $E(B-V)_{\rm g}$ per pixel, normalized by the total number of pixels in the $R_{\rm obs}$ image. The total line-of-sight color excess is always larger than the foreground reddening of $E(B-V) = 1.1$ mag (Pandey et al. 2000). More than 90% of the pixels have $E(B-V)_{\rm g}$ between 1.6 and 2.2 mag.

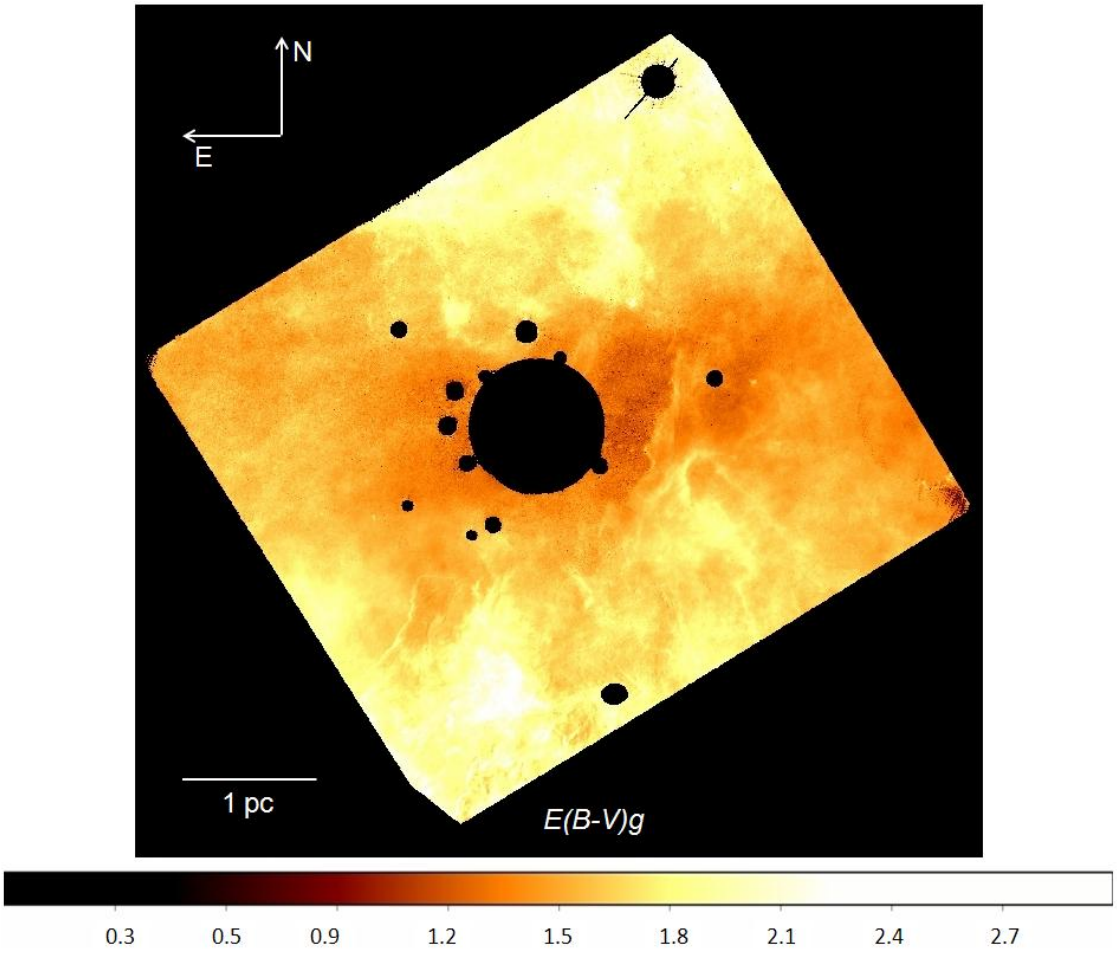


Figure 4.1: The two-dimensional map of the gas color excess, $E(B-V)_{\rm g}$, around the young cluster HD 97950 in the giant H II region NGC 3603. North is up and east is to the left. The image covers an area of 4.9 pc $\times$4.3 pc with a scale of 0.004 pc per pixel at a distance of 6.9 kpc. The inner 120 pixels ($r < 0.52$ pc) are masked out due to the luminous OB stars of the HD 97950 cluster, which are saturated in the *F555W* and *F814W* images obtained with *HST*/WFC3. The color excess is significantly lower along the east-west direction (1.5 – 1.6 mag) than in the north-south direction (where it is as high as 2.2 mag). A shell structure is seen westward of the cluster associated with a local enhancement of the color excess. The molecular pillars MM1 and MM2 are visible at 1.2 – 2.5 pc southwest and southeast of the HD 97950 cluster, see also Figure 4.6.

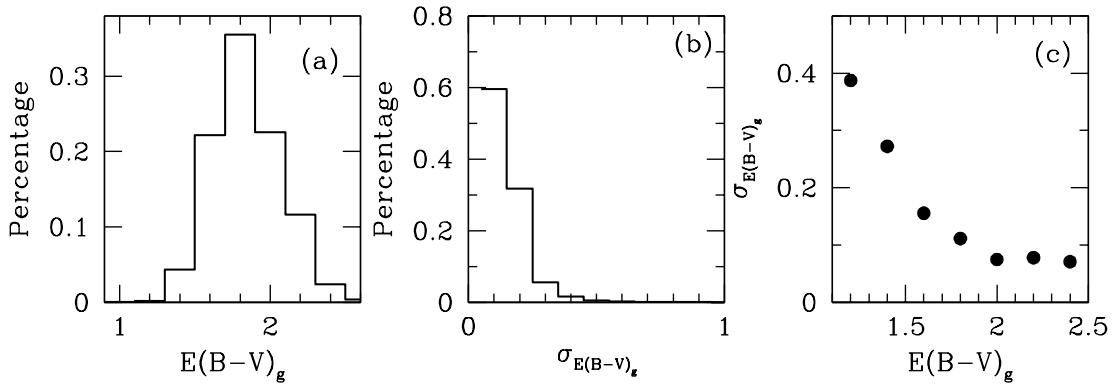


Figure 4.2: Panel a: Histogram of the pixel $E(B-V)_{\rm g}$. Panel b: Histogram of the uncertainty $\sigma_{E(B-V)_{\rm g}}$ of the pixel $E(B-V)_{\rm g}$ due to photon noise. Panel c: Dependence of $\sigma_{E(B-V)_{\rm g}}$ on $E(B-V)_{\rm g}$.

### 4.2.2 Uncertainty of $E(B-V)_{\rm g}$

In order to estimate the accuracy of our derived $E(B-V)_{\rm g}$ values, we assume that the electron counts in the images ($P'$: in units of $\rm e^-$) follow a Poisson distribution. Therefore we start with a Poisson error of the electron counts per pixel in the input images. The pipeline image ($P$) is in the unit of $\rm e^-/s$

$$P' = P \times t \tag{4.12}$$

$t$ is the exposure time in seconds.The uncertainty of the electron count is the Poisson error:

$$\sigma_{P'} = \sqrt{P \times t} \tag{4.13}$$

The flux density ($f$) is

$$f = P'/t \times \mathrm{PHOTFLAM} \tag{4.14}$$

$f$ is in units of $\rm ergs/s/cm^2/\AA$. Therefore, the uncertainty on the flux density image for each filter is

$$\sigma_{filter} = \sqrt{P_{filter} \times t_{filter}} \times \mathrm{PHOTFLAM}_{filter}/t_{filter} \tag{4.15}$$

We compute $\sigma_{filter}$ pixel by pixel for all our six filters and propagate these errors through the entire computation of the continua, and their subtraction from the *F656N* and *F128N* images.

The errors on the continua of the *F656N* and *F128N* images are:

$$\sigma_{continuum_{F656N}} = \sqrt{\sigma_{a_1}^2\,\lambda_{F656N}^2 + \sigma_{b_1}^2} \tag{4.16}$$

$$\sigma_{continuum_{F128N}} = \sqrt{\sigma_{a_2}^2\,\lambda_{F128N}^2 + \sigma_{b_2}^2} \tag{4.17}$$

where $a_1$ and $b_1$ ($a_2$ and $b_2$) are the coefficients of first-order polynomial fitting for interpolating the flux in the *F555W* and *F814W* images (*F127M* and *F139M*), see equations (4.2)-(4.7).

$$\sigma_{emission_{F656N}} = \sqrt{\sigma^2_{F656N} + \sigma^2_{continuum_{F656N}}} \tag{4.18}$$

$$\sigma_{emission_{F128N}} = \sqrt{\sigma^2_{F128N} + \sigma^2_{continuum_{F128N}}} \tag{4.19}$$

The observed H$\alpha$/Pa$\beta$ flux ratio is

$$R_{\rm obs} = f_{emission_{F656N}} \times \Delta\lambda_{F656N} / f_{emission_{F128N}} \times \Delta\lambda_{F128N} \tag{4.20}$$

$f_{emission_{F656N}}$ and $f_{emission_{F128N}}$ are the emission flux densities in the respective filters. $\Delta\lambda_{F656N}$ and $\Delta\lambda_{F128N}$ are the filter widths of *F656N* and *F128N*. The uncertainty of $R_{\rm obs}$ is

$$\sigma_{R_{\rm obs}} = \sqrt{\frac{\Delta\lambda^2_{F656N}\,\sigma^2_{emission_{F656N}}}{\Delta\lambda^2_{F128N}\,f^2_{emission_{F128N}}} + \frac{f^2_{emission_{F656N}}\,\Delta\lambda^2_{F656N}\,\sigma^2_{emission_{F128N}}}{f^4_{emission_{F128N}}\,\lambda^2_{F128N}}} \tag{4.21}$$

Therefore, the uncertainty of the reddening $E(B-V)_{\rm g}$ is computed according to Equation (4.1):

$$\sigma_{E(B-V)_{\rm g}} = -\frac{\sigma_{R_{\rm obs}}}{0.4\,[\kappa(\lambda_{\rm H\alpha}) - \kappa(\lambda_{\rm Pa\beta})]\,ln(10)\,R_{\rm obs}} \tag{4.22}$$

We present the histogram of the uncertainties $\sigma_{E(B-V)_{\rm g}}$ per pixel in panel (b) of Figure 4.2, normalized by the total number of pixels in the $R_{\rm obs}$ image. The histogram peaks at $\sigma_{E(B-V)_{\rm g}} = 0.1$ mag, and the percentage of pixels with $\sigma_{E(B-V)_{\rm g}} > 0.2$ mag is less than 10%. In panel (c) of Figure 4.2 we plot the average $\sigma_{E(B-V)_{\rm g}}$ per pixel in bins of $E(B-V)_{\rm g}$ per pixel. As can be seen, $\sigma_{E(B-V)_{\rm g}}$ gradually decreases with increasing $E(B-V)_{\rm g}$ from 0.4 mag at $E(B-V)_{\rm g} = 1.2$ mag to 0.1 mag at $E(B-V)_{\rm g} = 2.4$ mag.

In addition to photon noise, there are also some systematic errors because of the following effects:
(1) Broad-band and medium-band filters are contaminated by emission lines. The Pa$\beta$ emission falls in the *F127M* filter. Figure 4.3 show the throughput of the optical and infrared filters of WFC3. Assuming that the flux density of the continuum is the same in both the *F127M* and *F128N* filters ($c$), we can use the flux ratio *F128N/F127M* (where both filters were multiplied by their respective PHOTFLAM and band width),

$$\frac{Count_{F128N}\,{\rm PHOTFLAM}_{F128N}\,\Delta\lambda_{F128N}}{Count_{F127M}\,{\rm PHOTFLAM}_{F127M}\,\Delta\lambda_{F127M}} = 1/3 \tag{4.23}$$

to derive the contribution of the Pa$\beta$ line, $e$, to the flux in *F127M* ($c\,\Delta\lambda_{F127M} + e$),

$$\frac{c\,\Delta\lambda_{F128N} + e}{c\,\Delta\lambda_{F127M} + e} = 1/3 \tag{4.24}$$

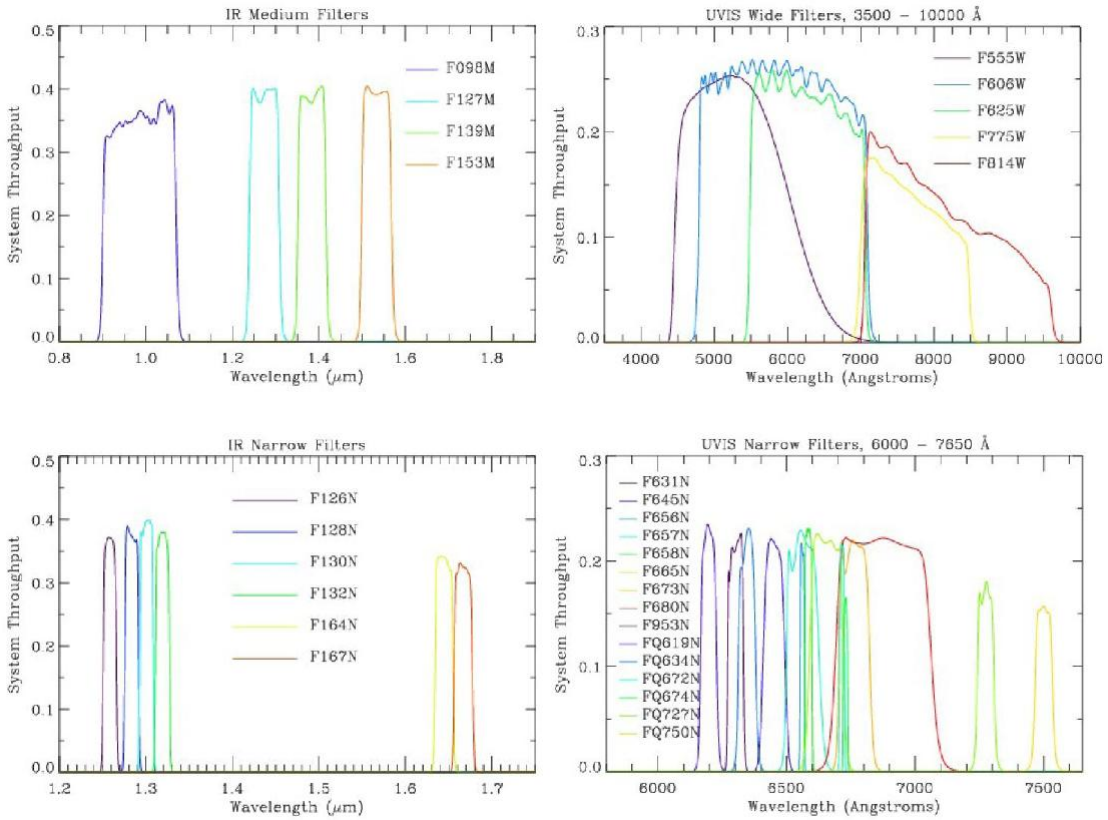


Figure 4.3: Throughput of infrared and optical filters of WFC3 camera taken from Dressel, et al. (2011).

Table 4.3: Contaminating emission lines in *F555W* and *F814W*

| *F555W* | | | |
|---|---|---|---|
| Emission line | wavelength (Å) | $I(\lambda)$ | throughput |
| H$\alpha$ | 6560 | 1639.4 | 0.03 |
| [OIII] | 4959 | 204.749 | 0.27 |
| [OIII] | 5007 | 641.906 | 0.28 |
| *F814W* | | | |
| HeI | 7065.28 | 59.096 | 0.15 |
| [ArIII] | 7135.78 | 154.166 | 0.24 |
| [OII] | 7319.99 | 30.523 | 0.21 |
| [ArIII] | 7751.10 | 53.803 | 0.17 |
| HI | 8750.47 | 26.668 | 0.11 |
| HI | 8862.79 | 36.948 | 0.1 |
| [SIII] | 9068.90 | 793.638 | 0.09 |
| HI | 9229.01 | 79.747 | 0.08 |
| [SIII] | 9530.60 | 2912.0 | 0.05 |
| HI | 9545.97 | 110.044 | 0.05 |

$I(\lambda)$ are the reddening-corrected line fluxes relative to H$\beta$ line, taken from Garcia-Rojas et al. (2006). $I(\mathrm{H}\beta)$=100, and its flux is $F(\mathrm{H}\beta)$=1.01$\times 10^{-12}\,\mathrm{erg/s/cm^{-2}}$. The spectrum was measured across an area of $3 \times 8.5\,\mathrm{arcsec}^2$ in the HII region NGC 3603 (Garcia-Rojas et al. 2006).

We find this contribution $e/(c\,\Delta\lambda_{F127M} + e)$ to be about 13%, which will increase the color excess by 0.05 mag. No hydrogen lines are found in the wavelength range of the *F139M* filter, only a few faint He emission lines, which should not significantly contribute to the flux in this filter.

The *F555W* filter includes three strong emission lines: the H$\alpha$, the [O III]($\lambda = 4959$ Å) and the [O III]($\lambda = 5007$ Å) lines. The filter response is $\sim 27\%$ at the oxygen lines and $\sim 3\%$ at the H$\alpha$ line. In order to roughly estimate the emission line contamination in this filter, we make use of the optical spectrum obtained by Garcia-Rojas et al. (2006) in NGC 3603 at a distance of 4 pc from the cluster HD 97950. The fluxes of the most prominent emission lines detected by Garcia-Rojas et al. (2006) are listed in Table 4.3 in units of H$\beta$ flux = 100.

The flux of an emission line in *F555W* is:

$$F_\lambda = I(\lambda) \times F(\mathrm{H}\beta) \times \mathrm{Throughput}/I(\mathrm{H}\beta) \tag{4.25}$$

The mean flux per pixel of *F555W* image is,

$$Flux_{F555W} = Count_{F555W} \times \Delta\lambda_{F555W} \times \mathrm{PHOTFLAM} \tag{4.26}$$

where $Count_{F555W}$ are the counts and $\Delta\lambda_{F555W}$ is the filter width of *F555W*. The spectrum measured by Garcia-Rojas et al. (2006) comes from an area of $3'' \times 8.5''$, which is much larger

than the pixel area $0.04'' \times 0.04''$ of UVIS. Therefore, we have to scale down the flux of the emission line $F_\lambda$ to the pixel area to get the contamination of the emission lines in the *F555W* filter:

$$\frac{F_\lambda}{Flux_{F555W}} \times \frac{0.04'' \times 0.04''}{3'' \times 8.5''} \sim 10\% \,. \tag{4.27}$$

The *F814W* filter contains the [S III] and [Ar III] emission lines (Table 4.3) at wavelengths where its response is lower than 10%. Similar to the computation in *F555W* (Eq.4.25-27), the contamination ratio in *F814W* is $\sim 16\%$. If we assume the contamination ratios computed above to be applicable to the fluxes in the *F555W* and *F814W* filters at the position of the cluster, the color excess would then increase by 0.05 mag on average.
(2) The adopted extinction law also contributes to the systematic uncertainties. If we replace Fitzpatrick's (1999) extinction law with that of Cardelli et al. (1989), we obtain an $E(B-V)_{\rm g}$ systematically smaller by 0.1 mag (for $R_V = 3.1$). When we vary $R_V$ by $\pm$0.5 in Cardelli et al.'s (1989) extinction law, $E(B-V)_{\rm g}$ decreases by $\sim$0.3 mag ($R_V = 3.6$) or increases by $\sim$0.2 mag ($R_V = 2.6$).
(3) The assumed electron temperature and density of the gas may be affected by systematic errors. Gárcia-Rojas et al. (2006) and Lebouteiller et al. (2008) obtained $T_e = 10\,000$ K and $N_e = 1000$ cm$^{-3}$ for the NGC 3603 giant H II region. Since this electron density is not available in Osterbrock (1989), we calculated $R_{\rm int}$ for $T_e = 10\,000$ K and $N_e = 10\,000$ cm$^{-3}$ and derived a new pixel-to-pixel map of $E(B-V)_{\rm g}$. A factor of 100 difference in $N_e$ results in an average difference of 0.0025 mag in $E(B-V)_{\rm g}$, which is well within the errors in $E(B-V)_{\rm g}$ due to photon noise.

## 4.3 A two-dimensional map of the color excess

### 4.3.1 Global properties of $E(B-V)_{\rm g}$

The pixel-to-pixel map of $E(B-V)_{\rm g}$ obtained for $T_e = 10\,000$ K and $N_e = 100$ cm$^{-3}$ is presented in Figure 4.1. The resulting $E(B-V)_{\rm g}$ is integrated along the different lines of sight towards NGC 3603 and includes the Galactic foreground reddening, which amounts to $E(B-V) = 1.1$ mag according to Pandey et al. (2000). The HD 97950 cluster ($r < 0.52$ pc), where dozens of OB stars reside, is masked out in order to avoid saturated bright stars in the *F555W* and *F814W* filters. Since the PSFs of the different filters may be slightly different even after the convolution procedure to obtain the same PSF described in Section 4.2.1, the subtraction of the continua from the $H\alpha$ and *Pa*$\beta$ images can produce negative values around the stars in the pure emission images, and thus negative $E(B-V)_{\rm g}$ in the color excess map. This is particularly true for saturated stars and their spikes. Therefore, we smooth the color excess map by replacing the negative $E(B-V)_{\rm g}$ at the position of a star with the median value of $E(B-V)_{\rm g}$ in an annulus around. The size of the annulus is proportional to the size of the star. Noise ($\sigma$) is added with the IRAF 'IMEDIT' routine depending on the location of the stars. For stars that are very bright and near the crowded center of the cluster, $\sigma$=0.05, while $\sigma$ decreases to 0.01 for faint and isolated stars.

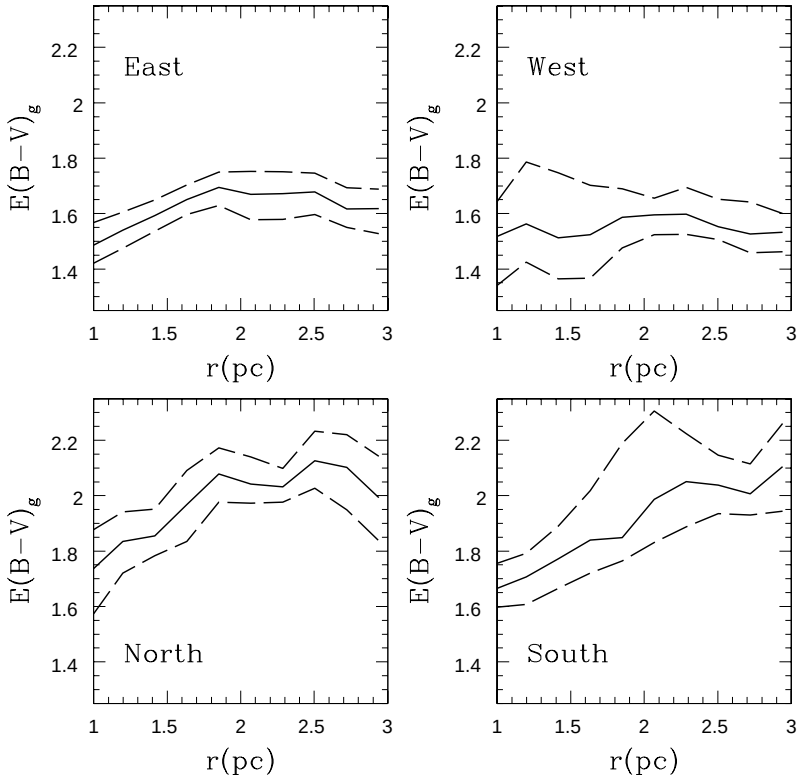


Figure 4.4: The radial dependence of $E(B-V)_{\rm g}$ from the cluster center towards the east, west, north, and south. The solid line is the median $E(B-V)_{\rm g}$ value, while the upper and lower long-dashed lines are the 84 and 16 percentile values, respectively, of the $E(B-V)_{\rm g}$ distribution as a function of distance from the cluster.

In Figure 4.1, $E(B-V)_{\rm g}$ is seen to decrease by 0.2 mag when going from the eastern or the western edge of the field of view to the cluster center. Overall, the gas color excess in the east is 0.1 mag larger than in the west. However, in the north-south direction $E(B-V)_{\rm g}$ is systematically larger by 0.4 – 0.5 mag than in the east-west direction. In general, the southern region has the largest color excess as it may be expected since here we are moving towards the densest regions of a giant molecular cloud (e.g., Nürnberger et al. 2002). Our findings support earlier suggestions that the line-of-sight dust density is uneven across the HD 97950 cluster surroundings.

As an alternative way of quantifying the differential reddening around the HD 97950 cluster, we show in Figure 4.4 the radial dependence of $E(B-V)_{\rm g}$ from the cluster towards the east, west, north, and south. We define a series of concentric annuli of the same width (0.2 pc) and at increasing distance from the cluster center, and we measure the median value and the 16 and 84 percentile values of the $E(B-V)_{\rm g}$ distribution within each annulus. The solid lines in Figure

Table 4.4: $E(B-V)_{\rm g}$ of specific objects in NGC 3603

| Object Name | Right Ascension [ h m s ] | Declination [ ° m s ] | $E(B-V)_{\rm g}$ [mag] |
|---|---|---|---|
| Proplyd 1 | 11 15 13.13 | −61 15 50.0 | 1.6 |
| Proplyd 3 | 11 15 01.41 | −61 14 45.7 | 1.9 |
| Sher 25: northeast lobe | 11 15 09.71 | −61 15 13.2 | 2.0 |
| Sher 25: southwest lobe | 11 15 05.89 | −61 15 25.0 | 1.6 |

The designations Proplyd 1 and 3 are adopted from Brandner et al. (2000), while the coordinates of Sher 25 are from Brandner et al. (1997a). All coordinates are J2000 coordinates.

4.4 trace the median $E(B-V)_{\rm g}$ as a function of cluster-centric distance, while the long-dashed lines indicate the 84 and 16 percentile values. Towards the west, the color excess increases by 0.1 mag from 1 pc to 1.2 pc and stays rather flat at about 1.55 mag over the distance range 1.2 pc $< r <$ 3 pc. In the eastern direction, $E(B-V)_{\rm g}$ steadily increases from 1.5 mag at $r = 1$ pc to 1.7 mag at $r = 2$ pc and then remains nearly constant at 1.7 mag for 2 pc $< r <$ 3 pc. The most dramatic changes in $E(B-V)_{\rm g}$ are seen along the northern and southern directions, where $E(B-V)_{\rm g}$ gets larger by 0.3 to 0.5 mag as the distance from the cluster center increases. Specifically, the color excess increases from about 1.7 mag at $r = 1$ pc to 2.2 mag at a distance of 2 pc. The pronounced increase towards the south does not come as a surprise since the overall density of the giant molecular clouds in NGC 3603 increases in this direction (see, e.g., Figure 1 in Brandner et al. 1997a).

In the two-dimensional map (grey) of the color excess (Figure 4.5), some specific sources are associated with a locally higher $E(B-V)_{\rm g}$. This is the case for two of the "proplyd"-like (protoplanetary-disks-like) objects first detected by Brandner et al. (2000). Proplyd 1 is located east of the HD 97950 cluster, while Proplyd 3 is in the northwest. Both are tadpole-shaped and rim-brightened sources with extended tails pointing away from the cluster.

Mid-infrared observations (Nürnberger & Stanke 2003) do not reveal any point-like source that might be associated with the proplyds. These authors suggest that these objects are small dense clumps of gas and dust, which are being photoevaporated by the intense ionizing radiation of the massive stars in the HD 97950 cluster instead of being disks around young stars as proposed by Brandner et al. (2000). In particular, Proplyd 3 shows extended faint emission at 11.9 $\mu$m, which may be caused by carbon-rich dust grains (see Goebel et al. 1995). Assuming that the dust properties are the same for these three proplyds, the higher color excess of Proplyd 3 (0.3 mag redder than Proplyd 1, see Table 4.4) would be consistent with a higher dust content (if both proplyds are at the same distance), and hence with the fact that Proplyd 3 is the only proplyd detected at 11.9 $\mu$m (Nürnberger & Stanke 2003).

To the north of the HD 97950 cluster, we find Sher 25, a blue supergiant with a circumstellar ring and an hourglass nebula (Brandner et al. 1997a, 1997b). We have measured the color excess in the bright rims of the northeastern and southwestern lobes of the hourglass nebula (Table 4.4;

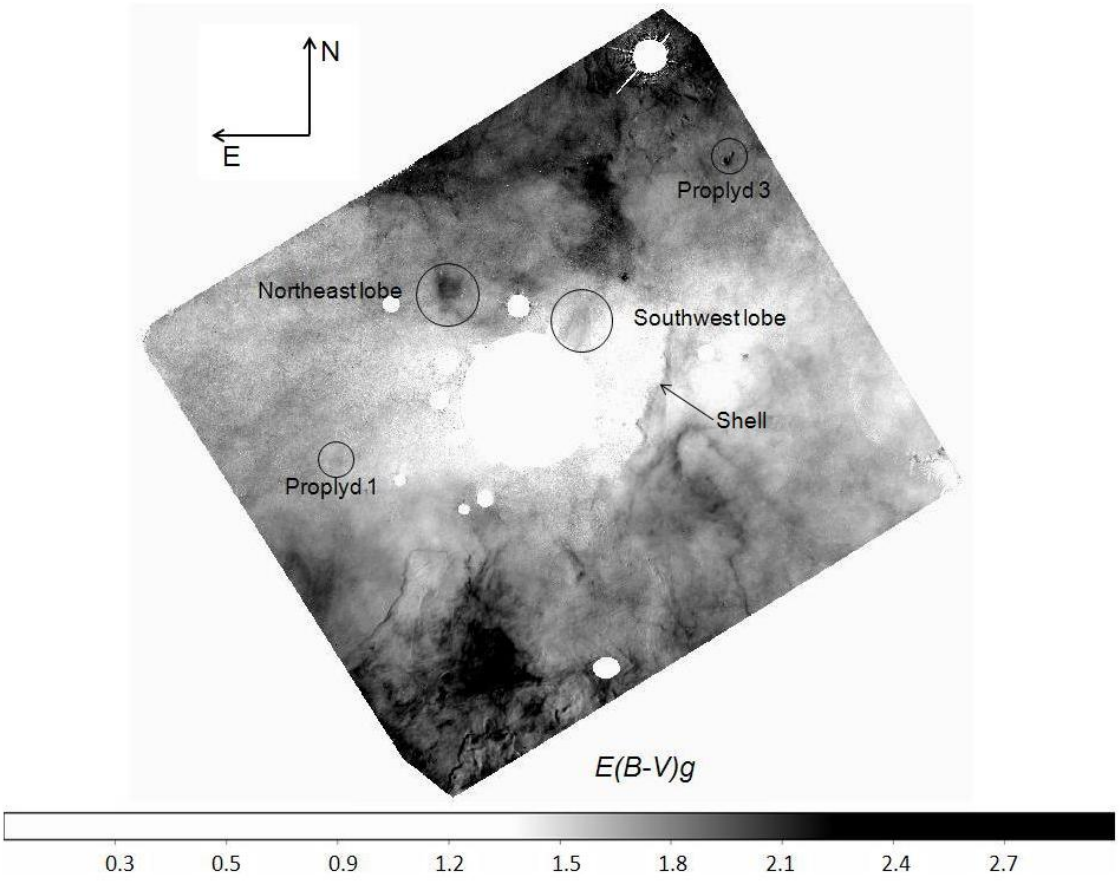


Figure 4.5: The two-dimensional map of the gas color excess, $E(B-V)_{\rm g}$ in giant NGC 3603 in grey scale. The locations of specific sources (Section 4.3.1) associated with a local $E(B-V)_{\rm g}$ enhancement are indicated.

see also Figure 4.5) and found that the hourglass nebula is more strongly extincted in the northeast (with $E(B-V)_{\rm g} = 2.0$ mag versus $E(B-V)_{\rm g} = 1.6$ mag in the southwest).

### 4.3.2 The shell structure

Optical images of NGC 3603 show an extended cavity around the HD 97950 cluster. Clayton (1986) estimated the diameter of this shell-like structure to be approximately 2 pc. Clayton analyzed the Doppler shifts of the H$\alpha$ emission in the central region of NGC 3603, and found a complex velocity structure in the ionized hydrogen. He interpreted the main velocity components as indicative of two expanding shells. One of these is a faint shell in the east-west direction with a mean heliocentric velocity of $\langle v \rangle_{\rm hel} = +120$ km s$^{-1}$, an expansion velocity of $\sim$ 30 km s$^{-1}$, and a diameter of $\sim$ 1 pc. The other one is a brighter shell in the north-south

direction and centered on the HD 97950 cluster. For this second shell-like feature Clayton (1986) found $\langle v \rangle_{\rm hel} = +50$ km s$^{-1}$ and $\sim 1.5$ pc as a lower limit for its diameter. (Note that Clayton assumed that NGC 3603 lies at a distance of 6 kpc from us.) From Clayton's Figure 4, we infer an expansion velocity of $\sim 55$ km s$^{-1}$ for this second shell, which Clayton identified with the above mentioned cavity.

In the $E(B-V)_{\rm g}$ map (Figures 4.1 and 4.5) we also find a cavity in correspondence with this expanding gas shell and with a radius of about 1.0 pc. The median color excess within the cavity is $E(B-V)_{\rm g} = 1.51 \pm 0.04$ mag. Moreover, we find a shell structure corresponding to a local enhancement of color excess with a mean $E(B-V)_{\rm g} = 1.59$ mag about 1.2 pc west of the cluster center (see Figure 4.5). This shell structure extends for 1.3 pc along the north-south direction. Judging from its position, it seems to lie along the high ionization front of the gas shell structure found by Clayton (1986) in the north-south direction.

Recently, Lebouteiller et al. (2007) observed NGC 3603 with Spitzer in order to search for PAH (polycyclic aromatic hydrocarbon) and [S IV] emission. They found that within 1.5 pc from the cluster center, the PAH and [S IV] emission is suppressed, possibly because the strong radiation field of the massive stars in the cluster (about 60 OB stars, see Melena et al. 2008) destroys dust grains, dissociates complex molecules and pushes the gas out. In doing so, these stars would thus reduce the color excess within the area and produce a cavity with lower $E(B-V)_{\rm g}$ in the reddening map. The western edge of this cavity appears to be delineated by the shell structure seen in the reddening map (Figure 4.5).

### 4.3.3 The molecular pillars

In the southern region of NGC 3603 we can see two prominent pillars to the southwest and southeast of the cluster (Figure 4.6). Following Nürnberger et al. (2002), we refer to them as MM1 and MM2, respectively. Figure 4.6 is a composite color image showing the H$\alpha$ emission (in blue), the Pa$\beta$ emission (in green), and the color excess (in red). The heads of both MM1 and MM2 stand out because of their strong H$\alpha$ and Pa$\beta$ emission. They are gradually being photoevaporated by the cluster's massive OB stars as is also indicated by the shocked and ionized material in their heads (Nürnberger et al. 2002, 2003). In the simulations of Gritschneder et al. (2010), the ionizing radiation emitted by a massive star can enhance the initial turbulent density distribution of a nearby molecular cloud and naturally lead to the formation of pillar-like structures within the cloud.

According to Bertoldi (1989) and Bertoldi & McKee (1990), in clouds experiencing photoevaporation a velocity gradient will eventually emerge, leading to a configuration where the head of a pillar moves more slowly than its tail. Applying this to the Eagle nebula (M16), Pound (1998) points out that the measured radial velocity gradients depend on our viewing angle and provide clues about the three-dimensional structure of the nebular features with respect to the ionizing stars. The tail of a pillar located in front of the ionizing stars will then have lower radial velocities than the pillar's head, since the tail is being blown toward the observer (while the opposite radial velocity gradient would be observed across a pillar located behind the ionizing OB stars). Both Nürnberger et al. (2002) and Röllig et al. (2011) found that the radial velocity in the head of MM1 is larger than that of the tail. Thus in NGC 3603 we have a configuration where the pillar is located

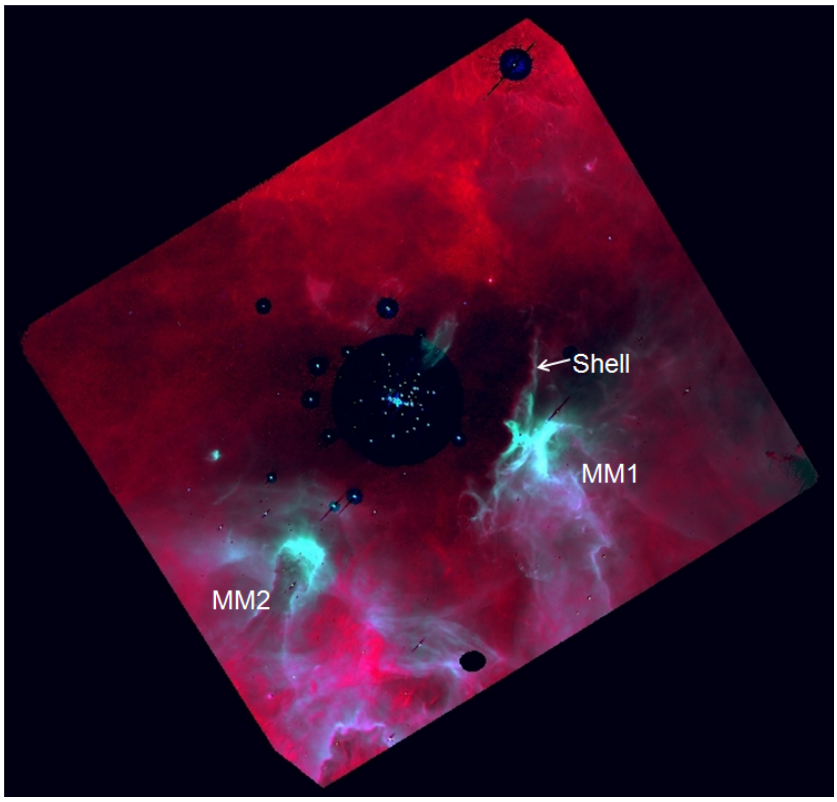


Figure 4.6: Color composite image of NGC 3603, obtained with the map of the color excess (red), the $Pa\beta$ emission image (green), and the $H\alpha$ emission image (blue). The positions of the shell and of the pillars MM1 and MM2 are indicated in the image.

in front of the stars of the HD 97950 cluster as seen from our position, with some tilt with respect to the light of sight.

The rims of MM1 and MM2 have a high $E(B-V)_{\rm g}$ of $\sim 1.8$ mag (see Figure 4.1), implying a large amount of dust. Along the pillars' main body, though, the color excess is lower than at the rim ($\sim 1.5$ mag) owing to "limb brightening" effects. We explain this phenomenon in a cartoon in Figure 4.7. The pillar is represented by a cylinder whose density decreases from the head to the tail (Mackey & Lim 2010). The radiation of the cluster's OB stars ionizes the outer layer of the pillar (A, B and C in Figure 4.7), while the interior is largely shielded and mostly neutral. Because of the long path traveled by the light emitted in A and B of the ionized layer, the color excess measured in the pillar rims is relatively high, yet a lower limit to the true $E(B-V)_{\rm g}$ associated with the main body of the pillar. The light emitted in C (i.e., the front side of the pillar in Figure 4.7) travels a shorter path within the ionized layer, and, for this reason, the $E(B-V)_{\rm g}$ measured in the front side of the pillar facing the observer is lower than that computed at the pillar rims.

We attempt to estimate the column density of atomic hydrogen ($N_{\rm H}$) per pixel across the

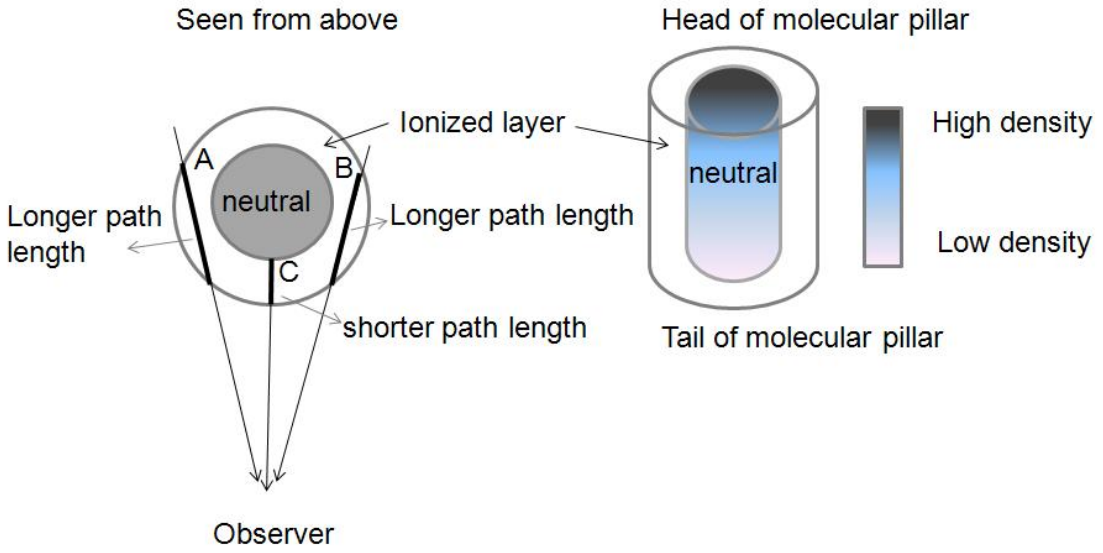


Figure 4.7: A cartoon to illustrate why the observed $E(B-V)_{\rm g}$ in the rims of a pillar is larger than at center. The pillar is represented by a cylinder (neutral in its interior and with a density gradient from head to tail) surrounded by an outer layer of gas ionized by the OB stars of the HD 97950 cluster. See the text for a more detailed description.

WFC3 field of Figure 4.1 by using the empirical relation (Equation 2.15) of Seward (1999):

$$N_{\rm H} = 1.9 \cdot 10^{21} A_{\rm V} \ {\rm atoms \ cm^{-2} \ mag^{-1}} \tag{4.28}$$

where $A_{\rm V}$ is computed from the two-dimensional map of $E(B-V)_{\rm g}$ in Figure 4.1 assuming $A_{\rm V} = 3.1 \cdot E(B-V)_{\rm g}$. The histogram of the pixel $\log_{10}(N_{\rm H})$ distribution is shown in Figure 4.8. The majority of the pixels have $\log_{10}(N_{\rm H})$ in the range of approximately 21.9 to 22.1. The rims of the pillars in NGC 3603 are characterized by $\log_{10}(N_{\rm H}) \simeq 22$. This value is probably only a lower limit to the true column density of $N_{\rm H}$ within the pillars. For example, Thompson et al. (2002) derived $\log_{10}(N_{\rm H}) = 22.8$ inside the dark region of the pillar column III in M16.

Since the column density of molecular hydrogen ($N_{\rm H_2}$) is one half of the $N_{\rm H}$ value (Thompson et al. 2002), the pillar rims in NGC 3603 likely have $\log_{10}(N_{\rm H_2}) \simeq 21.7$, which agrees well with the simulation results of Mackey & Lim (2010). With this column density at the rims, the central $H_2$ column density of the pillar, $\log_{10}(N_{\rm H_2})$, may be as high as about 22.7 to 23 according to Mackey & Lim (2010), which agrees with the the column density of MM1 and MM2 ($\log_{10}(N_{\rm H_2}) = 22.6 - 23$) as derived by Nürnberger et al. (2002).

This value is consistent with the $H_2$ column density of bright-rimmed clouds (BRCs) undergoing star formation. Urquhart et al. (2009) studied a number of BRCs, which are isolated molecular clouds located on the edges of evolved H II regions. Some BRCs show evidence of significant interaction between their molecular gas with the ionizing radiation from their nearby H II regions.

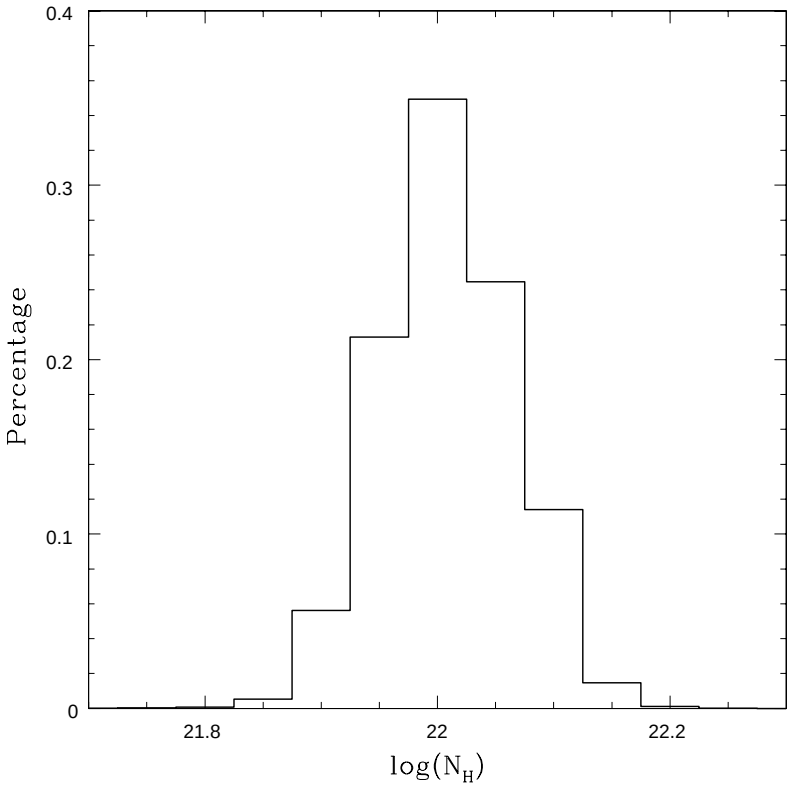


Figure 4.8: Histogram of the pixel column density of atomic hydrogen, which is derived from the color excess of each pixel through the empirical relation of Seward (1999).

These BRCs are thus comparable in their properties to the ionized heads of molecular clouds. They have been found to host star formation activity, most likely triggered by the ionizing front coming from the nearby H II regions. The column density of molecular hydrogen in BRCs with triggered star formation is $20.9 \leq \log_{10}(N_{\rm H_2}) \leq 22.8$ (Urquhart et al. 2009).

The similarity in $\log_{10}(N_{\rm H_2})$ between star-forming BRCs and the pillars in NGC 3603 suggests that the heads of MM1 and MM2 may experience gravitational collapse and undergo star formation. Indeed Caswell et al. (1989) and De Pree et al. (1999) found methanol and water maser sources in the heads of both MM1 and MM2; these sources are the typical signatures of newborn stars obscured by dusty molecular envelopes. The star formation in the pillars is likely triggered by photoionization-induced shocks due to the expansion of the H II region in which the HD 97950 cluster resides. The strong H$\alpha$ and Pa$\beta$ emission in the heads of MM1 and MM2 (Figure 4.6) is another indication that the OB stars in the HD 97950 cluster are ionizing the pillars. The ionization shock fronts were detected at mid-infrared wavelengths by Nürnberger & Stanke (2003).

## 4.4 Summary

In the present chapter we extend previous studies of the differential reddening around the young star cluster HD 97950 in the NGC 3603 giant H II region (e.g., Sung & Bessel 2004). We derive a two-dimensional map of the color excess of the gas around the cluster from HST/WFC3 images, which allows us to measure the H$\alpha$/Pa$\beta$ flux ratio and its decrement due to dust extinction (see Calzetti et al. 1996). Our reddening map covers an area of 4.9 pc $\times$ 4.3 pc with a scale of 0.004 pc per pixel (assuming that NGC 3603 is at a distance of 6.9 kpc). The median value of the color excess within the central cavity ($r < 1$ pc, where the HD 97950 cluster resides) is $E(B-V)_{\rm g} = 1.51 \pm 0.04$ mag. Going from the cavity to either the northern or the southern edge of the field of view, $E(B-V)_{\rm g}$ is seen to increase from 1.5 mag to 2.2 mag at a distance of 2 pc from the cluster. From the cluster towards either the eastern or western edge of the field of view (at a distance of 2 pc), $E(B-V)_{\rm g}$ rises from 1.5 mag to 1.6 mag. The average uncertainty of the derived color excess is about 0.1 mag.

We find a shell structure 1.2 pc west of the cluster with a mean $E(B-V)_{\rm g}$ of 1.59 mag, about 0.08 dex higher than in the central cavity. We interpret this shell structure as the surface at which the expanding gas shell detected by Clayton (1986) in the north-south direction interacts with a denser molecular cloud.

The ionizing radiation emitted by the OB stars in the HD 97950 cluster is likely to be responsible for the formation of the two molecular pillars MM1 and MM2 seen 1.2 – 2.5 pc south-west and south-east of the cluster, respectively. We use our reddening map to estimate the column density of $H_2$ in MM1 and MM2. We derive $\log_{10}(N_{\rm H_2}) = 21.7$ in the pillars' rims and up to $\log_{10}(N_{\rm H_2}) = 23$ in the pillars' center, in agreement with the earlier estimates by Nürnberger et al. (2002). Based on the velocity gradient detected in earlier studies, we argue that the pillars are closer to us than the ionizing HD 97950 cluster.

The strong H$\alpha$ and Pa$\beta$ emission in the heads of the pillars MM1 and MM2 traces the ionization of the pillar heads by the OB stars in the HD 97950 cluster. The pillar heads appear to be undergoing star formation as indicated by the presence of methanol and water maser sources (Caswell et al. 1989; De Pree et al. 1999). Such a star formation activity is likely triggered by photoionization-induced shocks due to the expansion of the H II region surrounding the HD 97950 cluster.

The two-dimensional map of $E(B-V)_{\rm g}$ derived in this work paves the way to deredden individual stars in the same field of view by providing an upper limit to the true stellar reddening. Individual reddening corrections in regions suffering substantial differential reddening are essential for analyses of stellar photometry, e.g., for constraining the age spread in the HD 97950 cluster and its surroundings.

**Part of this chapter was published as Pang X., Pasquali A., Grebel E.K. 2011, AJ, 142, 132.**

# 5

# The extinction curve in NGC 3603

The importance of dust:
*And the LORD God formed man of the dust of the ground, and breathed into his nostrils the breath of life; and man became a living soul. (Genesis 2:7)*

**Abstract** We use $UBV$ photometry from the High Resolution Channel of the Advanced Camera for Surveys and $RI$ photometry from the Wide Field and Planetary Camera 2 aboard HST to derive individual stellar reddenings and extinctions for stars inside and outside the HD 97950 cluster in the H II region NGC 3603. The mean reddening for 78 member main-sequence stars inside the cluster is $E(B-V) = 1.24 \pm 0.09$ mag. This mean reddening increases to $1.40 \pm 0.02$ mag for seven main-sequence stars outside the cluster. The foreground reddening of the cluster is estimated via the Q-method to be $E(B-V) \sim 0.824$ mag. After correcting for foreground reddening, the total to selective extinction ratio is $R_V = 3.49 \pm 0.79$ inside the cluster. The extinction curve in the $UBVRI$ filters inside the cluster is greyer than the average Galactic extinction laws from Cardelli et al. (1989) and Fitzpatrick et al. (1999), and closer to the extinction law derived by Calzetti et al. (2000) for starburst galaxies, indicating similar dust properties of the HD 97950 cluster and starburst galaxies. There is a linear relation between the stellar and the gas reddening, $E(B-V)_* = 0.293\,E(B-V)_g + 0.992$. Individual stellar reddenings of more than 7000 stars in the field of view of the Wide Field Camera 3 are derived by converting the gas reddening (at the stars' positions) according to this relation. Significant differential stellar reddening exists in the giant H II region NGC 3603, with $E(B-V)$ increasing from $\sim$1.35 mag at 0.52 pc around the central ionizing cluster to 1.7 mag at 3.2 pc. The differential reddening reflects local inhomogeneity in the distribution of gas and dust within NGC 3603.

## 5.1 Introduction

### 5.1.1 Extinction in the Galaxy

#### Extinction curve

The dependence of dust extinction on wavelength is the so-called extinction curve. The extinction curve rises from the infrared (IR) to shorter wavelengths with a power-law-like dependence, increases slightly in the optical region, shows a prominent bump at 2175 Å, and has a (sometimes) steep rise in far-ultraviolet (FUV) (figure 5.1). The Galactic extinction curve has been extensively studied in a large number of papers (Seaton 1979; Savage et al. 1985; Cardelli et al. 1989, 1988; Fitzpatrick et al. 1999; Valencic et al. 2004; Fitzpatrick & Massa 2007, 2009), which have shown it to vary considerably among different lines of sight as a result of different processing histories of dust grains in the interstellar medium (ISM).

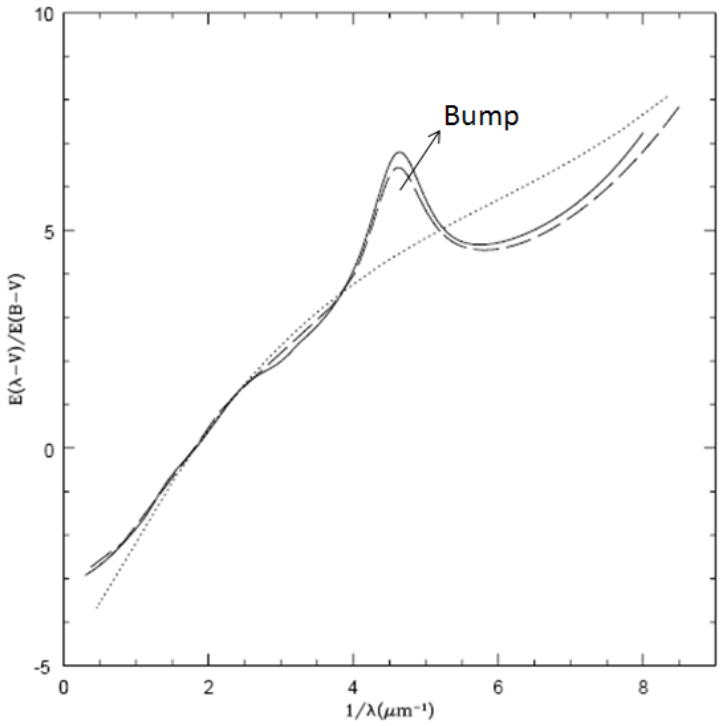


Figure 5.1: Average Galactic extinction curves ($R_V = 3.1$) of Cardelli et al. (1989), (solid line) and Fitzpatrick (1999), (dashed line). The dotted line is the mean extinction curve for 39 starburst galaxies (Calzetti et al. 2000), with $R_V = 4.05$. The bump at 2175 Å is indicated.

The typical way to determine the interstellar extinction is the standard "pair method", which matches the spectral features of reddened main-sequence (MS) stars with identical unreddened MS

Table 5.1: Anchor points from IR to optical (Fitzpatrick 1999)

| Wavelength (Å) | $\lambda^{-1}$ ($\mu$m$^{-1}$) | $E(\lambda-V)/E(B-V)$ |
|---|---|---|
| 26500 | 0.377 | -2.736 |
| 12200 | 0.820 | -2.172 |
| 6000 | 1.667 | -0.313 |
| 5470 | 1.828 | 0.054 |
| 4670 | 2.141 | 0.805 |
| 4110 | 2.433 | 1.314 |
| 2700 | 3.704 | 3.264 |
| 2600 | 3.846 | 3.59 |

standard stars (Massa et al. 1983). The extinction is derived for each star in terms of $A_\lambda/A_V$ or $E(\lambda-V)/E(B-V)$ as a function of inverse wavelength (Cardelli et al. 1988, 1989; Fitzpatrick et al. 1999). The individual extinction curves obtained for different lines of sight are averaged, and the mean extinction curve is parameterized with different analytical functions in different wavelength ranges. The average extinction curve is usually subdivided into three parts:

(1) IR/optical ($0.3\,\mu\mathrm{m}^{-1} \leq x \leq 3.3\,\mu\mathrm{m}^{-1}$, $x = \lambda^{-1}$):

The average extinction curve in the optical-through-IR range is reproduced with a cubic spline and a set of anchor points. Table 5.1 list the anchor points from Fitzpatrick (1999) which we plot in Figure 5.1.

At these wavelengths, the curve is characterized with the parameter $R_V = A_V/E(B-V)$, the ratio of total to selective extinction in the $V$ band ($\lambda = 5470$Å). A mean value of 3.1 is usually measured for the ISM in the Milky Way. $R_V$ is generally considered as a coarse indicator of the mean size of dust grains; larger than average grains yield larger than average $R_V$ (Mathis & Wallenhorst 1981). Cardelli et al. (1989) were the first to explain the variability of the Galactic extinction by introducing a $R_V$ dependent UV/optical/IR extinction curve. They suggested that the extinction curves with a large value of $R_V$ are likely caused by the presence of larger particles in dense regions. The extinction curve of Cardelli et al. (1989) is parameterized by $R_V$ as:

$$< A_\lambda/A_V >= a(x) + b(x)/R(V) \tag{5.1}$$

$a(x)$ and $b(x)$ are wavelength-dependent coefficients.

At infrared wavelengths: $0.3\,\mu\mathrm{m}^{-1} \leq x \leq 1.1\,\mu\mathrm{m}^{-1}$

$$a(x) = 0.574\,x^{1.61}; b(x) = -0.527\,x^{1.61}. \tag{5.2}$$

In the optical range: $1.1\,\mu\mathrm{m}^{-1} \leq x \leq 3.3\,\mu\mathrm{m}^{-1}$,

$$\begin{aligned} a(x) =& 1 + 0.17699\,y - 0.50447\,y^2 - 0.02427\,y^3 + 0.72085\,y^4 \\ &+ 0.01979\,y^5 - 0.77530y^6 + 0.32999y^7 \\ b(x) =& 1.41338\,y + 2.28305\,y^2 + 1.07233y^3 - 5.38434\,y^4 \\ &- 0.62251\,y^5 + 5.30260\,y^6 - 2.09002\,y^7, \end{aligned} \tag{5.3}$$

where $y = x - 1.82$. However, Fitzpatrick et al. (2007) claim that this relationship is only applicable to those lines of sight with large $R_V$. Alternatively, Fitzpatrick & Massa (2009) use two parameters to characterize the extinction at near-infared wavelengths:

$$\frac{E(\lambda - V)}{E(B - V)} = [0.349 + 2.087\, R_V] \frac{1}{1 + (\lambda/0.507)^{\alpha}} - R_V \tag{5.4}$$

where $R_V$ provides a measure of the mean grain size along the line of sight, and $\alpha$ is related to the grain size distribution. The large scatter among extinction curves derived for different lines of sight (Fitzpatrick & Massa 2009) demonstrates that besides the grain size distribution which affects all wavelengths, some other dust properties such as chemical composition, coagulation history of grains, coating, and hardness of interstellar radiation field must be involved in shaping the extinction curve (Seab & Shull 1983).

(2) UV ($3.3\,\mu\mathrm{m}^{-1} < x < 8\,\mu\mathrm{m}^{-1}$, $x = \lambda^{-1}$):

The coefficients $a(x)$ and $b(x)$ in the extinction curve of Cardelli et al. (1989) at ultraviolet wavelengths are:

$$a(x) = 1.752 - 0.316\, x - 0.104/[(x - 4.67)^2 + 0.341] + F_a(x), \tag{5.5}$$

$$b(x) = -3.090 + 1.825\, x + 1.206/[(x - 4.62)^2 + 0.263] + F_b(x). \tag{5.6}$$

$F_a(x)$ and $F_b(x)$ are wavelength-dependent coefficients,

$$F_a(x) = -0.04473\,(x - 5.9)^2 - 0.009779\,(x - 5.9)^3, \quad (5.9 \le x \le 8); \tag{5.7}$$

$$F_b(x) = 0.2130\,(x - 5.9)^2 + 0.1207\,(x - 5.9)^3, \quad (5.9 \le x \le 8); \tag{5.8}$$

$$F_a(x) = F_b(x) = 0 \quad (x < 5.9). \tag{5.9}$$

Fitzpatrick & Massa (1990) represent the UV extinction curve with a Lorentzian function peaking at the 2175 Å bump ($D(x, x_0, \gamma)$), and with a linear component underlying the entire UV wavelength range ($c_1 + c_2\, x$), plus a far-UV curvature component ($F(x)$):

$$\frac{E(\lambda - V)}{E(B - V)} = c_1 + c_2\, x + c_3\, D(x, x_0, \gamma), \quad x \le c_5 = 5.9\,\mu\mathrm{m}^{-1}; \tag{5.10}$$

$$\frac{E(\lambda - V)}{E(B - V)} = c_1 + c_2\, x + c_3\, D(x, x_0, \gamma) + c_4\, F(x), \quad x > c_5 = 5.9\,\mu\mathrm{m}^{-1}; \tag{5.11}$$

$$D(x, x_0, \gamma) = \frac{x^2}{(x^2 - x_0^2)^2 + x^2\gamma^2}; \tag{5.12}$$

$$F(x) = 0.5392\,(x - c_5)^2 + 0.05644\,(x - c_5)^3. \tag{5.13}$$

$c_1$, $c_2$, $c_3$, $c_4$, and $c_5$ are coefficients.

Fitzpatrick (1999) find a linear correlation between $c_2$ and $R_V^{-1}$,

$$c_2 = -0.824 + 4.717 \times R_V^{-1} \tag{5.14}$$

and between $c_2$ and $c_1$:

$$c_1 = 2.03 - 3.007 \times c_2 \tag{5.15}$$

The extinction laws of Cardelli et al. (1989) and Fitzpatrick (1999) both are $R$-dependent in the UV. Using $R_V = 3.1$ (the mean value for the diffuse ISM in the Milky Way), the coefficient values (equations 5.10-5.15) are: $c_1 = -0.06768$, $c_2 = 0.6976$, $c_3 = 3.23$ (bump strength), $c_4 = 0.41$ (FUV curvature), $x_0 = 4.596\,\mu m^{-1}$ (bump position), $\gamma = 0.99\,\mu m^{-1}$ (bump width).

### Dust model

The extinction curve depends on the chemical composition and the size distribution of the dust grains. To interpret the extinction curve, dust models with a proper chemical composition of grains have been developed. Mathis et al. (1977) developed a dust model consisting of silicate and graphite grains, with a power law distribution of the grains size which fits the observed extinction curve in a reasonable way. The more recent model by Draine & Li (2001) consists of a population of amorphous silicates and a population of carbonaceous grains including polycyclic aromatic hydrocarbons (PAHs). All dust models need to explain the 2175 Å bump (Figure 5.1) which is prominent in the UV extinction curve. Possible contributors to the bump are interstellar graphite grains (Mathis et al. 1977) or PAHs (Draine 1989). In particular, if the bump were generated by graphite grains, its central wavelength and profile would depend on their size, shape, and coating. However, the profile of the bump feature does not change and the central wavelength is very similar in different environments. Hence the carrier of the bump may be incorporated entirely into other grains. Small particles producing the bump likely stick to larger grains during the coagulation process. The model of Maclean et al. (1982) reproduced the bump by absorption in a thin $O^{2-}$ coating on the surfaces of MgO particles.

While the composition of dust grains determines the specific features in the extinction curve, the difference in grain sizes might contribute to significant variations in the magnitude of the extinction curve. In some young clusters, e.g., cluster HD 62542 and HD 29647, where strong stellar winds and shocks exist, a very high FUV extinction and strong 2175 Å bump are observed (Cardelli & Savage 1988). The rapid rise in the extinction shortward of 1500 Å requires a large number of grains smaller than $0.02\mu$m, which can be produced by grain-grain collisions, sputtering due to fast shocked gas (Draine & Salpeter 1979), or photoprocessing. Seab & Shull (1983) provided a shock processing model of the interstellar grains in which supernovae shocks propagating with a speed as low as 40 km/s can destroy a significant amount of dust grains. More than 50% of the large grains sputter into small grains, while the small grains remain almost intact. The over-abundance of small grains in the clusters results in a $R_V$ smaller than 3.1 (Cardelli & Savage 1988)

On the the other hand, some dense interstellar environments are found to have a lower (greyer) FUV extinction and $R_V$ ($> 3.1$) larger than the mean Galactic ISM (Chini & Krügel 1983; Mathis

1987; Cardelli et al. 1989; Fitzpatrick & Massa 2009). This decrease of FUV extinction and increase of $R_V$ might be attributed to the growth of grains (Draine 2009). In dense regions (dark clouds, or nebulosites) the size of grains grows beyond $0.4\,\mu\mathrm{m}$ and the number of large silicate particles is enhanced (Mathis & Wallenhorst 1981).

### 5.1.2 Extinction in starburst environments

#### Extinction curve in starburst galaxies

The extinction curve of the Galaxy does not work for other galaxies, especially for starburst galaxies, where the star formation rate is a few tens of $\mathrm{M}_\odot/\mathrm{yr}$, and $R_V$ ($\sim 4.05$; Calzetti et al. 2000) is much larger than the diffuse ISM in the Galaxy ($R_V = 3.1$). Calzetti et al. (1994, 1997, 2000) find greyer extinction curves for 39 starburst galaxies. Calzetti et al. express $E(\lambda - V)/E(B - V)$ as follows (with $R_V = 4.05$):

1) Red-IR: $0.63\,\mu\mathrm{m} \leq \lambda \leq 2.20\,\mu\mathrm{m}$

$$\frac{E(\lambda - V)}{E(B - V)} = 2.659\,(-1.857 + 1.040/\lambda) \tag{5.16}$$

2) UV-Optical: $0.12\,\mu\mathrm{m} \leq \lambda \leq 0.63\,\mu\mathrm{m}$

$$\frac{E(\lambda - V)}{E(B - V)} = 2.659\,(-2.156 + 1.509/\lambda - 0.198/\lambda^2 + 0.011/\lambda^3) \tag{5.17}$$

According to Calzetti et al. (1994), young massive stars are associated with dustier regions than the older and less-massive stars. The strong UV radiation and stellar winds of massive stars are likely to destroy dust grains and change the properties of the local ISM. Practically, the stellar feedback from young massive stars produces an inhomogeneous, clumpy distribution of dust within star-forming regions, which cannot be represented with the uniform dust screen model commonly used for the Milky Way. In the case of starburst galaxies, in fact, the scattering of photons by internal dust grains become effective at reconveying photons along the line of sight. On the contrary, in the diffuse Galactic ISM the distant dust forms an uniform extinction screen through which the absorption and the scattering concur in removing flux from the line of sight. Therefore the extinction curve of starburst galaxies is greyer (dotted line in Figure 5.1) than the average Galactic extinction curve.

#### Extinction in the starburst cluster

Unfortunately, most of the starburst galaxies are very far away so that we can not study their ISM with high angular resolution data. However, in the Milky Way, the environment of the H II region hosting a starburst cluster is similar to that of starburst galaxies. A systematic investigation of the reddened stars within the H II region can probe the effect of the presence of massive stars on the dust grains in the surrounding ISM, and bridge our knowledge of the ISM in starburst regions from parsec to kilo-parsec scales. There is an ideal H II region hosting a starburst cluster of which high-resolution and multi-band data are available. This is NGC 3603, a giant H II region.

The giant H II region NGC 3603 hosts the central young starburst cluster HD 97950 with a mass of $\sim 10^4\,\mathrm{M}_\odot$ (Harayama et al. 2008). The strong radiation field of the OB stars in the cluster (Drissen et al. 1995; Melena et al. 2008) ionizes and sweeps away the ISM, and generates a cavity around the cluster where the gas reddening is lowest (chapter 4). The ionization shock fronts were detected at mid-infrared wavelengths by Nürnberger & Stanke (2003). A shell structure is apparent at 1.2 pc west of the cluster core (see Figure 4.5 in Chapter 4) in the gas reddening map and overlaps spatially with the ionized front of the gas shell expanding at 55 km/s found by Clayton (1986). The engine of the expanding shell may be the stellar winds and the radiation pressure of the massive stars in the cluster. Such energy input into the ISM can change the dust grain properties significantly. Weingartner & Draine (2001) find that when the grains larger than $0.1\,\mu\mathrm{m}$ are exposed to the radiation of OB stars, they are subjected to the photodesorption force, applied by a radiation field which is anisotropic because of a spatially uneven distribution of stars. Under this force, the large grains decouple from the gas and shift away. Furthermore, the large grains are destroyed or reduced to 75% of their initial radius by a shock speed as low as 40 km/s, which can be generated by supernovae (Seab & Shull 1983) or by the radiation pressure and the stellar winds of OB stars in a cluster. The large grains are destroyed or sputter into small grains and pushed away. This agrees with the observation of Lebouteiller et al. (2007) that the emission of very small grains (VSGs) whose size is smaller than $0.02\,\mu\mathrm{m}$ (Wood et al. 2008) increases from the cluster center and peaks at cluster-centric distances of 1-1.5 pc. The emission of the VSGs is common in massive star formation regions (Churchwell et al. 2006), where the interstellar radiation field (ISRF) is very hard. Moving further away from the cluster center (2-3.5 pc), prominent silicate absorptions and bright PAH emissions are detected (Lebouteiller et al. 2007), indicating a softening of the ISRF and an increase in size of the dust grains. These results are consistent with a significant increase of the gas reddening from 1.5 mag at 1 pc to 2.2 mag at 4 pc (Chapter 4). In the south, at 1.2-2.5 pc from the cluster center, two giant molecular pillars MM1 and MM2 are the cradles of star formation (Caswell et al. 1989; De Pree et al. 1999). Both pillars stand out as high reddening regions in the two-dimensional gas reddening map (Figure 4.6 in Chapter 4).

In this chapter, we are going to study the extinction of stars in the H II region NGC 3603 and the central starburst cluster HD 97950. Section 5.2 will introduce the observations and data reduction. We will discuss individual stellar reddenings of cluster stars in Section 5.3. We refer to foreground reddening in Section 5.4. Section 5.5 will discuss the dust properties in the cluster. The extinction curve of the HD 97950 cluster (within 1.5 pc) will be presented in Section 5.6. In Section 5.7, we derive individual stellar reddening of over 7000 stars distributed across NGC 3603 at a distance of up to 4 pc from the HD 97950 cluster. Finally, we summarize our results in Section 5.8.

## 5.2 Observations and data reduction

The HD 97950 cluster and its immediate surrounding in NGC 3603 were observed with the Hubble Space Telescope (HST), see Figure 5.2. The ultraviolet data were taken with the High Resolution

Channel (HRC) of the Advanced Camera for Surveys (ACS) in 2005 (PI: Jesus Maiz Apellaniz) through the *F330W* ($U$) and *F435W* ($B$) filters. HRC is characterized by a spatial resolution of $0.03''$/pixel and a field of view of 29" $\times$ 25". The optical observations were carried out with the Wide Field and Planetary Camera 2 (WFPC2) in two epochs: 1997 (PI: Laurent Drissen) and 2007 (PI: Wolfgang Brandner) through the *F555W* ($V$), *F675W* ($R$), and *F814W* ($I$) filters. In Chapter 2 we reduced the two epoch WFPC2 data and identified more than 400 member stars in the core of the cluster (PC chip: $0.045''$/pix; $20'' \times 20''$) via relative proper motions. Of these member stars, 150 are in common between the HRC and PC images and have $UBVRI$ photometry available (Appendix Table B.1-B.5).

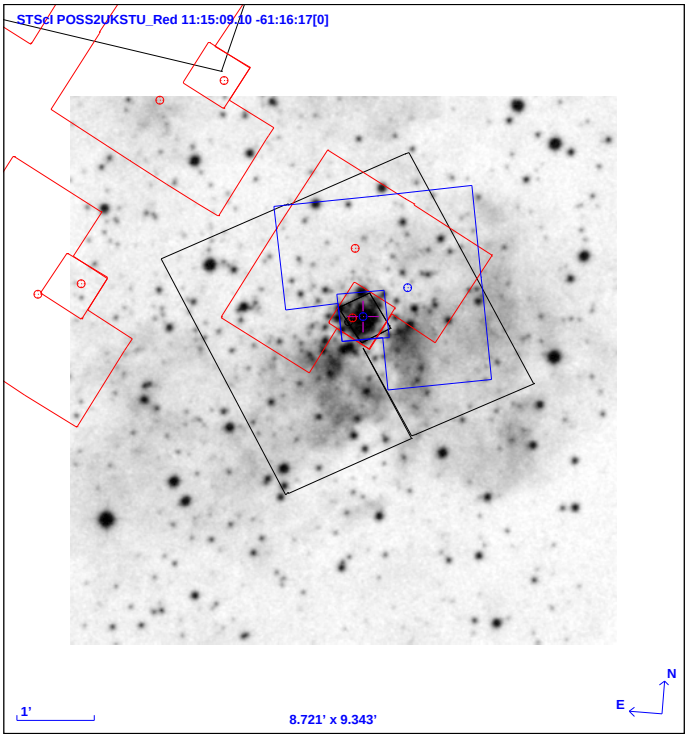


Figure 5.2: Image of a portion of the Galactic H II region NGC 3603 centered on the young ionizing HD 97950 cluster. The image was taken from a photographic plate (POSS2UKSTU-Red) obtained using the UK Schmidt Telescope. The digitized image is available from the Digitized Sky Survey at the Space Telescope Science Institute. The location of the field of view of the HST/WFPC2 observations done in 1997 (blue polygons) and in 2007 (red polygons) and ACS/HRC&WF observations (black polygons) are indicated.

In addition to the HST data for the stars in the core, we have also collected the photometry for stars outside the cluster published by Melnick et al. (1989) in $UBV$ and from Brandner et al. (1997a) in $RI$.

Table 5.2: Photometry of the five main sequence stars selected from Melena et al. (2008) inside the cluster

| Name | RA | DEC | V | B-V | U-B | V-I | Spectral type |
|---|---|---|---|---|---|---|---|
| 41 | 11:15:07.046 | -61:15:38.95 | 14.436 | 0.858 | -0.189 | 1.631 | O4V |
| 40 | 11:15:07.124 | -61:15:39.09 | 13.463 | 0.99 | -0.183 | 1.566 | O3V |
| A2 | 11:15:07.313 | -61:15:38.79 | 12.655 | 0.952 | -0.186 | 1.51 | O3V |
| 16 | 11:15:07.825 | -61:15:37.84 | 13.691 | 0.974 | -0.153 | 1.609 | O3V |
| 108 | 11:15:08.513 | -61:15:38.30 | 13.896 | 0.981 | -0.144 | 1.634 | O5.5V |

The ACS/HRC data are reduced using $Dolphot$ [1], a stellar photometry package that was adapted from $HSTphot$ to handle ACS images. We used the ACS module in $Dolphot$ for the *F330W* and *F435W* data. Both *F330W* and *F435W* data consist of four dithered images. The exposure time for each single exposure image (*.flt) is 10 s (*F330W*) and 2 s (*F435W*). We mask bad and saturated pixels in the 'flt' images with the routine 'ACSMASK'. The offsets between dithered images were calculated by a python script. The photometry was produced by the routine 'DOLPHOT', with the specific parameters suggested for ACS data (DOLPHIN/ACS User's Guide[1]). 'DOLPHOT' performs PSF photometry with the precomputed PSF of each filter. The WFPC2 data were reduced with $HSTphot$ (Dolphin et al. 2000), whose procedure is similar to $Dolphot$. A detailed description of the data reduction of the optical WFPC2 data is discussed in Chapter 2.

## 5.3 Individual stellar reddening of the cluster

Recently, Pang et al. (2011) (see Chapter 4) derived a two-dimensional map of the gas reddening $[E(B-V)_g]$ in the NGC 3603 giant H II region extending to 4 pc from the central HD 97950 cluster. In the ISM, a cavity is visible around the cluster within which the gas reddening is 0.2 mag lower than outside. The $E(B-V)_g$ increases from 1.5 mag to 2.2 mag with increasing distance from the cluster (1.0 pc–4 pc). This uneven distribution of the dust in the ISM affects stars located at different positions differently, causing the differential reddening found by other studies (Pandey et al. 2000; Sung & Bessell 2004). Previous studies of the stellar reddening in NGC 3603 used a limited number of stars. We are going to use the gas reddening map and derive individual stellar reddenings for a much larger sample of stars inside and outside the cluster, in order to 1) investigate the differential stellar reddening; and 2) to construct the extinction curve through which we can investigate the dust properties in the starburst environment of the HD 97950 cluster.

### 5.3.1 Reddening in the cluster

We select stars located in the cluster ($r < 0.7$ pc from the center) whose spectral types are available from Table 3 in Melena et al. (2008). There are five main-sequence (MS) stars in Melena et

[1] Version 1.0.3: http://purcell.as.arizona.edu/dolphot/

al. (2008), which are also included in the $UBVRI$ member catalog (Appendix Table B.1-B.5). The photometry of these five MS stars is presented in Table 5.2. We extrapolate the effective temperature of these MS stars from Table 1 in Martins et al. (2005) as a function of their spectral types. Since the Lejeune & Schaerer (2001) isochrones extend to masses above 100 $M_{\odot}$, which are appropriate for the HD 97950 cluster (see Schnurr et al. 2008), we derive the intrinsic $U$, $B$, $V$, $R$, $I$ magnitudes of these five stars corresponding to their assigned effective temperature from Lejeune & Schaerer's (2001) 1 Myr-old isochrone. Thus, the color excesses $E(U-B)$, $E(B-V)$, $E(V-R)$, $E(V-I)$, and the extinctions $A_U$, $A_B$, $A_V$, $A_R$, $A_I$ are calculated by comparing the intrinsic colors and magnitudes obtained from the isochrone with the observed values, having assigned a distance module of 14.2 mag from Sung & Bessell (2004). Table 5.3 presents the mean value of the color excess and extinction of these five MS stars.

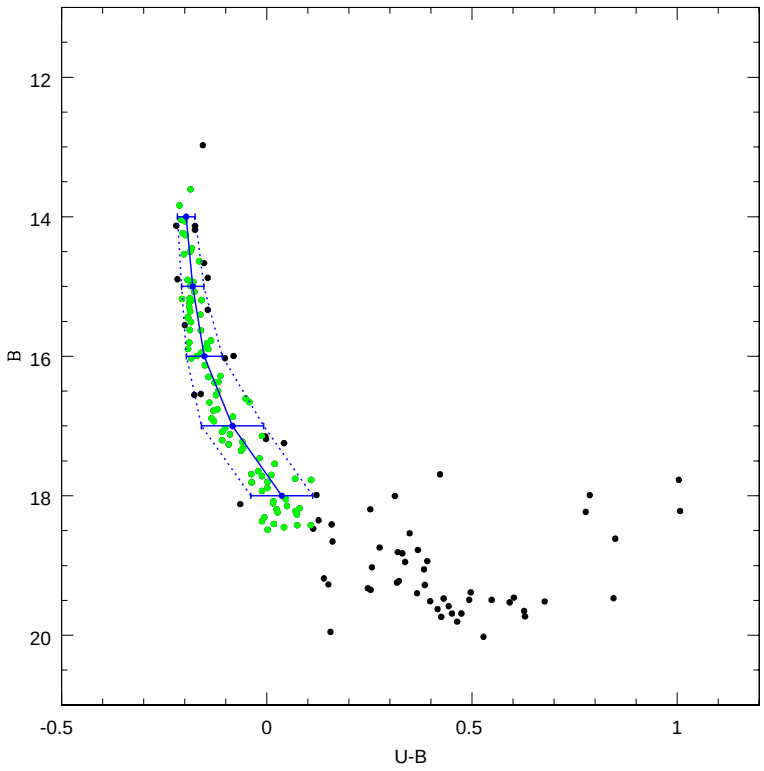


Figure 5.3: Color magnitude diagram of all member stars on the PC chip of WFPC2 (black dots). The green dots are the selected MS stars among the members, which are within 1.5 $\sigma$ from the mean $(U-B)$ color in each magnitude bin (the blue solid line: the locus of the MS).

We plot the member stars in the color magnitude diagram (CMD), [$B$ vs. $(U-B)$] in Figure 5.3. There is a color spread among the member stars, especially at the faint end. The stars fainter

Table 5.3: Mean color excesses, reddening vectors and extinctions for five main sequence stars selected from Melena et al. (2008) inside the cluster (without foreground reddening correction)

| Color excess & reddening vectors | | Extinction | |
|---|---|---|---|
| $E(U-B)$ | $1.00 \pm 0.02$ | $A_U$ | $7.44 \pm 0.71$ |
| $E(B-V)$ | $1.27 \pm 0.05$ | $A_B$ | $6.44 \pm 0.72$ |
| $E(V-R)$ | $0.92 \pm 0.02$ | $A_V$ | $5.17 \pm 0.75$ |
| $E(V-I)$ | $1.92 \pm 0.04$ | $A_R$ | $4.26 \pm 0.76$ |
| $E(U-B)/E(B-V)$ | $0.792 \pm 0.03$ | $A_I$ | $3.25 \pm 0.78$ |
| $E(V-R)/E(B-V)$ | $0.723 \pm 0.04$ | $R_V$ | $3.71 \pm 0.48$ |
| $E(V-I)/E(B-V)$ | $1.517 \pm 0.08$ | | |
| $E(V-R)/E(V-I)$ | $0.476 \pm 0.08$ | | |

Table 5.4: Mean color excess and extinctions for MS member stars selected from UBV colors (without foreground reddening correction)

| Color excess & extinction | |
|---|---|
| $E(U-B)$ | $0.96 \pm 0.07$ |
| $E(B-V)$ | $1.24 \pm 0.09$ |
| $E(V-R)$ | $0.89 \pm 0.05$ |
| $E(V-I)$ | $1.90 \pm 0.07$ |
| $A_U$ | $6.42 \pm 0.14$ |
| $A_B$ | $5.46 \pm 0.13$ |
| $A_V$ | $4.23 \pm 0.12$ |
| $A_R$ | $3.34 \pm 0.12$ |
| $A_I$ | $2.33 \pm 0.12$ |
| $R_V$ | $3.43 \pm 0.61$ |

than $B = 18.5$ mag and redder than $(U-B) = 0.2$ mag are probably pre-main-sequence (PMS) stars, which are intrinsically redder than MS stars in $(U-B)$. Since our procedure to compute individual reddening relies on MS stars, we have to exclude PMS stars from our further analysis due to their circumstellar disk or dust shell absorbing the ultraviolet radiation, and their age spread (up to 3 Myr, see Chapter 3). Stars brighter than $B = 18.5$ mag and bluer than $(U-B) = 0.2$ mag define a narrow MS in Figure 5.3. We use them to define the mean locus of the MS by calculating the mean $(U-B)$ color in magnitude bins, 1.0 mag in size. We set the width of the MS by considering only the stars (green dots) falling within 1.5 $\sigma$ (blue dotted lines) around the mean of each magnitude bin (blue solid line). We use the stars between the blue dotted lines (78, shown with green dots) to study the reddening and extinction curve within the cluster.

In the $UBV$ color-color diagram (Panel a in Figure 5.4), the mean reddening vector $E(U-B)/E(B-V)$ of the five stars selected from Melena (2008) is shown, which is used to project the 78 member MS stars (black dots) onto the 1 Myr-old isochrone of Lejeune & Schaerer (2001) to derive their individual $E(U-B)$ and $E(B-V)$. The color excesses $E(V-R)$ and $E(V-I)$

of the members are computed in the same way, but via the mean vectors $E(V-R)/E(B-V)$ and $E(V-I)/E(B-V)$ (Panel b and c in Figure 5.4). The mean reddening inside the cluster, $E(B-V) = 1.24 \pm 0.09$ (Table 5.4), agrees well with the result of Sung & Bessell (2004, $E(B-V) = 1.25$ mag). We plot the $E(B-V)$ of the member MS stars as a function of their cluster-centric distances in Figure 5.5. There is an apparent trend of increasing $E(B-V)$ with cluster-centric radius, implying that differential reddening even exists within the cluster ($r \leq 0.7$ pc).

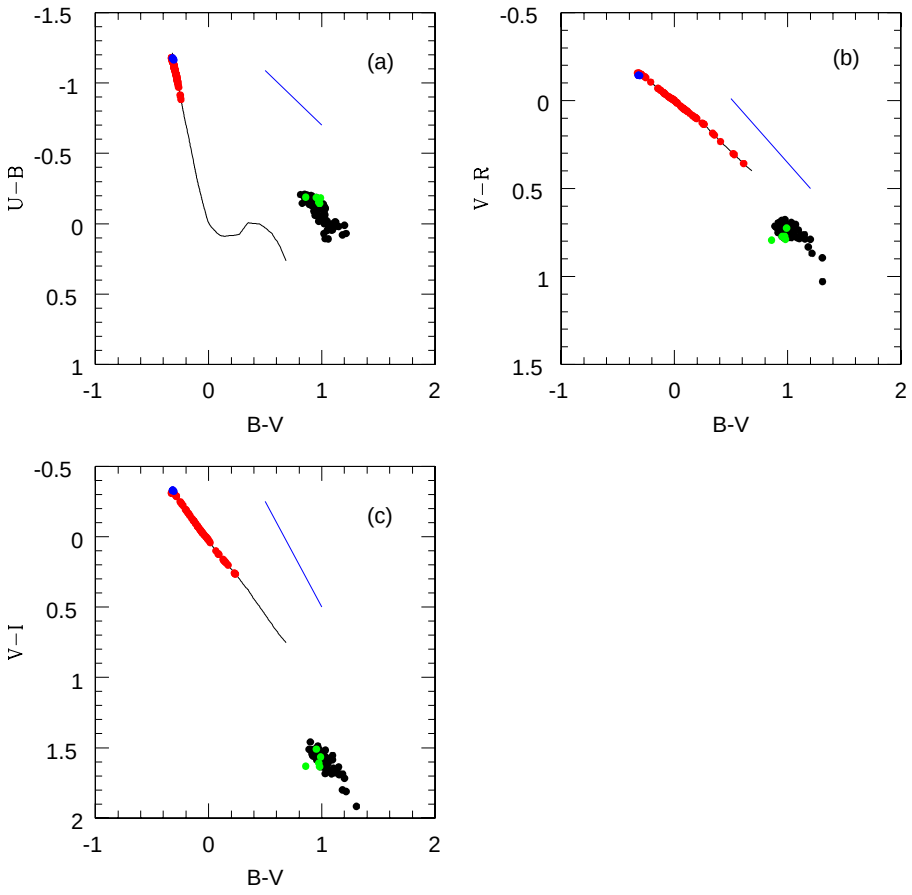


Figure 5.4: Color-color diagrams for the main sequence member stars (black dots). The black lines represent the 1 Myr-old isochrone of Lejeune & Schaerer (2001). The five main sequence stars from Melena et al. (2008) are shown by the blue dots (intrinsic colors) and the green dots (observed colors). The red dots are the members projected onto the isochrone following the reddening vectors (blue lines).

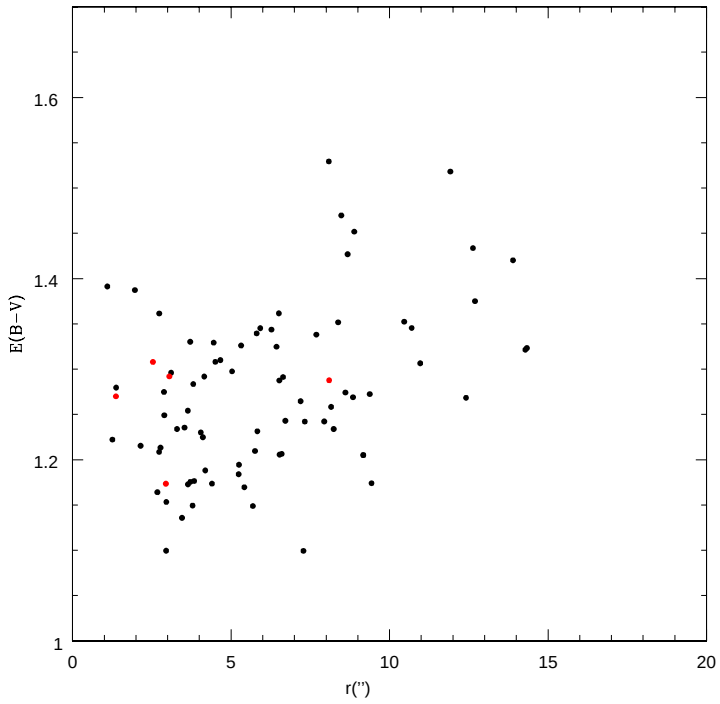


Figure 5.5: The dependence of the stellar reddening on the cluster-centric distance for the selected main sequence members (black dots) and those five main sequence stars (red dots) from Melena et al. (2008).

### 5.3.2 Reddening outside the cluster

Unfortunately, the member stars with HST $UBVRI$ photometry (Appendix table B.1-B.5) are all located inside the cluster (0.7 pc from the cluster center). In order to study the reddening outside the cluster, we select seven MS stars located outside the HD 97950 cluster with available spectral type information from Melnick et al. (1989). The location of these stars is shown in Figure 5.6 (red circles). We take the $UBV$ photometry of these stars from Melnick et al (1989) and the $RI$ photometry from Brandner et al. (1997a). We plot the difference in the $V$ magnitude between Melnick et al. (1989) and Brandner et al. (1997a) in Figure 5.7. With an average difference of 0.02 mag, we consider these two photometries to be in good agreement. The magnitudes of these stars are in Table 5.5.

The color excess and extinction are computed in the same way as for the stars in the cluster (see Section 5.3.1). The effective temperature of these MS stars is taken from Table 1 in Martins et al. (2005) according to their spectral types. The intrinsic $U$, $B$, $V$, $R$, $I$ magnitudes are read from the 1 Myr-old isochrone of Lejeune & Schaerer (2001) in correspondence with their effective temperature. The resulting mean color excesses $E(U-B)$, $E(B-V)$, $E(V-R)$, $E(V-I)$,

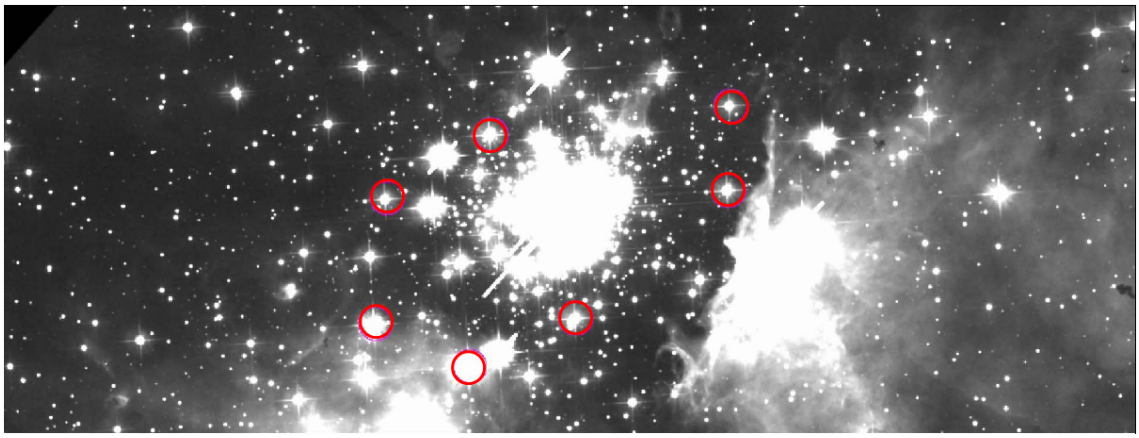

Figure 5.6: Image of the cluster HD 97950 in the *F555W* filter taken by the Wide Field Camera 3. The stars we used to derive the extinction curve outside the cluster are indicated with red circles.

Table 5.5: Photometry of MS stars outside the cluster

| Name | RA | DEC | $V$ | $B-V$ | $U-B$ | $V-I$ | Spectral type |
|---|---|---|---|---|---|---|---|
| Sher27 | $11:15:03.921$ | $-61:15:23.06$ | 15.04 | 1.05 | -0.23 | 1.54 | O7.5V |
| Sher54 | $11:15:03.976$ | $-61:15:35.72$ | 14.57 | 1.08 | -0.22 | 1.59 | O6V |
| Sher53 | $11:15:07.148$ | $-61:15:54.86$ | 14.47 | 1.12 | -0.13 | 1.696 | O8.5V |
| Sher47 | $11:15:09.353$ | $-61:16:02.07$ | 12.72 | 1.14 | -0.17 | 1.695 | O4V |
| Sher19 | $11:15:11.317$ | $-61:15:55.63$ | 13.65 | 1.02 | -0.28 | 1.516 | O3V((f)) |
| Sher21 | $11:15:11.074$ | $-61:15:36.85$ | 14.75 | 1.12 | -0.17 | 1.661 | O6V((f)) |
| Sher24 | $11:15:08.905$ | $-61:15:27.32$ | 14.27 | 1.11 | -0.21 | 1.603 | O6V |

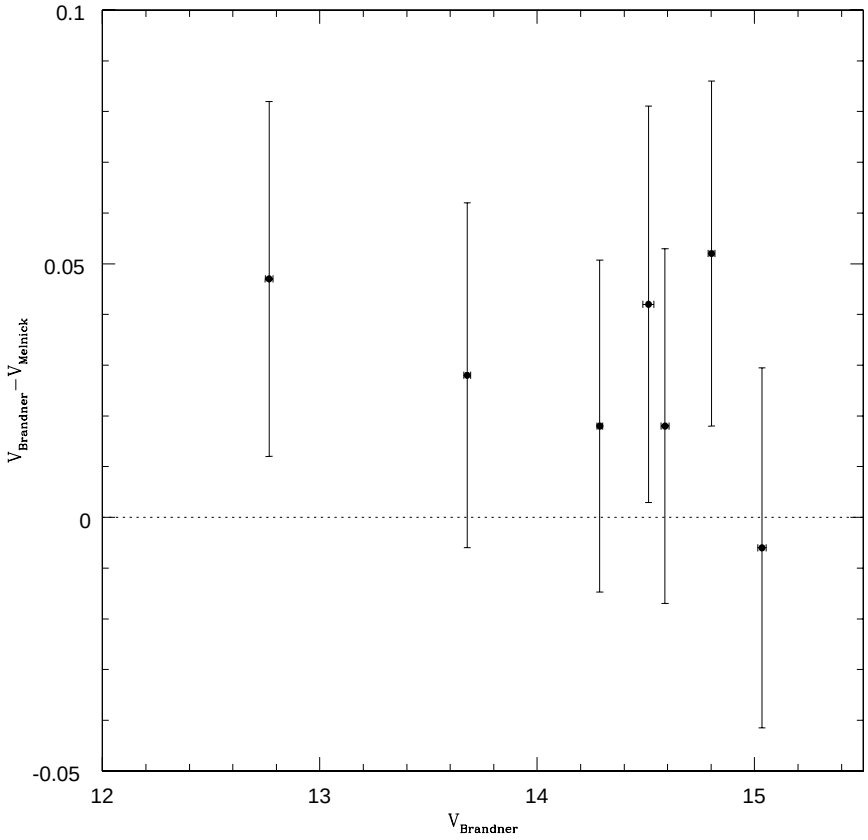


Figure 5.7: Difference in $V$ magnitude between Melnick et al.'s (1989) and Brandner et al.'s (1997) photometry plotted along that the $V$ magnitude of Brandner et al..

and extinctions $A_U$, $A_B$, $A_V$, $A_R$, $A_I$ are presented in Table 5.6. Melena et al. (2008) find that there may be an age spread of up to 4 Myr among stars with masses 20–40 $M_\odot$. We plot these seven MS stars in the CMD (Figure 5.8), correcting each star with its own stellar reddening, with $R_V = 3.55$ and a distance modulus of 14.2 (adopted from Sung & Bessell 2004). All stars except one lie close to the 3 Myr-old isochrone, although the large photometric uncertainties could match them with younger isochrones but not older ones, because some stars are hotter than isochrones older than 3 Myr. The individual stellar reddening is computed again with the 2- and 3 Myr-old isochrones of Lejeune & Schaerer (2001). The mean values of $E(B-V)$ and $R_V$ computed via 1–3 Myr isochrones are shown in Table 5.7. The $E(B-V)$ color excess does not significantly depend on age, while $R_V$ strongly does. Since younger stars are hotter and have stronger radiation fields, they can more efficiently destroy large dust grains and increase the amount of small dust grains. This would result in a smaller value of $R_V$, since $R_V$ is a rough indicator of mean grain

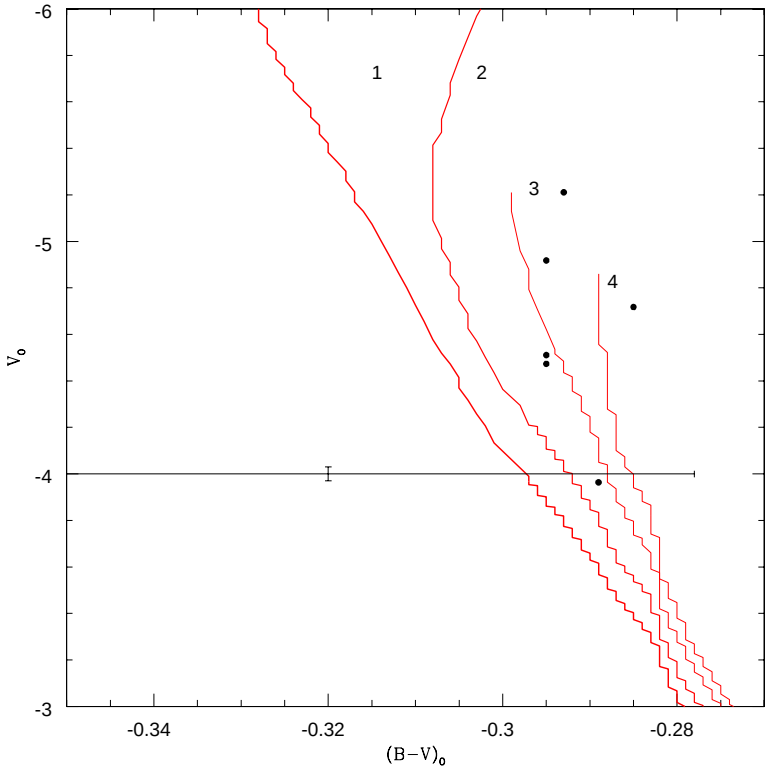


Figure 5.8: CMD of those seven stars outside the cluster HD 97950, with Lejeune & Schaerer (2001) isochrones. From left to right we plot isochrones with ages of 1, 2, 3, 4 Myr. Each star is corrected with its individual stellar reddening. The error bars indicate the photometric uncertainties of the color and magnitude. Since the scale of the $y$ axis ($V_0$) is two orders of magnitude larger the $x$ axis ($(B-V)_0$), the error bar along the $y$ axis looks very small.

size (Section 5.1.1). When the stars become older and cooler, their feedback is weaker and hence large dust grains can survive better. This would give a larger value of $R_V$. However, the small number statistics of the sample stars outside the cluster does not allow us to robustly constrain their $R_V$.

## 5.4 Foreground reddening

In order to constrain the extinction curve in the cluster, we need to subtract the foreground extinction. The foreground extinction may follow a different extinction law than what is valid for the giant HII region NGC 3603.

The foreground stars were selected from the photometry catalog of Pandey et al. (2000). We

Table 5.6: Mean color excess and extinctions for MS member stars outside the cluster (without foreground reddening correction)

| Reddening & extinction | |
|---|---|
| $E(U-B)$ | $0.91 \pm 0.02$ |
| $E(B-V)$ | $1.40 \pm 0.02$ |
| $E(V-R)$ | $0.99 \pm 0.01$ |
| $E(V-I)$ | $1.92 \pm 0.02$ |
| $A_U$ | $6.73 \pm 0.16$ |
| $A_B$ | $5.82 \pm 0.17$ |
| $A_V$ | $4.42 \pm 0.18$ |
| $A_R$ | $3.74 \pm 0.19$ |
| $A_I$ | $3.11 \pm 0.20$ |
| $R_V$ | $3.16 \pm 0.15$ |

Table 5.7: The dependence of the mean $E(B-V)$ and $R_V$ on the age of stars (without foreground reddening correction)

| Age | $\langle E(B-V) \rangle$ | $\langle R_V \rangle$ |
|---|---|---|
| 1 | $1.395 \pm 0.015$ | $3.17 \pm 0.15$ |
| 2 | $1.383 \pm 0.016$ | $3.78 \pm 0.29$ |
| 3 | $1.385 \pm 0.015$ | $5.17 \pm 0.65$ |

excluded member stars, which are labeled "m" in this catalog. The CMD of foreground stars is plotted in Figure 5.9 (red dots). The black dots are member stars in the $UBVRI$ catalog (Appendix Table B.1-B.5). Due to their lower reddening, the foreground stars form a blue diagonal sequence in the CMD (see also Figure 6 in Sung & Bessell 2004). In order to retrieve a clean sample of foreground stars, we only select stars with $(B-V) < 0.85$ mag, which are more than $1\,\sigma$ away (blue dotted lines) from the main sequence (blue solid line). The stellar reddening, $E(B-V)$, of the selected foreground stars is calculated with the reddening-free Q-method from Johnson & Morgan (1953). We calculate $Q$ according to the equation

$$Q = (U-B) - \frac{E(U-B)}{E(B-V)}(B-V)\ . \tag{5.18}$$

The $(U-B)$ and $(B-V)$ colors are taken from Pandey et al. (2000). We assume that the foreground stars follow Fitzpatrick's (1999) reddening law, with $E(U-B)/E(B-V) = 0.737$ ($R_V = 3.1$). The $Q$ value is used to calculate the $E(B-V)$ via equation (7) in Johnson & Morgan (1953):

$$E(B-V) = (B-V) - 0.337Q + 0.009\ . \tag{5.19}$$

The value of $E(B-V)$ that we derived with the Q-method is only $\sim 0.006$ mag different from that of Pandey et al, who assumed $E(U-B)/E(B-V) = 0.71$ (Schmidt-Kaler 1982).

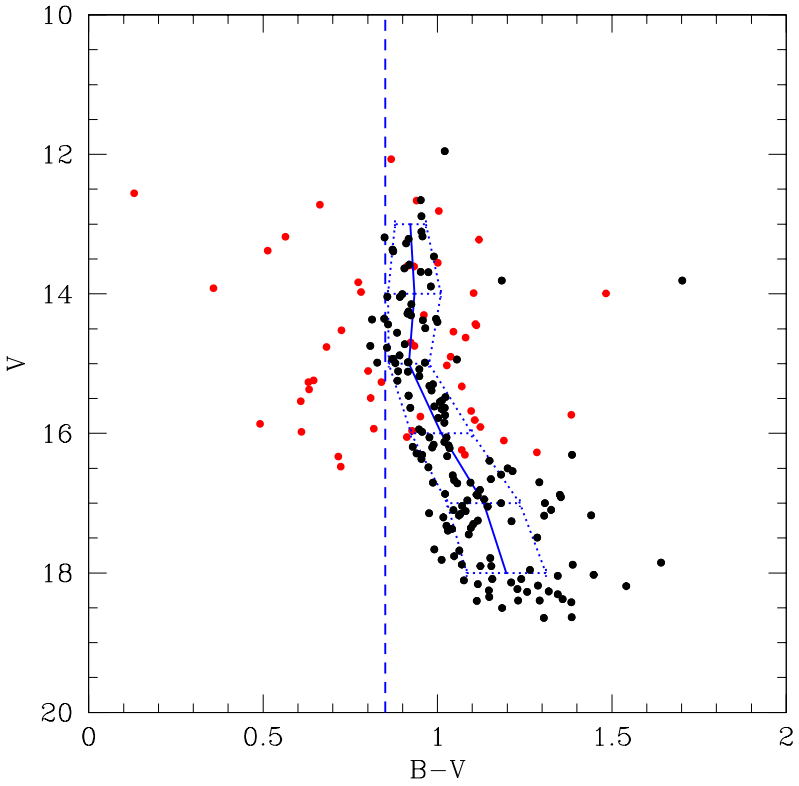


Figure 5.9: CMD of member stars on the PC chip of WFPC2 (black dots) and non-member stars (red dots) from Pandey et al. (2000). Stars bluer than $(B-V)=0.85$ (vertical blue dashed line) are considered as foreground stars. The blue solid line is the mean $(B-V)$ of the member stars (the locus of the MS) computed in magnitude bins, 2 mag in size. The blue dotted lines are $1\,\sigma$ standard deviations within each bin.

We compute the distance of the foreground stars, in order to select stars close to the NGC 3603 giant H II region so that they can better represent the reddening in front of the region. We extrapolate the spectral type of the foreground stars from their $Q$ parameters listed in Table 11 of Johnson & Walker (1953). All the foreground stars are B dwarfs and B giants. With the spectral type, their absolute $V$ magnitude is derived through interpolation of Table 9 in Johnson & Walker (1953). The distance of the foreground stars is derived by correcting their observed magnitudes for extincion ($A_V = 3.1 \times E(B-V)$). We adopt the distance of NGC 3603 from Sung & Bessell (2004), $d = 6.9 \pm 0.6$ kpc. All foreground stars whose distances are in the range $6.3-7.5$ kpc (dashed lines in Figure 5.10) are chosen to estimate the foreground reddening of NGC 3603. There are three stars satisfying this criterion, and they give an average foreground reddening $E(B-V) = 0.824$ mag. If we apply the Cardelli et al. (1989) reddening law instead of the one of Fitzpatrick (1999), we

obtain the same foreground reddening (within 0.004 mag).

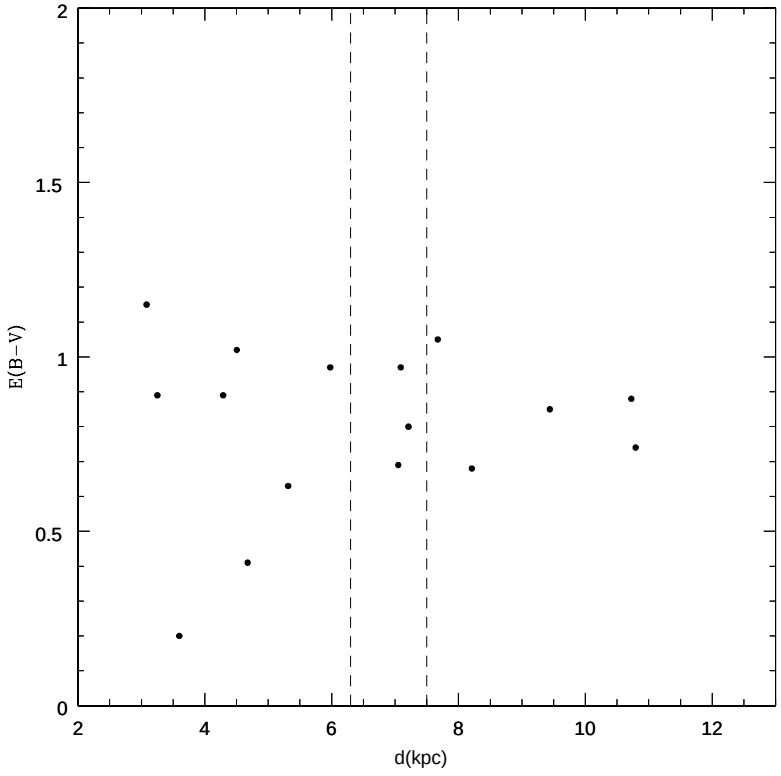


Figure 5.10: Stellar reddening $E(B-V)$ of foreground stars versus their distance. Stars located between the vertical dashed lines are used to compute the foreground reddening of the NGC 3603 giant H II region.

## 5.5 Dust properties in the cluster

The mean ratio of total to selective extinction inside the cluster is $R_V = 3.39 \pm 0.62$ computed from the 1 Myr isochrone. After we correct for foreground reddening, the total to selective extinction ratio increases to $R_V = 3.49 \pm 0.79$. A dispersion of 0.79 mag in $R_V$ among the member stars in the cluster also indicates an uneven, or clumpy distribution of the intracluster dust due to the stellar winds and radiation field of the cluster OB stars (Lebouteiller et al. 2007). Compared to the diffuse Galactic ISM with $R_V = 3.1$, the slightly higher value of $R_V$ inside the cluster may indicate an anomalous extinction curve in the HD 97950 cluster. Abnormal extinction is also found in starburst galaxies ($R_V \sim 4.05$, Calzetti et al. 2000). Pandey et al. (2000) estimated $R_V \sim 4.3$ for the surrounding H II region NGC 3603.

Subtracting the foreground reddening [$E(B-V) = 0.824$ mag], the internal reddening inside and outside the cluster is $E(B-V) \sim 0.4$ mag and $E(B-V) \sim 0.6$ mag respectively, which indicates a very high density of dust in the cluster (a few pc in size) compared with $E(B-V) \sim 0.2$ mag for the diffuse ISM on a scale of a few kpc in the Galactic plane (Draine 2009).

## 5.6 Extinction Curve

In Figure 5.11 and 5.12, we plot the extinction curves for the stars inside and outside the cluster (black lines) already corrected for foreground extinction (Section 5.4), and compare them with Cardelli et al.'s (1989), Fitzpatrick's (1999), and Calzetti et al.'s (2000) extinction laws (red lines). We assume that the foreground extinction follows Fitzpatrick's (1999) extinction law. We normalize the extinction curve to the optical extinction $A_V$, instead of using two colors, because $A_\lambda/A_V$ is more fundamental than $E(\lambda-V)/E(B-V)$ (Cardelli et al. 1989). The grey shaded area in Figure 5.11 shows the scatter associated with $A_\lambda/A_V$ averaged among the MS stars in the cluster. We also plot the error of the mean $A_\lambda/A_V$ in each filter, which is of the size of the points. Since the seven MS stars outside the cluster may show an age spread, we derive their extinctions with isochrones in the age range 1–3 Myr (Lejeune & Schaerer 2001). The extinction curves obtained for the 1-, 2-, 3 My-old isochrones of Lejeune & Schaerer (2001) are shown with black, blue and green lines in Figure 5.12.

When considering the error of the mean $A_\lambda/A_V$, the extinction curve inside the cluster is greyer than the average Galactic extinction laws of Cardelli et al. (1989) and Fitzpatrick (1999). It is closer to the extinction law of Calzetti et al. (2000) in the $UBVRI$ filters. Extinction curves greyer than the average Milky Way extinction law are also observed in starburst galaxies (Calzetti et al. 1994), where internal dust acts as a scattering slab contributing extra light to that naturally emitted by their stars. In this case, the scattering of photons by dust grains reconveys light along the line of sight. This is very different from the usual assumption for the diffuse ISM that the distant dust forms an uniform extinction screen between the star and the observer, through which the absorption and the scattering concur in removing flux from the line of sight. Our measurement of the color excess and extinction of stars in the HD 97950 cluster indicates that dust within this cluster has not been fully destroyed by the winds and radiation of massive stars, and that its distribution is clumpy (Section 5.5). Witt & Gordon (2000) suggest that clumpy dust structure leads to the greyness of the extinction curve. In these conditions, we may assume that the internal dust in the HD 97950 cluster behaves as a scattering slab like the dust in starburst galaxies. This would thus explain why the extinction curve in the cluster is greyer than that of the diffuse ISM in the Milky Way and more similar to the extinction curve of starburst galaxies. Nevertheless, with our own data, we cannot quantify the contribution of scattering and clumpiness to the slope of the extinction curve in the HD 97950 cluster. The extinction curve outside the cluster gets flatter as the age of isochrones increases. However, with such a small number of stars outside the cluster, we cannot constrain the extinction curve well to investigate the dust distribution there.

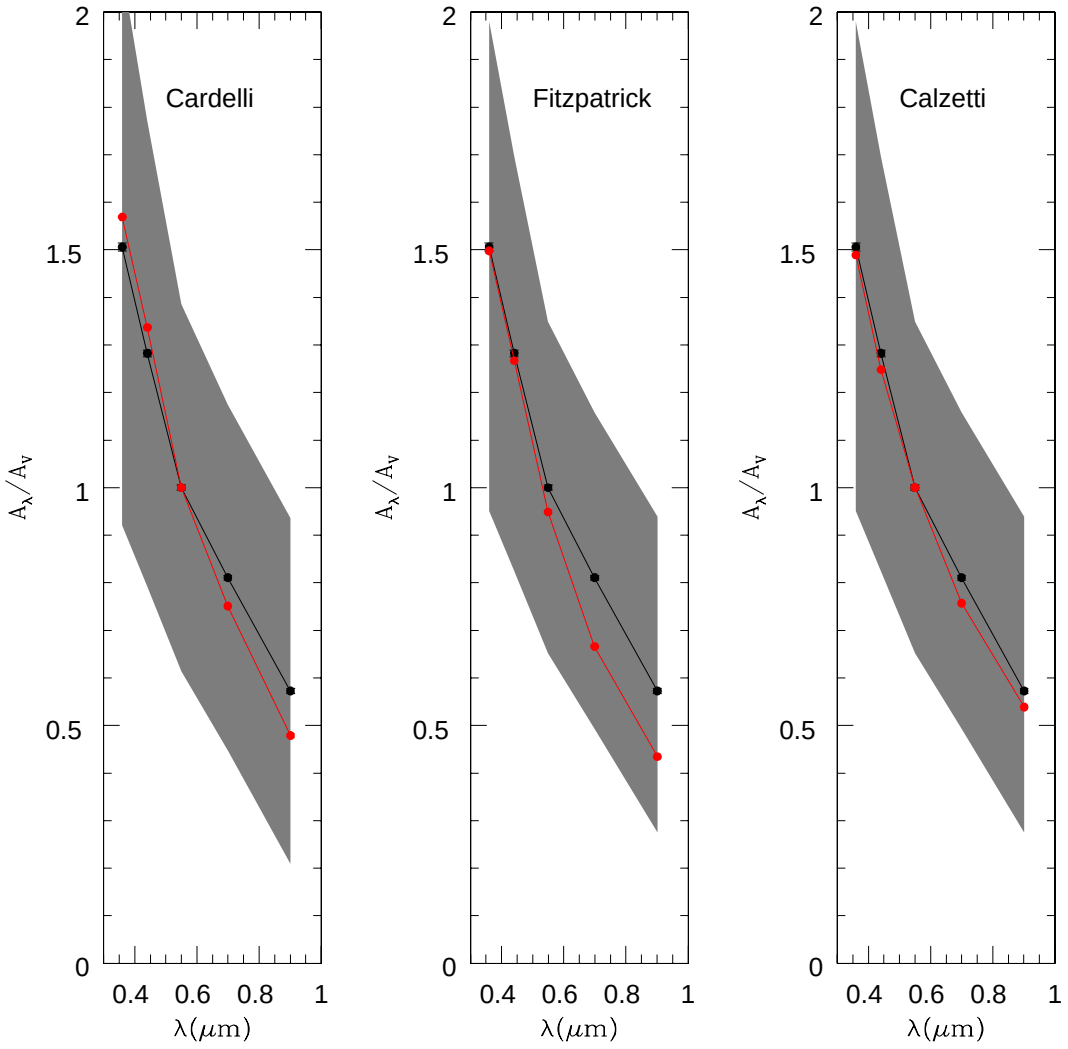


Figure 5.11: Extinction curve for the HD 97950 cluster (black line) already corrected for foreground extinction. The red lines trace Cardelli et al.'s (1989), Fitzpatrick's (1999) and Calzetti et al.'s (2000) extinction laws. The grey shaded area is the standard deviation of the $A_\lambda/A_V$ in each filter. The error bars, which are of the size of the black points and therefore essentially invisible, are the errors on the mean $A_\lambda/A_V$ in each filter.

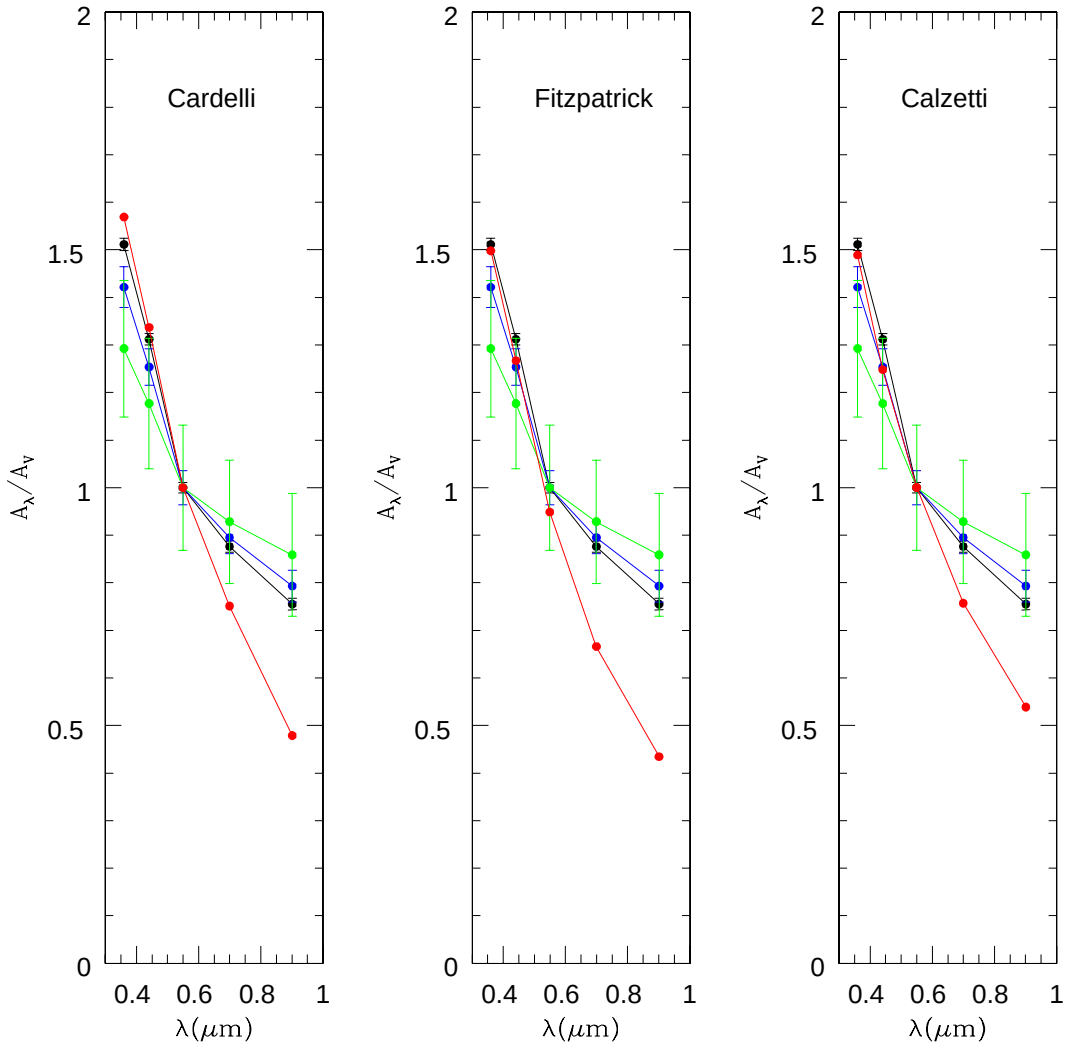


Figure 5.12: Extinction curve for the region outside the HD 97950 cluster, corrected for foreground extinction. The black, blue, and green lines are derived from the 1 Myr, 2 Myr, and 3 Myr isochrones respectively (Lejeune & Schaerer 2001). The red lines trace Cardelli et al.'s (1989), Fitzpatrick's (1999) and Calzetti et al.'s (2000) extinction laws. The error bars are the errors on the mean $A_\lambda/A_V$ in each filter.

## 5.7 The individual stellar reddening in NGC 3603

Significant differential stellar reddening exists in NGC 3603 (Sung & Bessell 2004; Pang et al. 2011). In Section 5.3 we have derived individual stellar reddenings for 78 member stars inside the cluster ($r \leq 0.7$ pc) and only seven stars outside the cluster ($r \sim 1$ pc). To investigate the pattern of differential reddening outside the cluster ($0.7 < r < 4$ pc), we need to derive individual stellar reddenings for a large sample of stars. However, we cannot derive the stellar reddening based on a color-color diagram, because $U$-band photometry is not available for the majority of the stars outside the cluster.

Calzetti et al. (1997) found a linear relation (empirical) between the stellar and the gas reddening [$E(B-V)_* \sim f\,E(B-V)_g$] ($f = 0.44 \pm 0.03$) for starburst galaxies. $f$ is the ratio of the average number of dust clumps in front of the stars to the number in front of the gas. In the star-forming regions, the dust is removed or destroyed by the stellar feedback, e.g., supernovae explosions and stellar winds of massive stars. Consequently, the covering factor of the dust for the star is smaller than for the gas, which results in a smaller value of the stellar reddening than the gas reddening. Following Calzetti et al. (1997), we aim at establishing a relation between the stellar and the gas reddening in NGC 3603. In the two-dimensional map of gas reddening (Chapter 4, Figure 4.1), the cluster is masked out due to saturation of the bright stars. Though the seven stars outside the cluster show an age spread (Section 5.3.2), their stellar reddening $E(B-V)$ does not depend significantly on age (Table 5.7). Therefore we use these seven stars to derive a relation between the stellar and the gas reddening. We take an aperture of 35 pixels around the seven stars in the $E(B-V)_g$ map, and measure the mode value of their $E(B-V)_g$ to represent the gas reddening at those positions. The aperture is 20 times the full width at half maximum (FWHM, 1.75 pixels) of the *F139M* image taken by the Wide Field Camera 3 (WFC3) (see Table 4.2 in Chapter 4), which is the reference image of the reddening map, to avoid local fluctuations. We increase the aperture size to 35×FWHM for the star Sher 24, because it is located at the border of the cluster, which is masked out.

The stellar reddening obtained for these seven stars with a 1 Myr-old isochrone (Lejeune & Schaerer 2001) is plotted as a function of their gas reddening in Figure 5.13. The uncertainty of their stellar reddening originates from the following sources:
1) The photometric uncertainty (Melnick et al. 1989) translates into $\sigma_{E(B-V)_*} = 0.03$ mag.
2) The uncertainty of the spectral types and luminosity classes published by Melena et al. (2008). We estimate the stellar reddening again by changing the spectral subtype by 2 and the luminosity class by 1. This introduces an average uncertainty of 0.03 mag of the $E(B-V)_*$.
3) There is a possible age spread as large as 3 Myr among these seven stars outside the cluster (Figure 5.8). If we use isochrones of different age up to a maximum of 3 Myr to derive the stellar reddening, there will be an average 0.02 mag difference in the $E(B-V)_*$ (Table 5.7).
The uncertainty of the stellar reddening for each star is a combination of the above uncertainties:

$$\sigma^2_{E(B-V)} = \sigma^2_{Melnick} + \sigma^2_{spectraltype} + \sigma^2_{age} \tag{5.20}$$

The red line in Figure 5.13 is the linear least-squares fit to the data points. The resulting relation

between the stellar and the gas reddening for our data is:

$$E(B-V)_* = 0.293\,E(B-V)_g + 0.992 \tag{5.21}$$

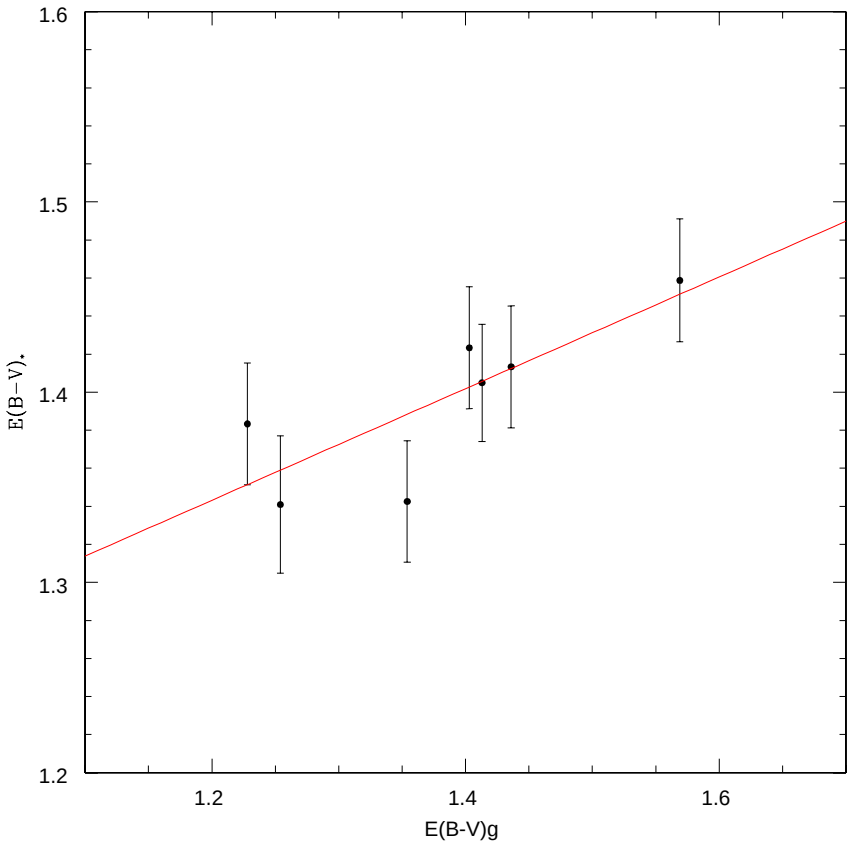


Figure 5.13: The dependence of stellar reddening $E(B-V)_*$ on the gas reddening $E(B-V)_g$. The red line is the linear least-squares fit to the black dots weighted by the errors. The stellar reddening is derived from the 1 Myr-old isochrone of Lejeune & Schaerer (2001).

We apply this relation to derive the stellar reddening for 7748 stars in the field of view of the WFC3 from the gas reddening measured at their positions. Figure 5.14 shows the dependence of the $E(B-V)_*$ of these 7748 stars on the their cluster-centric distances, and confirms the prominent differential reddening previously found in NGC 3603. The stellar reddening increases from 1.35 mag at $r = 0.26'$ (0.52 pc) to 1.7 mag at $r = 1.6'$ (3.2 pc), which agrees very well with the result of Sung & Bessell (2004). At a radius $r > 1'$ (2 pc), there are two separate sequences. The ascending branch corresponds to the north-south direction in the gas reddening map, along

where the molecular pillars and dense clouds lie. The decreasing branch is related to the east-west direction, where the density of gas and dust is much lower.

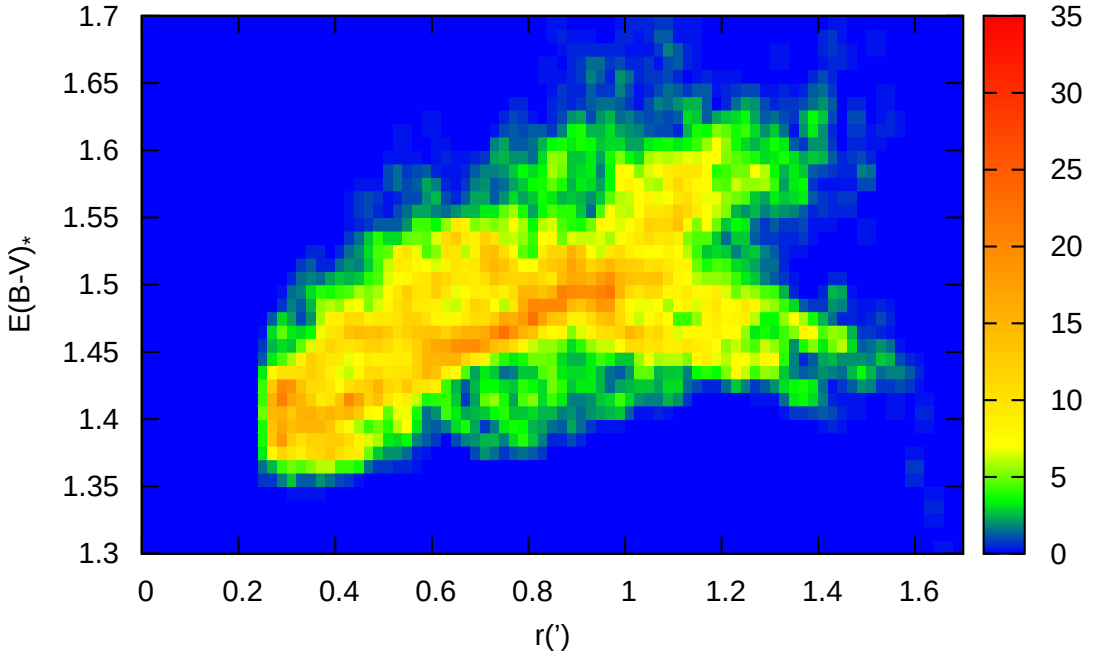


Figure 5.14: The dependence of the stellar reddening $E(B-V)_*$ for 7748 stars (WFC3) on their cluster-centric distances. The number of stars is indicated by the color bar. The innermost region ($0 < r < 0.26'$) was not considered since it was masked out in the gas reddening map due to saturation of bright stars.

## 5.8 Summary

We analyze the $UBVRI$ photometry obtained with HRC/ACS and WFPC2 to estimate individual stellar reddenings and extinctions for stars in NGC 3603. The main results of our analysis are:

1. We select foreground stars from the $UBV$ photometry of Pandey et al. (2000). The reddening of foreground stars is derived with the Q-method developed by Johnson & Morgan (1953). We assumed that the foreground stars follow Fitzpatrick's (1999) reddening law. The average foreground reddening of NGC 3603 is $E(B-V) \sim 0.824$ mag, and is estimated with three foreground stars located between 6.3–7.5 kpc.

2. We derive stellar reddenings for 78 individual MS member stars inside the HD 97950 cluster ($r < 0.7$ pc) and seven MS stars outside. The mean reddening inside the cluster is $E(B-V) = 1.24 \pm 0.09$ mag and increases to $1.40 \pm 0.02$ mag outside (without foreground reddening correction). Anomalous extinction is found in the cluster, with $R_V = 3.39 \pm 0.62$

($R_V = 3.49 \pm 0.79$ when corrected for foreground extinction).

3. The extinction curve in the $UBVRI$ filters corrected for foreground reddening, inside the cluster, is greyer than the average Galactic extinction laws of Cardelli et al. (1989) and Fitzpatrick et al. (1999). It is close to the extinction law for starburst galaxies (Calzetti et al. 2000), indicating that the dust in the HD 97950 cluster has similar properties to the dust in starburst galaxies. The photons scattering due to internal dust inside the cluster and the clumpiness of the dust might contribute to the greyness of this extinction curve. The extinction curve outside the cluster is based on only seven stars, and depends on age as it becomes greyer at older ages ($R_V$ increases from 3.2 to 5.2 in the age range 1–3 Myr). Unfortunately, with our limited data, we cannot characterize better the properties of the dust in NGC 3603.

4. We establish a linear relation between the stellar and the gas reddening: $E(B-V)_* = 0.293\,E(B-V)_g + 0.992$. The individual stellar reddening for 7748 stars is computed (WFC3) by converting their gas reddening as read from the map of $E(B-V)_g$ (Chapter 4) at their positions. Prominent differential reddening is found among these stars. The stellar reddening is lower, ranging from 1.35 mag at 0.52 pc from the cluster to 1.7 mag at 3.2 pc along the north-south direction of NGC 3603. The stellar reddening decreases at cluster-centric distances larger than 2 pc along the east-west direction. This differential reddening pattern in NGC 3603 reflects the local inhomogeneous distribution of dust in the ISM of NGC 3603.

# 6 Summary and prospects

What is a summary:
*Now a summary of the things of which we are speaking is, we have such a one high priest who has sat down on the right hand of the throne of the greatness in the heavens. (Hebrews 8:1)*
What is a prospect:
*The prospect of the righteous is joy. (Proverbs 10:2)*

## 6.1 Main Results

In this thesis, we carried out a comprehensive study of the young massive star cluster HD 97950 located in the giant H II region NGC 3603. We are going to summarize our main results in this chapter.

(1) **Membership of stars**

We analyzed HST/WFPC2 imaging of the HD 97950 cluster in the *F555W* (*F547W*) and *F814W* filters obtained in 1997 and in 2007. These two-epoch data allow us to derive relative proper motions of stars to determine their membership via two methods: 1) a relative proper motion cut and 2) a two-Gaussian model fitting over the relative proper motion distribution. The number of determined member stars of these two methods agrees well with each other when we consider stars as members with member probability larger than 70%. We found 411 members on the PC chip and 124 on the WFC chips from the second method. The contamination by foreground field stars (member probability less than 70%) is 7% on the PC chip, and 25.3% the WFC chips.

(2) **The fate of the cluster HD 97950**

We calculated the velocity dispersion based on the relative proper motions of the member stars of the cluster ($\sigma_c = 10.42 \pm 0.62$ km s$^{-1}$) and the cluster's virial mass ($1.7 \times 10^5$ M$_\odot$). We estimate the total luminosity of the cluster HD 97950 to be $L_V \sim 9.4 \times 10^6$ L$_\odot$, which is dominated by three WN stars. The ratio of the total luminosity over the dynamical mass is $L_V/M_{dyn} = 9.4 \times 10^6$ L$_\odot$/$1.7 \times 10^5$ M$_\odot$ = 55 M$_\odot$/L$_\odot$, corresponding to a SFE of about 50 percent. This may suggest that the HD 97950 cluster can survive after the gas expulsion and is capable to re-establish equilibrium (Goodwin & Bastian 2006).

(3) **Age spread**

Based on the relative proper-motion-selected sample of probable cluster members, we find an approximate age spread of up to 3 Myr among pre-main-sequence (PMS) stars, indicated by non-accreting isochrones (Siess 2000). On the other hand, the main sequence (MS) stars are consistent with an age of 1 Myr (Lejeune & Schaerer 2001). Based on our data, it remains unclear whether there is a real age spread in the cluster.

(4) **The mass function and mass segregation**

We confirm the mass segregation in the HD 97950 cluster as found in previous studies. The mass function varies radially. It is flat and top-heavy near the center of the cluster and becomes steeper at larger radii. The global slope of the incompleteness-corrected mass function of member stars on the PC and WFC chips is $\Gamma = -0.89 \pm 0.18$. The slope of mass function varies from $-0.26 \pm 0.32$ within $5''$ from the cluster center to $-1.49 \pm 0.33$ in an annulus of $15''$ – $20''$ around the center. We apply the $\Lambda$ minimum spanning tree ($\Lambda$-MST) technique to quantify the mass segregation in HD 97950. We find the cluster to be mass-segregated down to 30 M$_\odot$. The more massive the star, the higher degree of segregation, suggesting a likely dynamical origin for mass segregation in HD 97950.

(5) **A two-dimensional gas reddening map**

We derived a two-dimensional map of the gas reddening covering an area of 4.9 pc $\times$ 4.3 pc around the HD 97950 cluster from HST/WFC3 images, which were taken in the UVIS *F555W*, *F656N*, and *F814W* filters, and the IR *F127M*, *F128N*, and *F139M* filters. The gas reddening measured by the H$\alpha$/Pa$\beta$ flux ratio shows significant spatial variations. The median value of the gas reddening within the central cavity ($r < 1$ pc) is $E(B-V)_{\rm g} = 1.51 \pm 0.04$ mag. Outside the cluster (at $r > 1$ pc), the gas reddening is seen to increase with cluster-centric distance towards both north and south, reaching a value of about 2.2 mag at $r = 2$ pc from the cluster center. The radial dependence of $E(B-V)_{\rm g}$ in the east and west directions of the cluster appears rather flat, with $E(B-V)_{\rm g}$ values in the range of 1.55 to 1.7 mag. We interpret the variations of $E(B-V)_{\rm g}$ as the result of stellar radiation and stellar winds interacting with an inhomogeneous dusty local interstellar medium (ISM) whose density varies spatially.

(6) **Stellar Reddenings in NGC 3603**

We made use of the $UBVRI$ photometry obtained with HRC/ACS and WFPC2 to estimate individual stellar reddenings of stars in NGC 3603. Stellar reddenings are derived for 78 individual MS member stars inside the HD 97950 cluster and seven MS stars outside. The mean reddening increases from $E(B-V) = 1.24 \pm 0.09$ mag inside the cluster to $1.40 \pm 0.02$ mag outside (without foreground reddening correction). We estimate the foreground reddening of the cluster via the Q-method to be $E(B-V) \sim 0.824$ mag. After correcting for foreground reddening, anomalous

extinction is found in the cluster, with a total to selective extinction ratio of $R_V = 3.49 \pm 0.79$.

(7) **Extinction Curve in the HD 97950 cluster**

The extinction curve in the $UBVRI$ filters corrected for foreground reddening, inside the cluster, is greyer than the average Galactic extinction laws of Cardelli et al. (1989) and Fitzpatrick et al. (1999), but close to the extinction law for starburst galaxies (Calzetti et al. 2000). This indicates that the dust in the HD 97950 cluster has similar properties to the dust in starburst galaxies. The photon scattering due to internal dust inside the cluster and the clumpiness of the dust might contribute to the greyness of this extinction curve.

(8) **Differential Stellar Reddening in NGC 3603**

We established a linear relation between the stellar and the gas reddening: $E(B-V)_* = 0.293\,E(B-V)_g + 0.992$. Individual stellar reddenings of more than 7000 stars in the WFC3 field of view are derived by converting the gas reddening (at the stars' positions) according to this relation. Significant differential stellar reddening exists in the giant H II region NGC 3603, with $E(B-V)$ increasing from ∼1.35 mag at 0.52 pc around the HD 97950 cluster to 1.7 mag at 3.2 pc. This differential reddening pattern in NGC 3603 reflects the local inhomogeneous distribution of dust in the ISM.

## 6.2 Prospects

We are going to determine the age among PMS stars in the HD 97950 cluster with correction for their individual stellar reddenings using very deep photometric data from WFC3. If the claimed 10-20 Myr age spread is true (Beccari et al. 2010), we plan to apply the Λ-MST method to the age of the PMS stars, and study whether there is an age gradient in the outskirts of the HD 97950 cluster with respect to the cluster core. We aim at finding out the type of star formation triggering an age gradient with higher mass and younger stars in the center of the HD 97950 cluster, and lower mass and older stars in the outskirts. One option is that two separate, unconnected star formation events might have taken place.

## 6.3 Look into the future

The method used to study the HD 97950 cluster can be extended to other young star clusters (YSCs) in our own and in nearby galaxies, or even in galaxies further away. Our closest neighboring dwarf galaxy, the Large Magellanic Cloud (LMC), contains many YSCs. Mackey & Gilmore (2003) compiled a catalog of 53 rich star clusters, among which about 15 clusters with ages in the range of 3-100 Myr. Moreover, YSCs whose mass reaches an order of $10^6\,\mathrm{M}_\odot$ are found in starburst galaxies (e.g., M82-F, McCrady et al. 2005; NGC 1569-B, Larson et al. 2008). A lot of these YSCs are found to be mass-segregated. For example, two LMC clusters, NGC 1805 (10 Myr; $10^{3.52}\,\mathrm{M}_\odot$) and NGC 1818 (25 Myr; $10^{4.13}\,\mathrm{M}_\odot$), are segregated down to about $1.6\,\mathrm{M}_\odot$ (de Grijs & Gilmore 2003). In the partially resolved star cluster NGC 1569-B (about 20 Myr) located in nearby starburst galaxy NGC 1569, an evidence of mass segregation are found by observations

that the $(V - I)$ color decreases with radius by about 0.1–0.2 mag (Larsen et al. 2008; Gaburov & Gieles 2008).

A few of the segregated YSCs in the Milky Way (e.g., NGC 6611, NGC 2244, NGC 6530 etc.) even have multi-epoch data (ESO/VLT) from which proper motions can be derived. A kinematic study of a larger sample of YSCs helps us better understand whether dynamical segregation is the dominant mode among YSCs.

As the relaxation time is proportional to the inverse of the cluster mass, we expect the dynamical mass segregation to be dominant in more massive clusters at a given age. The older clusters also undergo longer dynamical evolution, this exhibit a larger degree of mass segregation. Using samples of YSCs with a large range of age and mass, we can find out the age and the mass scale at which dynamical mass segregation kicks in and establish 1) the relation between cluster age and the segregated mass that determined by the $\Lambda$-MST method; 2) the relation between the cluster mass and segregated mass at a given age, which reveals how the cluster mass affects the time scale of dynamical segregation in the cluster.

Furthermore, since the majority of YSCs is still surrounded by gas and dust, we can investigate the changes of their extinction curves depending on age. How will the dust properties be changed from being in the formidable environment (super star clusters in starburst galaxies) to being in a dwarf galaxy with lower star formation rate (YSCs in the LMC)? These questions will be answered with a systematic study on samples of YSCs with different age, mass, and ISM environment.

# A

# The fate of the young HD 97950 cluster from relative proper motions

Table A.1: The $VI$ photometry and relative proper motions of the member stars on the PC chip of WFPC2 (I).

| No. | $X$ | $Y$ | $V$ | $I$ | $r(''$) | $\mu_x$(mas/yr) | $\mu_y$(mas/yr) |
|---|---|---|---|---|---|---|---|
| 1 | 430.97 | 515.83 | 15.31 | 13.79 | 4.16 | -0.32063 | 0.42928 |
| 2 | 707.94 | 502.85 | 15.24 | 13.60 | 13.74 | -0.37145 | -0.52531 |
| 3 | 79.76 | 548.09 | 15.25 | 13.70 | 16.59 | -0.06742 | 0.05419 |
| 4 | 385.40 | 354.77 | 15.10 | 13.60 | 3.63 | 0.05419 | 0.22629 |
| 5 | 444.91 | 284.16 | 15.25 | 13.71 | 6.64 | 0.14993 | -0.08465 |
| 6 | 279.54 | 568.62 | 15.45 | 13.93 | 9.17 | -0.04913 | 0.32400 |
| 7 | 557.71 | 456.41 | 15.31 | 13.77 | 6.52 | -0.06514 | 0.08690 |
| 8 | 407.94 | 298.04 | 15.43 | 13.88 | 5.92 | 0.18306 | 0.26771 |
| 9 | 516.83 | 420.49 | 15.60 | 14.01 | 4.50 | -0.25409 | 0.29719 |
| 10 | 279.54 | 568.62 | 15.42 | 13.93 | 9.17 | -0.04913 | 0.32400 |
| 11 | 456.94 | 492.47 | 15.49 | 14.01 | 3.51 | 0.12929 | 0.45399 |
| 12 | 544.61 | 364.36 | 15.47 | 13.95 | 6.43 | 0.21759 | 0.35839 |
| 13 | 635.45 | 511.55 | 15.71 | 14.15 | 10.70 | -0.19092 | 0.01979 |
| 14 | 617.10 | 474.51 | 15.57 | 13.97 | 9.37 | -0.01656 | -0.18250 |
| 15 | 529.95 | 486.75 | 15.62 | 14.07 | 5.81 | -0.03313 | -0.06219 |

$X$ and $Y$ are star positions in pixel coordinates on the PC chip of WFPC2 based on the 2007 data. $r$ is the cluster-centric distance in arcsecond. $\mu_x$ and $\mu_y$ are relative proper motions' components along the $x$ and $y$ directions of (PC) pixel coordinates (2007). $V$ and $I$ magnitudes are from the 1997 WFPC2 data.

Table A.2: The $VI$ photometry and relative proper motions of the member stars on the PC chip of WFPC2 (II).

| No. | $X$ | $Y$ | $V$ | $I$ | $r(''$) | $\mu_x$(mas/yr) | $\mu_y$(mas/yr) |
|---|---|---|---|---|---|---|---|
| 16 | 307.54 | 535.20 | 15.57 | 14.14 | 7.18 | 0.23008 | 0.34927 |
| 17 | 621.77 | 258.26 | 16.07 | 14.27 | 12.11 | 0.14319 | 0.10486 |
| 18 | 111.78 | 470.14 | 15.69 | 14.19 | 14.28 | 0.17895 | 0.37945 |
| 19 | 401.23 | 486.53 | 15.90 | 14.45 | 2.89 | 0.21113 | 0.12059 |
| 20 | 113.38 | 486.10 | 15.80 | 14.23 | 14.33 | 0.07268 | 0.13336 |
| 21 | 460.79 | 473.05 | 16.02 | 14.53 | 2.88 | -0.31459 | -0.09939 |
| 22 | 512.66 | 392.70 | 16.41 | 14.26 | 4.57 | -0.03173 | 0.12227 |
| 23 | 327.54 | 484.04 | 16.08 | 14.58 | 4.98 | -0.86166 | 0.29901 |
| 24 | 445.04 | 601.72 | 15.91 | 14.40 | 8.16 | 0.00969 | 0.46382 |
| 25 | 284.47 | 448.25 | 16.00 | 14.49 | 6.28 | -0.31094 | 0.21296 |
| 26 | 273.67 | 439.32 | 16.21 | 14.42 | 6.72 | -0.49077 | 0.22405 |
| 27 | 444.34 | 510.54 | 16.32 | 14.81 | 4.05 | -0.63803 | 0.38001 |
| 28 | 78.40 | 300.69 | 16.16 | 14.53 | 16.70 | -0.02625 | 0.09012 |
| 29 | 391.77 | 478.92 | 16.16 | 14.68 | 2.73 | 0.16284 | 0.18951 |
| 30 | 350.35 | 341.22 | 16.07 | 14.52 | 5.03 | 0.04183 | 0.12831 |
| 31 | 243.53 | 570.81 | 16.15 | 14.65 | 10.46 | -0.03720 | 0.16790 |
| 32 | 206.53 | 509.92 | 16.12 | 14.64 | 10.51 | -0.29852 | 0.14431 |
| 33 | 464.23 | 466.28 | 16.23 | 14.73 | 2.77 | -0.22952 | 0.42044 |
| 34 | 464.23 | 238.36 | 16.34 | 14.76 | 8.89 | 0.17337 | 0.26125 |
| 35 | 286.48 | 587.12 | 16.57 | 14.70 | 9.59 | -0.10023 | 0.65642 |
| 36 | 504.90 | 503.73 | 16.24 | 14.71 | 5.32 | -0.16242 | -0.06429 |
| 37 | 489.07 | 675.78 | 16.46 | 14.68 | 11.92 | 0.34127 | 0.29508 |
| 38 | 230.44 | 136.61 | 16.60 | 14.86 | 15.90 | 0.55240 | 0.11455 |
| 39 | 572.25 | 340.07 | 16.47 | 14.78 | 8.08 | -0.14235 | 0.53303 |
| 40 | 522.21 | 564.68 | 16.46 | 14.83 | 7.94 | 0.23612 | 0.08142 |
| 41 | 210.33 | 156.48 | 16.70 | 14.97 | 15.69 | 0.51471 | 0.24840 |
| 42 | 317.97 | 375.49 | 16.66 | 14.77 | 5.21 | -0.11638 | 0.59072 |
| 43 | 502.33 | 376.68 | 16.56 | 14.98 | 4.45 | 0.15512 | 0.13856 |
| 44 | 766.53 | 443.54 | 16.67 | 15.03 | 16.00 | -0.15695 | -0.36850 |
| 45 | 401.53 | 512.21 | 17.44 | 15.32 | 4.04 | -0.69910 | 0.00449 |
| 46 | 451.09 | 399.54 | 17.06 | 15.25 | 1.91 | -0.17351 | -0.77827 |
| 47 | 505.32 | 258.49 | 16.77 | 15.14 | 8.67 | -0.03580 | 0.17239 |
| 48 | 376.85 | 433.00 | 16.64 | 15.13 | 1.97 | -0.19738 | 0.21984 |
| 49 | 339.71 | 440.82 | 16.63 | 15.10 | 3.72 | -0.28750 | 0.11273 |
| 50 | 213.40 | 397.73 | 16.88 | 14.83 | 9.55 | -0.29122 | 0.39138 |
| 51 | 250.75 | 313.46 | 16.59 | 14.94 | 9.32 | 0.06071 | 0.35881 |
| 52 | 508.77 | 415.49 | 17.03 | 15.40 | 4.15 | -0.29522 | 0.06429 |
| 53 | 553.60 | 460.42 | 16.83 | 15.19 | 6.38 | -0.00590 | 0.27332 |
| 54 | 476.66 | 441.44 | 17.09 | 15.50 | 2.74 | -0.01474 | 0.68716 |
| 55 | 458.81 | 631.43 | 16.98 | 14.97 | 9.61 | 0.32807 | 0.41946 |

Table A.3: The $VI$ photometry and relative proper motions of the member stars on the PC chip of WFPC2 (III).

| No. | $X$ | $Y$ | $V$ | $I$ | $r(''$) | $\mu_x$(mas/yr) | $\mu_y$(mas/yr) |
|---|---|---|---|---|---|---|---|
| 56 | 182.45 | 455.58 | 16.64 | 15.07 | 10.97 | -0.31193 | -0.01741 |
| 57 | 574.46 | 582.99 | 16.84 | 15.18 | 10.15 | -0.37426 | 0.04296 |
| 58 | 381.50 | 256.05 | 16.89 | 15.22 | 8.02 | -0.35278 | 0.11638 |
| 59 | 359.85 | 620.92 | 17.49 | 15.35 | 9.36 | 0.45217 | 0.30771 |
| 60 | 282.83 | 503.05 | 16.65 | 15.18 | 7.20 | -0.43476 | -0.05377 |
| 61 | 390.49 | 543.12 | 17.46 | 15.56 | 5.54 | -0.19962 | -0.47954 |
| 62 | 379.32 | 246.33 | 16.95 | 15.19 | 8.48 | -0.00365 | 0.18355 |
| 63 | 486.73 | 425.43 | 16.85 | 15.24 | 3.11 | -0.02808 | 0.38450 |
| 64 | 484.66 | 300.92 | 16.94 | 15.29 | 6.50 | -0.21254 | 0.28203 |
| 65 | 435.64 | 515.56 | 17.09 | 15.55 | 4.18 | 0.10908 | 0.26897 |
| 66 | 558.53 | 473.92 | 17.09 | 15.49 | 6.78 | 0.10585 | 0.25030 |
| 67 | 244.54 | 139.89 | 17.17 | 15.48 | 15.43 | 0.32842 | 0.10809 |
| 68 | 146.55 | 393.10 | 16.92 | 15.29 | 12.63 | -0.06345 | 0.14768 |
| 69 | 540.35 | 668.07 | 17.15 | 15.28 | 12.44 | -0.43799 | 0.19681 |
| 70 | 411.99 | 403.55 | 17.19 | 15.62 | 1.09 | 0.18250 | 0.24651 |
| 71 | 519.81 | 297.07 | 17.20 | 15.35 | 7.53 | -0.07833 | 0.67607 |
| 72 | 320.04 | 447.85 | 17.05 | 15.51 | 4.67 | -0.12971 | 0.48403 |
| 73 | 299.46 | 703.65 | 17.26 | 15.60 | 13.90 | 0.86208 | 0.70668 |
| 74 | 250.97 | 496.05 | 16.99 | 15.45 | 8.38 | -0.08605 | -0.29115 |
| 75 | 150.01 | 446.89 | 17.11 | 15.59 | 12.42 | -0.32982 | -0.09012 |
| 76 | 356.35 | 271.34 | 17.13 | 15.53 | 7.69 | 0.04562 | 0.38310 |
| 77 | 572.93 | 791.49 | 17.39 | 15.63 | 18.23 | -0.84397 | 0.79428 |
| 78 | 270.57 | 441.35 | 17.54 | 15.95 | 6.87 | -0.44950 | 0.48445 |
| 79 | 473.68 | 382.05 | 17.30 | 15.69 | 3.23 | 0.10809 | 0.17056 |
| 80 | 752.85 | 244.18 | 17.19 | 15.56 | 17.49 | 0.75441 | 0.37854 |
| 81 | 314.85 | 525.04 | 17.31 | 15.66 | 6.61 | -0.27781 | 0.16228 |
| 82 | 604.62 | 451.54 | 17.30 | 15.70 | 8.61 | 0.45427 | -0.31277 |
| 83 | 568.64 | 233.36 | 17.62 | 15.64 | 11.22 | -0.22854 | -0.11273 |
| 84 | 521.79 | 476.31 | 17.52 | 15.74 | 5.25 | -0.35292 | -0.29213 |
| 85 | 555.38 | 670.06 | 17.41 | 15.60 | 12.85 | -0.53317 | -0.09518 |
| 86 | 151.26 | 451.30 | 17.66 | 15.76 | 12.38 | 0.07173 | 0.03130 |
| 87 | 451.83 | 568.40 | 17.26 | 15.70 | 6.71 | -0.27374 | -0.28890 |
| 88 | 511.70 | 159.67 | 17.68 | 15.83 | 12.98 | 0.21998 | -0.22033 |
| 89 | 604.04 | 218.05 | 17.48 | 15.84 | 12.81 | 0.00646 | 0.44711 |
| 90 | 449.27 | 215.57 | 17.39 | 15.71 | 9.79 | 0.19780 | 0.24609 |
| 91 | 670.74 | 386.80 | 17.48 | 15.85 | 11.71 | -0.09939 | 0.01334 |
| 92 | 193.08 | 584.60 | 17.37 | 15.87 | 12.70 | 0.01699 | 0.09153 |
| 93 | 671.99 | 184.11 | 17.67 | 15.76 | 16.10 | 0.32175 | 0.03629 |
| 94 | 467.53 | 605.53 | 17.62 | 15.99 | 8.54 | 0.41497 | 0.25325 |
| 95 | 557.67 | 470.34 | 17.81 | 16.13 | 6.69 | 0.36920 | 0.30266 |

Table A.4: The $VI$ photometry and relative proper motions of the member stars on the PC chip of WFPC2 (IV).

| No. | $X$ | $Y$ | $V$ | $I$ | $r(''$) | $\mu_x$(mas/yr) | $\mu_y$(mas/yr) |
|---|---|---|---|---|---|---|---|
| 96 | 543.90 | 442.44 | 17.80 | 16.11 | 5.79 | -0.08928 | -0.23135 |
| 97 | 517.16 | 241.73 | 17.58 | 15.97 | 9.61 | -0.02555 | 0.13343 |
| 98 | 193.34 | 554.39 | 17.62 | 16.04 | 11.94 | -0.12375 | -0.54552 |
| 99 | 409.75 | 345.83 | 17.78 | 16.12 | 3.72 | 0.07581 | 0.22812 |
| 100 | 477.45 | 543.01 | 17.56 | 15.97 | 6.00 | 0.25170 | -0.33130 |
| 101 | 316.49 | 413.99 | 17.57 | 15.97 | 4.76 | -0.21998 | -0.01334 |
| 102 | 357.70 | 534.96 | 17.75 | 16.21 | 5.75 | -0.47322 | -0.23191 |
| 103 | 391.92 | 654.89 | 17.96 | 16.13 | 10.59 | 0.33621 | -0.03173 |
| 104 | 510.25 | 472.14 | 17.84 | 16.20 | 4.69 | 0.01656 | 0.38226 |
| 105 | 461.91 | 527.86 | 17.73 | 16.17 | 5.07 | 0.01979 | 0.18502 |
| 106 | 250.08 | 586.77 | 17.70 | 16.06 | 10.73 | 0.12003 | 0.18699 |
| 107 | 497.25 | 528.50 | 17.81 | 16.16 | 5.92 | -0.16888 | 0.01067 |
| 108 | 564.22 | 162.64 | 17.69 | 16.12 | 13.84 | 0.08282 | -0.29529 |
| 109 | 427.06 | 127.39 | 17.82 | 16.20 | 13.75 | 0.10023 | -0.59936 |
| 110 | 264.47 | 598.97 | 17.84 | 16.29 | 10.67 | 0.18811 | 0.01544 |
| 111 | 353.77 | 218.74 | 17.97 | 16.32 | 10.01 | 0.13799 | 0.15547 |
| 112 | 495.22 | 666.32 | 18.05 | 15.64 | 11.59 | 0.03229 | 0.25942 |
| 113 | 455.06 | 364.98 | 17.93 | 16.29 | 3.27 | -0.66976 | -0.22124 |
| 114 | 470.14 | 230.05 | 18.01 | 15.91 | 9.32 | 0.13252 | -0.15547 |
| 115 | 179.39 | 681.67 | 18.14 | 16.21 | 16.12 | 0.48488 | 0.49583 |
| 116 | 575.56 | 539.14 | 18.07 | 16.08 | 8.87 | -0.08367 | -0.22826 |
| 117 | 571.41 | 188.10 | 18.22 | 16.21 | 13.00 | -0.20468 | -0.19962 |
| 118 | 198.09 | 379.40 | 17.99 | 16.11 | 10.39 | -0.01607 | 0.22910 |
| 119 | 603.89 | 188.19 | 18.02 | 16.34 | 13.86 | -0.08142 | -0.09019 |
| 120 | 312.83 | 676.51 | 18.15 | 16.40 | 12.51 | 0.30168 | 0.03594 |
| 121 | 386.64 | 426.83 | 18.07 | 16.18 | 1.50 | 0.39096 | 0.40023 |
| 122 | 655.30 | 382.07 | 18.16 | 16.45 | 11.05 | -0.02583 | 0.02667 |
| 123 | 562.86 | 303.39 | 18.24 | 16.58 | 8.70 | -0.33635 | 0.04913 |
| 124 | 331.55 | 619.25 | 18.06 | 16.44 | 9.75 | 0.16551 | 0.28188 |
| 125 | 684.28 | 368.62 | 18.18 | 16.47 | 12.48 | 0.35376 | 0.06219 |
| 126 | 611.78 | 306.67 | 18.15 | 16.42 | 10.43 | 0.10725 | 0.37636 |
| 127 | 622.19 | 143.00 | 18.06 | 16.46 | 16.03 | 0.11455 | -0.42732 |
| 128 | 653.65 | 341.11 | 18.21 | 16.51 | 11.48 | 0.15582 | 0.35923 |
| 129 | 435.61 | 237.91 | 18.00 | 16.35 | 8.70 | -0.14726 | 0.08191 |
| 130 | 666.45 | 601.80 | 18.19 | 16.39 | 13.95 | -0.97424 | -0.14740 |
| 131 | 373.24 | 178.94 | 18.15 | 16.31 | 11.57 | 0.41075 | 0.00232 |
| 132 | 502.23 | 531.60 | 18.32 | 16.63 | 6.17 | -0.17885 | 0.14291 |
| 133 | 101.71 | 572.66 | 18.18 | 16.53 | 16.08 | 0.27371 | -0.37341 |
| 134 | 234.41 | 525.98 | 18.08 | 16.47 | 9.66 | -0.22959 | -0.24679 |
| 135 | 527.26 | 464.69 | 18.36 | 16.65 | 5.28 | 0.03622 | 0.08226 |

Table A.5: The $VI$ photometry and relative proper motions of the member stars on the PC chip of WFPC2 (V).

| No. | $X$ | $Y$ | $V$ | $I$ | $r(''$) | $\mu_x$(mas/yr) | $\mu_y$(mas/yr) |
|---|---|---|---|---|---|---|---|
| 136 | 213.02 | 369.59 | 18.05 | 16.46 | 9.83 | -0.15828 | 0.03495 |
| 137 | 250.01 | 539.40 | 18.13 | 16.54 | 9.36 | -0.45722 | -0.43293 |
| 138 | 618.62 | 555.78 | 18.20 | 16.52 | 10.94 | -0.07833 | -0.19288 |
| 139 | 599.73 | 231.76 | 18.75 | 16.44 | 12.21 | 0.34534 | -0.10718 |
| 140 | 479.53 | 379.96 | 18.20 | 16.55 | 3.50 | -0.03636 | -0.13112 |
| 141 | 397.68 | 634.78 | 18.98 | 16.51 | 9.64 | 0.24791 | -0.12747 |
| 142 | 760.66 | 435.76 | 18.44 | 16.71 | 15.72 | -0.45511 | -0.64631 |
| 143 | 245.66 | 347.20 | 18.19 | 16.57 | 8.77 | -0.21254 | 0.42830 |
| 144 | 143.99 | 486.59 | 18.28 | 16.66 | 12.96 | -0.39742 | -0.34786 |
| 145 | 497.53 | 735.73 | 18.56 | 16.57 | 14.69 | 0.20060 | 0.72802 |
| 146 | 409.92 | 315.33 | 19.26 | 16.75 | 5.12 | 0.16649 | 0.14908 |
| 147 | 343.81 | 790.84 | 18.59 | 16.83 | 17.13 | 0.92693 | 0.93157 |
| 148 | 242.07 | 484.76 | 18.77 | 16.64 | 8.58 | -0.19366 | -0.10121 |
| 149 | 731.05 | 433.17 | 18.52 | 16.80 | 14.35 | -0.08844 | -0.01713 |
| 150 | 473.15 | 474.39 | 18.30 | 16.62 | 3.33 | -0.36948 | 0.17520 |
| 151 | 222.98 | 408.93 | 18.27 | 16.68 | 9.06 | -0.08739 | 0.13982 |
| 152 | 145.19 | 501.83 | 18.37 | 16.69 | 13.07 | 0.04099 | -0.16242 |
| 153 | 351.87 | 471.22 | 18.30 | 16.37 | 3.72 | -0.01095 | 0.09335 |
| 154 | 300.08 | 353.20 | 18.37 | 16.72 | 6.43 | -0.37032 | 0.22264 |
| 155 | 573.05 | 265.03 | 19.03 | 17.04 | 10.25 | 0.14656 | -0.20524 |
| 156 | 441.97 | 649.70 | 18.89 | 16.80 | 10.33 | 0.34913 | 0.35292 |
| 157 | 419.03 | 397.64 | 18.67 | 17.04 | 1.31 | -0.34913 | -0.08423 |
| 158 | 382.21 | 423.33 | 18.38 | 16.73 | 1.70 | -0.40009 | 0.19597 |
| 159 | 491.39 | 518.76 | 18.57 | 16.94 | 5.40 | 0.01558 | 0.03594 |
| 160 | 280.30 | 594.79 | 18.47 | 16.92 | 10.05 | 0.09981 | 0.35488 |
| 161 | 403.15 | 195.38 | 18.59 | 16.89 | 10.64 | 0.03032 | 0.14122 |
| 162 | 52.95 | 493.82 | 19.27 | 16.87 | 17.13 | 0.18579 | -0.79161 |
| 163 | 554.81 | 427.33 | 19.39 | 16.89 | 6.24 | 0.42479 | -0.09518 |
| 164 | 710.68 | 449.69 | 18.73 | 17.00 | 13.45 | -0.53597 | -0.25255 |
| 165 | 229.32 | 382.84 | 18.83 | 16.86 | 8.96 | -0.30638 | 0.47056 |
| 166 | 522.65 | 396.29 | 19.80 | 17.11 | 4.96 | -0.09012 | -0.24426 |
| 167 | 294.38 | 237.72 | 19.00 | 16.83 | 10.40 | 0.18081 | 0.21022 |
| 168 | 381.34 | 322.34 | 18.78 | 17.09 | 5.09 | -0.05334 | 0.19232 |
| 169 | 616.79 | 586.90 | 19.84 | 16.99 | 11.72 | -0.30294 | -0.43546 |
| 170 | 240.35 | 400.95 | 19.67 | 16.96 | 8.31 | -0.58511 | -0.22910 |
| 171 | 270.03 | 453.71 | 19.98 | 17.29 | 6.98 | -0.84860 | -0.11722 |
| 172 | 405.76 | 104.51 | 18.79 | 17.10 | 14.81 | 0.32849 | -0.75118 |
| 173 | 608.04 | 127.54 | 18.91 | 17.16 | 16.26 | 0.10388 | -0.65688 |
| 174 | 291.79 | 637.15 | 19.66 | 16.94 | 11.33 | 0.32568 | -0.01656 |
| 175 | 574.51 | 366.38 | 19.78 | 17.05 | 7.66 | 0.17716 | 0.08240 |

Table A.6: The $VI$ photometry and relative proper motions of the member stars on the PC chip of WFPC2 (VI).

| No. | $X$ | $Y$ | $V$ | $I$ | $r(''$) | $\mu_x$(mas/yr) | $\mu_y$(mas/yr) |
|---|---|---|---|---|---|---|---|
| 176 | 290.31 | 282.35 | 18.82 | 17.08 | 8.88 | 0.39152 | 0.10543 |
| 177 | 377.34 | 446.03 | 18.43 | 16.77 | 2.13 | 0.01755 | 0.42648 |
| 178 | 131.16 | 629.49 | 19.85 | 17.24 | 16.22 | 0.09335 | 0.13280 |
| 179 | 362.71 | 704.77 | 19.06 | 17.33 | 13.07 | 0.52811 | 0.56854 |
| 180 | 234.71 | 412.42 | 19.62 | 17.14 | 8.51 | -0.39335 | 0.12592 |
| 181 | 381.51 | 415.86 | 18.60 | 16.92 | 1.80 | -0.24328 | 0.30449 |
| 182 | 546.06 | 189.09 | 19.05 | 17.33 | 12.37 | 0.36948 | -0.29992 |
| 183 | 726.07 | 416.65 | 19.32 | 17.53 | 14.13 | 0.06317 | -0.41623 |
| 184 | 401.07 | 301.89 | 20.17 | 17.48 | 5.78 | -0.51843 | 0.17941 |
| 185 | 383.01 | 623.72 | 19.68 | 17.29 | 9.24 | 0.25662 | 0.28160 |
| 186 | 551.70 | 411.56 | 20.06 | 17.39 | 6.13 | 0.13336 | 0.07763 |
| 187 | 577.22 | 744.61 | 19.67 | 17.45 | 16.35 | -0.75497 | -0.13027 |
| 188 | 638.51 | 183.63 | 19.23 | 17.49 | 15.04 | 0.02583 | -0.05608 |
| 189 | 540.50 | 694.19 | 19.90 | 17.56 | 13.53 | 0.27655 | 0.25240 |
| 190 | 335.88 | 578.06 | 20.14 | 17.44 | 7.97 | -0.06219 | -0.21029 |
| 191 | 143.77 | 267.34 | 19.93 | 17.40 | 14.62 | -0.03727 | 0.36008 |
| 192 | 168.84 | 314.35 | 19.27 | 17.47 | 12.61 | 0.23921 | 0.09532 |
| 193 | 283.33 | 574.14 | 19.71 | 17.71 | 9.24 | 0.71749 | 0.33860 |
| 194 | 326.00 | 287.11 | 20.18 | 17.49 | 7.70 | -0.10529 | 0.36892 |
| 195 | 100.00 | 403.04 | 19.35 | 17.47 | 14.72 | 0.28750 | -0.17014 |
| 196 | 731.38 | 269.55 | 20.12 | 17.45 | 16.07 | 0.53962 | 0.16017 |
| 197 | 680.15 | 535.04 | 20.45 | 17.66 | 13.01 | -0.25549 | -0.61318 |
| 198 | 119.14 | 437.01 | 19.94 | 17.43 | 13.81 | -0.07268 | -0.36653 |
| 199 | 497.98 | 232.01 | 19.42 | 17.68 | 9.64 | 0.15638 | -0.26686 |
| 200 | 504.09 | 629.38 | 19.49 | 17.57 | 10.13 | 0.10851 | -0.04885 |
| 201 | 506.81 | 430.19 | 20.45 | 17.68 | 4.04 | -0.77925 | 0.51071 |
| 202 | 378.11 | 171.24 | 19.38 | 17.68 | 11.88 | 0.13673 | -0.07082 |
| 203 | 256.40 | 594.80 | 20.37 | 17.68 | 10.78 | 0.21198 | 0.08591 |
| 204 | 234.24 | 377.92 | 20.26 | 17.63 | 8.79 | -0.24054 | -0.15596 |
| 205 | 101.74 | 352.14 | 19.58 | 17.70 | 14.99 | -0.10858 | 0.11090 |
| 206 | 566.42 | 620.90 | 20.60 | 17.81 | 11.23 | -0.23724 | -0.13926 |
| 207 | 689.64 | 369.47 | 19.47 | 17.91 | 12.71 | 0.32288 | -0.44304 |
| 208 | 490.24 | 376.90 | 20.36 | 17.70 | 3.98 | -0.00730 | 0.15919 |
| 209 | 340.77 | 530.73 | 20.58 | 18.03 | 6.01 | -0.50930 | 0.14431 |
| 210 | 546.62 | 496.01 | 19.60 | 17.82 | 6.68 | -0.23640 | -0.20468 |
| 211 | 117.87 | 638.09 | 20.97 | 18.03 | 16.94 | 0.11778 | -0.66035 |
| 212 | 563.43 | 724.04 | 20.49 | 17.83 | 15.22 | -0.68955 | 0.03706 |
| 213 | 159.79 | 308.04 | 20.61 | 17.88 | 13.11 | 0.19415 | 0.11188 |
| 214 | 157.63 | 628.02 | 20.43 | 17.83 | 15.19 | 0.33993 | -0.58511 |
| 215 | 512.09 | 179.66 | 19.89 | 18.07 | 12.12 | 0.49175 | -0.95354 |

Table A.7: The $VI$ photometry and relative proper motions of the member stars on the PC chip of WFPC2 (VII).

| No. | $X$ | $Y$ | $V$ | $I$ | $r(''$) | $\mu_x$(mas/yr) | $\mu_y$(mas/yr) |
|---|---|---|---|---|---|---|---|
| 216 | 459.75 | 766.73 | 19.85 | 18.03 | 15.77 | 0.55156 | 0.57472 |
| 217 | 675.83 | 519.51 | 20.96 | 18.14 | 12.56 | -0.73082 | -0.44248 |
| 218 | 258.53 | 486.98 | 20.65 | 17.86 | 7.90 | -0.07637 | -0.22124 |
| 219 | 313.93 | 596.28 | 20.39 | 17.92 | 9.20 | 0.22489 | -0.15835 |
| 220 | 425.45 | 560.04 | 20.47 | 17.75 | 6.16 | -0.15877 | -0.07946 |
| 221 | 204.88 | 370.95 | 20.66 | 17.91 | 10.18 | -0.09981 | -0.01011 |
| 222 | 453.90 | 502.19 | 20.86 | 17.92 | 3.84 | -0.19134 | -0.33902 |
| 223 | 382.37 | 528.90 | 19.50 | 17.24 | 5.02 | -0.00646 | -0.55029 |
| 224 | 242.65 | 433.90 | 20.59 | 17.90 | 8.13 | -0.61683 | -0.20145 |
| 225 | 402.07 | 287.19 | 20.95 | 18.19 | 6.44 | 0.12873 | -0.20608 |
| 226 | 331.25 | 515.62 | 20.55 | 17.89 | 5.77 | -0.07216 | 0.04520 |
| 227 | 547.83 | 500.57 | 20.87 | 18.09 | 6.84 | 0.03257 | -0.12564 |
| 228 | 307.16 | 734.36 | 21.42 | 18.30 | 15.08 | 1.08192 | 0.43518 |
| 229 | 363.68 | 184.93 | 21.15 | 18.21 | 11.39 | -0.07047 | -0.07082 |
| 230 | 236.32 | 486.55 | 21.03 | 18.19 | 8.86 | -0.22215 | -0.11680 |
| 231 | 422.46 | 586.79 | 20.79 | 18.04 | 7.39 | -0.05292 | 0.44248 |
| 232 | 350.02 | 555.14 | 20.81 | 18.19 | 6.73 | -0.40107 | -0.17211 |
| 233 | 95.01 | 358.38 | 20.90 | 18.07 | 15.23 | -0.07816 | 0.07272 |
| 234 | 428.68 | 561.42 | 20.32 | 17.67 | 6.23 | -0.02850 | -0.07946 |
| 235 | 641.32 | 161.10 | 20.95 | 18.27 | 15.91 | 0.16677 | -0.45266 |
| 236 | 540.91 | 607.99 | 20.31 | 18.47 | 10.06 | 0.23893 | -0.03229 |
| 237 | 466.77 | 272.93 | 21.14 | 18.33 | 7.38 | 0.32105 | 0.10346 |
| 238 | 688.51 | 254.40 | 21.06 | 18.30 | 14.70 | 0.20917 | -0.38177 |
| 239 | 706.83 | 337.01 | 21.36 | 18.54 | 13.85 | 0.16144 | -0.21899 |
| 240 | 250.16 | 131.29 | 21.47 | 18.47 | 15.64 | 0.28883 | -0.28434 |
| 241 | 423.77 | 182.03 | 20.30 | 18.42 | 11.23 | -0.02625 | -0.07314 |
| 242 | 240.92 | 418.74 | 20.74 | 18.43 | 8.21 | 0.64259 | -0.58005 |
| 243 | 127.84 | 489.44 | 20.63 | 18.49 | 13.71 | -0.27785 | -0.10753 |
| 244 | 562.75 | 136.24 | 20.56 | 18.54 | 14.89 | 0.62469 | -0.75665 |
| 245 | 431.40 | 730.28 | 20.54 | 18.71 | 14.00 | 0.46649 | 0.57472 |
| 246 | 219.06 | 233.82 | 21.41 | 18.53 | 12.77 | 0.24658 | 0.18860 |
| 247 | 426.46 | 587.68 | 20.64 | 18.05 | 7.43 | -0.41581 | -0.11427 |
| 248 | 592.99 | 549.44 | 21.65 | 18.67 | 9.80 | -0.16565 | -0.11680 |
| 249 | 407.14 | 554.03 | 20.67 | 17.86 | 5.91 | 0.32428 | -0.15358 |
| 250 | 404.25 | 677.95 | 21.31 | 18.69 | 11.60 | 0.29480 | 0.22517 |
| 251 | 225.81 | 373.98 | 21.63 | 18.80 | 9.21 | -0.15821 | -0.31866 |
| 252 | 238.35 | 435.13 | 21.67 | 18.72 | 8.33 | -0.66702 | 0.14894 |
| 253 | 403.79 | 155.25 | 20.59 | 18.67 | 12.48 | -0.46143 | -0.66976 |
| 254 | 484.29 | 248.52 | 21.48 | 18.79 | 8.71 | 0.14572 | 0.14993 |
| 255 | 90.01 | 592.62 | 21.71 | 18.82 | 16.97 | -0.41153 | -0.39559 |

Table A.8: The $VI$ photometry and relative proper motions of the member stars on the PC chip of WFPC2 (VIII).

| No. | $X$ | $Y$ | $V$ | $I$ | $r(''$) | $\mu_x$(mas/yr) | $\mu_y$(mas/yr) |
|---|---|---|---|---|---|---|---|
| 256 | 599.69 | 302.53 | 21.88 | 18.83 | 10.07 | 0.27908 | -0.10248 |
| 257 | 186.43 | 496.98 | 22.11 | 18.99 | 11.19 | -0.26960 | -0.48614 |
| 258 | 327.61 | 278.30 | 21.71 | 18.71 | 8.00 | -0.14038 | 0.36667 |
| 259 | 197.21 | 450.92 | 22.06 | 19.01 | 10.27 | -0.17569 | -0.04787 |
| 260 | 131.38 | 452.85 | 21.73 | 18.77 | 13.29 | -0.03587 | -0.19148 |
| 261 | 183.51 | 507.34 | 21.60 | 18.79 | 11.46 | -0.30680 | -0.71019 |
| 262 | 649.41 | 211.26 | 21.70 | 18.91 | 14.49 | 0.48319 | -0.11406 |
| 263 | 486.86 | 418.10 | 21.52 | 18.46 | 3.14 | -0.21857 | -0.46747 |
| 264 | 309.93 | 136.43 | 21.82 | 18.95 | 14.25 | 0.03173 | -0.29901 |
| 265 | 531.46 | 724.53 | 21.10 | 19.07 | 14.66 | 0.22321 | 0.47786 |
| 266 | 465.79 | 723.09 | 22.35 | 19.16 | 13.82 | 0.06710 | -0.12269 |
| 267 | 470.67 | 620.37 | 21.77 | 18.98 | 9.24 | 0.12143 | -0.13870 |
| 268 | 232.22 | 419.38 | 21.86 | 18.90 | 8.60 | -0.56672 | 0.25255 |
| 269 | 87.98 | 542.33 | 21.84 | 18.70 | 16.14 | 0.47930 | -0.31417 |
| 270 | 574.17 | 601.13 | 22.32 | 19.14 | 10.75 | -0.25325 | 0.07974 |
| 271 | 559.22 | 530.71 | 21.81 | 19.02 | 8.04 | 0.03762 | -0.07665 |
| 272 | 110.24 | 389.10 | 22.32 | 19.25 | 14.31 | 0.16425 | -0.07272 |
| 273 | 706.85 | 345.66 | 21.59 | 19.04 | 13.74 | -0.12606 | 0.46227 |
| 274 | 350.83 | 563.06 | 21.71 | 18.84 | 7.04 | 0.03720 | -0.29424 |
| 275 | 371.11 | 309.50 | 21.86 | 18.89 | 5.81 | -0.03215 | 0.37201 |
| 276 | 252.77 | 545.45 | 21.91 | 18.97 | 9.42 | 0.22587 | -0.30322 |
| 277 | 294.07 | 344.15 | 21.96 | 19.04 | 6.88 | -0.22447 | 0.20060 |
| 278 | 492.61 | 136.02 | 22.29 | 19.21 | 13.77 | 0.22629 | -0.86573 |
| 279 | 504.27 | 244.87 | 22.08 | 19.08 | 9.22 | 0.03720 | 0.54145 |
| 280 | 598.15 | 470.15 | 22.08 | 19.07 | 8.48 | -0.33579 | -0.49175 |
| 281 | 535.65 | 471.43 | 21.73 | 18.96 | 5.75 | -0.35601 | -0.27318 |
| 282 | 203.54 | 291.56 | 21.86 | 19.15 | 11.69 | 0.01614 | 0.45175 |
| 283 | 130.39 | 548.45 | 22.21 | 19.33 | 14.42 | 0.07223 | -0.59802 |
| 284 | 565.69 | 475.11 | 21.91 | 18.97 | 7.11 | 0.16425 | 0.11357 |
| 285 | 374.71 | 193.74 | 21.93 | 19.27 | 10.89 | 0.28385 | 0.30870 |
| 286 | 172.11 | 551.78 | 22.07 | 19.19 | 12.75 | -0.33347 | -0.74851 |
| 287 | 382.03 | 311.09 | 22.31 | 19.22 | 5.56 | 0.58286 | 0.16060 |
| 288 | 518.54 | 375.99 | 22.20 | 19.22 | 5.12 | 0.27374 | 0.21984 |
| 289 | 542.15 | 430.54 | 21.91 | 18.95 | 5.66 | -0.17491 | -0.08647 |
| 290 | 390.34 | 314.54 | 22.08 | 19.02 | 5.31 | 0.04141 | 0.08605 |
| 291 | 312.83 | 713.58 | 22.26 | 19.44 | 14.09 | 0.43925 | -0.31698 |
| 292 | 162.72 | 606.54 | 22.05 | 19.35 | 14.42 | 0.04548 | -0.99642 |
| 293 | 185.59 | 676.73 | 21.53 | 19.02 | 15.76 | 0.30771 | 0.19541 |
| 294 | 350.87 | 227.09 | 22.67 | 19.36 | 9.68 | -0.21212 | 0.06212 |
| 295 | 575.71 | 373.76 | 22.37 | 19.33 | 7.60 | 0.22742 | 0.29073 |

Table A.9: The $VI$ photometry and relative proper motions of the member stars on the PC chip of WFPC2 (IX).

| No. | $X$ | $Y$ | $V$ | $I$ | $r(''$) | $\mu_x$(mas/yr) | $\mu_y$(mas/yr) |
|---|---|---|---|---|---|---|---|
| 296 | 395.04 | 133.17 | 22.46 | 19.33 | 13.53 | -0.25212 | -0.68730 |
| 297 | 331.37 | 730.53 | 22.62 | 19.49 | 14.57 | 0.95585 | -0.44220 |
| 298 | 377.08 | 600.84 | 22.22 | 19.25 | 8.26 | 0.13168 | 0.12325 |
| 299 | 377.58 | 676.63 | 22.36 | 19.44 | 11.68 | 0.62090 | -0.24482 |
| 300 | 584.51 | 403.87 | 22.44 | 19.40 | 7.68 | -0.15807 | -0.19639 |
| 301 | 369.68 | 336.49 | 22.29 | 19.37 | 4.71 | -0.21113 | 0.32007 |
| 302 | 85.75 | 450.33 | 22.77 | 19.60 | 15.38 | -0.40416 | -0.46452 |
| 303 | 573.63 | 350.44 | 22.03 | 19.33 | 7.91 | -0.02021 | 0.46410 |
| 304 | 230.44 | 615.37 | 22.16 | 19.41 | 12.29 | 0.08788 | -0.67523 |
| 305 | 157.54 | 461.24 | 22.30 | 19.32 | 12.14 | -0.39559 | -0.17393 |
| 306 | 105.12 | 621.86 | 22.20 | 19.45 | 17.02 | 0.04829 | -0.93437 |
| 307 | 385.25 | 392.83 | 21.92 | 19.03 | 2.19 | -0.31796 | -0.39559 |
| 308 | 463.12 | 589.64 | 21.95 | 19.12 | 7.78 | 0.30084 | 0.30042 |
| 309 | 255.82 | 417.31 | 22.68 | 19.57 | 7.52 | -0.21113 | 0.03734 |
| 310 | 269.30 | 658.02 | 21.82 | 19.59 | 12.70 | 0.44978 | 0.07187 |
| 311 | 451.33 | 725.92 | 21.57 | 19.71 | 13.87 | 0.19499 | -0.84341 |
| 312 | 468.90 | 348.70 | 22.27 | 19.38 | 4.24 | -0.38549 | -0.24103 |
| 313 | 352.97 | 565.98 | 22.49 | 19.49 | 7.11 | -0.51927 | -0.06851 |
| 314 | 479.29 | 553.63 | 22.08 | 19.43 | 6.48 | -0.98309 | -0.22573 |
| 315 | 225.82 | 307.63 | 22.50 | 19.59 | 10.43 | 0.46922 | 0.32105 |
| 316 | 417.98 | 133.75 | 22.93 | 19.73 | 13.45 | 0.56588 | -0.68906 |
| 317 | 491.65 | 221.39 | 23.02 | 19.71 | 9.99 | -0.10500 | -0.37257 |
| 318 | 500.55 | 509.52 | 22.32 | 19.21 | 5.36 | -0.17660 | -0.73040 |
| 319 | 310.01 | 634.66 | 22.49 | 19.46 | 10.82 | 0.61585 | 0.10472 |
| 320 | 493.72 | 141.20 | 22.36 | 19.32 | 13.55 | 0.02766 | -0.74472 |
| 321 | 328.22 | 643.91 | 22.77 | 19.86 | 10.85 | 0.61234 | -0.63284 |
| 322 | 182.95 | 444.14 | 23.13 | 19.84 | 10.90 | -0.51562 | -0.01151 |
| 323 | 63.96 | 479.98 | 22.77 | 19.71 | 16.52 | 0.29159 | -0.42872 |
| 324 | 269.99 | 380.50 | 22.57 | 19.64 | 7.18 | 0.08647 | 0.39966 |
| 325 | 286.80 | 493.20 | 22.65 | 19.66 | 6.82 | -0.16649 | -0.74921 |
| 326 | 340.32 | 185.16 | 22.72 | 19.84 | 11.67 | 0.06078 | 0.37994 |
| 327 | 571.79 | 391.68 | 22.30 | 19.57 | 7.20 | -0.49863 | -0.57303 |
| 328 | 306.83 | 264.24 | 22.63 | 19.64 | 9.07 | -0.15681 | 0.17295 |
| 329 | 458.58 | 345.75 | 22.36 | 19.63 | 4.12 | 0.16649 | -0.04927 |
| 330 | 248.72 | 282.59 | 22.52 | 19.66 | 10.25 | -0.02709 | 0.68211 |
| 331 | 216.86 | 587.50 | 22.50 | 19.70 | 11.90 | 0.16972 | -0.69573 |
| 332 | 276.80 | 661.89 | 22.85 | 19.90 | 12.66 | 0.34492 | 0.28104 |
| 333 | 493.62 | 148.09 | 22.66 | 19.71 | 13.24 | -0.03538 | -0.69832 |
| 334 | 351.32 | 372.16 | 22.78 | 19.94 | 3.99 | 0.45638 | -0.25942 |
| 335 | 314.21 | 634.73 | 22.86 | 19.78 | 10.74 | 0.12382 | -0.58174 |

Table A.10: The $VI$ photometry and relative proper motions of the member stars on the PC chip of WFPC2 (X).

| No. | $X$ | $Y$ | $V$ | $I$ | $r(''$) | $\mu_x$(mas/yr) | $\mu_y$(mas/yr) |
|---|---|---|---|---|---|---|---|
| 336 | 630.95 | 358.39 | 22.78 | 19.85 | 10.23 | 0.01320 | -0.24609 |
| 337 | 518.27 | 514.03 | 22.64 | 19.80 | 6.09 | 0.76283 | -0.59185 |
| 338 | 479.36 | 536.28 | 22.80 | 19.66 | 5.77 | 0.05012 | -0.43883 |
| 339 | 197.39 | 541.10 | 22.90 | 19.89 | 11.49 | 0.30814 | -1.04050 |
| 340 | 312.93 | 160.34 | 22.96 | 19.98 | 13.17 | 0.50832 | -0.33488 |
| 341 | 630.16 | 230.87 | 22.80 | 19.83 | 13.23 | -0.85183 | 0.18629 |
| 342 | 359.10 | 645.25 | 23.02 | 19.90 | 10.45 | 0.37075 | 0.24735 |
| 343 | 430.92 | 257.46 | 22.71 | 19.83 | 7.78 | 0.01011 | 0.07777 |
| 344 | 227.27 | 503.89 | 22.95 | 19.97 | 9.52 | -0.08781 | 0.13617 |
| 345 | 494.82 | 542.73 | 23.13 | 19.93 | 6.39 | 0.08016 | -0.29115 |
| 346 | 686.48 | 466.80 | 23.18 | 20.11 | 12.44 | -0.29396 | -0.46915 |
| 347 | 494.75 | 616.96 | 23.02 | 20.04 | 9.44 | -0.09799 | -0.83162 |
| 348 | 486.31 | 253.52 | 23.26 | 20.05 | 8.52 | -0.41216 | 0.13013 |
| 349 | 513.33 | 224.84 | 23.14 | 20.13 | 10.23 | -0.24482 | -0.35558 |
| 350 | 251.46 | 220.78 | 22.87 | 19.87 | 12.20 | 0.19646 | 0.01930 |
| 351 | 491.54 | 196.42 | 22.88 | 19.76 | 11.08 | 0.23233 | 0.42409 |
| 352 | 526.76 | 442.33 | 23.00 | 20.12 | 5.01 | 0.72380 | -0.85745 |
| 353 | 184.48 | 235.34 | 23.22 | 20.33 | 13.91 | -0.03495 | 0.19366 |
| 354 | 670.90 | 196.29 | 22.87 | 20.17 | 15.68 | 0.65417 | 0.04001 |
| 355 | 479.29 | 101.17 | 23.28 | 20.06 | 15.21 | -0.04955 | -0.66976 |
| 356 | 593.33 | 539.75 | 23.19 | 20.16 | 9.56 | 0.87935 | -0.29677 |
| 357 | 135.32 | 454.56 | 22.91 | 19.94 | 13.12 | -0.92188 | 0.71580 |
| 358 | 385.40 | 354.77 | 15.10 | 13.60 | 3.63 | 0.05419 | 0.22629 |
| 359 | 440.93 | 405.71 | 11.92 | 10.32 | 1.38 | -0.13799 | 0.04590 |
| 360 | 433.96 | 452.25 | 12.82 | 11.15 | 1.38 | 0.00000 | 0.32203 |
| 361 | 335.29 | 483.77 | 12.86 | 11.34 | 4.68 | -0.50593 | 0.00000 |
| 362 | 406.67 | 507.55 | 13.09 | 11.56 | 3.78 | 0.00000 | -0.18404 |
| 363 | 423.50 | 492.46 | 13.12 | 11.61 | 3.05 | 0.09195 | 0.55198 |
| 364 | 358.09 | 414.45 | 13.15 | 11.59 | 2.86 | -0.23008 | 0.69011 |
| 365 | 411.37 | 509.35 | 13.32 | 11.80 | 3.84 | 0.00000 | 0.32203 |
| 366 | 306.55 | 575.18 | 13.18 | 11.70 | 8.59 | 0.22994 | 0.00000 |
| 367 | 430.67 | 443.18 | 13.22 | 11.66 | 0.94 | 0.13799 | 0.22994 |
| 368 | 360.83 | 482.14 | 13.33 | 11.85 | 3.72 | -0.13799 | -0.04590 |
| 369 | 424.64 | 481.43 | 13.46 | 11.90 | 2.55 | 0.09209 | 0.59802 |
| 370 | 592.23 | 510.22 | 13.57 | 11.96 | 8.85 | 0.18390 | -0.18404 |
| 371 | 508.60 | 581.52 | 13.62 | 12.02 | 8.24 | 0.78206 | 0.04604 |
| 372 | 397.40 | 442.74 | 13.58 | 12.08 | 1.26 | -0.13799 | -0.23008 |
| 373 | 456.37 | 371.75 | 13.66 | 12.08 | 3.03 | -0.13799 | 0.04604 |
| 374 | 451.85 | 453.88 | 13.70 | 12.12 | 1.97 | 0.04604 | 0.23008 |
| 375 | 328.58 | 495.70 | 13.93 | 12.46 | 5.25 | -0.32203 | -0.27599 |

Table A.11: The $VI$ photometry and relative proper motions of the member stars on the PC chip of WFPC2 (XI).

| No. | $X$ | $Y$ | $V$ | $I$ | $r(''$) | $\mu_x$(mas/yr) | $\mu_y$(mas/yr) |
|---|---|---|---|---|---|---|---|
| 376 | 415.71 | 490.41 | 14.31 | 12.81 | 2.96 | -0.27599 | -0.04604 |
| 377 | 519.94 | 282.52 | 13.81 | 12.26 | 8.07 | 0.00000 | 0.32189 |
| 378 | 400.62 | 351.65 | 14.04 | 12.49 | 3.53 | -0.55198 | -0.18404 |
| 379 | 458.24 | 569.57 | 13.97 | 12.46 | 6.83 | 0.27599 | -0.22994 |
| 380 | 406.78 | 569.06 | 14.13 | 12.55 | 6.60 | -0.04604 | -0.45989 |
| 381 | 395.27 | 497.29 | 14.22 | 12.74 | 3.45 | 0.00000 | -0.22994 |
| 382 | 391.78 | 549.92 | 14.20 | 12.71 | 5.83 | 0.36794 | -0.09209 |
| 383 | 512.30 | 419.52 | 14.40 | 12.81 | 4.30 | -0.09209 | 0.22994 |
| 384 | 296.12 | 315.53 | 14.26 | 12.65 | 7.61 | -0.13799 | 0.87401 |
| 385 | 402.49 | 382.63 | 14.18 | 12.66 | 2.15 | 0.32189 | -0.09195 |
| 386 | 397.69 | 446.10 | 14.35 | 12.76 | 1.35 | -0.13799 | 0.18404 |
| 387 | 264.53 | 464.97 | 14.23 | 12.73 | 7.33 | -0.82797 | -0.41398 |
| 388 | 383.91 | 479.85 | 14.24 | 12.78 | 2.95 | 0.00000 | 0.09209 |
| 389 | 342.85 | 107.87 | 14.29 | 12.73 | 15.06 | 0.32203 | 0.13803 |
| 390 | 411.70 | 515.19 | 14.52 | 13.00 | 4.11 | 0.41412 | 0.50593 |
| 391 | 752.70 | 234.66 | 14.32 | 12.80 | 17.69 | -0.13785 | -0.09195 |
| 392 | 477.39 | 496.02 | 14.47 | 12.94 | 4.18 | 0.13813 | -0.78206 |
| 393 | 336.64 | 433.13 | 14.96 | 13.46 | 3.81 | -0.09195 | 0.00000 |
| 394 | 317.77 | 326.86 | 14.63 | 13.13 | 6.53 | 0.00000 | -0.04604 |
| 395 | 343.07 | 484.10 | 14.85 | 13.34 | 4.40 | -0.18390 | -0.09195 |
| 396 | 676.63 | 327.21 | 15.07 | 13.56 | 12.69 | 0.27599 | 0.22994 |
| 397 | 302.45 | 467.14 | 14.61 | 13.07 | 5.69 | -0.09195 | -0.41398 |
| 398 | 652.42 | 324.93 | 14.93 | 13.42 | 11.70 | 0.04604 | -0.32203 |
| 399 | 318.17 | 548.02 | 14.77 | 13.18 | 7.28 | 0.27613 | -0.59802 |
| 400 | 391.70 | 470.68 | 14.76 | 13.19 | 2.40 | -0.41398 | -0.27599 |
| 401 | 547.33 | 266.18 | 14.74 | 13.21 | 9.43 | -0.36780 | -0.32203 |
| 402 | 385.12 | 538.86 | 14.88 | 13.35 | 5.41 | 0.59802 | -0.55198 |
| 403 | 93.93 | 382.69 | 14.83 | 13.19 | 15.09 | 0.00000 | -0.09195 |
| 404 | 385.31 | 354.76 | 15.22 | 13.71 | 3.64 | 0.09195 | 0.13799 |
| 405 | 631.82 | 261.16 | 14.84 | 13.35 | 12.38 | -0.04604 | -0.32203 |
| 406 | 473.73 | 446.04 | 14.95 | 13.35 | 2.67 | -0.18390 | -0.04590 |
| 407 | 525.52 | 360.33 | 14.89 | 13.35 | 5.76 | 0.18418 | -0.09209 |
| 408 | 415.36 | 515.59 | 15.05 | 13.57 | 4.11 | 0.13799 | 0.32203 |
| 409 | 339.21 | 346.45 | 14.95 | 13.38 | 5.19 | 0.09195 | -0.04590 |
| 410 | 451.68 | 490.01 | 14.96 | 13.44 | 3.29 | -0.36808 | -0.04590 |
| 411 | 396.13 | 537.73 | 15.10 | 13.60 | 5.24 | -0.04604 | -0.27599 |

Table A.12: The $VI$ photometry and relative proper motions of the member stars on the WFC2 chip of WFPC2 (I).

| No. | $X$ | $Y$ | $V$ | $I$ | $r(''$) | $\mu_x$(mas/yr) | $\mu_y$(mas/yr) |
|---|---|---|---|---|---|---|---|
| 1 | 550.24 | 101.76 | 16.91 | 15.33 | 41.30 | -0.08606 | -0.16502 |
| 2 | 719.24 | 79.45 | 17.27 | 15.20 | 52.46 | -0.16724 | -0.10483 |
| 3 | 568.64 | 183.71 | 16.93 | 15.37 | 47.71 | -0.38513 | 0.75699 |
| 4 | 306.83 | 94.90 | 18.51 | 16.65 | 28.67 | -0.27374 | 0.03670 |
| 5 | 570.07 | 323.19 | 18.77 | 17.02 | 57.72 | -0.17029 | -0.17395 |
| 6 | 612.66 | 166.41 | 18.55 | 16.89 | 49.38 | -0.61340 | 0.55496 |
| 7 | 435.92 | 216.66 | 18.86 | 17.19 | 43.29 | -0.39001 | 0.47302 |
| 8 | 650.87 | 108.70 | 19.07 | 16.99 | 48.71 | -0.26123 | -0.25101 |
| 9 | 541.53 | 200.57 | 18.80 | 17.20 | 47.29 | 0.02197 | 0.55008 |
| 10 | 580.36 | 348.42 | 19.29 | 17.13 | 60.12 | 0.63782 | 0.38910 |
| 11 | 783.14 | 312.92 | 19.40 | 17.29 | 69.59 | -0.32410 | 0.16113 |
| 12 | 598.51 | 207.28 | 19.05 | 17.26 | 51.09 | 0.18921 | 0.39795 |
| 13 | 499.89 | 58.45 | 19.65 | 17.27 | 35.33 | -0.27802 | 0.18848 |
| 14 | 434.89 | 60.65 | 19.10 | 17.42 | 31.46 | 0.00183 | -0.51270 |
| 15 | 756.71 | 133.74 | 19.76 | 17.41 | 57.86 | -0.00916 | -0.22888 |
| 16 | 393.03 | 183.24 | 19.55 | 17.71 | 38.89 | -0.01190 | 0.04791 |
| 17 | 380.83 | 193.30 | 20.50 | 17.65 | 39.28 | -0.12695 | -0.45609 |
| 18 | 774.88 | 165.64 | 19.49 | 17.84 | 60.80 | -1.08276 | 0.59402 |
| 19 | 618.54 | 158.25 | 19.45 | 17.79 | 49.27 | 0.16663 | 0.52109 |
| 20 | 790.41 | 386.74 | 19.86 | 18.01 | 74.70 | 1.10535 | 0.68481 |
| 21 | 505.67 | 257.21 | 20.14 | 18.02 | 49.58 | 0.06104 | 1.36597 |
| 22 | 557.61 | 125.01 | 19.97 | 18.08 | 43.22 | -0.33203 | -0.35904 |
| 23 | 598.44 | 292.96 | 20.93 | 18.08 | 56.99 | 0.12634 | -0.16205 |
| 24 | 437.48 | 138.01 | 21.01 | 18.23 | 37.23 | 0.65094 | -0.17105 |
| 25 | 377.79 | 105.99 | 21.01 | 18.38 | 32.04 | 0.60303 | 0.00603 |
| 26 | 424.70 | 137.99 | 20.55 | 18.65 | 36.62 | 0.30975 | -0.25406 |
| 27 | 674.67 | 177.47 | 21.41 | 18.66 | 54.21 | 0.02136 | 0.27100 |
| 28 | 681.05 | 245.23 | 21.08 | 19.02 | 58.73 | -0.41138 | -0.16800 |
| 29 | 604.91 | 318.79 | 21.07 | 18.93 | 59.20 | 0.90515 | -0.58594 |
| 30 | 323.33 | 77.77 | 20.63 | 18.77 | 27.70 | -0.48920 | -0.01053 |
| 31 | 447.54 | 136.91 | 21.77 | 18.87 | 37.65 | 0.25299 | -0.75409 |
| 32 | 550.40 | 156.52 | 20.66 | 18.88 | 44.80 | -0.88989 | -0.81909 |
| 33 | 354.72 | 155.30 | 21.80 | 19.02 | 35.23 | -0.15381 | -0.12100 |
| 34 | 700.93 | 157.17 | 21.03 | 18.92 | 54.93 | -0.15198 | 0.14694 |
| 35 | 577.11 | 280.32 | 20.84 | 19.18 | 54.93 | -1.06690 | -0.42877 |

$X$ and $Y$ are star positions in pixel coordinates on the WFC2 chip of WFPC2 based on the 2007 data. $r$ is the cluster-centric distance in arcsecond. $\mu_x$ and $\mu_y$ are relative proper motions' components along the $x$ and $y$ directions of (WFC2) pixel coordinates (2007). $V$ and $I$ magnitudes are from the 1997 WFPC2 data.

Table A.13: The $VI$ photometry and relative proper motions of the member stars on the WFC2 chip of WFPC2 (II).

| No. | $X$ | $Y$ | $V$ | $I$ | $r(''$) | $\mu_x$(mas/yr) | $\mu_y$(mas/yr) |
|---|---|---|---|---|---|---|---|
| 36 | 330.58 | 53.92 | 20.89 | 19.09 | 25.96 | -0.11383 | 0.53989 |
| 37 | 509.13 | 184.44 | 22.09 | 19.11 | 44.35 | 0.09705 | 0.12909 |
| 38 | 597.13 | 280.49 | 21.44 | 19.17 | 56.03 | -0.52063 | 0.26398 |
| 39 | 633.55 | 263.40 | 21.21 | 19.03 | 56.95 | 0.27100 | 0.01221 |
| 40 | 605.45 | 234.53 | 21.67 | 19.42 | 53.33 | -0.11597 | -0.07095 |
| 41 | 360.84 | 84.45 | 22.25 | 19.40 | 29.61 | 0.30518 | -0.04715 |
| 42 | 552.52 | 245.27 | 21.80 | 19.57 | 51.08 | -0.27405 | 0.08804 |
| 43 | 661.16 | 257.19 | 21.98 | 19.76 | 58.23 | -0.18921 | -0.99121 |
| 44 | 337.96 | 98.91 | 22.62 | 19.77 | 29.95 | 0.10193 | -0.12527 |
| 45 | 553.96 | 235.75 | 22.80 | 19.75 | 50.47 | 0.87585 | -0.57800 |
| 46 | 312.83 | 92.39 | 22.73 | 19.78 | 28.62 | 0.09308 | -0.16891 |
| 47 | 475.60 | 66.45 | 22.58 | 19.74 | 34.28 | 0.67993 | 0.24353 |
| 48 | 747.63 | 165.59 | 22.27 | 19.88 | 58.77 | 0.02991 | -0.74402 |
| 49 | 405.26 | 153.35 | 21.73 | 19.63 | 36.96 | -1.03699 | -0.68298 |
| 50 | 733.53 | 55.20 | 22.58 | 19.97 | 52.55 | 0.01953 | 0.67150 |
| 51 | 575.66 | 235.96 | 22.08 | 19.96 | 51.70 | -0.54626 | 0.27206 |
| 52 | 525.22 | 64.82 | 22.96 | 19.94 | 37.40 | -0.23804 | -0.00397 |
| 53 | 761.10 | 173.55 | 22.37 | 20.02 | 60.18 | 0.59509 | 0.75897 |
| 54 | 403.81 | 141.45 | 23.17 | 20.14 | 35.95 | 0.52002 | 0.55801 |
| 55 | 369.42 | 57.80 | 22.98 | 20.08 | 27.87 | -0.45715 | 0.67631 |
| 56 | 630.77 | 59.81 | 22.28 | 20.00 | 44.73 | -0.23499 | -0.75268 |
| 57 | 349.77 | 139.17 | 22.87 | 20.17 | 33.71 | -0.41687 | -0.29800 |
| 58 | 340.80 | 137.12 | 23.20 | 20.16 | 33.25 | 0.78400 | -0.01892 |
| 59 | 326.88 | 61.06 | 22.59 | 19.75 | 26.42 | -0.40802 | 0.31590 |
| 60 | 752.56 | 366.82 | 22.46 | 20.18 | 71.05 | 0.29968 | -0.43274 |
| 61 | 567.24 | 118.30 | 23.10 | 20.14 | 43.43 | 0.64819 | 0.08797 |
| 62 | 614.13 | 201.20 | 22.43 | 20.12 | 51.67 | 1.14258 | -0.29999 |
| 63 | 741.31 | 83.13 | 22.14 | 20.14 | 54.35 | -0.31433 | -0.14107 |
| 64 | 424.91 | 55.56 | 23.41 | 20.32 | 30.54 | -0.40100 | -0.37369 |
| 65 | 466.82 | 133.40 | 23.64 | 20.27 | 38.39 | 0.97809 | -0.24704 |
| 66 | 371.79 | 92.15 | 23.37 | 20.22 | 30.68 | 0.30304 | -0.01244 |
| 67 | 492.06 | 97.91 | 22.82 | 20.27 | 37.36 | 1.08002 | -0.36453 |
| 68 | 493.20 | 233.06 | 23.26 | 19.88 | 47.14 | -0.70984 | -0.05203 |
| 69 | 645.85 | 115.29 | 23.65 | 20.52 | 48.70 | 0.49988 | 0.19806 |
| 70 | 769.15 | 162.10 | 22.86 | 20.77 | 60.19 | 0.30884 | -0.48996 |
| 71 | 638.54 | 197.21 | 22.99 | 20.58 | 52.98 | -0.16724 | -0.45792 |
| 72 | 512.09 | 189.55 | 22.77 | 20.74 | 44.88 | -0.47913 | -0.62897 |
| 73 | 463.45 | 245.64 | 23.47 | 20.86 | 46.76 | 1.23108 | 0.32104 |
| 74 | 561.30 | 81.19 | 23.43 | 21.01 | 40.83 | 0.59326 | -0.49355 |
| 75 | 695.94 | 94.14 | 23.45 | 21.14 | 51.34 | 0.00488 | 0.48660 |

Table A.14: The $VI$ photometry and relative proper motions of the member stars on the WFC4 chip of WFPC2 (I).

| No. | $X$ | $Y$ | $V$ | $I$ | $r(''$) | $\mu_x$(mas/yr) | $\mu_y$(mas/yr) |
|---|---|---|---|---|---|---|---|
| 1 | 331.16 | 211.81 | 17.89 | 14.87 | 48.98 | -0.07019 | 0.22003 |
| 2 | 194.24 | 169.76 | 17.31 | 15.33 | 36.84 | -0.16998 | 0.34409 |
| 3 | 121.32 | 188.19 | 18.00 | 16.17 | 30.16 | -0.44304 | 0.15900 |
| 4 | 509.04 | 119.85 | 18.33 | 16.26 | 65.49 | -0.24994 | 0.79407 |
| 5 | 331.39 | 242.91 | 18.56 | 16.51 | 49.10 | -0.24994 | 0.64194 |
| 6 | 465.06 | 326.40 | 18.84 | 16.88 | 61.93 | -0.16388 | 0.74524 |
| 7 | 362.65 | 200.63 | 18.88 | 16.99 | 51.83 | 0.24292 | 0.54993 |
| 8 | 387.38 | 176.65 | 19.17 | 17.10 | 54.13 | -0.12604 | 0.32410 |
| 9 | 188.60 | 71.17 | 18.86 | 17.32 | 38.24 | 0.39307 | 1.06903 |
| 10 | 515.26 | 161.27 | 20.27 | 17.30 | 65.70 | 0.63660 | 0.66299 |
| 11 | 317.60 | 345.95 | 19.42 | 17.26 | 49.32 | 0.57281 | -0.01221 |
| 12 | 177.99 | 120.84 | 19.36 | 17.32 | 36.09 | -0.55801 | 0.50400 |
| 13 | 69.27 | 78.94 | 19.48 | 17.46 | 28.00 | -0.85289 | -0.33165 |
| 14 | 165.81 | 225.45 | 19.40 | 17.50 | 34.13 | -0.07401 | 0.05096 |
| 15 | 286.92 | 99.31 | 19.80 | 17.42 | 46.08 | -0.10284 | 0.15472 |
| 16 | 446.87 | 215.81 | 19.75 | 17.62 | 59.40 | -0.41992 | 0.69992 |
| 17 | 352.35 | 242.43 | 19.68 | 17.73 | 50.98 | -1.16913 | -0.14999 |
| 18 | 354.09 | 245.77 | 20.15 | 18.22 | 51.15 | 0.03998 | -0.06592 |
| 19 | 285.43 | 299.33 | 20.23 | 18.15 | 45.59 | 0.15808 | -0.47211 |
| 20 | 58.98 | 111.96 | 20.76 | 18.39 | 26.02 | -0.23930 | -0.26199 |
| 21 | 86.85 | 93.25 | 20.39 | 18.56 | 28.96 | -0.78171 | 0.26367 |
| 22 | 504.60 | 96.09 | 20.76 | 18.69 | 65.40 | -0.01007 | 0.02281 |
| 23 | 158.24 | 100.59 | 21.44 | 18.77 | 34.83 | 0.14709 | -0.45296 |
| 24 | 440.08 | 121.06 | 20.97 | 18.85 | 59.32 | -0.16296 | -0.30693 |
| 25 | 80.86 | 121.03 | 22.24 | 19.26 | 27.63 | 0.60005 | -0.37399 |
| 26 | 458.54 | 107.33 | 21.14 | 19.17 | 61.14 | 0.19012 | -0.13794 |
| 27 | 441.84 | 370.88 | 21.75 | 19.27 | 60.71 | 0.05798 | -0.29205 |
| 28 | 377.99 | 92.63 | 21.35 | 19.25 | 54.23 | -0.18524 | -0.54657 |
| 29 | 226.03 | 153.90 | 21.07 | 19.28 | 39.84 | -0.01404 | 0.52094 |
| 30 | 417.73 | 272.87 | 21.20 | 19.43 | 57.06 | 0.12390 | -0.32196 |

$X$ and $Y$ are star positions in pixel coordinates on the WFC4 chip of WFPC2 based on the 2007 data. $r$ is the cluster-centric distance in arcsecond. $\mu_x$ and $\mu_y$ are relative proper motions' components along the $x$ and $y$ directions of (WFC4) pixel coordinates (2007). $V$ and $I$ magnitudes are from the 1997 WFPC2 data.

Table A.15: The $VI$ photometry and relative proper motions of the member stars on the WFC4 chip of WFPC2 (II).

| No. | $X$ | $Y$ | $V$ | $I$ | $r(''$) | $\mu_x$(mas/yr) | $\mu_y$(mas/yr) |
|---|---|---|---|---|---|---|---|
| 31 | 267.39 | 275.64 | 22.75 | 19.60 | 43.65 | 0.21118 | -0.44678 |
| 32 | 109.85 | 151.71 | 21.35 | 19.39 | 29.53 | 0.12604 | -0.25513 |
| 33 | 461.05 | 219.06 | 23.02 | 19.60 | 60.68 | -0.29694 | 0.37399 |
| 34 | 519.69 | 99.26 | 22.63 | 19.63 | 66.70 | 0.29114 | -0.24399 |
| 35 | 250.84 | 135.20 | 21.49 | 19.45 | 42.29 | -0.10712 | -1.21704 |
| 36 | 492.18 | 198.55 | 21.57 | 19.49 | 63.48 | -0.71106 | -0.59097 |
| 37 | 448.13 | 107.07 | 21.86 | 19.70 | 60.22 | -0.23804 | -0.73097 |
| 38 | 226.51 | 76.14 | 22.13 | 19.73 | 41.35 | -0.29190 | -0.36797 |
| 39 | 549.20 | 160.43 | 21.85 | 19.87 | 68.75 | -0.49316 | -0.61111 |
| 40 | 557.28 | 273.59 | 22.52 | 20.03 | 69.57 | 0.62317 | -0.60394 |
| 41 | 592.70 | 147.33 | 22.38 | 20.03 | 72.74 | -0.07019 | -0.02304 |
| 42 | 386.56 | 203.95 | 22.28 | 20.12 | 53.97 | 0.29297 | -1.01608 |
| 43 | 155.64 | 196.91 | 22.01 | 19.95 | 33.21 | 0.25696 | -1.33789 |
| 44 | 397.20 | 142.06 | 22.92 | 20.25 | 55.26 | 1.11816 | -0.46707 |
| 45 | 394.49 | 392.47 | 23.07 | 20.28 | 57.11 | -0.54321 | 0.22980 |
| 46 | 288.93 | 111.01 | 23.02 | 20.45 | 46.05 | 0.16693 | -1.11801 |

# B

# The extinction curve in NGC 3603

Table B.1: The $UBVRI$ photometry of the member stars on the PC chip of WFPC2 (I).

| No. | $X$ | $Y$ | $U$ | $B$ | $V$ | $R$ | $I$ |
|---|---|---|---|---|---|---|---|
| 1 | 440.96 | 405.70 | 12.82 | 12.98 | 11.95 | 11.15 | 10.32 |
| 2 | 433.96 | 452.18 | 13.42 | 13.61 | 12.65 | 11.88 | 11.15 |
| 3 | 335.40 | 483.77 | 13.63 | 13.84 | 12.89 | 12.15 | 11.34 |
| 4 | 406.67 | 507.59 | 13.83 | 14.04 | 13.19 | 12.41 | 11.56 |
| 5 | 423.48 | 492.34 | 13.86 | 14.06 | 13.11 | 12.36 | 11.61 |
| 6 | 358.14 | 414.30 | 13.96 | 14.13 | 13.18 | 12.40 | 11.59 |
| 7 | 411.37 | 509.28 | 14.07 | 14.26 | 13.39 | 12.60 | 11.80 |
| 8 | 306.50 | 575.18 | 13.91 | 14.13 | 13.21 | 12.49 | 11.70 |
| 9 | 430.64 | 443.13 | 14.01 | 14.19 | 13.28 | 12.51 | 11.66 |
| 10 | 360.86 | 482.15 | 14.03 | 14.24 | 13.36 | 12.63 | 11.85 |
| 11 | 424.62 | 481.30 | 14.27 | 14.45 | 13.46 | 12.74 | 11.90 |
| 12 | 592.19 | 510.26 | 14.47 | 14.64 | 13.69 | 12.86 | 11.96 |
| 13 | 508.43 | 581.51 | 14.31 | 14.50 | 13.58 | 12.80 | 12.02 |
| 14 | 397.43 | 442.79 | 14.34 | 14.54 | 13.63 | 12.91 | 12.08 |
| 15 | 456.40 | 371.74 | 14.51 | 14.66 | 13.69 | 12.92 | 12.08 |

$X$ and $Y$ are star positions in pixel coordinates on the PC chip of WFPC2 based on the 2007 data. $UB$ photometry is from ACS, and $VRI$ WFPC2 2007.

Table B.2: The $UBVRI$ photometry of the member stars on the PC chip of WFPC2 (II).

| No. | $X$ | $Y$ | $U$ | $B$ | $V$ | $R$ | $I$ |
|---|---|---|---|---|---|---|---|
| 16 | 451.84 | 453.83 | 14.81 | 14.99 | 13.81 | 13.05 | 12.12 |
| 17 | 451.84 | 453.83 | 15.32 | 15.51 | 13.81 | 13.05 | 12.12 |
| 18 | 328.65 | 495.76 | 14.76 | 14.94 | 14.04 | 13.29 | 12.46 |
| 19 | 415.77 | 490.42 | 15.10 | 15.29 | 14.44 | 13.64 | 12.81 |
| 20 | 519.94 | 282.45 | 14.73 | 14.88 | 13.90 | 13.11 | 12.26 |
| 21 | 400.74 | 351.69 | 14.90 | 15.07 | 14.15 | 13.33 | 12.49 |
| 22 | 458.18 | 569.62 | 14.68 | 14.90 | 14.04 | 13.27 | 12.46 |
| 23 | 406.79 | 569.16 | 14.71 | 14.90 | 14.01 | 13.28 | 12.55 |
| 24 | 395.27 | 497.34 | 15.02 | 15.20 | 14.35 | 13.57 | 12.74 |
| 25 | 391.70 | 549.94 | 14.98 | 15.17 | 14.25 | 13.51 | 12.71 |
| 26 | 512.32 | 419.47 | 15.24 | 15.40 | 14.40 | 13.68 | 12.81 |
| 27 | 296.15 | 315.34 | 15.19 | 15.34 | 14.38 | 13.48 | 12.65 |
| 28 | 402.42 | 382.65 | 15.04 | 15.20 | 14.28 | 13.48 | 12.66 |
| 29 | 397.72 | 446.06 | 15.17 | 15.35 | 14.36 | 13.63 | 12.76 |
| 30 | 264.71 | 465.06 | 15.04 | 15.23 | 14.31 | 13.55 | 12.73 |
| 31 | 383.91 | 479.83 | 14.97 | 15.18 | 14.37 | 13.59 | 12.78 |
| 32 | 411.61 | 515.08 | 15.26 | 15.46 | 14.49 | 13.80 | 13.00 |
| 33 | 477.36 | 496.19 | 15.25 | 15.44 | 14.56 | 13.80 | 12.94 |
| 34 | 336.66 | 433.13 | 15.79 | 15.95 | 14.98 | 14.26 | 13.46 |
| 35 | 317.77 | 326.87 | 15.47 | 15.63 | 14.72 | 13.90 | 13.13 |
| 36 | 343.11 | 484.12 | 15.61 | 15.80 | 14.93 | 14.15 | 13.34 |
| 37 | 302.47 | 467.23 | 15.44 | 15.63 | 14.77 | 13.94 | 13.07 |
| 38 | 318.11 | 548.15 | 15.67 | 15.81 | 14.98 | 14.04 | 13.18 |
| 39 | 391.79 | 470.74 | 15.35 | 15.55 | 14.75 | 13.97 | 13.19 |
| 40 | 547.41 | 266.25 | 15.64 | 15.77 | 14.88 | 14.07 | 13.21 |
| 41 | 384.99 | 538.98 | 15.61 | 15.80 | 14.93 | 14.18 | 13.35 |
| 42 | 93.93 | 382.71 | 15.91 | 16.00 | 14.94 | 14.05 | 13.19 |
| 43 | 385.29 | 354.73 | 15.98 | 16.13 | 15.24 | 14.44 | 13.71 |
| 44 | 473.77 | 446.05 | 15.72 | 15.87 | 14.99 | 14.19 | 13.35 |
| 45 | 525.48 | 360.35 | 15.75 | 15.90 | 14.98 | 14.21 | 13.35 |
| 46 | 415.33 | 515.52 | 15.85 | 16.03 | 15.12 | 14.36 | 13.57 |
| 47 | 339.19 | 346.46 | 15.93 | 16.03 | 15.08 | 14.25 | 13.38 |
| 48 | 451.76 | 490.02 | 15.70 | 15.90 | 14.98 | 14.27 | 13.44 |
| 49 | 396.14 | 537.79 | 15.82 | 15.99 | 15.11 | 14.39 | 13.60 |
| 50 | 385.39 | 354.72 | 15.98 | 16.13 | 15.18 | 14.50 | 13.64 |
| 51 | 431.04 | 515.74 | 16.15 | 16.30 | 15.32 | 14.62 | 13.77 |
| 52 | 444.88 | 284.18 | 16.17 | 16.28 | 15.30 | 14.54 | 13.69 |
| 53 | 557.72 | 456.39 | 16.25 | 16.37 | 15.39 | 14.64 | 13.81 |
| 54 | 516.89 | 420.43 | 16.61 | 16.66 | 15.64 | 14.89 | 13.99 |
| 55 | 407.90 | 297.98 | 16.38 | 16.50 | 15.48 | 14.74 | 13.89 |

Table B.3: The $UBVRI$ photometry of the member stars on the PC chip of WFPC2 (III).

| No. | $X$ | $Y$ | $U$ | $B$ | $V$ | $R$ | $I$ |
|---|---|---|---|---|---|---|---|
| 56 | 456.91 | 492.37 | 16.38 | 16.54 | 15.53 | 14.81 | 13.98 |
| 57 | 279.55 | 568.55 | 16.25 | 16.38 | 15.46 | 14.77 | 13.95 |
| 58 | 279.55 | 568.55 | 16.25 | 16.38 | 15.46 | 14.77 | 13.95 |
| 59 | 544.56 | 364.28 | 16.43 | 16.56 | 15.55 | 14.81 | 13.98 |
| 60 | 617.10 | 474.55 | 16.55 | 16.61 | 15.61 | 14.84 | 13.98 |
| 61 | 529.96 | 486.76 | 16.52 | 16.66 | 15.65 | 14.91 | 14.07 |
| 62 | 307.49 | 535.12 | 16.38 | 16.55 | 15.63 | 14.94 | 14.15 |
| 63 | 635.49 | 511.55 | 16.64 | 16.76 | 15.74 | 14.99 | 14.16 |
| 64 | 111.74 | 470.06 | 16.65 | 16.78 | 15.78 | 15.06 | 14.24 |
| 65 | 113.36 | 486.07 | 16.78 | 16.87 | 15.85 | 15.10 | 14.21 |
| 66 | 512.67 | 392.67 | 18.11 | 17.69 | 16.31 | 15.27 | 14.14 |
| 67 | 401.18 | 486.50 | 16.76 | 16.89 | 15.94 | 15.24 | 14.43 |
| 68 | 445.04 | 601.62 | 16.80 | 16.93 | 15.98 | 15.27 | 14.42 |
| 69 | 460.86 | 473.07 | 16.93 | 17.03 | 16.06 | 15.38 | 14.54 |
| 70 | 78.41 | 300.67 | 17.29 | 17.25 | 16.21 | 15.41 | 14.50 |
| 71 | 284.54 | 448.20 | 16.97 | 17.08 | 16.06 | 15.33 | 14.50 |
| 72 | 391.73 | 478.88 | 17.03 | 17.12 | 16.19 | 15.50 | 14.63 |
| 73 | 327.73 | 483.97 | 17.15 | 17.15 | 16.16 | 15.42 | 14.61 |
| 74 | 350.34 | 341.19 | 17.13 | 17.14 | 16.12 | 15.38 | 14.52 |
| 75 | 464.28 | 466.19 | 17.17 | 17.23 | 16.29 | 15.57 | 14.73 |
| 76 | 243.54 | 570.77 | 17.09 | 17.20 | 16.17 | 15.48 | 14.65 |
| 77 | 206.59 | 509.89 | 17.18 | 17.19 | 16.20 | 15.47 | 14.66 |
| 78 | 273.78 | 439.27 | 17.17 | 17.26 | 16.31 | 15.53 | 14.63 |
| 79 | 504.94 | 503.74 | 17.29 | 17.35 | 16.33 | 15.56 | 14.71 |
| 80 | 444.48 | 510.46 | 17.26 | 17.32 | 16.37 | 15.65 | 14.78 |
| 81 | 489.00 | 675.72 | 17.83 | 17.76 | 16.54 | 15.67 | 14.73 |
| 82 | 464.19 | 238.30 | 17.56 | 17.54 | 16.39 | 15.63 | 14.76 |
| 83 | 572.28 | 339.95 | 17.71 | 17.70 | 16.50 | 15.71 | 14.78 |
| 84 | 522.16 | 564.66 | 17.44 | 17.46 | 16.49 | 15.70 | 14.82 |
| 85 | 286.50 | 586.98 | 18.78 | 17.77 | 16.59 | 15.73 | 14.69 |
| 86 | 318.00 | 375.36 | 18.78 | 17.99 | 16.70 | 15.79 | 14.76 |
| 87 | 213.46 | 397.64 | 19.01 | 18.23 | 16.88 | 15.85 | 14.75 |
| 88 | 502.30 | 376.65 | 17.63 | 17.65 | 16.60 | 15.84 | 14.98 |
| 89 | 250.74 | 313.38 | 17.77 | 17.81 | 16.66 | 15.87 | 14.96 |
| 90 | 376.89 | 432.95 | 17.80 | 17.80 | 16.70 | 15.97 | 15.12 |
| 91 | 458.74 | 631.34 | 18.30 | 18.31 | 17.00 | 15.97 | 14.97 |
| 92 | 339.77 | 440.80 | 17.71 | 17.72 | 16.67 | 15.94 | 15.07 |
| 93 | 182.52 | 455.58 | 17.88 | 17.77 | 16.72 | 15.97 | 15.11 |
| 94 | 505.33 | 258.45 | 17.92 | 17.93 | 16.81 | 16.03 | 15.13 |
| 95 | 282.92 | 503.06 | 17.65 | 17.69 | 16.70 | 15.99 | 15.17 |

Table B.4: The $UBVRI$ photometry of the member stars on the PC chip of WFPC2 (IV).

| No. | $X$ | $Y$ | $U$ | $B$ | $V$ | $R$ | $I$ |
|---|---|---|---|---|---|---|---|
| 96 | 381.58 | 256.02 | 18.34 | 18.27 | 16.91 | 16.11 | 15.17 |
| 97 | 381.58 | 256.02 | 19.91 | 19.51 | 16.91 | 16.11 | 15.17 |
| 98 | 574.54 | 582.98 | 18.32 | 18.00 | 16.89 | 16.10 | 15.20 |
| 99 | 486.74 | 425.35 | 17.89 | 17.89 | 16.87 | 16.13 | 15.25 |
| 100 | 553.60 | 460.36 | 18.11 | 17.99 | 16.88 | 16.10 | 15.21 |
| 101 | 146.56 | 393.07 | 18.10 | 18.08 | 16.95 | 16.17 | 15.28 |
| 102 | 451.13 | 399.71 | 19.23 | 18.22 | 17.15 | 16.19 | 15.20 |
| 103 | 379.32 | 246.29 | 18.26 | 18.18 | 17.00 | 16.17 | 15.20 |
| 104 | 484.71 | 300.86 | 18.09 | 18.05 | 16.96 | 16.18 | 15.28 |
| 105 | 508.83 | 415.48 | 18.45 | 18.19 | 17.05 | 16.28 | 15.40 |
| 106 | 519.83 | 296.92 | 19.47 | 18.62 | 17.17 | 16.29 | 15.28 |
| 107 | 540.45 | 668.03 | 18.49 | 18.49 | 17.18 | 16.29 | 15.26 |
| 108 | 558.51 | 473.87 | 18.50 | 18.42 | 17.10 | 16.34 | 15.44 |
| 109 | 476.66 | 441.29 | 18.22 | 18.19 | 17.11 | 16.38 | 15.54 |
| 110 | 435.62 | 515.50 | 18.06 | 18.12 | 17.14 | 16.40 | 15.53 |
| 111 | 250.99 | 496.11 | 18.12 | 18.11 | 17.04 | 16.33 | 15.46 |
| 112 | 320.07 | 447.74 | 18.20 | 18.15 | 17.10 | 16.38 | 15.50 |
| 113 | 150.08 | 446.91 | 18.29 | 18.22 | 17.20 | 16.47 | 15.61 |
| 114 | 356.34 | 271.26 | 18.26 | 18.24 | 17.18 | 16.40 | 15.52 |
| 115 | 451.89 | 568.46 | 18.59 | 18.47 | 17.26 | 16.49 | 15.66 |
| 116 | 411.95 | 403.50 | 18.42 | 18.40 | 17.30 | 16.52 | 15.66 |
| 117 | 299.27 | 703.50 | 18.35 | 18.36 | 17.25 | 16.49 | 15.57 |
| 118 | 314.91 | 525.00 | 18.48 | 18.35 | 17.33 | 16.56 | 15.66 |
| 119 | 555.50 | 670.08 | 19.15 | 18.78 | 17.49 | 16.60 | 15.63 |
| 120 | 604.52 | 451.61 | 18.53 | 18.42 | 17.39 | 16.61 | 15.71 |
| 121 | 473.66 | 382.01 | 18.57 | 18.41 | 17.37 | 16.62 | 15.72 |
| 122 | 449.23 | 215.52 | 18.89 | 18.54 | 17.45 | 16.64 | 15.72 |
| 123 | 193.08 | 584.58 | 18.49 | 18.45 | 17.36 | 16.66 | 15.80 |
| 124 | 467.44 | 605.47 | 19.02 | 18.74 | 17.68 | 16.89 | 16.00 |
| 125 | 193.37 | 554.51 | 18.82 | 18.66 | 17.66 | 16.88 | 16.07 |

Table B.5: The $UBVRI$ photometry of the member stars on the PC chip of WFPC2 (V).

| No. | $X$ | $Y$ | $U$ | $B$ | $V$ | $R$ | $I$ |
|---|---|---|---|---|---|---|---|
| 126 | 461.91 | 527.82 | 19.13 | 18.81 | 17.76 | 17.02 | 16.15 |
| 127 | 409.73 | 345.78 | 19.16 | 18.83 | 17.81 | 17.01 | 16.15 |
| 128 | 543.92 | 442.49 | 20.04 | 19.49 | 17.85 | 17.04 | 16.12 |
| 129 | 391.85 | 654.90 | 19.54 | 19.22 | 17.96 | 17.08 | 16.15 |
| 130 | 510.25 | 472.06 | 19.29 | 18.95 | 17.88 | 17.09 | 16.16 |
| 131 | 357.80 | 535.01 | 19.33 | 18.94 | 17.79 | 17.05 | 16.22 |
| 132 | 497.29 | 528.50 | 19.44 | 19.06 | 17.90 | 17.10 | 16.23 |
| 133 | 427.04 | 127.52 | 19.42 | 19.27 | 17.88 | 17.10 | 16.18 |
| 134 | 179.28 | 681.56 | 19.57 | 19.33 | 18.09 | 17.16 | 16.14 |
| 135 | 264.43 | 598.97 | 19.28 | 19.03 | 17.90 | 17.16 | 16.33 |
| 136 | 353.74 | 218.71 | 19.88 | 19.39 | 18.04 | 17.21 | 16.32 |
| 137 | 435.64 | 237.89 | 19.91 | 19.47 | 18.03 | 17.23 | 16.35 |
| 138 | 666.66 | 601.83 | 20.36 | 19.73 | 18.19 | 17.30 | 16.36 |
| 139 | 331.51 | 619.19 | 19.56 | 19.24 | 18.09 | 17.32 | 16.44 |
| 140 | 473.23 | 474.35 | 20.28 | 19.65 | 18.31 | 17.45 | 16.55 |
| 141 | 312.76 | 676.50 | 20.31 | 19.47 | 18.18 | 17.35 | 16.40 |
| 142 | 234.46 | 526.03 | 19.32 | 19.18 | 18.11 | 17.34 | 16.47 |
| 143 | 213.05 | 369.58 | 19.60 | 19.35 | 18.14 | 17.34 | 16.47 |
| 144 | 479.54 | 379.99 | 19.76 | 19.40 | 18.25 | 17.44 | 16.53 |
| 145 | 618.64 | 555.82 | 20.03 | 19.58 | 18.26 | 17.43 | 16.51 |
| 146 | 250.11 | 539.49 | 19.66 | 19.28 | 18.16 | 17.40 | 16.54 |
| 147 | 245.71 | 347.11 | 20.06 | 19.46 | 18.23 | 17.44 | 16.57 |
| 148 | 562.93 | 303.38 | 20.12 | 19.53 | 18.27 | 17.47 | 16.59 |
| 149 | 144.08 | 486.67 | 19.99 | 19.49 | 18.34 | 17.55 | 16.66 |
| 150 | 527.25 | 464.67 | 20.14 | 19.69 | 18.40 | 17.56 | 16.65 |
| 151 | 145.18 | 501.87 | 20.19 | 19.51 | 18.40 | 17.61 | 16.71 |
| 152 | 223.00 | 408.90 | 20.16 | 19.74 | 18.38 | 17.59 | 16.71 |
| 153 | 382.30 | 423.29 | 20.04 | 19.63 | 18.39 | 17.63 | 16.69 |
| 154 | 300.16 | 353.15 | 20.27 | 19.80 | 18.42 | 17.60 | 16.74 |
| 155 | 280.28 | 594.71 | 20.16 | 19.69 | 18.50 | 17.75 | 16.88 |
| 156 | 343.61 | 790.64 | 20.55 | 20.02 | 18.64 | 17.78 | 16.82 |
| 157 | 491.39 | 518.75 | 20.11 | 19.95 | 18.65 | 17.86 | 16.99 |

# References


Alves, J. F., Lada, C. J., & Lada, E. A. 2001, nature, 409, 159

Adén, D., Wilkinson, M. I., Read, J. I., et al. 2009, ApJ, 706, L150

Allison, R. J., Goodwin, S. P., Parker, R. J., Portegies Zwart, S. F., & de Grijs, R. 2010, MNRAS, 407, 1098

Allison R.J., Goodwin S.P., Parker R.J., De Grijs R., Portegies Zwart S.F., Kouwenhoven M.B., 2009a, MNRAS, 395, 1449

Allison, R.J., Goodwin, S.P., Parker, R.J., De Grijs, R., Portegies, Zwart S.F., Kouwenhoven, M.B. 2009b, ApJ , 700, L99

Anderson, J., & King, I. R. 2003, AJ, 126, 772

Ascenso, J., Alves, J., & Lago, M. T. V. T. 2009, AAP, 495, 147

Baraffe, I., Chabrier, G., & Gallardo, J. 2009, ApJ 702, L27

Bastian, N. 2008, IAU Symposium, 246, 32

Bastian, N., & Goodwin, S. P. 2006, MNRAS, 369, L9

Bastien, P., Arcoragi, J.-P., Benz, W., Bonnell, I., & Martel, H. 1991, ApJ, 378, 255

Bate, M. R. 2009, MNRAS, 392, 590

Bate, M. R., & Bonnell, I. A. 2005, MNRAS, 356, 1201

Bate, M. R., Lubow, S. H., Ogilvie, G. I., & Miller, K. A. 2003a, MNRAS, 341, 213

Bate, M. R., Bonnell, I. A., & Bromm, V. 2003b, MNRAS, 339, 577

Baumgardt, H., & Kroupa, P. 2007, MNRAS, 380, 1589

Beccari, G., et al. 2010, ApJ, 720, 1108

Belloche, A., André, P., & Motte, F. 2001, From Darkness to Light: Origin and Evolution of Young Stellar Clusters, 243, 313

Bertoldi, F., & McKee, C. F. 1996, Self-regulated star formation in molecular clouds. In Amazing Light, ed. R.Y. Chiao (New York: Springer), 41

Bertoldi, F., & McKee, C. F. 1990, ApJ, 354, 529

Bertoldi, F. 1989, ApJ, 346, 735

Binney, J. & Tremaine, S. 1987, Galactic Dynamics

Bonatto, C., Santos, J. F. C., Jr., & Bica, E. 2006, AAP, 445, 567

Bonazzola, S., Perault, M., Puget, J. L., et al. 1992, Journal of Fluid Mechanics, 245, 1

Bonnell, I. A., Larson, R. B., & Zinnecker, H. 2007, Protostars and Planets V, 149

Bonnell, I. A., & Bate, M. R. 2006, MNRAS, 370, 488

Bonnell, I. A., Bate, M. R., & Vine, S. G. 2003, MNRAS, 343, 413

Bonnell, I. A., Bate, M. R., Clarke, C. J., & Pringle, J. E. 2001, MNRAS, 323, 785

Bonnell, I. A., Bate, M. R., & Zinnecker, H. 1998, MNRAS, 298, 93

Bonnell, I. A., & Davies, M. B. 1998, MNRAS, 295, 691

Bonnell, I. A., Bate, M. R., Clarke, C. J., & Pringle, J. E. 1997, MNRAS, 285, 201

Brandner, W., et al. 2000, AJ, 119, 292

Brandner, W.,Grebel, E. K., Chu, Y.-H., & Weis, K. 1997a, ApJ, 475, L45

Brandner, W., Chu, Y.-H., Eisenhauer, F., Grebel, E. K., & Points, S. D. 1997b, ApJ, 489, L153

Bressert, E., Bastian, N., Gutermuth, R., et al. 2010, MNRAS, 409, L54

Burkert, A., & Hartmann, L. 2004, ApJ, 616, 288

Burkert, A., Bate, M. R., & Bodenheimer, P. 1997, MNRAS, 289, 497

Calzetti, D., Armus, L., Bohlin, R. C., et al. 2000, ApJ, 533, 682

Calzetti, D., Kinney, A. L., & Storchi-Bergmann, T. 1996, ApJ, 458, 132

Calzetti, D., Kinney, A. L., & Storchi-Bergmann, T. 1994, ApJ, 429, 582

Cardelli, J. A., Clayton, G. C., & Mathis, J. S. 1989, ApJ, 345, 245

Cardelli, J. A., & Savage, B. D. 1988, ApJ, 325, 864

Caswell, J. L., Batchelor, R. A., Forster, J. R., & Wellington, K. J. 1989, Australian Journal of Physics, 42, 331

Chabrier, G. 2003, ApJ, 586, L133

Chini, R., & Kruegel, E. 1983, AAP, 117, 289

Clarke, C.J., Bonnell, I.A., Hillenbrand, L.A. 2000, In Protostars Planets IV, ed. Mannings, V. Boss, A.P., & Russell, S.S. (Tucson: Univ.Ariz.Press), 151

Clayton, C. A. 1990, MNRAS, 246, 712

Clayton, C. A. 1986, MNRAS, 219, 895

Chen, L., de Grijs, R., & Zhao, J. L. 2007, AJ, 134, 1368

Churchwell, E., Povich, M. S., Allen, D., et al. 2006, ApJ, 649, 759

Corbelli, E., Palla, F., & Zinnecker, H. 2005, The Initial Mass Function 50 Years Later, 327

Cottaar, M., Meyer, M. R., Andersen, M., & Espinoza, P. 2012, AAP, 539, A5

Crowther, P. A., Schnurr, O., Hirschi, R., Yusof, N., Parker, R. J., Goodwin, S. P., & Kassim, H. A. 2010, MNRAS, 408, 731

Crowther, P. A., Lennon, D. J., Walborn, N. R., & Smartt, S. J. 2008, in ASP Conf. Ser. 388, Mass Loss from Stars and the Evolution of Stellar Clusters, ed. A. de Koter, L. J. Smith, & L. B. F. M. Waters, (San Francisco, CA: ASP), 109

Crowther, P. A., & Dessart, L. 1998, MNRAS, 296, 622

Dame, T. M., Koper, E., Israel, F. P., & Thaddeus, P. 1993, ApJ, 418, 730

de Grijs, R., Gilmore, G. F., Mackey, A. D., et al. 2002, MNRAS, 337, 597

de Koter, A., Heap, S. R., & Hubeny, I. 1997, ApJ, 477, 792

de Pree, C. G., Nysewander, M. C., & Goss, W. M. 1999, AJ, 117, 2902

de Wit, W. J., Testi, L., Palla, F., & Zinnecker, H. 2005, AAP, 437, 247

Dolphin, A.E. 2005, HSTphot User's Guide, http://purcell.as.arizona.edu/hstphot/

Dolphin, A.E. 2000a, PASP, 112, 1383

Dolphin, A. E. 2000b, PASP, 112, 1397

Draine, B. T. 2010, Physics of the Interstellar and Intergalactic Medium, Priceton University Press

Draine, B. T. 2009, CosmicDust - Near and Far, 414, 453

Draine, B. T., & Li, A. 2001, ApJ, 551, 807

Draine, B. 1989, Interstellar Dust, 135, 313

Draine, B. T., & Salpeter, E. E. 1979, ApJ, 231, 438

Dressel, L., et al. 2011, Wide Field Camera 3 Instrument Handbook, Version 4.0 (Baltimore: STScI), http://www.stsci.edu/hst/wfc3/phot_zp_lbn

Drissen, L. 1999, in IAU Symp. 193, Wolf-Rayet Phenomena in Massive Stars and Starburst Galaxies, ed. van der Hucht, K. A., Koenigsberger, G., & Eenens, P. R. J. (San Francisco: ASPS), 403

Drissen, L., Moffat, A. F. J., Walborn, N. R., & Shara, M. M. 1995, AJ, 110, 2235

Edgar, R., & Clarke, C. 2004, MNRAS, 349, 678

Eisenhauer, F., Quirrenbach, A., Zinnecker, H., & Genzel, R. 1998, ApJ, 498, 278

Fitzpatrick, E. L., & Massa, D. 2009, ApJ, 699, 1209

Fitzpatrick, E. L., & Massa, D. 2007, ApJ, 663, 320

Fitzpatrick, E. L. 1999, PASP, 111, 63

Fitzpatrick, E. L., & Massa, D. 1990, ApJS, 72, 163

García-Rojas, J., Esteban, C., Peimbert, M., Costado, M. T., Rodríguez, M., Peimbert, A., & Ruiz, M. T. 2006, MNRAS, 368, 253

Geyer, M. P., & Burkert, A. 2001, MNRAS, 323, 988

Gies, D. R. 1987, ApJS, 64, 545

Gieles, M., Sana, H., & Portegies Zwart, S. F. 2010, MNRAS, 402, 1750

Goebel, J. H., Cheeseman, P., & Gerbault, F. 1995, ApJ, 449, 246

Golimowski, D. A., Burrows, C. J., Kulkarni, S. R., Oppenheimer, B. R., & Brukardt, R. A. 1998, AJ, 115, 2579

Goodwin, S. P. 2009, Astrophysics and Space Science, 324, 259

Goodwin, S. P., Bastian, N. 2006, MNRAS, 373, 752

Gouliermis, D., Keller, S. C., Kontizas, M., Kontizas, E., & Bellas-Velidis, I. 2004, AAP, 416, 137

Grebel, E. K. 2005, in The Initial Mass Function 50 Years Later, ASSL Vol. 327, ed. E. Corbelli, F. Palla, & H. Zinnecker (Dordrecht: Springer), 153

Grebel, E. K., & Gallagher, J. S. 2004, in ASP Conf. Ser. 322, The Formation and Evolution of Massive Young Star Clusters, ed. H. J. G. L. M. Lamers, L. J. Smith, & A. Nota (San Francisco,CA: ASP), 101

Grebel, E. K., & Chu, Y.-H. 2000, AJ, 119, 787

Grebel, E. K., Roberts, W. J., & Brandner, W. 1996, AAP, 311, 470

Gritschneder, M., Burkert, A., Naab, T., & Walch, S. 2010, ApJ, 723, 971

Harayama, Y., Eisenhauer, F., Martins, F. 2008, ApJ, 675, 1319

Hendry, M. A., Smartt, S. J., Skillman, E. D., Evans, C. J., Trundle, C., Lennon, D. J., Crowther, P. A., & Hunter, I. 2008, MNRAS, 388, 1127

Hillenbrand, L. A., & Carpenter, J. M. 2000, ApJ, 540, 236

Hillenbrand, L.A., Hartmann, L.E. 1998, ApJ, 492, 540

Hillenbrand, L. A. 1997, AJ, 113, 1733

Hills, J. G. 1980, ApJ, 235, 986

Holtzman, J. A., Afonso, C., & Dolphin, A. 2006, ApJS, 166, 534

Holtzman, J. A., Burrows, C. J., Casertano, S., Hester, J. J., Trauger, J. T., Watson, A. M., & Worthey, G. 1995, PASP, 107, 1065

Hosokawa, T., Offner, S. S. R., & Krumholz, M. R. 2011, ApJ, 738, 140

Ianna, P. A., Adler, D. S., & Faudree, E. F. 1987, AJ, 93, 347

Ibata, R. A., & Lewis, G. F. 1998, AJ, 116, 2569

Jiang, Z., Yao, Y., Yang, J., et al. 2002, ApJ, 577, 245

Jones, B. F., & Walker, M. F. 1988, AJ, 95, 1755

Johnson, H. L., & Morgan, W. W. 1953, ApJ, 117, 313

Kirk, H., Johnstone, D., & Tafalla, M. 2007, ApJ, 668, 1042

Kirk, J. M., Ward-Thompson, D., & André, P. 2005, MNRAS, 360, 1506

King, I. 1962, AJ, 67, 471

Klessen, R. S., Burkert, A., & Bate, M. R. 1998, ApJ, 501, L205

Koekemoer, A.M., et al. 2002, HST Dither Handbook, Version 2.0, (Baltimore: STScI)

Kouwenhoven, M. B. N., Brown, A. G. A., Portegies Zwart, S. F., & Kaper, L. 2007, AAP, 474, 77

Krist, J. 1993, Astronomical Data Analysis Software and Systems II, 52, 536

Kroupa, P., Weidner, C., Pflamm-Altenburg, J., et al. 2011, arXiv:1112.3340

Kroupa, P. 2002, Science, 295, 82

Kroupa, P. 2001, MNRAS, 322, 231

Küpper, A. H. W., Maschberger, T., Kroupa, P., & Baumgardt, H. 2011, MNRAS, 417, 2300

Lada, C. J., & Lada, E. A. 2003, ARAA, 41, 57

Larson, R. B. 2003, Galactic Star Formation Across the Stellar Mass Spectrum, 287, 65

Larson, R. B. 1972, MNRAS, 157, 121

Larson, R. B., & Starrfield, S. 1971, AAP, 13, 190

Larsen, S. S., Origlia, L., Brodie, J., & Gallagher, J. S. 2008, MNRAS, 383, 263

Lata, S., Pandey, A. K., Maheswar, G., Mondal, S., & Kumar, B. 2011, MNRAS, 418, 1346

Lebouteiller, V., Bernard-Salas, J., Brandl, B., Whelan, D. G., Wu, Y., Charmandaris, V., Devost, D., & Houck, J. R. 2008, ApJ, 680, 398

Lebouteiller, V., Brandl, B., Bernard-Salas, J., Devost, D., & Houck, J. R. 2007, ApJ, 665, 390

Lejeune, T., Schaerer, D. 2001, AAP, 366, 538

Luhman, K. L., Rieke, G. H., Young, E. T., et al. 2000, ApJ, 540, 1016

Luhman, K. L., Rieke, G. H., Lada, C. J., & Lada, E. A. 1998, ApJ, 508, 347

Nakano, T., Hasegawa, T., Morino, J.-I., & Yamashita, T. 2000, ApJ, 534, 976

Nürnberger, D. E. A., & Stanke, T. 2003, AAP, 400, 223

Nürnberger, D. E. A., Bronfman, L., Yorke, H. W., & Zinnecker, H. 2002, AAP, 394, 253

Mackey, A. D., & Gilmore, G. F. 2003, MNRAS, 338, 85

Mackey, J., & Lim, A. J. 2010, MNRAS, 403, 714

Maclean, S., Duley, W. W., & Millar, T. J. 1982, ApJ, 256, L61

Martins, F., Schaerer, D., & Hillier, D. J. 2005, AAP, 436, 1049

Maschberger, T., & Clarke, C. J. 2011, MNRAS, 416, 541

Massa, D., Savage, B. D., & Fitzpatrick, E. L. 1983, ApJ, 266, 662

Massey, P., & Hunter, D. A. 1998, ApJ, 493, 180

Mathis, J. S. 1987, Exploring the Universe with the IUE Satellite, 129, 517

Mathis, J. S., & Wallenhorst, S. G. 1981, ApJ, 244, 483

Mathis, J. S., Rumpl, W., & Nordsieck, K. H. 1977, ApJ, 217, 425

Maíz Apellániz, J. 2008, ApJ, 677, 1278

McCrady, N., Graham, J. R., & Vacca, W. D. 2005, ApJ, 621, 278

McCrady, N., Gilbert, A. M., & Graham, J. R. 2003, ApJ, 596, 240

McKee, C. F., & Ostriker, E. C. 2007, ARAA, 45, 565

McKee, C. F., & Tan, J. C. 2003, ApJ, 585, 850

McKee, C. F., & Tan, J. C. 2002, Nature, 416, 59

McMaster, M., Biretta, J., et al. 2008, WFPC2 Instrument Handbook, Version 10.0 (Baltimore: STScI)

McMillan, S. L. W., Vesperini, E., & Portegies Zwart, S. F. 2007, ApJ, 655, L45

Megeath, S. T., Wilson, T. L., & Corbin, M. R. 2005, ApJ, 622, L141

Mengel, S., & Tacconi-Garman, L. E. 2008, IAU Symposium, 246, 113

Melena, N. W., Massey, P., Morrell, N. I., & Zangari, A. M. 2008, AJ, 135, 878

Melnick, J., Tapia, M., & Terlevich, R. 1989, AAP, 213, 89

Miller, G. E., & Scalo, J. M. 1979, ApJS, 41, 513

Moeckel, N., & Bate, M. R. 2010, MNRAS, 404, 721

Moeckel, N., & Bonnell, I. A. 2009, MNRAS, 400, 657

McMillan, S. L. W., Vesperini, E., & Portegies Zwart, S. F. 2007, ApJ, 655, L45

Moffat, A. F. J. 1983, AAP, 124, 273

Odenkirchen, M., Grebel, E. K., Dehnen, W., Rix, H.-W., & Cudworth, K. M. 2002, AJ, 124, 1497

Olczak, C., Spurzem, R., & Henning, T. 2011, AAP, 532, A119

Osterbrock, D.E. 1989, Astrophysics of Gaseous Nebulae and Active Galactic Nuclei, (Mill Vally, CA: University Science Books)

Pandey, A. K., Ogura, K., & Sekiguchi, K. 2000, PASJ, 52, 847

Pang, X., Pasquali, A., & Grebel, E. K. 2012b, The extinction curve in NGC 3603, in preparation

Pang, X., Grebel, E. K. & Altmann, M. 2012a, submitted to AJ, now is under review

Pang, X., Pasquali, A., & Grebel, E. K. 2011, AJ, 142, 132

Pang, X., Grebel, E. K., & Altmann, M. 2010, in Star clusters: basic galactic building blocks throughout time and space, IAU Symp. 266, ed. R. de Grijs, & J. Lepine (Cambridge: CUP), 24

Parker, R. J., Bouvier, J., Goodwin, S. P., et al. 2011, MNRAS, 412, 2489

Pfalzner, S. 2009, AAP, 498, L37

Pringle, J. E., Allen, R. J., & Lubow, S. H. 2001, MNRAS, 327, 663

Pound, M. W. 1998, ApJ, 493, L113

Portegies Zwart, S. F., McMillan, S. L. W., & Gieles, M. 2010, ARAA, 48, 431

Proszkow, E.-M., & Adams, F. C. 2009, ApJS, 185, 486

Proszkow, E.-M., Adams, F. C., Hartmann, L. W., & Tobin, J. J. 2009, ApJ, 697, 1020

Pryor, C., & Meylan, G. 1993, Structure and Dynamics of Globular Clusters, 50, 357

Rochau, B., Brandner, W., Stolte, A., Gennaro, M., Gouliermis, D., Da Rio, N., Dzyurkevich, N., & Henning, T. 2010, ApJ, 716, L90

Röllig, M., Kramer, C., Rajbahak, C., et al. 2011, AAP, 525, A8

Román-Zúñiga, C. G., Lada, C. J., Muench, A., & Alves, J. F. 2007, ApJ, 664, 357

Sagar, R., Munari, U., & de Boer, K. S. 2001, MNRAS, 327, 23

Salpeter, E. E. 1955, ApJ, 121, 161

Sana, H., Momany, Y., Gieles, M., et al. 2010, AAP, 515, A26

Sanders, W. L. 1971, AAP, 14, 226

Savage, B. D., Massa, D., Meade, M., & Wesselius, P. R. 1985, ApJS, 59, 397

Seab, C. G., & Shull, J. M. 1983, ApJ, 275, 652

Seaton, M. J. 1979, MNRAS, 187, 73P

Seward, F.D. 1999, in Allen's Astrophysical Quantities, ed. A.N. Cox (New York: Springer), 197

Scalo, J. M. 1986, Fundamentals of Cosmic Physics, 11, 1

Schilbach, E., Kharchenko, N. V., Piskunov, A. E., Röser, S., & Scholz, R.-D. 2006, AAP, 456, 523

Schnurr, O., Casoli, J., Chené, A.-N., Moffat, A.F.J., St-Louis, N. 2008, MNRAS, 389, 38

Schmidt-Kaler Th. 1982, in Landolt-Börnstein, Neue Serie Gr.VI, Vol 2b (Springer, Berlin, Heidelberg, New York), p19

Schmutz, W., & Drissen, L. 1999, Revista Mexicana de Astronomia Astrofisica Conference Series, 8, 41

Shu, F. H., Milione, V., Gebel, W., et al. 1972, ApJ, 173, 557

Siess, L., Dufour, E.,& Forestini, M. 2000, AAP, 358, 593

Silk, J. 1982, ApJ, 256, 514

Smith, L. J., & Gallagher, J. S. 2001, MNRAS, 326, 1027

Smith, R., Fellhauer, M., Goodwin, S., & Assmann, P. 2011, MNRAS, 414, 3036

Spitzer, L., Jr. 1987, Dynamical Evolution of Globular Clusters, Princeton University Press

Spitzer, L., Jr. 1958, ApJ, 127, 17

Stahler, S. W., Shu, F. H., & Taam, R. E. 1980, ApJ, 241, 637

Stolte, A., Brandner, W., Brandl, B., & Zinnecker, H. 2006, AJ, 132, 253

Stolte, A., Brandner, W., Brandl, B., Zinnecker, H., Grebel, E.K., 2004, ApJ, 128, 765

Stolte, A., Grebel, E. K., Brandner, W., & Figer, D. F. 2002, AAP, 394, 459

Sung, H., & Bessell, M., 2004, ApJ, 127, 1014

Tapia, M., Bohigas, J., Pérez, B., Roth, M., & Ruiz, M. T. 2001, RMXAA, 37, 39

Testi, L., Sargent, A. I., Olmi, L., & Onello, J. S. 2000, ApJ, 540, L53

Thompson, R. I., Smith, B. A., & Hester, J. J. 2002, ApJ, 570, 749

Trumpler, R. J. 1930, Publications of the Astronomical Society of the Pacific, 42, 267

Urquhart, J. S., Morgan, L. K., & Thompson, M. A. 2009, AAP, 497, 789

Valencic, L. A., Clayton, G. C., & Gordon, K. D. 2004, ApJ, 616, 912

Vesperini, E., McMillan, S. L. W., & Portegies Zwart, S. 2009, ApJ, 698, 615

Walborn, N. R., Barbá, R. H., Brandner, W., et al. 1999, AJ, 117, 225

Weingartner, J. C., & Draine, B. T. 2001, ApJ, 548, 296

Williams, J. P., Blitz, L., & McKee, C. F. 2000, Protostars and Planets IV, 97

Wolfire, M. G., & Cassinelli, J. P. 1987, ApJ, 319, 850

Wood, K., Whitney, B. A.,Robitaille, T., & Draine, B. T. 2008, ApJ, 688, 1118

Yu, J., de Grijs, R., & Chen, L. 2011, ApJ, 732, 16

Zhai, C., Shao, M., Goullioud, R., & Nemati, B. 2011, arXiv:1102.2248

## List of some abbreviations:

A&A : Astronomy and Astrophysics
AAP : Astronomy and Astrophysics Panel Reports
AJ : Astronomical Journal
ApJ : Astrophysical Journal
ApJS : Astrophysical Journal Supplement
ARA&A: Annual Review of Astonomy and Astrophysics
PASJ : Publications of the Astronomical Society of Japan
PASP : Publications of the Astronomical Society of of the Pacific
MNRAS : Monthly Notices of the Royal Astronomical Society
RMXAA : Revista Mexicana de Astronomía y Astrofísica

# Acknowledgments

Thanksgiving is the will of God:
*Be joyful always; pray continually; give thanks in all circumstances, for this is God's will for you in Christ Jesus. (1 Thessalonians 5:18 )*
*Enter His gates with thanksgiving and His courts with praise; give thanks to Him and praise His name. (Psalm 100:4)*

It is my great pleasure to write the acknowledgments after all the hard work writing my thesis. With all my heart and all my soul, I first own my thanks to my LORD, Jesus Christ. Thanks for His presence when I faced difficulty in reducing dither-pattern images. I thank Him for being a patient listener when I complained about the dust and said I did not like it! He told me that love is patient; love is kind; love does not envy and boast; love always protects, always trusts, always hopes, always perseveres. And love never fails! Finally, instead of disliking the dust, I gradually fall in love with the tiny particles that are floating everywhere in the space. (The only bad thing is that I am reluctant to dust my room afterward.)

I am indebted to Him for placing all the lovely, kind, helpful persons around me. These people stand by my side, support me and shed tears with me all through those hard times whenever I wanted to give up.

I want to express my sincere gratitude to Prof. Dr. Eva Grebel, who supervised my PhD study. During the last three and a half years, I have been nourished with her broad knowledge of photometry on space telescopes and of star cluster evolution, have been inspired by her brilliant

insights, and guided by her scientific rigorousness. At the same time, she endowed me with considerable freedom for developing my ideas. I am also indebted to her for the helps with various non-scientific matters, such as lending me her comic book "Calvin & Hobbes", which makes her not only a supervisor but also a friend. Above all, I enjoyed a lot working with her.

I would like to cordially thank Dr. Anna Pasquali, who is an angel sent to me by God. When I cracked my brain on deriving a stellar reddening map of NGC 3603 and did not have an idea, I was "blind" like Paul on the road to Damascus (*Acts 9:1-9*). Anna showed up and open my eyes like the disciple Ananias open the eyes of Paul (*Acts 9:10-18*), introducing the Balmer decrement method to me. I thank Anna for her patience whenever I make mistakes, her encouragement when I made a mess, and her humbleness for letting me being the "boss". It is great fun to work with Anna as a colleague and a friend.

I thank my thesis committee: Dr. Henrik Beuther, Prof. Dr. Cornelis Dullemond and Prof. Dr. Jürgen Schaffner-Bielich for getting up early to attend my defense at 9:00 a.m. on 21 May 2012. I am grateful to my thesis referee Dr. Henrik Beuther for giving me advice on the star formation in the molecular cloud and for spending time on reviewing my thesis. I would like to thank Prof. Dr. Rainer Spurzem for the invitation to work in the Kavli Institute for Astronomy and Astrophysics at Peking University, and for many useful discussions on the dynamical evolution of star clusters. I want to convey my gratitude to Prof. Dr. Jay Gallagher who had great interest in my work and many fruitful discussions. I thank Dr. Guido De Marchi and Dr. Giacomo Beccari for joyful collaboration on the pre-main-sequence stars in NGC 3603 and the invitation to work at ESO in Garching. I thank Prof. Dr. Norbert Christlieb for discussions on the ESO proposal of cycle 86. Many thanks to IMPRS coordinator, Dr. Christian Fendt for helping me settle down in Heidelberg after my arrival in 2008.

I would like to thank all colleagues in Astronomisches Rechen-Institut in Heidelberg. I am grateful to Dr. Katrin Jordi and Dr. Katherina Glatt for helping me start research on star clusters. Many thanks to Dr. Martin Altmann for teaching me to derive relative proper motions of stars with IRAF and to plot "complicated" figures using Supermongo. I thank Dr. Christoph Olczak for his nice explanation about the dynamical evolution of star clusters, which served to significantly expand the discussion on the tangential velocity profile in Chapter 2. I thank Matthias Frank for providing his script to compute the shifts of ACS/HRC images. Special thanks to Angelos Kaloviduris for his painstaking German translation of the thesis abstract, to Avon Huxor for proof reading of this acknowledgment, and to Raoul Haschke for helps in debugging the latex file of my thesis. I thank Dr. Sophia Liano and Dr. Denija Crnojevic for introducing to me the software HSTphot and Dolphot. I thank my office mate Dr. Stefano Pasetto for numerous discussions on scientific matters. In particular, I thank Oleksiy Golubov for helpful discussions on the two-Gaussian fitting of the relative proper motion distribution and for helping me plot Figure 5.14. I thank my colleagues Jan Rybizki, Johannes Ludwig, and Raoul Haschke for many useful tips and advice with regard to German life. I also want to express my gratitude to Dr. Sonia Duffau and Dr. Shoko Jin for organization of social activities which I had a lot of fun with the Grebelians. Many

thanks to the company of my deskmate Samuel who teaches me to calm down whenever I am in panic. I am grateful to Frau Meyer for her administrative service. I thank Dr. Peter Schwekendiek for his numerous help with my computer problems.

This work could not have been completed in such a peaceful way without encouragements of my friends Xiaohui Zhang and Oleksiy Golubov whom I came to know in Heidelberg. In particular, I am deeply indebted to those who sincerely shared with me authentic fellowship and brotherhood of Christian faith in Heidelberg, Shanghai, Kaiserslautern, Vancouver, Darmstadt, Frankfurt, Göttingen, Karlsruhe, Hamburg. Especially, I want to express my deep acknowledgement to my close friends, sister Shirel Chao in Shanghai and brother John Hu in Vancouver for their prayers and supports. I am deeply grateful to brothers and sisters in the Kaiserslautern Gemeinschaft Christlicher Mission and Glory & Grace fellowship in Seckenheim for their earnest prayers. I thank Li Cui for her partnership in the children ministry. I also own my gratitude to Pastor Yang and his wife Yanzi, Pastor Jonni and his wife Ria for their guidance in building faith. In particular, I thank brother Xiaotong Zhu, sister Jia Li and Jia's mother for continually providing Friday dinner for me when I buried my head in writing the thesis. I thank brother Zhe Jiang and sister Yilu Chen who are my Chinese tea provider for the last few months of thesis writing. Special thanks to Oleksiy's mother, Antonina, for providing medical care when I was sick.

I am greatly indebted to my parents for their love, prayers, supports, and understanding. I thank my father for his encouragement when I got lost facing the future. I am grateful to my mother for teaching me the character of perseverance. I also thank my brother Xiaojia for his support and company during growth up. I am deeply indebted to the company of my "sons": Aslan, Nicky, Chandler, Runningtiger, Boaz, Romeo; my "daughters": Betty, Minzy, Juliet. Finally, I dedicate this thesis to my parents, whose love is more than I can describe.

March 12, 2012, Heidelberg

*But by the grace of God I am what I am, and his grace to me was not without effect. No, I worked harder than all of them–yet not I, but the grace of God that was with me.*
*(1 Corinthians 15:10 )*